(16)

IRRADIATION ASSISTED STRESS CORROSION CRACKING SUSCEPTIBILITY OF LOW FLUENCE STAINLESS STEELS EVALUATED BY IN-FLUX SLOW STRAIN RATE TESTS

by

BRUCE A. HILTON

B.S. Physics
Brigham Young University
(1990)

S.M. Nuclear Engineering
Massachusetts Institute of Technology
(1993)

Submitted to the Department of Nuclear Engineering
in Partial Fulfillment of the Requirements for the Degree of

Doctor of Philosophy
at the
Massachusetts Institute of Technology
February 1996

Signature of Author _____
Department of Nuclear Engineering
October 1995

Certified by _____
Otto K. Harling, Ph. D.
Professor of Nuclear Engineering
Director, Nuclear Reactor Laboratory
Thesis Supervisor

Certified by _____
Gordon E. Kohse, Ph. D.
Principal Research Scientist, Nuclear Reactor Laboratory
Thesis Supervisor

Accepted by _____
Jeffrey P. Freidberg, Ph. D.
Chairman, Department Committee on Graduate Students

IRRADIATION ASSISTED STRESS CORROSION CRACKING SUSCEPTIBILITY OF LOW FLUENCE STAINLESS STEELS EVALUATED BY IN-FLUX SLOW STRAIN RATE TESTS

by

Bruce A. Hilton

Submitted to the Department of Nuclear Engineering
on October 4, 1995 in Partial Fulfillment of the Requirements of the Degree of
Doctor of Philosophy in Nuclear Materials Engineering
at the Massachusetts Institute of Technology

ABSTRACT

Irradiation assisted stress corrosion cracking (IASCC) is a form of environmentally assisted cracking distinguished by radiation effects that enhance or induce material susceptibility and environmental aggressiveness. Austenitic stainless steel structures, employed in in-core and near-core boiling water reactors (BWR), are susceptible to IASCC. Susceptibility has been extensively investigated by out-of-flux tests, primarily by the slow strain rate (SSR) technique, which only include effects of accumulated radiation damage. To evaluate the contribution of instantaneous radiation effects on IASCC susceptibility, comparative in-flux IASCC tests were completed.

SSR tests, at ~4 x 10^{-7} s^{-1}, were performed on unirradiated and low fluence (~0.8 x 10^{25} n/m^2, E> 1 MeV) types 304 and 316L stainless steel (SS) in 288°C water flowing at a linear velocity of 1.3 m/s in an autoclave situated in the MIT Research Reactor (MITR-II) core. The neutron and gamma ray fields were 5 x 10^{13} n/m^2 and 1 x 10^5 R/s, respectively. The autoclave water chemistry, characterized by SS electrochemical potential (ECP) of ~0-0.1 V (SHE), simulated BWR primary coolant under normal oxidizing conditions.

Mild susceptibility (~2% IG) to IASCC was observed in the pre-irradiated CP 304 alloy. No IASCC was observed on the pre-irradiated 316L specimens. This suggested a higher fluence susceptibility threshold for 316L. For low fluence CP type 304 and type 316L, the IASCC susceptibility, fracture mode and dependence on mechanical, microchemical and electrochemical parameters evaluated by in-flux SSRT were comparable to results determined by out-of-flux SSRT with 8-32 ppm dissolved oxygen. This indicated that in-flux and out-of-flux environments with the same ECP are equivalent. Predictions of in-flux ECP based on total oxidant were inadequate. Based on one data, instantaneous radiation damage was indicated to increase the yield strength and decrease ductility. The measured increase in yield strength was on the order of the predicted increase.

Yield stress was indicated as a fundamental parameter influencing IASCC behavior. Extrapolated electrochemical potentiokinetic reactivation (EPR) data and transpassive potentiostatic dissolution (TPD), similar to Coriou (HNO_3/Cr^{6+}) tests, trended with %IG.

Thesis Supervisors: Dr. Otto K. Harling, Professor of Nuclear Engineering and Director of Nuclear Reactor Laboratory
Dr. Gordon E. Kohse, Principal Research Engineer of Nuclear Reactor Laboratory

ACKNOWLEDGMENTS

What we are is in part only of our making: The greater part of ourselves has come down to us from the past. What we know and what we think is not a new fountain gushing fresh from the barren rock of the unknown at the stroke of the rod of our own intellect: It is a stream which flows by us and through us, fed by the far off rivulets of long ago. As what we think and say today will mingle with and shape the thoughts of Man in the years to come, so in the opinions and view are we proud to hold today we may by looking back, trace the influence of the thoughts of those who have gone before.

Sir Michael Foster
(1836-1907)

I want to acknowledge the many contributions of Prof. O. K. Harling and Dr. G. E. Kohse as advisors of this work and as mentors throughout my graduate education. Prof. Harling, for the integrity and sincerity of his commitment to my professional development and his genuine concern for my family's and mine own welfare. Dr. Kohse, for his energy and enthusiasm and engineering expertise. And for rising and meeting his expanded advisory role, which was a service not only to me but to my other advisor.

I greatly appreciate the assistance of T. J. Weber in the experimental work and A. Lewis for operating the scanning electron microscope. I acknowledge the technical expertise provided by project engineers P. Stahle, E. Cabello and Y. Ostrovsky and the contributions made by previous graduate students Dr. J. O' Donnell, H. Mansoux and Dr. S. Boerigter. Essential support provided by personnel in Reactor Operations, Reactor Maintenance, Reactor Machine Shop and Radiation Protection Office is gratefully acknowledged.

The author would like to acknowledge Dr. J. L. Nelson and Dr. C. Spalaris at the Electric Power Research Institute (EPRI) and Dr. M. Aoki, Mr. S. Suzuki and Mr. Y. Tanaka at Tokyo Electric Power Company (TEPCO) for their technical oversight and helpful suggestions. The author gratefully acknowledges beneficial comments from Prof. R. G. Ballinger, Prof. K. Russell, Prof. R. Balluffi, Prof. T. Shoji and Prof. Y. Watanabe. Funding for the design, construction and in-core operation of the experimental facility was provided by EPRI and TEPCO. Supplementary support from the MIT Nuclear Reactor Laboratory and Department of Nuclear Engineering during the analysis and write-up is gratefully acknowledged.

On a more personal note, I want to thank my family and many friends that have sustained me through the fulfillment of all my Ph. D. degree requirements. I greatly appreciate my parents, both by blood and marriage, for their enduring faith, selfless generosity and unending attention. My father deserves special mention for his assistance in editing and revising the final drafts. His companionship at the end of the road has been especially sweet and memorable. I want to acknowledge my brother Brian for his professional suggestions on the print and page layout. I am grateful to my children Conor, Alistair and Isabel whose cherubic cheerfulness and heavenly

hugs buoyed my confidence and gave me strength to persevere. Finally, I want to thank my wife Mariann for her constant encouragement, warmth and devotion, refreshing sense of humor and indomitable spirit, all of which carried me through to the completion of my thesis and Ph. D. degree. I am eternally grateful for her willingness and desire to share her talents, time and affection with the three stars in our constellation- Conor, Alistair and Isabel. She is my angel sent from our God above.

To Mariann,
my happiness, strength and inspiration:
For filling my cup when it was empty
and lighting my eyes when they grew dim.

CONTENTS

Science is nothing but trained and organized common sense, differing from the latter only as a veteran may differ from a raw recruit: and its methods differ from those of common sense only as far as the guardsman's cut and thrust differ from the manner in which a savage wields his club.

Thomas Henry Huxley
(1825-1895)

APPENDIXES

ILLUSTRATIONS

Every artist dips his brush in his own soul and paints his own nature into his pictures.

Henry Ward Beecher
(1813-1887)

FIGURE

FIGURE

FIGURE

FIGURE

FIGURE

FIGURE

FIGURE

FIGURE

TABLES

Facts are ventriloquists' dummies. Sitting on a wise man's knee they may be made to utter words of widom; elsewhere, they say nothing, or talk nonsense, or indulge in sheer diabolism.

Aldous Huxley
(1894-1963)

TABLE

CHAPTER 1

INTRODUCTION

...Concerning all acts of initiative (and creation), there is one elementary truth the ignorance of which kills countless ideas and splendid plans: that the moment one definitely commits oneself, then providence moves you...

Whatever you can do or dream you can, begin it. Boldness has genius, power and magic in it. Begin it now.

Johann Wolfgang von Goethe
(1755- 1802)

1.1 BACKGROUND

Materials degradation of nuclear power plant materials has been very costly with an estimated outlay by electric utilities of $1 billion for repairs and remedial actions in 1990[1] and has been identified as the key process affecting components' regulatory residual life[2]. At a point in time when 24,578 MWe of U.S. currently operating nuclear power plants' licenses will expire by the year 2010 and an additional 20,929 MWe will expire by the year 2015[3], the understanding of life-limiting conditions is vital for qualifying these plants for future service and providing insights into design changes that will increase reliability and operating lifetimes of future plants. Irradiation assisted stress corrosion cracking (IASCC) is one of several environmental degradation phenomena that challenges nuclear power plants' ability to deliver safe, reliable and economical electricity.

An increasing number of papers submitted on IASCC topics are found in symposia proceedings on environmental degradation and radiation effects in materials[4-9]. A special international cooperative group on irradiation assisted stress corrosion cracking (ICG-IASCC) was founded in 1986 to provide a forum for the timely dissemination and discussion of insights and results of experimental research. In 1994, a Cooperative IASCC Research (CIR) Program was organized to combine the intellectual, research facility and monetary resources of participants in

an effort to develop a mechanistic understanding and predictive modeling capability and identify potential mitigating solutions in as short as time as possible[10]. All these outward evidences point to the practical need for investigating IASCC and demonstrate the high priority level and large global extent of this interest.

Most IASCC susceptibility research to date relies on out-of-flux materials tests with pre-irradiated specimens subject to a simulated light water reactor (LWR) water coolant environment. Obviously, there are differences between the conditions of these tests and the operating conditions of in-core materials subject to neutron and gamma flux. To eliminate uncertainties about zero-flux tests results being applicable to in-core structural materials IASCC behavior, suitable mechanical property tests should be performed in an in-core radiation field and under LWR water chemistry. Hence, the interest in an in-core materials testing facility that operates at LWR water chemistries and can accept radioactive specimens. Furthermore, conjoint experimental evaluation of the microchemistry, microstructure, and corrosion characteristics of unirradiated and irradiated materials (specific alloy and heat) is necessary for identifying mechanisms that contribute to and engineering parameters that correlate with IASCC susceptibility. All of these reasons support the rationale for the experimental and analytical work presented in this thesis.

1.2 OVERVIEW

This section provides a broad overview of the phenomenon named irradiation assisted stress corrosion cracking. The focus here is introductory and draws on a number of reviews published in the literature[11-14]. Irradiation assisted stress corrosion cracking occurs due to the simultaneous effect of a susceptible material, in an aggressive environment-material combination, subject to a tensile load. The peculiar effects of neutron, gamma and ionizing radiation on material chemistry and substructure and on the aqueous environment serving as coolant and moderator in nuclear power systems are the hallmarks of IASCC. It is these effects which distinguish IASCC from other forms of stress corrosion cracking (SCC) and environmentally assisted failures; their independent and synergistic contributions make a complex interplay which has challenged investigators' ability to identify the mechanism or mechanisms responsible for this type of cracking. Figure 1-1 depicts the definitive parameters of all stress corrosion cracking (susceptible material, aggressively corrosive environment and tensile load) and the accumulated and instantaneous effects of radiation on the material and environment unique to irradiation assisted stress corrosion cracking.

To appreciate the scope of materials and structures subject to this form of environmental attack, the accumulated service experience of components that have exhibited

degradation due to IASCC is summarized first. The contribution of radiation effects on LWR materials and on water chemistry are introduced in the succeeding subsections. The phenomena specific to IASCC are categorized as radiation damage accumulated over time and instantaneously, radiation induced segregation and water radiolysis. In the last subsection of the overview, motivations for the work reported in this document are reviewed.

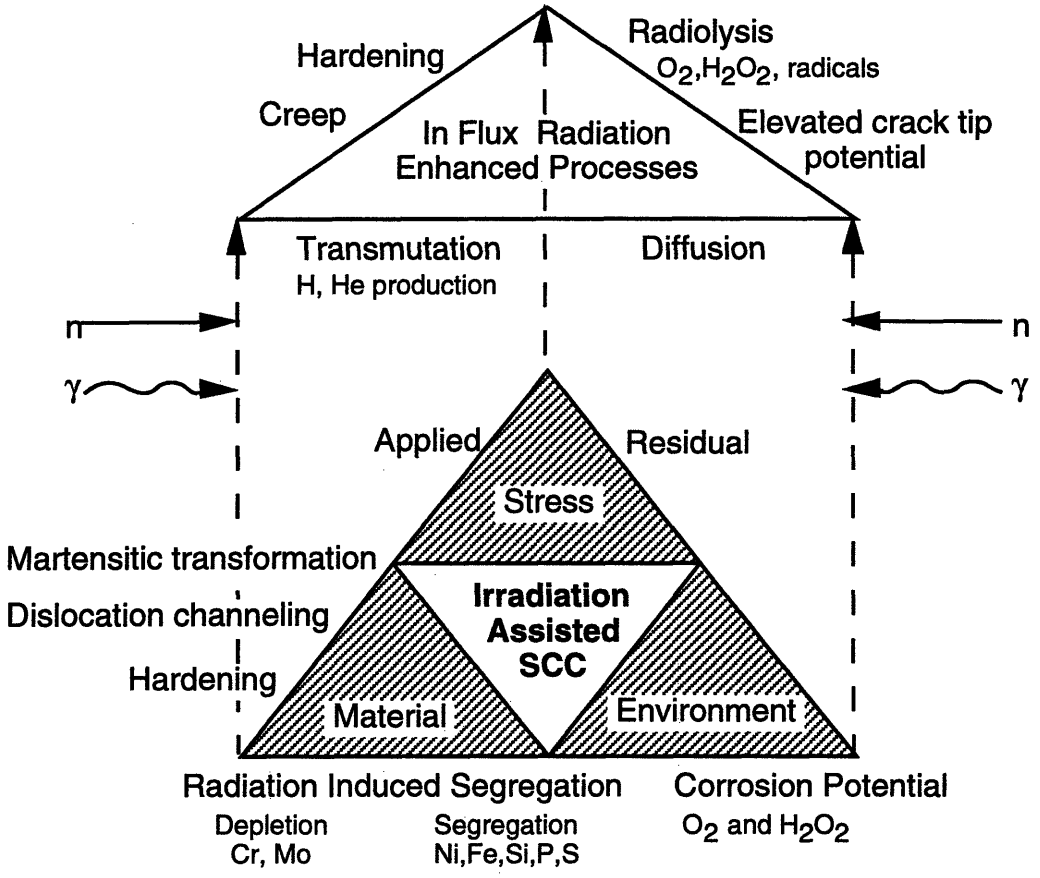

Figure 1-1. Diagram illustrating classical and instantaneous effects of radiation on the definitive parameters (material, environment, stress) of stress corrosion cracking that contribute to Irradiation Assisted Stress Corrosion Cracking.

1.2.1 Summary of Irradiation Assisted Stress Corrosion Cracking (IASCC) Service Experience

Experience with irradiation assisted stress corrosion cracking in the nuclear power industry is extensive and varied. Some of the first failures occurred in the 1950's when stainless

steel fuel cladding suffered from SCC and irradiation damage, an event which finalized the choice of Zircaloy cladding for fuel element use in boiling water reactors (BWR). Other IASCC failures have been observed in various in-core structural components such as control guide handles in BWRs, fuel assembly springs in pressurized water reactors (PWR) and BWRs and control assembly claddings. These components represent a variety of materials, fluence levels, and stress magnitudes which span the environmental-mechanical-material triad space (see Table 1-1). Hence, the spectrum of components which may degrade by IASCC is wide and can include both in-core and near-core components in light water reactor pressure vessels which are exposed to high and low neutron fluences, respectively.

The present research is limited to type 300 austenitic stainless steels because of their application to certain in-core and near-core structures that are very difficult, if not completely impractical to replace (e.g. top guide, core shroud, bottom fuel plate). Although there has been a long and wide ranging experience of IASCC failures, there does not exist the capability to predict future failures. Because of the advancing age of operating nuclear power plants and reduced service life caused by IASCC, developing this predictive capability is a major focus of IASCC research. An understanding of the fundamental mechanisms is sought in an effort to develop quantitative life-prediction capabilities. A number of material and environmental effects of radiation have been proposed or identified as contributing to the IASCC mechanism. The effects of radiation on austenitic stainless steels and LWR water chemistry that contribute to IASCC are discussed next.

1.2.2 Radiation Effects on LWR Materials

The effects of radiation damage on LWR structural materials results in microstructural and microchemical changes. Independently the former changes decrease the fracture toughness and the latter changes decrease the corrosion resistance of austenitic stainless steels. The combined effect of these changes results in enhanced cracking susceptibility.

The microstructural evolution of austenitic stainless steels under irradiation varies with temperature and shows a transition at ~300°C[15], which is in the operating temperature regime of light water reactor reactors (see Figure 1-2). The development of black dots, identified as interstitial loops, and Frank faulted loops with a burger's vector, b, equal to $^{a}o/3<111>$ are considered the dominant microstructural features affecting post-irradiation mechanical behavior of LWR austenitic stainless steels[16]. The radiation induced defect structures primarily act as obstacles which impede plastic flow and strengthen the matrix material. This is manifest as an increase in yield stress and decrease in strain to failure. The loss of ductility is explained as a premature plastic instability often associated with "dislocation channeling." When the obstacles are cut by a leading dislocation, an avalanche of dislocations follow which concentrate the slip

Table 1-1. IASCC service experience (after Scott[11] and Andresen et al[14]).

Core Component	Material	Reactor Type	Sources of Stress
Fuel Cladding	304 SS	BWR and PWR[a]	Fuel Swelling
Fuel Cladding	20%Cr/25%Ni/Nb	AGR[b]	Fuel Swelling
Fuel element component	20%Cr/25%Ni/Nb	SGHWR	Fabrication
Neutron Source Tubes	304 SS	BWR	Welding and Be Swelling
Control Blade Plate	304 SS	BWR	Fabrication
Control Blade Handle	304 SS	BWR	B_4C Swelling
Control Blade Sheath	304 SS	BWR	Fabrication
Control rod cladding	304 SS	PWR	
Instrument Dry Tubes	304 SS	BWR	Fabrication
Control Rod Absorber Tubes	304 SS	BWR	B_4C Swelling
Core spray line and sparger	304 SS	BWR	
Core baffle bolts	316 SS	PWR	
Fuel Bundle Cap Screws	304 SS	BWR	Fabrication
Control Rod Follower Rivets	304 SS	BWR	Fabrication
Absorber pins	I 600	PWR	
Bolts[c] thermal shield fuel assembly core baffle steam separator dryer	A 286	PWR&BWR	Service
Bolts shroud head[c] fuel assembly	I 600	BWR	Service
Bolts and springs core baffle fuel assembly control rod drive seal fuel assembly finger jet pump beams[c]	IX 750	BWR and PWR	Service
Control rod guide tube support pins	IX 750	PWR	Service

[a] Attributed originally to poor water chemistry.
[b] Cracking occurred in the fuel cooling pond.
[c] Cracking occurs away from high gamma and neutron fluxes.

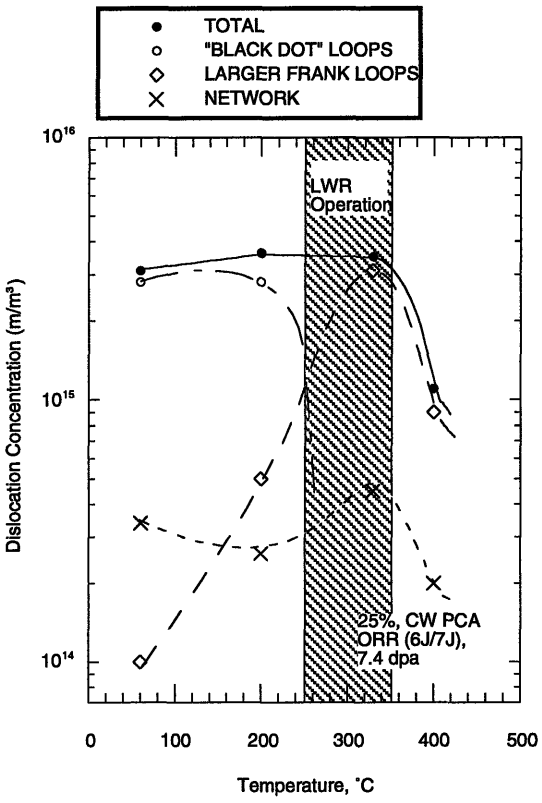

Figure 1-2. Temperature dependence of the dislocation concentration from various components of the dislocation microstructure in 25% CW PCA irradiated in ORR-MFE 6J/7J (7.4 dpa) (after Maziasz[16]).

deformation in these paths which are called dislocation channels[17]. These changes in mechanical behavior are observed in post-irradiation tests, hence are associated with accumulated radiation damage or fluence. It is interesting to note that a number of macroscopic behaviors, including IASCC susceptibility, exhibit a transition in behavioral dependence at a similar fluence range.

Fluences between $\approx 1 \times 10^{25}$ n/m^2 to 1×10^{26} n/m^2 (E> 1.0 MeV) correspond to an incubation damage before swelling occurs and to a saturation damage with regards to yield stress increase[16,18-20]. The IASCC susceptibility of type 304 stainless steel tested in out-of-pile slow strain rate tests (SSRT) shows a sharp increase at this same fluence range (see Figure 1-3). Differences in "threshold" fluences (integrated radiation flux) reported by Jacobs[21] ($\sim 0.5 \times 10^{25}$ /m^2) and by Kodama et al.[22] ($\sim 1\text{-}2 \times 10^{25}$ /m^2) were explained by high and low stresses in the failed pieces, respectively. Tests with pre-irradiated specimens can be used to understand the effects of fluence, but instantaneous effects cannot be produced without a neutron flux. An important question in IASCC research is the effect of instantaneous radiation damage.

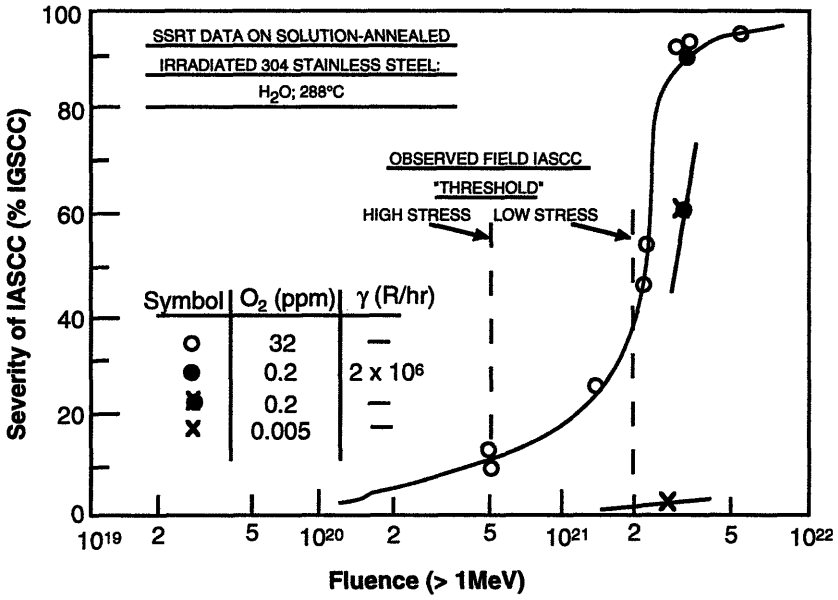

Figure 1-3. Relationship between the severity of IASCC and fluence for irradiated type 304 stainless steel under slow strain rate conditions in water at 288°C containing different amounts of oxygen (Andresen et al.[14]).

Segregation of major and minor elements in austenitic stainless steels is a keystone process of IASCC which diminishes the corrosion resistance of the metal. In the late 1970s, thermally induced segregation in "weld-sensitized" stainless steel was identified as a fundamental parameter in the increased frequency of BWR recirculation piping failures[23]. Thermally induced segregation occurs in stainless steels heat treated to temperatures between 550°C and 800°C and results in chromium depletion in regions near the grain boundaries where chromium carbide precipitates are formed. These chromium depleted regions are susceptible to localized attack and can lead to intergranular failures. A similar phenomena has been observed for solution annealed stainless steels that have been subject to sufficiently high radiation levels. Due to a large non-equilibrium defect population produced from a radiation (dominated by neutrons in LWR) flux and Fickian flow of defects to sinks like the grain boundary, the different mobilities of solute atoms (Cr, Ni, Si, P) leads to a localized depletion of chromium near the grain boundaries. The mechanism of sensitization by radiation induced segregation (RIS) differs from thermal heat treatment induced segregation in several ways. First, chromium carbide may precipitate at the grain boundary in irradiated materials, but the precipitates do not cause susceptibility as they do for thermally treated steels. Second, RIS depletion profiles are much narrower and deeper compared to profiles of thermally sensitized material. Another important difference of RIS is the simultaneous enrichment of smaller elements in regions where chromium is depleted. These enriched elements include such corrosion deleterious impurities as silicon (Si),

phosphorus (P), sulfur (S) and nitrogen (N). Characterization of grain boundary composition changes have been advanced by the advent of high resolution electron microscopy. Shown in Figure 1-4 is a classic example of radiation induced segregation from Jacobs et al.'s[24] scanning transmission electron microscopy (STEM) results for a high purity (HP) type 348 stainless steel irradiated to 3.4×10^{25} n/m^2. The microchemical composition profile near the grain boundary is typical of RIS: depletion of Cr and Fe and enrichment of Ni and Si. Hence, in commercial purity (CP) alloys where there are non-negligible amounts of these impurities and higher levels of segregation as well as chromium depletion, it is uncertain which effect or combination of effects is the dominant contributor to the IASCC mechanism. Since RIS is essentially fluence dependent, its effect on IASCC susceptibility can be adequately evaluated with post-irradiation tests. However, there are also in-flux microchemical changes postulated to contribute to IASCC mechanisms.

IASCC mechanical property tests to date (slow strain rate, fracture mechanics test) have not included the radiation effects produced *in situ* by a fast neutron flux, but only the cumulative effects such as hardening, embrittlement and RIS. Some other phenomena expected to affect IASCC susceptibility that occur *in situ* under a radiation flux are transmutation, enhanced diffusion (i.e. hydrogen) and radiation enhanced creep. Transmutation of elements to produce helium and hydrogen are considered as candidate in-flux mechanisms that lead to embrittlement and enhanced cracking[11]. The supersaturation of point defects may also increase the diffusivity of hydrogen which would allow faster migration to stress concentrations, i.e. the crack tip, and shorter times to reach a critical "embrittling" concentration.

It is well documented that accumulated radiation damage increases hardening and results in increased resistance to dislocation motion and a corresponding increase in the yield strength, but it has been proposed that radiation softening also occurs[17]. For the fluxes pertinent to stainless steel structures in a power reactor (~5×10^{13} n/cm^{2}s), radiation enhanced creep has been calculated to be a non-negligible contribution to the local strains[14]. It is difficult to quantify the actual contribution because of the paucity of data for power reactor conditions. Most tests have been performed at higher fluxes or temperatures which are more relevant to fast reactor conditions. In Chapter 6, a review of creep rate data pertinent to LWR technology is presented and a simplified expression applicable to LWR components developed.

1.2.3 Radiation Water Chemistry

The effect of radiation on water has been studied for many years and continues to be researched[25-29]. The water molecule breaks down into a number of species when bombarded with radiation (neutrons, gamma rays, electrons and ions). There are over 20 species, but only

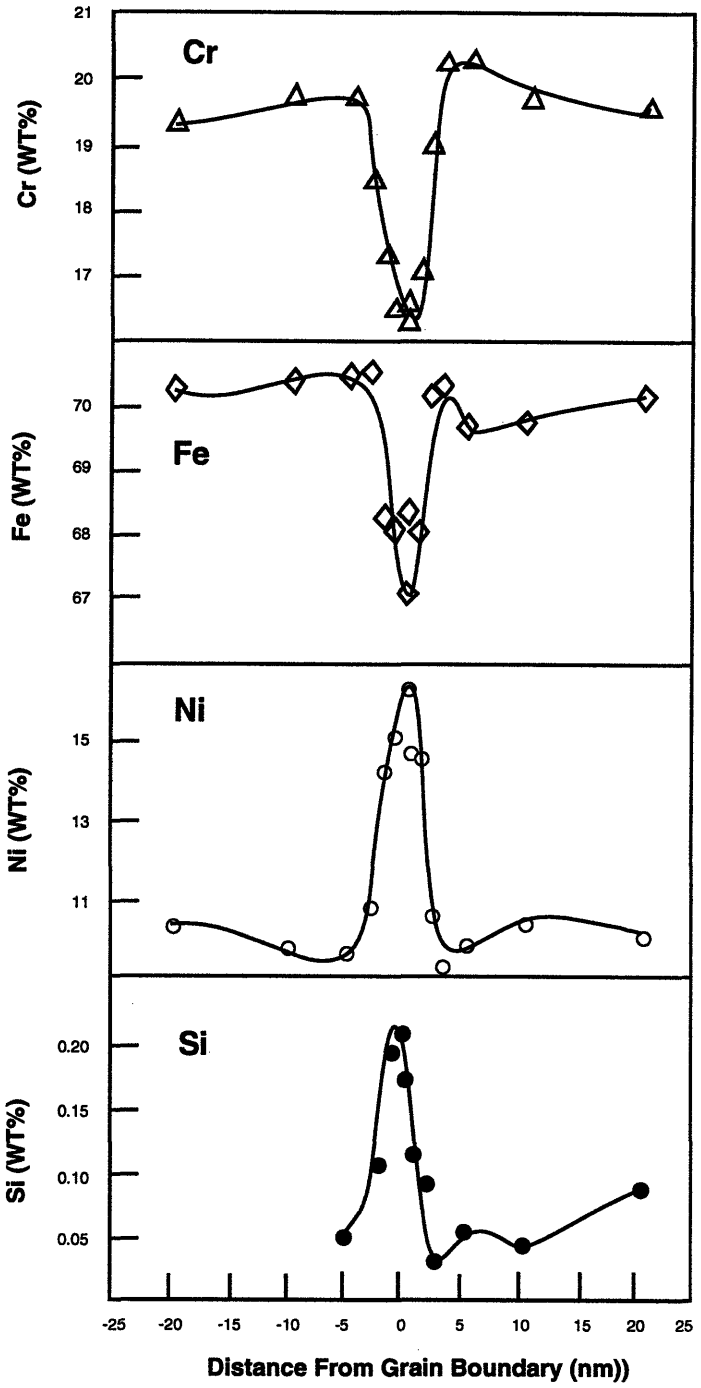

Figure 1-4. Composition profiles across grain boundaries obtained by dedicated STEM from a low-strain, HP 348 stainless steel swelling-tube specimen irradiated to 3.4 x 10^{25} n/m^2 at 288°C in a BWR (after Jacobs et al.[24]).

eight species of primary importance produced from H_2O (e^-_{aq}, H^+, H, H_2, O_2, OH, H_2O_2, HO_2). These species include molecules and radicals which are both oxidizing and reducing. In a closed system with no solutes, production of radiolysis products is proportional to the square root of the flux [25] and subsequent interaction of species proceeds according to fairly well defined chemical reactions[30,31]. Although there is fairly high confidence in computer modeling of these reactions and calculations of the species concentrations at different locations in a BWR primary loop, the corrosive nature of the water environment has been better defined in terms of the corrosion potential which is commonly designated as the electrochemical potential (ECP) of the subject metal[32].

Intergranular (IG) cracking in out-of-core laboratory test environments has been correlated very successfully with the ECP. This alleviates many of the difficulties with identifying the separate and synergistic effects of hydrogen peroxide, oxygen and hydrogen concentrations. It presents a single measurable quantity that can be used to describe a corrosive environment. Since neutron and ionizing radiation causes water radiolysis, a change in ECP under irradiation is expected. Measurements from neutron and gamma-ray in-core and accelerator proton bombardment in lab (see Figure 1-5) show the effects of radiation on ECP at oxygen levels ranging from normal water chemistry (NWC) to hydrogen water chemistry (HWC). Justification of its application to an irradiated environment has been discussed by Andresen[14]. In this paper, Andresen examines the evidence based on three considerations: 1) similarity of processes and reactions which control the corrosion potential under unirradiated and irradiated conditions, 2) the effect of irradiation on the stagnant solution and associated ECP within the crack, and 3) similarity in the effect on cracking kinetics of ECP specifically, and water chemistry in general. His analysis of in-core and out-of-core data indicates that the corrosion potential is a physical quantity that represents the corrosive nature of the water chemistry environment. For the research reported here, the in-core ECP was measured and correlated with letdown line oxygen and out-of-pile ECP measured in an autoclave on the letdown line (see Chapter 3).

1.2.4 Motivation for MIT Research

Materials testing facilities available for investigating irradiation assisted stress corrosion cracking have not had the capability of in-situ neutron radiation until recently[33,34]. For out-of-pile IASCC tests, long term radiation damage has been studied using pre-irradiated specimens (either samples taken from operating plants or specimens irradiated in test or research reactors to the desired fluence or "damage" level). The fluence is commonly measured in displacements per atom (dpa). Also the corrosive environment of radiation modified water

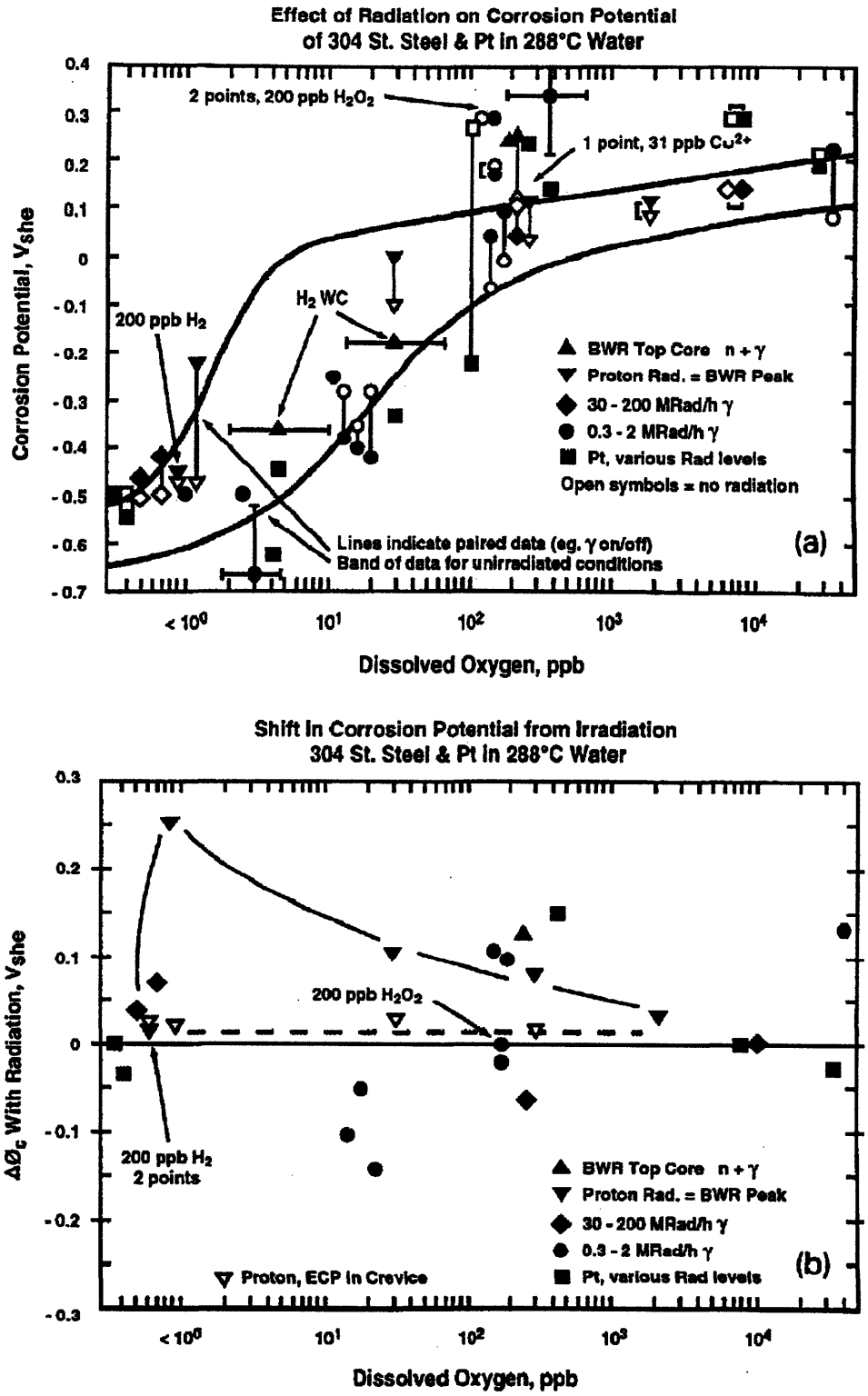

Figure 1-5. Effect of radiation on (a) the corrosion potential of type 304 stainless steel in 288°C water (b) the shift in corrosion potential relative to unirradiated conditions (Andresen et al.[14]).

chemistry has been simulated by supplying sufficient amounts of oxidizing species like oxygen or hydrogen peroxide. These out-of-pile studies have produced volumes of valuable data, but the equivalence to the behavior of in-core structural components is still a question. Hence, a facility that loads a tensile specimen while being subject to a neutron and gamma flux was designed, constructed, and commissioned for operation in the MIT Research Reactor (MITR-II)[35].

Under slow strain rate (SSR) conditions, the time scale of mechanical and corrosion events may be comparable to radiation flux induced events resulting in a synergism different than observed in out-of-flux SSR tests. Because of the complex interaction of all these effects, it is not possible to predict the behavior in-flux. Experimental results from mechanical property tests conducted in-flux in a BWR simulated environment are needed to compare with post-irradiation test results and determine the impact of in-flux mechanisms.

Formulating a mechanism for IASCC also requires the evaluation of microstructural and microchemical changes of the stainless steel induced by accumulated irradiation damage. Conventional material characterization techniques like analytical electron microscopy and electrochemical dissolution can help quantify the damage incurred over time. These tasks were performed previously in support of the present experimental work and analysis of mechanistic parameters that contribute to irradiation assisted stress corrosion cracking. The compilation of all these material chemistry, structure and SCC susceptibility tests on the same materials (alloy and heat) will provide a broad and detailed database for evaluating in-flux effects on IASCC.

1.3 SYNOPSIS OF EXPERIMENTAL AND ANALYTICAL PROGRAM

This work represents the final phase of a six year experimental and analytical investigation of irradiation assisted stress corrosion cracking of structural materials relevant to the nuclear power industry. Because the present analysis draws on the previous results to form a comprehensive picture of IASCC, a synopsis of each component of the intensive program is provided in this section. Major accomplishments of this program are the following: 1) design, construction and use of a dry-irradiation facility in which tensile specimens, transmission electron microscopy (TEM) specimens, and scanning Auger microscopy specimens were irradiated to fluences between 0.35 and 0.86 dpa at a constant temperature of 300°C, 2) analysis by TEM and STEM and by electrochemical potentiokinetic reactivation (EPR) ratio and transpassive potentiostatic dissolution (TPD) testing that characterized the degree of radiation induced segregation in these specimens, 3) the design, construction and use of a rig in which the ECP of specimen materials was measured under water chemistry conditions that simulated a BWR environment with different key parameters (e.g. oxygen and hydrogen concentrations, flow rate,

flux, accumulated dose, and reactor power level), and 4) the design, construction, commissioning and utilization of an in-core SSRT rig for studying stress corrosion cracking of tensile specimens (unirradiated or pre-irradiated) in a BWR environment (e.g. normal water chemistry or hydrogen water chemistry). This thesis presents details of the in-core SSR tests data, the fractographic analyses performed by scanning electron microscopy (SEM), discussion of in-flux material effects postulated to affect IASCC behavior and evaluation of the aforementioned microchemical and electrochemical material tests as service performance indicators of IASCC susceptibility.

1.3.1 Dry Irradiation and RIS Modeling

Because radiation induced segregation is considered a primary effect in making a material "sensitized" to IASCC, a dry irradiation (i.e. under inert gas conditions) facility for the MIT Research Reactor was designed, constructed and operated[36] to provide a catalog of specimens for the experimental portion of this program. This catalog includes 64 tensile specimens of four 300 series stainless steel alloys (CP 304, low carbon 316L, niobium-stabilized 347L, and high purity 304), over 200 TEM samples of commercial and experimental alloys doped with specific impurity elements to be used for transmission electron microscopy and field emission gun scanning transmission electron microscopy (FEG-STEM) for measuring grain boundary profiles, and auger specimens (sized for the facility at Oak Ridge National Laboratory) for comparison with the FEG-STEM profile results.

This foundation of developing a catalog of pre-irradiated specimens also included the development of an analytical model capable of predicting RIS in Fe-Ni-Cr ternary alloy systems. The RIS model applies the random alloy theory of Manning and lattice defect-atom jump energies to calculate chromium depletion and nickel enrichment near the grain boundary. By suitable adjustment of a grain boundary structure parameter that limits the recombination rate of lattice defects, the model predictions closely match experimentally measured profiles of high fluence materials.

1.3.2 RIS Evaluations by Analytical Electron Microscopy (AEM) and Electrochemical Techniques

The effect of radiation on microchemistry was experimentally investigated by analytical electron microscopy and by electrochemical techniques. Radiation induced changes in microstructure were not a focus of this research, but some results for CP 304 alloys were determined by transmission electron microscopy. The analysis of grain boundary chemistries of pre-irradiated specimens was determined by energy dispersive x-ray spectroscopy (EDX) in scanning transmission electron microscopes. Of the austenitic stainless steels analyzed, the CP

304, high purity 304 (with and without doped phosphorus), and 316L alloys showed modest chromium depletion and nickel enrichment at some of the boundaries[37]. No measurable segregation was found in the 347L or high purity 304 alloys doped with sulfur. Trends observed in the experimental Fe-Ni-Cr ternary alloys indicate enhanced Ni enrichment and Cr depletion occur when increased concentrations of these elements are alloyed in the matrix[38].

Electrochemical potentiokinetic reactivation and transpassive polarization tests are accelerated corrosion tests that correspond to chromium depletion and impurity elements (Si and P) enrichment, respectively. These electrochemical tests as well as other chemical corrosion tests can provide a more global and average evaluation of material damage compared to analytical microscopy; they provide an indication of the influence of a material's combined bulk and grain boundary corrosion on stress corrosion cracking susceptibility. The EPR ratios for unirradiated and irradiated specimens[39] showed enhanced dissolution in three out of the four irradiated austenitic alloys examined. Furthermore, the dissolution susceptibility trended with neutron exposure (i.e. accumulated fluence). The greatest increase in EPR ratio was for 347L alloy and high purity 304 alloy doped with S. Modest increase was found for the CP 304 alloy, but no change for the 316L alloy. The treated surfaces were visually examined by scanning electron microscope and showed a significant difference between the unirradiated and irradiated samples. The primary dissolution mode is by crystallographic pit formation in the matrix and not grain boundary attack. These observations are considered indirect evidence of segregation at defects and faulted dislocation loops produced by the neutron radiation.

Under potentiostatic transpassive exposure, a correlation between silicon and phosphorus content (wt%Si + wt%P x 10) and dissolution susceptibility was found for the unirradiated materials[40]. A critical impurity value of 0.5 was observed which corresponds to the region where intergranular attack becomes visible. Tests on irradiated CP 304 alloy showed an increase in grain boundary attack and small multiple sites of preferential dissolution in the matrix. The orientation suggests that these sites are faulted dislocation loops which have segregated silicon and phosphorus.

TEM studies[37] of irradiated CP 304 alloy samples indicated extensive radiation damage in the form of contrast spots. The spots were attributed to both "black dot" dislocations and small faulted loops (< 10 nm). No faulted loops greater than several nanometers in diameter were detected, which is not unexpected for the modest fluences of the specimens examined (<0.86 x 10^{25} n/m^2).

1.3.3 Crack Chemistry Modeling

Crack growth is dominated by local chemistry conditions in the crack enclave which can significantly differ from the bulk water chemistry which is monitored and used for

determining safe operating conditions. Because of the technical difficulty in making measurements at the crack tip in the laboratory and impracticality of making such measurements in the field, an analytical model was developed for calculating local crack tip conditions and the resulting rate of crack propagation[41]. The model is based on electric circuit theory and assumes that the total current corresponds to anodic dissolution of the metal substrate. As such it represents a limiting crack propagation rate since some of the charge goes into the oxide film repair and in potential drop across the electric double layer. The model has been benchmarked for low alloy systems (i.e. pressure vessel steels) where manganese sulfide (MnS) plays a dominant role in determining local chemistry conditions. Calculated crack propagation rates are within a factor of two to four of experimental data measured for low alloy steel at 288°C and aluminum at low temperature.

1.3.4 In-core SSR Testing

The last phase of the IASCC investigation and the experimental focus of this work has been the slow strain rate testing of pre-irradiated specimens in an autoclave placed in the MITR-II central core position. Seven specimens were tested with the in-core SSRT facility. The specimens were either CP type 304 or 316L stainless steel. Of the CP 304 stainless steel samples, there was one unirradiated, one furnace sensitized, and three pre-irradiated to a fluence of 0.8×10^{25} n/m^2. Two 316L samples, pre-irradiated to a fluence of 0.74×10^{25} n/m^2, were tested as part of this work. Each fractured specimen was analyzed by SEM to determine the intergranular fraction (%IG). Results of the SSR tests are presented in Chapter 4 and details of the SEM can be found in Chapter 5 of this thesis.

1.4 RELATED RESEARCH

There are a number of projects being conducted at the MIT Nuclear Reactor Laboratory (NRL) which are related to the MIT IASCC program although conducted under different auspices. The first is the BWR Coolant Chemistry Loop (BCCL) which is a 1/3 scale simulator of a BWR intra-fuel coolant channel that can operate in boiling and single phase modes. Initial design and development and proof of principle tests were provided by seed money from Electric Power Research Institute (EPRI), and Empire State Electric Energy Research Corporation (ESEERCO). Three succeeding experimental campaigns under Toshiba and Hitachi joint funding were conducted to examine chemical additive effects on nitrogen-16 carryover in the steam phase, radiolysis product concentrations, and ECP in the water letdown line. Results of the first three campaigns are described in a comprehensive EPRI Report[42]. The most recent campaign

(1993) results included data obtained under recirculation and once-through operation and are reported in the thesis by Guimpelson[43]. Much of the technology and operational experience of the BCCL, particularly the water chemistry control, was directly applicable to the in-core SSRT facility.

Another in-core experiment undertaken by the MIT NRL and Nuclear Engineering Department with funding by General Electric (GE), EPRI, Toshiba and Hitachi was the SENSOR project. An in-core autoclave operated at BWR water chemistry conditions (both normal oxidizing chemistry and alternative hydrogen chemistry for reducing environment) housed a string of ten passively loaded double cantilever beam (DCB) specimens interspersed with seven radiation hardened ECP reference sensors[44]. The DCB specimens provided real time crack propagation data using a reversed DC potential drop technique (DCPD) under a monitored radiation environment (defined by the corrosion potential) . The specimen materials are representative of nuclear reactor vessel internal components and weld overlay. The effect of alternate water chemistries, such as hydrogen addition for ECP suppression, were evaluated with regards to cracking susceptibility. With relation to IASCC studies, no pre-irradiated specimens were included for the current set of tests, but the accumulated radiation damage over a year of steady operation will exceed the 0.5×10^{25} n/m^2 fluence "threshold" observed in laboratory tests. This facility and the SSR Test Rig provide an invaluable capability within the MIT NRL for conducting in-flux material property tests vital to qualifying in-vessel service components and for benchmarking life prediction models.

1.5 ORGANIZATION OF THIS THESIS

This thesis is divided into 8 chapters. The scope and overview of the work is introduced in Chapter 1. Chapter 2 details the experimental approach adopted for studying irradiation assisted stress corrosion susceptibility and gives a brief description of the facility employed, since details are included in the thesis by O'Donnell[35]. In Chapter 3, an analysis of the ECP data is presented along with predicted potentials based on oxidant concentration correlations determined in laboratory tests. The results of the SSR tests conducted in-flux and some pertinent results conducted in laboratory autoclaves are presented in Chapter 4. Reproductions of many of the SEM fractographs are shown in Chapter 5 along with descriptions of prominent features included in the text. An evaluation of in-flux radiation effects on materials that can influence irradiation assisted stress corrosion cracking is presented in Chapter 6. This chapter considers the time constants involved in instantaneous radiation damage compared to deformation induced time constants and the impact on observed mechanical properties. Chapter 7 provides a comprehensive picture of the observed IASCC susceptibility data correlated with

four kinds of measurable indicators: fluence, mechanical property data, radiation induced segregation profiles, and electrochemical corrosion test results. In Chapter 8, the major findings of this work are summarized and a discussion of additional insights and recommendations for future work are included.

1.6 REFERENCES

1. T. U. Marston and R. L. Jones, "Materials Degradation Problems in the Advanced Light Water Reactors," *Proc. 5th Int. Symp. on Env. Deg. of Mat. in Nucl. Pow. Systems-Water Reactors*, ANS, Monterey, CA (1991) p. 3.

2. G. A. Arlotto, J. E. Richardson and J. P. Vora, "United States Nuclear Regulatory Commission Research Program to Understand Aging and Manage Its Effects in Nuclear Power Plants," *Proc. Symp. Safety Aspects of the Ageing and Maintenance of Nuclear Power Plants*," IAEA, Vienna (1987) p. 3.

3. A. D. Rossin, "Meeting Future Power Needs in Licensing Space," *Effects of Radiation on Materials: 16th International Symposium, ASTM STP 1175*, A. S. Kumar, D. S. Gelles, R. K. Nanstad, and E. A. Little, Eds., American Society for Testing and Materials, Philadelphia (1993) p. 3.

4. *Proceedings of the Fourth International Symposium on Environmental Degradation of Materials in Nuclear Power Systems-Water Reactors*, NACE, Jekyll Island, GA (1989).

5. *Proceedings of the 5th International Symposium on Environmental Degradation of Materials in Nuclear Power Systems-Water Reactors*, ANS, Monterey, CA (1991).

6. *Proceedings of the Sixth International Symposium on Environmental Degradation of Materials in Nuclear Power Systems-Water Reactors*, TMS, San Diego, CA (1993).

7. *Effects of Radiation on Materials: 16th International Symposium, ASTM STP 1175*, A. S. Kumar, D. S. Gelles, R. K. Nanstad and E. A. Little, Eds., American Society for Testing and Materials, Philadelphia (1993).

8. *Effects of Radiation on Materials: 15th International Symposium, ASTM STP 1125*, R. E. Stoller, A. S. Kumar and D. S. Gelles, Eds., American Society for Testing and Materials, Philadelphia (1992).

9. *Effects of Radiation on Materials: 14th International Symposium, Volumes I and II, ASTM STP 1046*, N. H. Packan, R. E. Stoller and A. S. Kumar, Eds., American Society for Testing and Materials, Philadelphia (1989).

10. L. Nelson, "Cooperative IASCC Research (CIR) Program", ICG-IASCC Task Force Meeting (September 1993).

11. P. Scott, "A Review of Irradiation Assisted Stress Corrosion Cracking," *J. Nucl. Mat.*, 211 (1994) p. 101.

12. G. S. Was and P. L. Andresen, "Irradiation-Assisted Stress-Corrosion Cracking in Austenitic Alloys," *J. Metals* (April 1992) p. 8.

13. J. L. Nelson and P. L. Andresen, "Review of Current Research and Understanding of Irradiation-Assisted Stress Corrosion Cracking," *Proc. 5th Int. Symp. on Env. Deg. of Mat. in Nucl. Pow. Systems-Water Reactors*, ANS, Monterey, CA (1991) p. 10.

14. P. L. Andresen, F. P. Ford, S. M. Murphy and J. M. Perks, "State of Knowledge of Radiation Effects on Environmental Cracking in Light Water Reactor Core Materials," *Proc. 4th Int. Symp. on Env. Deg. of Mat. in Nucl. Pow. Systems-Water Reactors*, NACE, Jekyll Island, GA (1989) p. 1-83.

15. P. J. Maziasz, "Temperature Dependence of the Dislocation Microstructure of PCA Austenitic Stainless Steel Irradiated in ORR Spectrally-tailored Experiments," *J. Nucl. Mat.*, 191-194 (1992) p. 701.

16. P. J. Maziasz, "Overview of Microstructural Evolution in Neutron-Irradiated Austenitic Stainless Steels," *J. Nucl. Mat.*, 205 (1993) p. 118.

17. E. E. Bloom, "Irradiation Strengthening and Embrittlement," *Radiation Damage in Metals*, N.L. Peterson and S. D. Harkness, Eds., American Society for Metals, Metals Park, Ohio (1975) p. 295.

18. D. R. Harries, "Irradiation Creep in Non-Fissile Metals and Alloys," *J. Nucl. Mat.*, 65 (1977) p. 157.

19. *Mechanical Behaviour and Nuclear Applications of Stainless Steel at Elevated Temperatures*, The Metals Society, London (1982).

20. J. J. Holmes and J. L. Straalsund, "Effects of Fast Reactor Exposure on the Mechanical Properties of Stainless Steels," *Int. Conf. Rad. Effects in Breeder Reactor Struct. Mat.*, M. L. Bleiberg and J. W. Bennett, Eds., The Metallurgical Society of AIME, New York, NY (1977) p. 53.

21. A. J. Jacobs, D. A. Hale, and M. Siegler, Unpublished Data, GE Nuclear Energy, San Jose, CA, January (1986).

22. M. Kodama, S. Nishimura, J. Morisawa, S. Suzuki, S. Shima and M. Yamamoto, "Effects of Fluence and Dissolved Oxygen on IASCC in Austenitic Stainless Steels," *Proc. 5th Int. Symp. on Env. Deg. of Mat. in Nucl. Pow. Systems-Water Reactors*, ANS, Monterey, CA (1991) p. 948.

23. J. C. Danko, "Boiling Water Reactor Pipe Cracking: The Problem and Solution," *Proc. Conf. Mat. Nucl. Energy*, ASM (1982).

24. A. J. Jacobs, R. E. Clausing, M. K. Miller and C. Shepherd, "Influence of Grain Boundary Composition on the IASCC Susceptibility of Type 348 Stainless Steel," *Proc. 4th Int. Symp. on Env. Deg. of Mat. in Nucl. Pow. Systems-Water Reactors*, NACE, Jekyll Island, GA (1989) p. 14.

25. A. O. Allen, *The Radiation Chemistry of Water and Aqueous Solutions*, D. Van Nostrand Company, Inc., Princeton, New Jersey (1961).

26. J. W. T. Spinks and R. J. Woods, *An Introduction to Radiation Chemistry*, 3rd Edition, John Wiley & Sons Inc., New York, NY (1990).

27. *Proceedings of the 5th International Conference on Water Chemistry of Nuclear Reactor Systems*, BNES, London (1989).

28. *Proceedings of the 6th International Conference on Water Chemistry of Nuclear Reactor Systems,* BNES, London (1992).

29. *Proceedings of the JAIF International Conference on Water Chemistry of Nuclear Power Plants,* Fukui City, Japan (1991).

30. C. P. Ruiz, C. C. Lin, R. N. Robinson, W. G. Burns, J. Henshaw and R. Pathania, "Model Calculations of Water Radiolysis and Electrochemical Potentials in BWR Primary Coolant II," *Proc. 6th Int. Conf. Water Chemistry Nucl. Reactor Syst., Vol. 2,* BNES, London (1992) p. 141.

31. N. Ichikawa, Y. Hemmi and J. Takagi, "Estimation on Corrosion Potential of Stainless Steel in BWR Primary Circuit," *Proc. 6th Int. Conf. Water Chemistry Nucl. Reactor Syst., Vol. 2,* BNES, London (1992) p. 127.

32. S. Sawochka, "Corrosion Potential (ECP) Measurement Sourcebook," EPRI Report NP-7142, Electric Power Research Institute, Palo Alto, CA (January 1991).

33. C. Vitanza and T. Karlsen, "In-Pile IASCC Test Programme in the Halden Reactor," *Proc. 6th Int. Symp. on Env. Deg. of Mat. in Nucl. Pow. Systems-Water Reactors,* TMS, San Diego, CA (1993) p. 651.

34. D. Weinstein, "Real Time, In-Reactor Monitoring of Double Cantilever Beam Crack Growth Sensors," *Proc. 6th Int. Symp. on Env. Deg. of Mat. in Nucl. Pow. Systems-Water Reactors,* TMS, San Diego, CA (1993) p. 645.

35. J. R. O'Donnell, "Design, Construction, and Commissioning of an In-Core Materials Testing Facility for Slow Strain Rate Testing," PhD Thesis, Department of Nuclear Engineering, Massachusetts Institute of Technology, Cambridge, MA (September 1994).

36. S. T. Boerigter, "An Investigation of Neutron-Irradiation Induced Segregation in Austenitic Stainless Steels," PhD Thesis, Department of Nuclear Engineering, Massachusetts Institute of Technology, Cambridge, MA (December 1992).

37. H. Mansoux, "Experimental Determination of Radiation Induced Segregation Susceptibility in Austenitic Stainless Steels," SM Thesis, Department of Nuclear Engineering, Massachusetts Institute of Technology, Cambridge, MA (June 1994).

38. C. Flores, "Evaluation of Radiation Induced Segregation in Fe-Ni-Cr Alloys," SM Thesis, Department of Nuclear Engineering, Massachusetts Institute of Technology, Cambridge, MA (June 1994).

39. Irradiation Assisted Stress Corrosion Cracking and BWR Chemistry Studies, Fifth Annual Progress Report for Period August 1992 - August 1993, Report No. MITNRL-055 (August 1993) p. 2-68.

40. Y. Watanabe, R. G. Ballinger and G. E. Kohse, "Effects of Neutron Irradiation on Transpassive Corrosion Behavior of Austenitic Stainless Steels," submitted to *J. Nucl. Mat.*

41. J. Chun, "Modeling of Chemistry Related to Environmentally Assisted Cracking (EAC) in Low-Alloy Steels," PhD Thesis, Department of Nuclear Engineering, Massachusetts Institute of Technology, Cambridge, MA (June 1995).

42. M. J. Driscoll, O. K. Harling and G. E. Kohse, "Development and Use of an In-Pile Loop for BWR Chemistry Studies," EPRI Report TR-102248, Electric Power Research Institute, Palo Alto, CA (September 1993).

43. B. Guimpelson, "BWR Coolant Chemistry Studies Using a Recirculating In-pile Loop," SM Thesis, Department of Nuclear Engineering, Massachusetts Institute of Technology, Cambridge, MA (February 1995).

44. J. A. Vergara-Aimone, "The Development of a Facility for the Evaluation of Environmentally Assisted Stress Corrosion Cracking of In-Core Structural Materials in Light Water Reactors," PhD Thesis, Department of Nuclear Engineering, Massachusetts Institute of Technology, Cambridge, MA (June 1992).

CHAPTER 2

EXPERIMENTAL APPROACH

Whoever wills the end, wills also (so far as reason decides his conduct) the means in his power which are indispensably necessary thereto.

Immanuel Kant
(1724-1804)

2.1 INTRODUCTION

The integrity of experimental investigations requires a similitude between laboratory testing conditions and field operating conditions. For IASCC research, similitude was assumed for the environment by matching stainless steel's corrosion potential (ECP) in the bulk fluid (n.b. not necessarily the crack) and for the materials by utilizing similar levels of irradiation exposure. Service life trends observed for field data were qualitatively reproduced by out-of-pile testing. But no unified mechanism has been determined that accurately predicts susceptibility in different alloys or similar alloys with varying matrix chemistries. *In situ* effects of radiation flux on irradiation assisted stress corrosion cracking susceptibility are unquantified. Yet these effects have been proposed to explain the lack of correlation with measurable physico-chemical parameters and discrepancies between some in-core and in-laboratory results. To evaluate the contribution of *in situ* radiation effects on IASCC susceptibility, an experimental investigation utilizing a standard material test technique with the added presence of a radiation flux was considered an optimum choice. The susceptibility testing technique chosen to be applied in the radiation environment and compared with out-of-flux results was slow strain rate testing. It is described more fully below. First, various environmental assisted cracking mechanisms that have been invoked to explain irradiation assisted SCC are briefly reviewed.

2.2 ENVIRONMENTAL ASSISTED CRACKING (EAC) MECHANISMS FOR IRRADIATION ASSISTED STRESS CORROSION CRACKING

2.2.1 Dissolution

The idea of dissolution as the rate limiting step for stress corrosion cracking has been considered since the 1950s[1-3]. A number of variations on the mechanism that produces the bare surface have been proposed, but one most often applied to nuclear power systems at present is film rupture/slip dissolution. The mechanism essentially involves the passive film is ruptured by slip steps and the active metal dissolves until a passive film grows again over the newly bared metal substrate. Crack propagation proceeds in a semi-continuous manner based on the discrete film rupture events and corresponding metal loss by dissolution before repassivation (see Figure 2-1). The length of crack growth is directly related to the current passed between film fracture events by Faraday's second law. The average crack velocity, v_{avg}, can be related to the current transient, Q^*, and a characteristic time, t^*, defined as the quotient of fracture strain of the passive film, ε_f, and strain rate at the crack tip, $\dot{\varepsilon}_{CT}$:

$$v_{avg} = \frac{MQ^*}{n\rho F t^*} = \frac{MQ^*}{n\rho F \varepsilon_f} \bullet \dot{\varepsilon}_{CT}, \qquad \text{(eq. 2-1)}$$

where M and ρ are the molecular weight and density of the metal, n is the valence, and F is Faraday's constant (96,500 C). Experiments have shown that environment sensitive crack growth rates fall within upper and lower bounds set by purely mechanical crack growth at high strain rates and crack blunting and cessation at low strain rates. Ford and Andresen[4,5] have developed a deterministic crack growth model based on the film rupture/slip dissolution mechanism which has had good success in predicting environmental assisted crack growth rates of reactor pressure vessel steels and thermally sensitized austenitic stainless steels. Their model relates the microstructure susceptibility and environment aggressiveness as a function of EPR, ECP and conductivity. With the development of radiation hardened ECP sensors, it has been applied to predicting cracking in radiation environments.

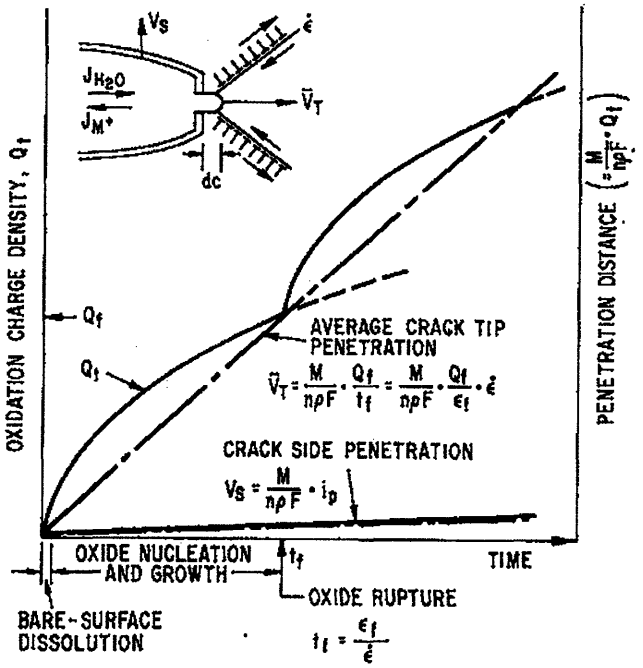

Figure 2-1. Schematic oxidation charge density/crack depth penetration as a function of time for film rupture/slip dissolution mechanism of SCC (after Ford et al.[6]).

Comparison between predicted and measured crack growth rates of solution annealed and furnace sensitized alloys has demonstrated the predictive accuracy of the model for these microstructures of stainless steel employed in LWRs[7]. The complex effects of radiation on the environment seem to be sufficiently characterized by the ECP, however no single measurable parameter has been recognized as enveloping the dominant radiation effects on microstructure. While the use of EPR, a measure of chromium segregation, has been verified as a measure of microstructure susceptibility in "weld-sensitized" stainless steel, it has not been substantiated as a single measure of radiation sensitized alloys. Radiation induced segregation of chromium certainly affects IASCC microstructure susceptibility, but results from IASCC studies have implicated many other effects ranging from impurity element enrichment to hydrogen or helium embrittlement and deformation processes. The latter two mechanisms will be discussed in turn.

2.2.2 Embrittlement

Mechanisms that do not fall under the category of dissolution can generally be described by embrittlement. In these mechanisms, crack growth then progresses by cleavage rather than corrosion, along preferential crystallographic planes. Quite often embrittlement mechanisms have been proposed for models that are also explained by dissolution. One example is the film rupture model where dealloying or embrittlement, rather than emerging slip steps,

have been proposed to lead to isolated film rupture that penetrates the metal substrate and causes a transgranular or intergranular cleavage step (see Figure 2-2).

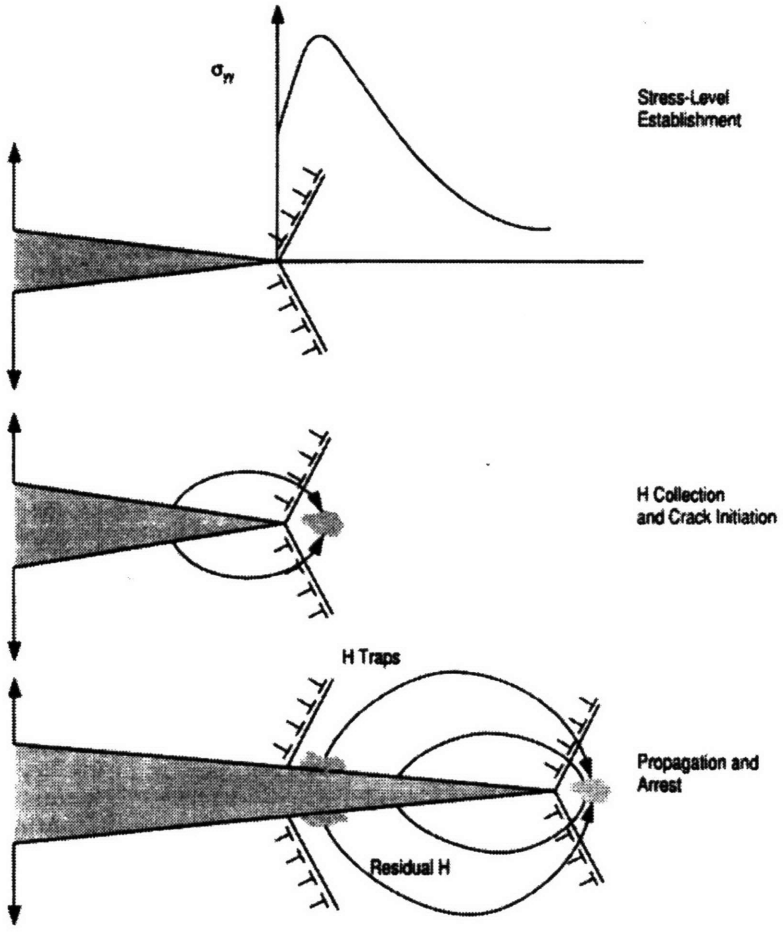

Figure 2-2. A schematic illustration of a hydrogen-assisted cracking event (after Chen et al.[8]).

The essential feature of other mechanisms contest that an embrittling element or species, e.g. hydrogen or helium, is adsorbed and/or absorbed onto/into the oxide or matrix, resulting in a lower fracture stress path on a microscopic scale. Considering hydrogen assisted cracking (HAC) or embrittlement (HE) specifically, when the hydrogen concentration in the matrix reaches a critical level or when the hydrogen reacts to form a weaker phase (i.e. hydride), fracture ensued along microscopic steps producing discreet increments of crack growth, as shown in Figure 2-3. The classic feature of embrittlement, a reduction in decohesive stress, can be interpreted in terms of the Griffith equation for an elliptical crack:

$$\sigma_c = \sqrt{\left(2E\gamma_s/\pi c\right)}, \qquad \text{(eq. 2-2)}$$

where σ_c is the fracture stress, E is Young's modulus, γ_s is the surface energy term and $2c$ is the width of the crack. Details of the interaction of the embrittling species and dislocations distinguish the various theories. Some propose initiation caused by hydrogen blocked glide planes, decohesion via hydrogen agglomeration due to dislocation-induced stress fields or dislocation trapping and plastic instability via a localized decrease in the resistance to dislocation motion[9].

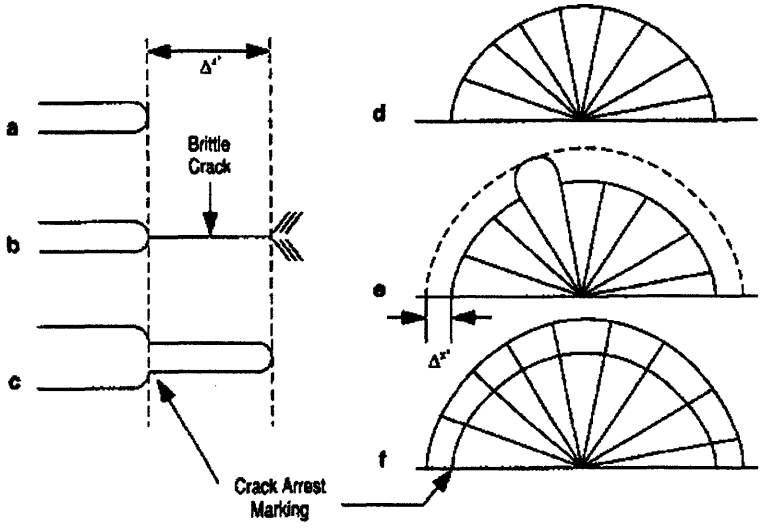

Figure 2-3. A schematic illustration of successive events during the propagation of transgranular stress corrosion cracks by cleavage. Figures a-c represent a section at the crack tip, while d-f represent a plan view of a semicircular crack radiating from the initiation site; (c) and (e) indicate the crack advance distance per event (Δx^*) (after Pugh[10]).

Because of the seeming inability of applying dissolution mechanism rationale to explain all IASCC service failures and out-of-flux laboratory results and the presence of embrittlement constituents in LWRs, embrittlement has been proposed as a mechanism in IASCC. Furthermore, the acidic conditions at the crack tip are consistent with both dissolution and hydrogen embrittlement, so neither can be ruled out on environmental grounds even though the bulk chemistry can be reducing or oxidizing. Since embrittlement leads to cleavage on a microscale, the fracture surfaces should match exactly. In contrast, dissolution leads to metal loss and faces will not correspond. Hence fractographic analysis can distinguish the two mechanisms, but has not produced decisive evidence thus far. Therefore many of the embrittling mechanisms have been suggested to explain IASCC, particularly in light of the effect of impurity elements and their interactions with hydrogen and helium which enhance intergranular corrosion and stress corrosion cracking.

Both hydrogen and helium have been suggested to embrittle stainless steels in LWR vessel service. Nuclear reactions, (n,p) and (n,α), with nickel, iron, chromium, nitrogen and boron are likely sources of hydrogen and helium. Additional potential sources of hydrogen are radiolysis and corrosion processes. Helium embrittlement has generally been considered only operative at higher temperatures than found in LWRs where helium bubbles can migrate to grain boundaries; the lowest temperature definitely found to show migration of helium to grain boundaries is 370°C. But because of the severe effects of helium on the fracture of stainless steel compared to the same concentration of hydrogen , it may be a contributing factor to IASCC[11].

The embrittling effect of hydrogen has been postulated to reconcile variation in cracking trends with chromium depletion. Jacobs[12] and Jacobs et al.[13] have advocated an alternative mechanism of IASCC rather than the classical sensitization by chromium depletion. TEM examination of type 304 stainless steel irradiated to fluences between 1.90×10^{22} and 9×10^{25} n/m^2 (E> 1 MeV) showed hydrogen concentrations more than three times higher than in unirradiated type 304. This fact in conjunction with high resistance observed in a very low impurity type 348, and restored IASCC resistance of type 304 after a low temperature anneal are cited as evidence of a hydrogen enhanced cracking mechanism. Various hydrogen interactions with the impurities silicon, phosphorus and sulfur have been suggested to explain differences between IASCC susceptibility measured in out-of-flux SSR and in-core swelling mandrel tests[14]. Although in other swelling mandrel tests[15] IASCC susceptibility of 300 series stainless steel did not correlate with any of these impurity elements. Impurity nitrogen (a potential hydrogen source via (n,p) reactions) has also been postulated to reduce IASCC resistance. While the superior low impurity type 348, mentioned above, had a very low nitrogen content (80 ppm), followup in-core mandrel tests showed no such dependence for stainless steels with a nitrogen content in the range of 140-580 ppm. At present there is no direct evidence that strongly supports hydrogen assisted cracking over a dissolution controlled mechanism, but on the other hand there is no evidence to dismiss it either.

2.2.3 Deformation

The influence of deformation on environment sensitive cracking (i.e. EAC) is probably the least understood component. Although the macroscopic appearance of EAC is essentially brittle, there is much evidence that the microscopic mechanism involves plastic deformation. For example, corrosion assisted cracking of many alloy-environment systems shows a dependence on yield stress and strain rate and an indication of slip deformation in the vicinity of cracking[9]. The latter does not necessarily prove that microplasticity initiates cracking since some deformation is likely to occur at the crack tip because of the high stress concentration. In fact some SCC models argue that an array of blocked dislocations precipitate crack initiation.

In IASCC, deformation is also not well understood, but recent investigations suggest that it is a significant factor. Work by Fukuya et al.[16] and a review of SSR data by Bruemmer et al.[17] have found that yield stress correlated with IASCC susceptibility better than with fluence. Dislocation channeling, an inhomogeneous deformation mechanism observed in radiation damaged metals, has been observed in stainless steels strained in 288°C oxygenated water. Based on this observation and the effects of slip planarity, Bruemmer et al. considered stress concentrations due to dislocation pile ups could promote IG cracking. Contributing effects of the environment are possibly crack tip sharpening by dissolution (which would increase the local stress) and hydrogen ingress from corrosion reactions (which would reduce the interfacial cohesive energy). Another deformation mechanism suggested to influence IASCC is localized plasticity near the grain boundary. The region next to the grain boundary (~ nanometers) has a very low density of defects, like faulted loops, that impede dislocation motion, therefore a large concentration of slip or grain boundary sliding can occur in the "denuded" area. This would also promote crack initiation and could work in concert with a hydrogen decohesion mechanism. For understanding IASCC mechanisms, the influence of the deformation process is an area that needs further research.

2.3 SLOW STRAIN RATE (SSR) TESTING FOR IASCC

Slow strain rate tests are conducted to quantify materials performance in service environments. In SSRTs, the specimen is monotonically strained under a dynamic load. Historically, the SSR technique has been referred to by a number of terms. Some of them being constant extension rate, constant extension rate tests, slow extension rate test or technique, constant strain rate, slow strain rate or slow strain rate test[18]. Since neither the extension rate nor the strain rate are constant in the technique, the terms "constant extension rate" and "constant strain rate" are considered misrepresentative and have generally been replaced by slow strain rate in the literature. In this thesis, the terms slow strain rate (SSR) and slow strain rate test (SSRT) are used in reference to this material test technique. This section presents some background information on the application of SSRTs to investigate IASCC and the rationale for adopting this technique in this research. The two experimental conditions considered to have the greatest impact on SSRTs, strain rate and environment, are discussed explicitly. In particular, the choice of operating conditions during in-flux testing is elucidated. In conclusion, some comments on susceptibility indices used for SSRTs are given.

2.3.1 Background

Slow strain rate testing, developed in the 1960s by Henthorne[19] and Parkins, is a method for ranking SCC susceptibility of alloys in specific environments. It was first applied to nuclear power industry materials in the 1970s for PWR and BWR conditions motivated by intergranular stress corrosion cracking (IGSCC) failures of steam generator components and welded stainless steel piping, respectively[20-22]. Broad application of SSR testing as a research and diagnostic technique for BWR was pioneered by General Electric for the evaluation of different heats and alloys and the development and implementation of alternate hydrogen water chemistry as mitigation technologies of IGSCC in weld-sensitized austenitic stainless steel piping[23].

It is probably due to the successful experience of applying this technique to evaluating SCC susceptibility of LWR material that SSR testing was also adopted for evaluating IASCC susceptibility. Since the first published paper[24] reporting the effects of irradiation on the environmentally assisted intergranular cracking of type 304 stainless steel, the SSR technique has been extensively utilized in laboratory and field experiments for measuring irradiation assisted SCC susceptibility[13,14,16,25-42]. Besides the conventional SSR technique, there is also a modified SSR test for in-reactor data that uses irradiation induced swelling of ceramic mandrels[14,15,43-45]. SSRT is not universally applied for IASCC studies, however, because of different interests and preferences. Some researchers[7,46] desire deterministic data for crack growth rates and some[47] believe constant load tests are more appropriate than SSRTs for investigating IASCC.

While there existed a number of alternatives for investigating IASCC, the SSR technique was adopted in this work for the following reasons:

- the focus was to evaluate the susceptibility of 300 series stainless steel to irradiation assisted stress corrosion cracking, hence the complex specimen geometry and instrumentation of crack growth rate measurements were not necessary.
- the development of a facility that actively loaded a specimen provided the capability of performing SSR or constant load tests, whereas the swelling mandrel test is a passively loaded in-flux technique without the possibility of varying load or strain independent of fluence.
- comparison between in-flux and out-of-flux results behooved the use of SSRTs because of a much larger number of SSR tests reported in the literature as compared with constant load tests.
- a greater number of specimens could be tested because of the shorter time duration of SSRTs compared to constant load tests.

For comparing the susceptibility of different alloys in a BWR environment a standard strain rate and electrochemical potential were utilized for all in-flux SSRTs. These two parameters are considered the most important for controlling SSRT results[18], therefore the choice

of strain rate and potential were critical for meaningful results. The rationale for determining these two components of the SSR is presented in the next subsections.

2.3.2 Strain Rate

The dependence of SCC susceptibility on applied strain rate is commonly recognized for many alloy/environment combinations. The 300 series stainless steel/oxygenated water system is no exception. The difference in the kinetics of corrosion processes compared to deformation processes essentially underlies the strain rate dependence of SSRTs. At high strain rates, material deformation induced by straining occurs faster than the electrochemical reactions and the mechanical component dominates the fracture mode. At low strain rates, the mechanical baring action is not rapid enough to maintain preferential corrosion at the crack tip (compared to dissolution of the crack sides) resulting in pitting or blunting and eventual crack growth cessation. Between these two critical strain rates, the SCC susceptibility of a material shows a relatively flat dependence on strain rate. Since critical strain rates differ for the particular alloy and environment examined, data for types 304 and 316 in BWR simulated environments were evaluated.

For types 304 and 316 stainless steel in such an environment the critical strain rate range has been identified to have an upper bound[48,49] of $\leq 1 \times 10^{-6}\ s^{-1}$ and a lower bound[49] interpreted at $\sim 1 \times 10^{-8}\ s^{-1}$. For the MIT in-flux SSR tests, the strain rate was controlled by the total extension rate which was kept constant throughout the tests. In this method the true strain rate increases by more than an order of magnitude over the test duration as shown in Figure 2-4. As the specimen yields the strain rate increases dramatically because a much greater fraction of the extension comes from the plastic straining of the specimen compared to the elastic strain of the rig. The strain rate remains relatively constant during uniform elongation then changes rapidly at the ultimate stress due to the contraction of the rig on the load decrease. After this short transient, the strain rate increases dramatically because of the concentrated straining of the specimen during necking. During SSRTs, the strain rate during uniform elongation was chosen as the target strain rate to provide the most aggressive straining conditions and to facilitate comparison with out-of-flux tests. The strain rate before yield is irrelevant since plastic deformation is necessary for cracking and the test time after the onset of necking was less than the time of uniform straining. Since most out-of-flux SSRTs have been conducted at uniform strain rates in the range of $2.5\text{-}7 \times 10^{-7} s^{-1}$, using a similar strain rate for the in-flux SSRTs limited the differences of the tests to the in-flux environment. By comparison of in-flux and out-of-flux results, *in situ* radiation flux effects can be more easily distinguished and the applicability of out-of-flux testing for IASCC investigations better understood.

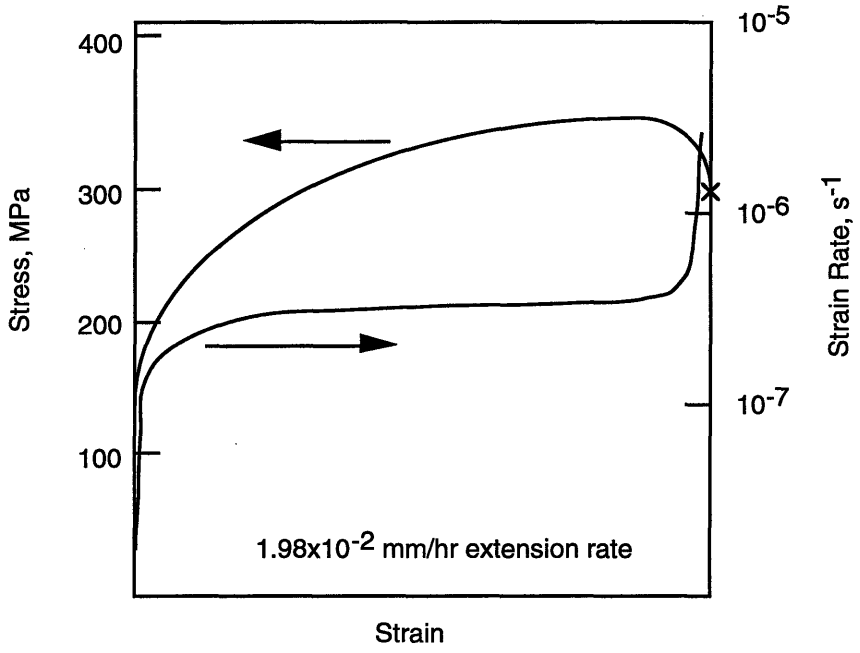

Figure 2-4. Schematic of stress and strain rate dependence of 300 series stainless steel during SSRT.

2.3.3 Environment

SSRTs have been used to research and identify the specific environment conditions that lead to SCC susceptibility. The corrosion potential, commonly referred to as the electrochemical potential (ECP), is the significant parameter for defining the electrochemical environment provided the particular ions are known. For stainless steels, the negative effect of certain anions (sulfate, chloride, nitrate, fluoride and silica) on cracking resistance has been observed in plant and laboratory tests[50-53] and has prompted the adoption of very high purity water chemistry criteria for operation in nuclear power plants[54]. While ionic impurities can influence the cracking behavior, the ECP has been utilized as the controlling parameter for investigating IGSCC of materials in nuclear power systems. Studies of SCC in stainless steel recirculation piping often adopted a high oxygen (8-32 ppm) water chemistry that was considered much more aggressive than the 0.2 ppm dissolved oxygen measured in the recirculation line. The typical ECP response of stainless steel as a function of dissolved oxygen displayed in Figure 2-5 indicates a 0.2 V difference over this range of oxygen concentrations. Although oxygen concentration measurements are not feasible in-core, predictions from computer simulations indicate values at the higher concentrations. Development and employment of in-flux radiation hardened ECP sensors have provided direct measurement of the in-core corrosion potential which corresponded to high oxygen levels in out-of-flux laboratory tests. In IASCC studies, oxygen levels have typically been maintained at 8-32 ppm, but some researchers use a level of 0.2 ppm. Since the

ECP has been identified as a controlling parameter in SSRTs, it has been adopted for characterizing the in-flux SSRT environment. The scope of this thesis was to examine IASCC of stainless steels in BWR normal water chemistry environments, so the ECP criterion was defined as 0-0.1 V versus a standard hydrogen electrode (SHE). Some insights into the oxygen concentration used in out-of-flux SSRTs, with regard to in-flux results, are presented in Chapter 8.

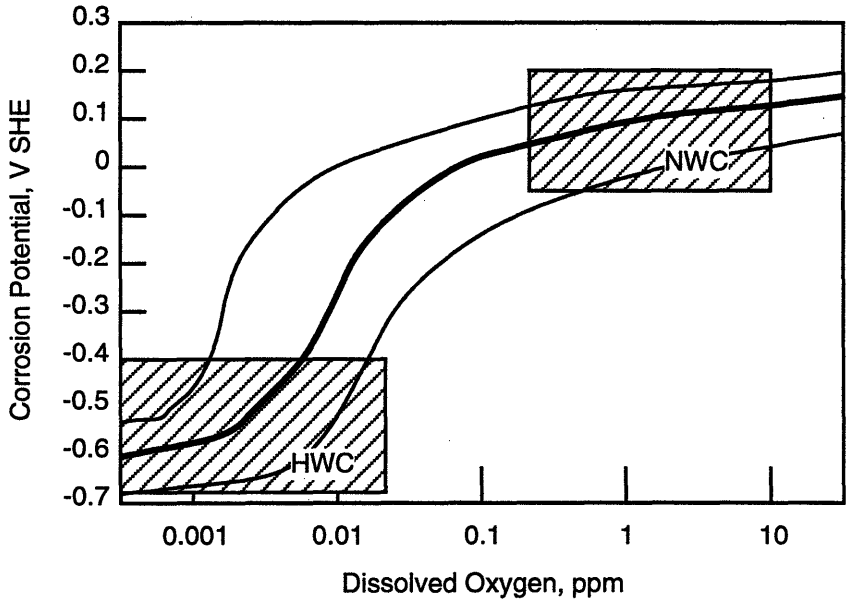

Figure 2-5. ECP of stainless steel at 288°C as a function of dissolved oxygen concentration.

2.3.4 Susceptibility Indices

Interpretation of SSRT data requires a ranking system for defining the SCC susceptibility of materials. The merit of a susceptibility index relies on its sensitivity to SCC and its performance in distinguishing SSR resistance between samples. A simple approach utilizes mechanical properties measured in the aggressive environment normalized against properties measured in inert environments. Some of the properties and data which can be utilized are yield stress, ultimate stress, total elongation and test time[55]. Susceptibility indices that have a high sensitivity are preferred, therefore parameters that combine the effect of multiple properties or that represent some overall average measure have often been used. Some of the susceptibility indices in this category are the area under the stress strain curve and combined ratios of normalized properties like $\sigma_y (1+e_f)$. With the advent of electron microscopy, highly sensitive fracture areal quantification methods have become very popular susceptibility indices. These indices include reduction of area (RA), fracture area ratio or percentage intergranular fracture (%IG) and the average crack propagation rate of the deepest crack.

From a detailed mechanics perspective, an interpretation of SSRT results is difficult because of the two different processes occurring within the specimen: deformation resulting in microvoid coalescence and ductile failure and stress corrosion cracking resulting in intergranular or transgranular brittle failure. Often there is more than one intergranular or transgranular region which further complicates the combined effect of these two processes. However from an engineering perspective, experience has shown that SSR results correlate well with in-service performance for a wide spectrum of alloy-environment combinations[56]. In particular, SSRT and the susceptibility index %IG have been used extensively in IASCC investigations[57].

While recognizing a lack of detailed understanding of simultaneous ductile and brittle crack growth, the high sensitivity and favorable experience of utilizing fracture areal quantification have shown the merit of this susceptibility index. Thus these methods were used in this thesis as IASCC susceptibility indices of the in-flux SSRT data.

2.4 FACILITY DESCRIPTION

The MIT In-core Materials Testing Facility consisted of two internal components: 1) the ECP Mapping internals and 2) the SSR Testing internals. Both internal components utilized the same autoclave and thimble housing. In the ECP Mapping Rig, radiation qualified ECP reference sensors were placed in the MITR-II core region of the SSRT Rig to correlate letdown oxygen concentrations with in-core stainless steel ECP values, measured with silver/silver-chloride and platinum reference sensors. The ECP Mapping was completed prior to initiation of SSR tests (see O'Donnell[58] for details). In the SSR Testing Rig, pre-irradiated tensile specimens were positioned in the MITR-II core and dynamically loaded in tension at a constant extension rate until failure. A brief summary of the facilities is presented in the following sections. Detailed descriptions can be found in the thesis by O'Donnell[58].

2.4.1 Materials and Specimen Geometry

A standard tensile specimen geometry (see Figure 2-6) was employed with gage diameter of 2.54 mm (0.1 in.), gage length of 12.7 mm (0.50 in.) and shoulder diameter of 4.01 mm (0.158 in.). Total specimen length was 52.07 mm (2.05 in.) with 9.500 mm (0.3740 in.) diameter button heads for accepting the load. Pre-irradiation of tensile specimens was performed in the Dry Irradiation Facility in the MITR-II core (cf. section 1.3.1) as fully described in the thesis by Boerigter[59]. The pre-irradiated specimens were dissolved from aluminum capsules by a 3.5N NaOH solution. Before testing, the specimens were rinsed in a de-ionized (DI) water bath, mechanically polished in the longitudinal direction with 600 grit paper followed by 10 μm

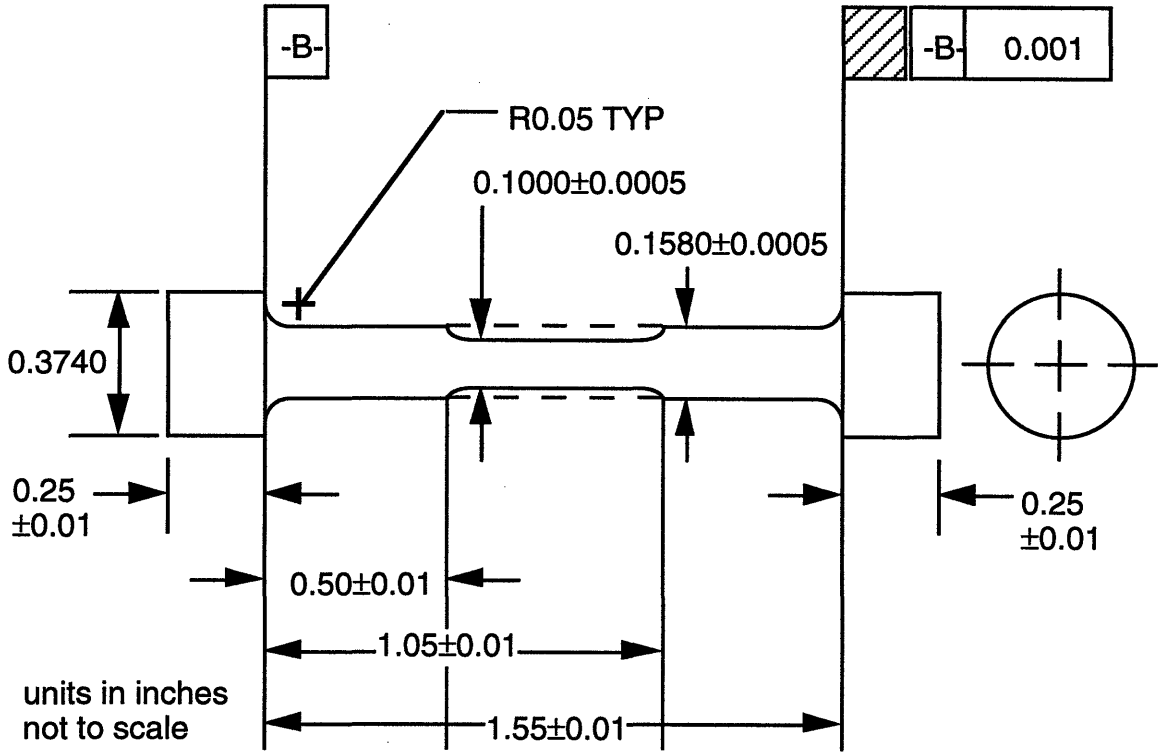

Figure 2-6. SSR tensile specimen geometry.

Table 2-1. Material chemistries[a] for alloys tested in the MIT IASCC program

Alloy (Heat)	CP[b] 304 (AJ9139)	316L (K5)	347L (K12)	UHP[c] 304L (V945)
C	0.066	0.010	0.011	0.0046
Si	0.470	0.50	0.12	0.03
Mn	0.93	0.83	0.84	1.11
P	0.026	0.010	0.012	<0.005
S	0.028	0.001	0.001	0.0051
Ni	8.13	12.15	9.38	9.03
Cr	18.37	16.70	17.55	19.21
Mo	0.250	2.15	0.16	<0.005
N	0.048	0.033	0.036	0.0031
Nb	•	0.00	0.30	•
T	•	•	•	•
Co	0.154	0.004	0.000	•

a Composition by wt%
b CP (commercial purity), 0.29 Cu
c UHP (ultra-high purity)

alumina powder and ultrasonically cleaned in DI water at room temperature. While a total of seven commercial and ten Fe-Ni-Cr ternary alloys were available for testing in the IASCC

program, only five commercial alloys were fabricated into SSRT specimens. In this thesis, the results of in-flux SSR testing performed on two alloys (commercial purity type 304 and type 316L) and the analytical microscopy and electrochemical results of these two and two other 300 stainless steel series alloys, ultra high purity (UHP) type 304L and type 347L, pre-irradiated in the MITR-II core are presented. The material chemistries of the alloys investigated are shown in Table 2-1.

2.4.2 MITR-II In-core Materials Testing Components

The portions of these materials testing rigs that were placed within the MITR-II will be discussed in this section. The major components consisted of a thimble, autoclave and experiment-specific internals. The aluminum thimble served two main purposes; it isolated the experiment from the MITR-II primary water and served as a final barrier in the event of a leak from the facility. To reduce heat loss from the experiment and prevent boiling on the thimble outside wall, an inert fill gas was purged through the annular gap separating the thimble inside wall and autoclave.

The autoclave acts as a pressure barrier for the high pressure and high temperature water simulating BWR conditions in single phase. The same autoclave was used for both the ECP Mapping Rig and the SSR Testing Rig. It was designed with safety factors for operation at a pressure of 22.1 MPa (3200 psig) and a temperature of 300°C (572°F). This design allows the flexibility of operating at thermal hydraulic conditions simulating either boiling water reactor primary or pressurized water reactor primary coolant.

2.4.2.1 ECP Mapping Rig

The internal component for ECP Mapping is an electrode fixture that contains six ECP sensors arranged in two clusters separated by an axial length of 229 mm (9 in.) (see Figure 2-7). Each cluster consists of one silver/silver-chloride reference, one platinum reference and one stainless steel working electrode and a dual junction thermocouple. All ECP sensors were provided by GE and qualified for service in a radiation environment. For the tests conducted in this program, ECP measurements were made at two in-core positions. In position number 1, the lower cluster was located 305 mm (12 in) below the top of the core and the upper cluster 76 mm (3 in) below the top of the core. In this position, the lower cluster is in the center of the MITR-II core which is the same axial position as the tensile specimens during SSR testing. The ECP measurements made in position number 1 were used to characterize the water chemistry

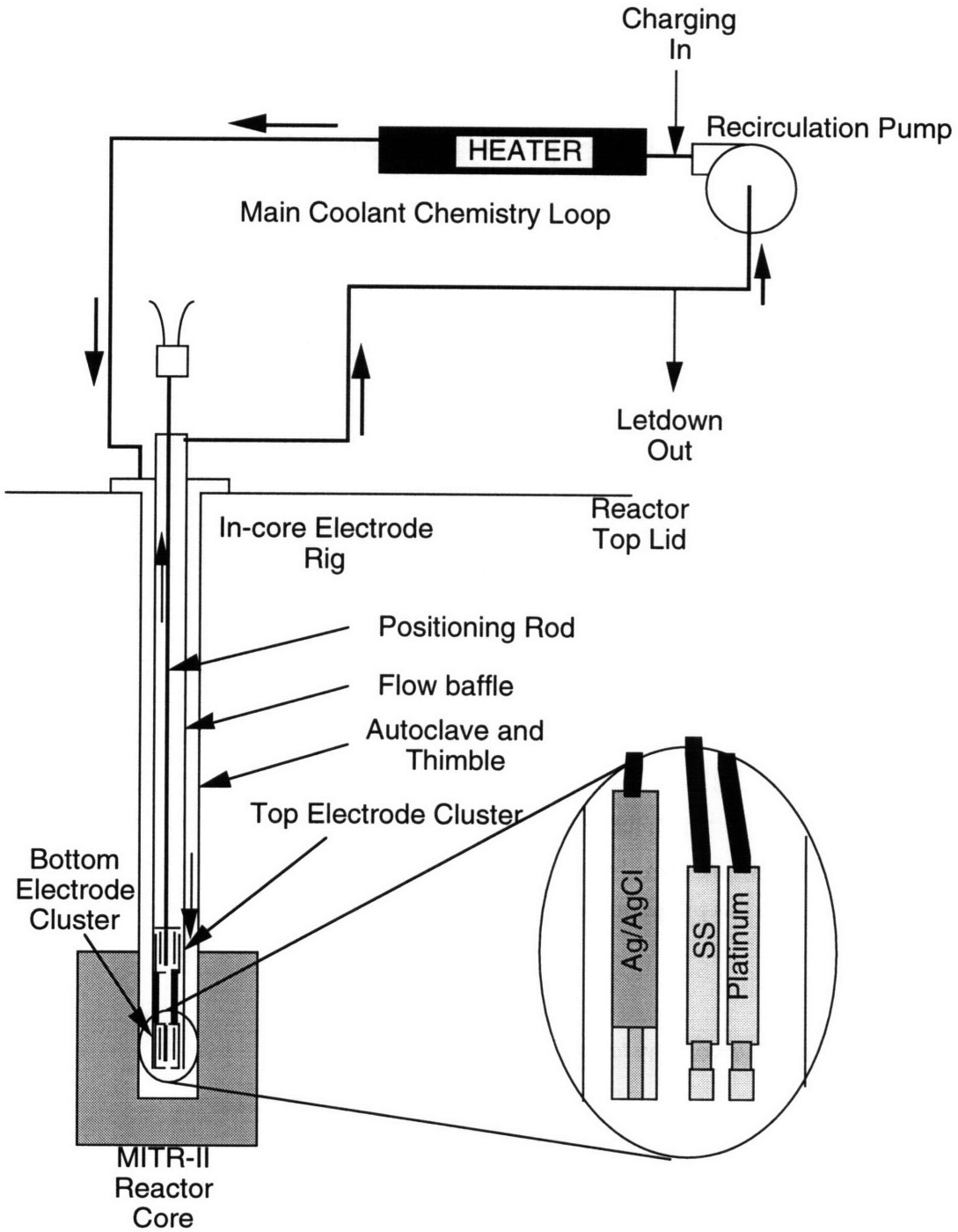

Figure 2-7. Schematic of in-core ECP Mapping Rig.

environment relative to laboratory results and in-pile measurements made in some reactors. In position number 2, the lower cluster was located 76 mm (3 in) below the top of the core and the upper cluster 152 mm (6 in) above the top of the core. These ECP measurements also provided a comparison between the two clusters at the same conditions. These measurements were used to verify the integrity of the sensors employed and the in-core ECP values used to characterize the coolant chemistry near the tensile specimens.

2.4.2.2 SSR Testing Rig

A schematic of the SSR Testing Rig is shown in Figure 2-8. As noted before, the outer housings (aluminum thimble and autoclave) were the same as used for the ECP Mapping Rig. The internal (in autoclave) component for SSR testing was the load train. It consisted of a concentric pull rod and reaction tube. The pull rod connected the loading machine (see section 2.4.3.1) to the tensile specimen and transmitted the tensile load. It was constructed in two parts which were connected by a threaded sleeve. The upper part of the pull rod was stainless steel and the lower (in-core) part was titanium making a total length of 4.52 m (178 in). The reaction tube was constructed of an upper stainless steel section and a lower titanium section. The bottom of the tensile specimen was held in place by the lower grip which mated with the bottom of the reaction tube (see Figure 2-9). When the specimen is loaded in tension, the reaction tube supports the compressive force exerted by the loading machine. Due to the long length of the load train an independent test was performed to determine the rig's compliance. The compliance was used to estimate the extension of the rig and calculate the specimen strain based on the total extension measured (see Appendix B.3). During the compliance test, a maximum load of 6.67 kN (1500 lbs) was employed. For the load train utilized in tensile tests the nominal design load was 5.34 kN (1200 lbs). This capacity has provided sufficient margin for the tensile specimen geometry and materials employed in this program. The highest load during any of the SSR tensile tests was 4.39 kN (986 lbs).

2.4.3 Out-of-core Support Systems

2.4.3.1 SSRT Loading Machine

The loading machine provided a controllable tensile force on the SSRT specimen to achieve a constant strain rate or constant extension rate depending on the control mode selected. For the tests reported in this work, a constant extension rate of 0.00198 mm/hr (which corresponded to strain rates between 2-6 x 10^{-7} s^{-1}) was employed. The load machine was a

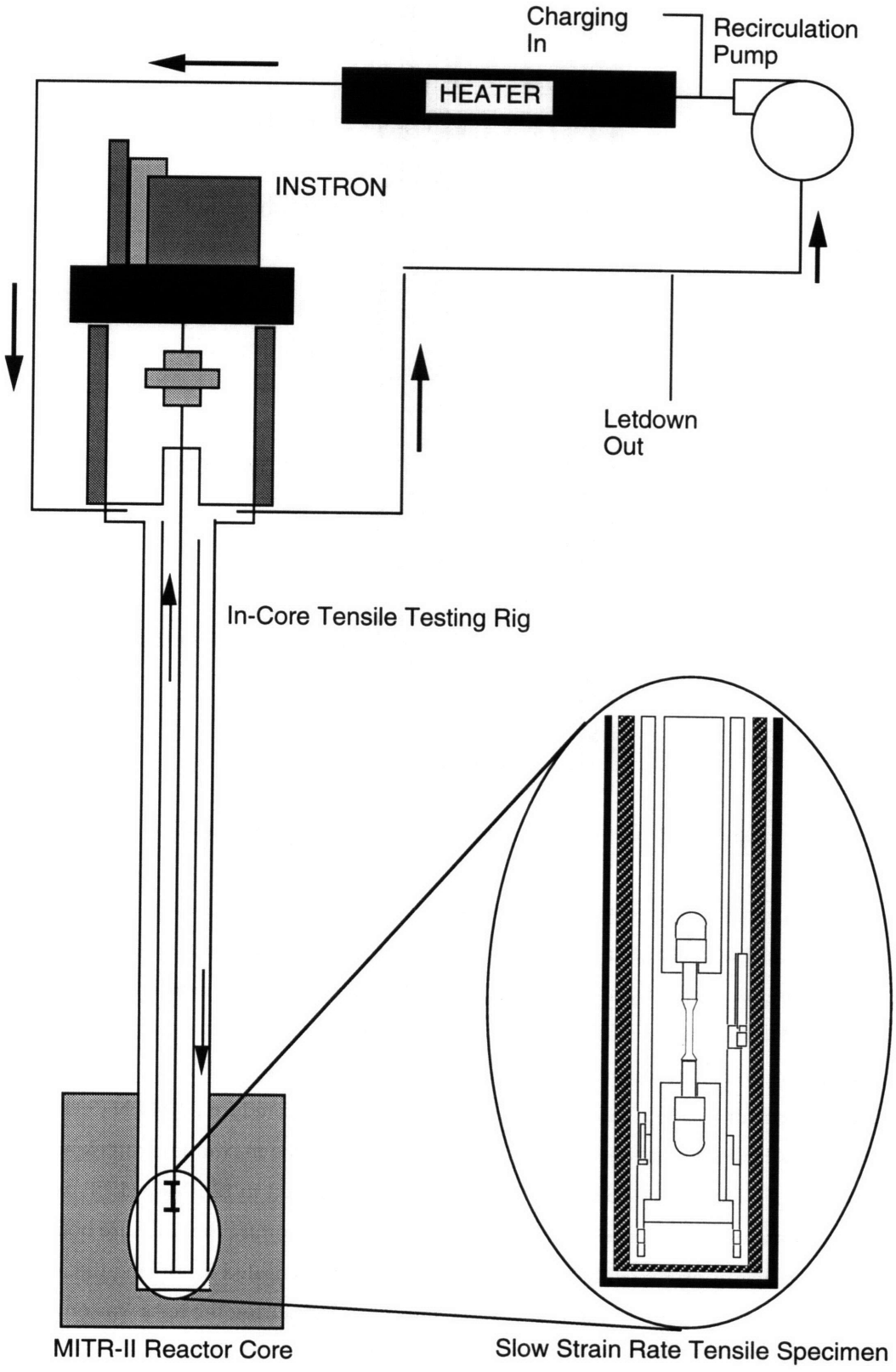

Figure 2-8. Schematic of in-core SSR Testing Rig.

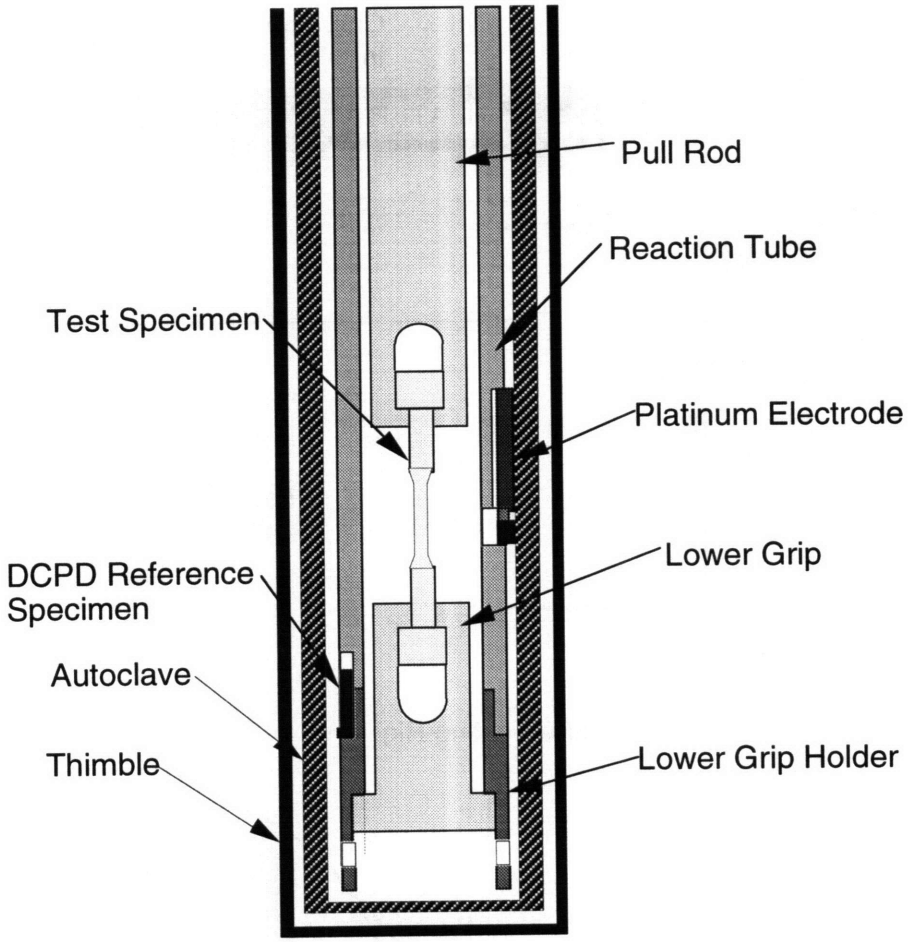

Figure 2-9. Details of in-core SSR Testing Rig components.

standard Instron series 8500 electro-mechanical test system. It was purchased in a single commercially available package and included all the features required to run tensile tests.

The Instron actuator was attached to the platen, inverted, and mounted on the loading machine support. The loading machine support was aligned with the pull rod in the SSRT internals by guide bolts that secured the loading machine to the MITR-II lid. The loading machine was rated for 88.96 kN (20,000 lbs) and the load cell was rated for 22.24 kN (5000 lbs) which well exceed the nominal design load of the load train and the maximum load experienced during SSR testing. During the SSR tests, the water was pressurized to 12.1 MPa (1750 psi) which exerted a compressive load on the load cell (via the pull rod penetrating the pressure boundary). This load, which was approximately 3.43 kN (772 lbs), was compensated for during the initial calibration sequence; therefore, the load measured and recorded during the tests was only that due to the electro-mechanical drive of the loading machine.

2.4.3.2 Water Chemistry Control

Water chemistry control was very important in accurately simulating BWR primary coolant and for making any comparisons between these in-pile results and out-of-pile laboratory data. The system employed is similar to that of other MIT in-pile loops like the PWR Coolant Chemistry Loop (PCCL) and the BCCL[60,61]. The important water chemistry parameters include pH, conductivity, dissolved oxygen and hydrogen concentrations and the ECP of the stainless steel.

For boiling water reactors operating in a NWC environment, a neutral pH, oxidizing condition is maintained. Guidelines for water purity are suggested in an EPRI publication[54] and were adopted for this program. On the low pressure side of the water chemistry system, there were dissolved oxygen and hydrogen analyzers, a pH meter, two conductivity cells, sample points, demineralizers, and filters (see Figure 2-10). The desired oxygen and hydrogen concentration in the feedwater was achieved by sparging with an oxygen/ helium gas mixture and recirculating the sparged gases (oxygen, hydrogen and helium) through a dry bed catalyst.

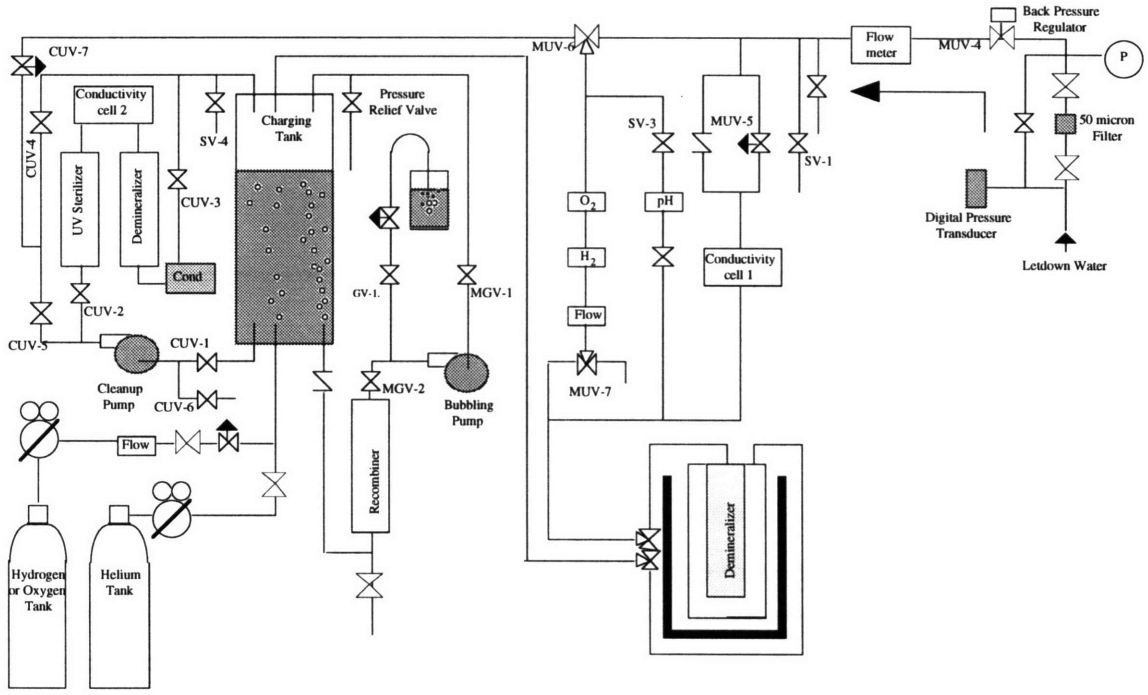

Figure 2-10. MIT NRL water chemistry control for IASCC Testing Rigs.

Hydrogen water chemistry was achieved by sparging with a hydrogen/ helium gas mixture. The water quality was within EPRI guidelines except for the overall conductivity. The 1993 revised EPRI water chemistry guidelines recommend 0.11 μS/cm, whereas the measured letdown line conductivity was ~0.7 μS/cm. The higher conductivity was not due to the presence

of deleterious ions, as their concentrations determined by on-line ion chromatography were below the critical values cited in the EPRI reference[54]. Moreover, it is recognized that bulk conductivity is a poor parameter to correlate corrosion effects since the corrosion process depends on concentrations of specific ions[50]. Evaluations by the MIT staff indicated that organics, leached into the system through plastic components or resin breakthrough and decomposed by radiation, were the major contributors to conductivity. Hence, it was concluded that the in-core SSRT Rig's water purity with regards to aggressive ion species, was comparable to BWR plant and laboratory autoclaves despite the higher bulk conductivity measured. Table 2-2 identifies the water chemistry conditions maintained during in-core SSR testing and the EPRI recommended chemistry guidelines.

Table 2-2. Measured values and guidelines of water chemistry parameters during in-core SSR testing.

Parameter	Observed Range	EPRI Guidelines			
		medi-an[a]	Level 1[b]	Level 2[c]	Level 3[d]
dissolved oxygen	200-500 ppb				
conductivity	0.5-0.8 μS/cm	0.11	>0.3	>1.0	>5.0
Cl^-	<5 ppb	~1	>5	>20	>100
$NO_3^{2-} + SO_4^{2-}$	<10 ppb	~2	>5	>20	>100
F^-	<0.1 ppb				
CrO_4^{2-}	<20 ppb				
ECP (as measured by reference autoclave)	>0 mV, SHE*				
Potential of in-core platinum vs. Gnd	50-150mV*				

*This implies that the ECP of stainless steel in-core is >100 mV, SHE.
a median of BWR plants from INPO 1st quarter 1993 database.
b Level 1- value above which engineering judgment indicates long term reliability may be threatened.
c Level 2- value above which engineering judgment indicates short term reliability may be threatened (i.e. for chloride and sulfate crack growth rate is ~10 times that at the median value).
d Level 3- value above which engineering judgment indicates continued operation is inadvisable.

2.4.3.3 Temperature and Pressure Control

The temperature and pressure control components were positioned outside of the MITR-II primary tank vessel to facilitate maintenance and operation. The system (see Figure 2-11) consisted of an electric heater, thermocouples, a regenerative and a non-regenerative heat exchanger (RHX and NRHX), a back pressure regulator, a pressurizer, a positive displacement metering pump and a magnetic drive centrifugal recirculation pump. The triplex head metering pump drew suction from the charging tank (~27°C) and pumped it to the loop pressure of 12.1 MPa (1750 psig) at a flowrate of 500 ml/min. The pressure was maintained with a single back pressure regulator located on the letdown line after the RGHX and NRHX. The auxiliary

pressurizer did not affect loop pressure during normal operation, but served a safety function in the event of a loss of coolant incident. Water in the auxiliary pressurizer was maintained at 296°C (565°F), 16°C higher than the main loop temperature. In the event of a loop depressurization, steam would form in the auxiliary pressurizer and thus act to prevent boiling in the rest of the facility. The main loop flowrate was 45,200 ml/min (12.0 gpm), circulated by the centrifugal pump. For the feedwater flowrate of 550 ml/min, the main loop water volume was refreshed every 10 minutes which was ~3 times slower than the typical refresh rate of an operating BWR. The chemical injection line was not used in this series of tests, but can be used to examine the effect of chemical additives on cracking susceptibility. The operating temperature for the SSR tests was 280°C and was maintained by the electric heater. A thermocouple near the tensile specimen was used to control the electric heater. Other thermocouples were positioned in the out-of-pile components for monitoring and control purposes. With this temperature and pressure system, all tests were reliably conducted at the design conditions of 12.1 MPa (1750 psig) and 280°C (535°F).

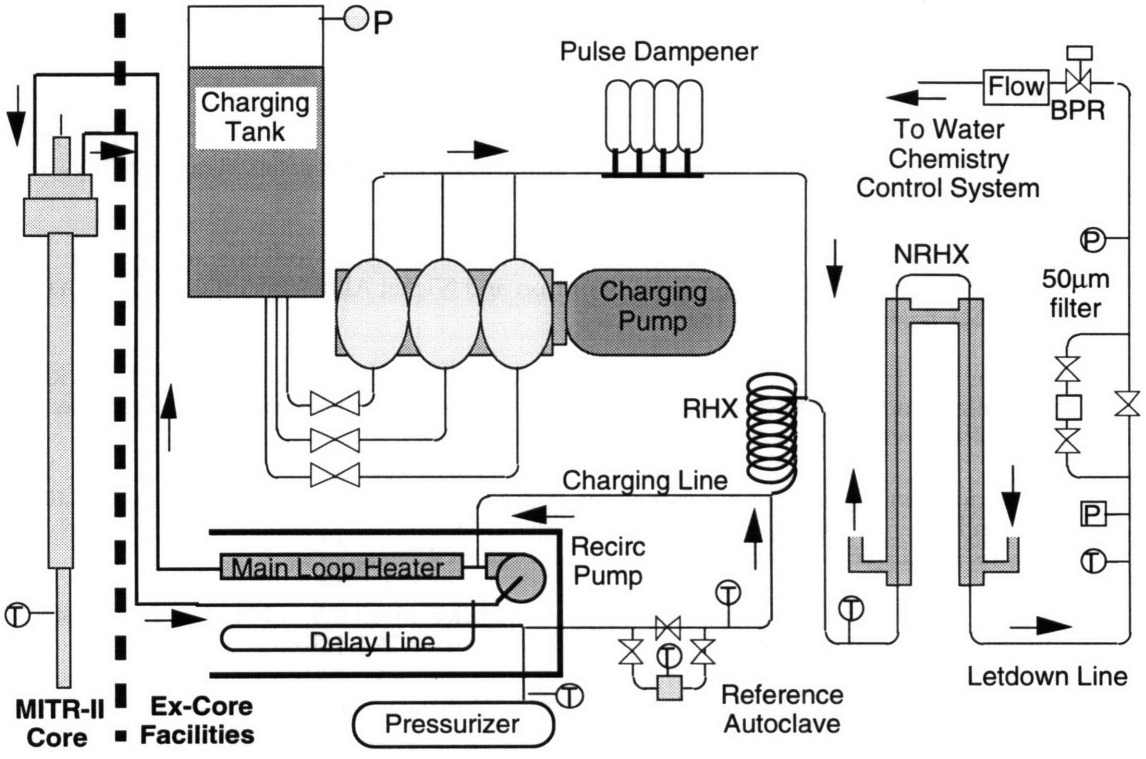

Figure 2-11. Temperature and pressure control for IASCC Testing Rigs.

2.5 SUMMARY

The slow strain rate experimental approach and its historical background in nuclear power material applications was introduced in this chapter. The rationale for adopting the SSR technique for development and operation in an in-core environment were elucidated. In-flux SSRTs were concluded to be the best choice for evaluating IASCC susceptibility of 300 series stainless steel alloys and for comparing the differences between in-flux and out-of-flux environments on corrosion assisted cracking performance of materials. A brief description of the experimental facilities employed in this work was presented.

2.6 REFERENCES

1. F. A. Champion, *Symposium on Internal Stresses in Metals and Alloys*, Inst. of Metals, London (1948) p. 468.

2. H. L. Logan, *JRNBS* , 48, no. 99 (1952).

3. T. P. Hoar and J. G. Hines, *Stress Corrosion Cracking and Embrittlement*, Wiley & Sons, NY (1956) p. 107.

4. F. P. Ford and P. L. Andresen, "Development and Use of a Predictive Model of Crack Propagation in 304/316L, A533B/A508 and Inconel 600/182 Alloys in 288°C Water," *Proc. 3rd Int. Symp. on Env. Deg. of Mat. in Nucl. Pow. Systems-Water Reactors*, Traverse City, MI, TMS (1987) p. 789.

5. P. L. Andresen and F. P. Ford, "Life Prediction by Mechanistic Modeling and System Monitoring of Environmental Cracking of Iron and Nickel Alloys in Aqueous Systems," *Mater. Sci. E.*, A103 (1987) p. 167.

6. F. P. Ford, D. F. Taylor, P. L. Andresen and R. G. Ballinger, "Corrosion-Assisted Cracking of Stainless and Low-Alloy Steels in LWR Environments," EPRI Report NP-5064S, Electric Power Research Institute, Palo Alto, CA (February 1987).

7. P. L. Andresen and F. P. Ford, "Modeling of Irradiation Effects on Stress Corrosion Crack Growth Rates," *CORROSION / 89*, National Association of Corrosion Engineers, New Orleans (April 1989) Paper 497.

8. X. Chen and W. W. Gerberich, "The Kinetics and Micromechanics of Hydrogen-Assisted Cracking in Fe-3 pct Si Single Crystals," *Metall. Trans. A*, 22A (1991) p. 59.

9. R. N. Parkins, "Current Understanding of Stress-Corrosion Cracking," *J. Metals*, (December 1992) p. 12.

10. E. N. Pugh, "Progress Toward Understanding the Stress Corrosion Problem," *Corrosion*, 41 (1985) p. 517.

11. P. Scott, "A Review of Irradiation Assisted Stress Corrosion Cracking," *J. Nucl. Mat.*, 211 (1994) p. 101.

12. A. J. Jacobs, "Hydrogen Buildup in Irradiated Type-304 Stainless Steel," *Effects of Radiation on Materials: 13th International Symposium, Part II, ASTM STP 956*, F. A. Garner, C. H. Henager, Jr. and N. Igata, Eds., American Society for Testing and Materials, Philadelphia (1987) p. 239.

13. A. J. Jacobs, R. E. Clausing, L. Heatherly and R. M. Kruger, "Irradiation-Assisted Stress Corrosion Cracking and Grain Boundary Segregation in Heat Treated Type 304 SS," *Effects of Radiation on Materials: 14th International Symposium, Vol. I, ASTM STP 1046*, N. H. Packan, R. E. Stoller and A. S. Kumar, Eds., American Society for Testing and Materials, Philadelphia (1989) p. 424.

14. A. J. Jacobs, G. P. Wozadlo, K. Nakata, S. Kasahara, T. Okada, S. Kawano and S. Suzuki, "The Correlation of Grain Boundary Composition in Irradiated Stainless Steel with IASCC Resistance," *Proc. 6th Int. Symp. on Env. Deg. of Mat. in Nucl. Pow. Systems-Water Reactors*, TMS, San Diego, CA (1993) p. 597.

15. F. Garzarolli, P. Dewes, R. Hahn and J. L. Nelson, "Deformability of High-Purity Stainless Steels and Ni-Base Alloys in the Core of a PWR," *Proc. 6th Int. Symp. on Env. Deg. of Mat. in Nucl. Pow. Systems-Water Reactors*, TMS, San Diego, CA (1993) p. 607.

16. K. Fukuya, S. Shima, K. Nakata, S. Kasahara, A. J. Jacobs. G. P. Wozadlo, S. Suzuki and M. Kitamura, "Mechanical Properties and IASCC Susceptibility in Irradiated Stainless Steels," *Proc. 6th Int. Symp. on Env. Deg. of Mat. in Nucl. Pow. Systems-Water Reactors*, TMS, San Diego, CA (1993) p. 565.

17. S. W. Bruemmer, J. I. Cole, J. L. Brimhall, R. D. Carter and G. S. Was, "Radiation Hardening Effects on Localized Deformation and Stress Corrosion Cracking of Stainless Steels," *Proc. 6th Int. Symp. on Env. Deg. of Mat. in Nucl. Pow. Systems-Water Reactors*, TMS, San Diego, CA (1993) p. 537.

18. J. A. Beavers and G. H. Koch, "Limitations of the Slow Strain Rate Test for Stress Corrosion Cracking Testing," *Corrosion*, 48 (March 1992) p. 256.

19. M. Henthorne, PhD Thesis, Dept. Met. Eng. Mat., University of Newcastle upon Tyne, England (1965).

20. H. D. Solomon, M. J. Povich and T. M. Devine, "Slow Strain-Rate Testing in High Temperature Water," *Stress Corrosion Cracking-The Slow Strain-Rate Technique, ASTM STP 665*, G. M. Ugiansky and J. H. Payer, Eds., American Society for Testing and Materials (1979) p. 132.

21. W. L. Clarke, R. L. Cowand and J. C. Danko, "Dynamic Straining Stress Corrosion Test for Predicting Boiling Water Reactor Materials Performance," *Stress Corrosion Cracking-The Slow Strain-Rate Technique, ASTM STP 665*, G. M. Ugiansky and J. H. Payer, Eds., American Society for Testing and Materials (1979) p. 149.

22. M. E. Indig, "Slow Strain-Rate Stress Corrosion Testing for Liquid Metal Fast Breeder Reactor Steam Generator Applications," *Stress Corrosion Cracking- The Slow Strain-Rate Technique, ASTM STP 665*, G. M. Ugiansky and J. H. Payer, Eds., American Society for Testing and Materials (1979) p. 170.

23. M. E. Indig, "SSRT for Hydrogen Water Chemistry Verification in BWRs," *Slow Strain Rate Testing for the Evaluation of Environmentally Induced Cracking: Research and Engineering Applications, ASTM STP 1210,* R. D. Kane, Ed., American Society for Testing and Materials, Philadelphia (1993) p. 56.

24. W. L. Clarke and A. J. Jacobs, "Effect of Radiation Environment on SCC of Austenitic Materials," *Proceedings of the International Symposium on Environmental Degradation of Materials in Nuclear Power Systems-Water Reactors,* NACE, Myrtle Beach, SC (1983) p. 451.

25. A. J. Jacobs, G. P. Wozadlo, K. Nakata, T. Yoshida and I. Masaoka, "Radiation Effects on the Stress Corrosion and Other Selected Properties of Type-304 and Type-316 Stainless Steels," *Proc. 3rd Int. Symp. on Env. Deg. of Mat. in Nucl. Pow. Systems-Water Reactors,* TMS, Traverse City, MI (1987) p. 673.

26. H. M. Chung, W. E. Ruther, J. E. Sanecki and T. F. Kassner, "Irradiation-Induced Sensitization and Stress Corrosion Crakcing of Type 304 Stainless Steel Core-Internal Components," *Proc. 5th Int. Symp. on Env. Deg. of Mat. in Nucl. Pow. Systems,* ANS, Monterey, CA (1991) p. 795.

27. J. M. Cookson, R. D. Carter, D. L. Damcott, M. Atzmon, G. S . Was and P. L. Andresen, "Stress Corrosion Cracking of High Energy Proton-Irradiated Stainless Steels," *Proc. 5th Int. Symp. on Env. Deg. of Mat. in Nucl. Pow. Systems,* ANS, Monterey, CA (1991) p. 806.

28. K. Fukuya, K. Nakata and A. Horie, "An IASCC Study Using High Energy Ion Irradiation," *Proc. 5th Int. Symp. on Env. Deg. of Mat. in Nucl. Pow. Systems,* ANS, Monterey, CA (1991) p. 814.

29. S. M. Bruemmer, L. A. Charlot and E. P. Simonen, "Irradiation-Induced Chromium Depletion and Its Influence on Intergranular Stress Corrosion Cracking of Stainless Steels," *Proc. 5th Int. Symp. on Env. Deg. of Mat. in Nucl. Pow. Systems,* ANS, Monterey, CA (1991) p. 821.

30. A. J. Jacobs, C. M. Shepherd, G. E. C. Bell and G. P. Wozadlo, "High-Temperature Solution Annealing as an IASCC Mitigation Technique," *Proc. 5th Int. Symp. on Env. Deg. of Mat. in Nucl. Pow. Systems,* ANS, Monterey, CA (1991) p. 917.

31. M. E. Indig, J. L. Nelson and G. P. Wozadlo, "Investigation of the Protection Potential Against IASCC," *Proc. 5th Int. Symp. on Env. Deg. of Mat. in Nucl. Pow. Systems,* ANS, Monterey, CA (1991) p. 941.

32. M. Kodama, S. Nishimura, J. Morisawa, S. Suzuki, S. Shima and M. Yamamoto, "Effects of Fluence and Dissolved Oxygen on IASCC in Austenitic Stainless Steels," *Proc. 5th Int. Symp. on Env. Deg. of Mat. in Nucl. Pow. Systems-Water Reactors,* ANS, Monterey, CA (1991) p. 948.

33. S. W. Bruemmer, B. W. Arey and L. A. Charlot, "Grain Boundary Chromium Concentration Effects on the IGSCC and IASCC of Austenitic Stainless Steels," *Proc. 6th Int. Symp. on Env. Deg. of Mat. in Nucl. Pow. Systems-Water Reactors,* TMS, San Diego, CA (1993) p. 277.

34. H. M. Chung, W. E. Ruther, J. E. Sanecki and T. F. Kassner, "Grain-Boundary Microchemistry and Intergranular Cracking fo Irradiate Austenitic Stainless Steels," *Proc. 6th Int. Symp. on Env. Deg. Mat. in Nucl. Pow. Systems,* TMS, San Diego, CA (1993) p. 511.

35. A. Jenssen and L. G. Ljungberg, "Irradiation Assisted Stress Corrosion Cracking of Stainless Alloys in BWR Normal Water Chemistry and Hydrogen Water Chemistry," *Proc. 6th Int. Symp. on Env. Deg. Mat. in Nucl. Pow. Systems*, TMS, San Diego, CA (1993) p. 547.

36. J. M. Cookson, D. L. Damcott, G. S .Was and P. L. Andresen, "The Role of Microchemical and Microstructural Effects in the IASCC of High Purity Austenitic Stainless Steels," *Proc. 6th Int. Symp. on Env. Deg. Mat. in Nucl. Pow. Systems-Water Reactors*, TMS, San Diego, CA (1993) p. 573.

37. M. Kodama, R. Katsura, J. Morisawa, S. Nishimura, S. Suzuki, K. Asano, K. Fukuya and K. Nakata, "IASCC Susceptibility of Austenitic Stainless Steels Irradiated to High Neutron Fluence," *Proc. 6th Int. Symp. on Env. Deg. of Mat. in Nucl. Pow. Systems-Water Reactors*, TMS, San Diego, CA (1993) p. 583.

38. W. J. Liu, C. H. Tsai and J. J. Kai, "Microstructure and Stress Corrosion Cracking Study of AISI 304 and AISI 304L Stainless Steels Subjected to Proton Irradiation," *Proc. 6th Int. Symp. on Env. Deg. Mat. in Nucl. Pow. Systems*, TMS, San Diego, CA (1993) p. 591.

39. H. M. Chung, W. E. Ruther, J. E. Sanecki, A. G. Hins and T. F. Kassner, "Stress Corrosion Cracking Susceptibility of Irradiated Type 304 Stainless Steels," *Effects of Radiation on Materials: 16th International Symposium, ASTM STP 1175*, A. S. Kumar, D. S. Gelles, R. K. Nanstad and E. A. Little, Eds., American Society for Testing and Materials, Philadelphia (1993) p. 851.

40. W. J. Liu, C. H. Tsai and J. J. Kai, "Raidation-Induced Solute Segregation and Stress Corrosion Cracking Study of AISI 304 and AISI 304L Stainless Steels," *Effects of Radiation on Materials: 16th International Symposium, ASTM STP 1175*, A. S. Kumar, D. S. Gelles, R. K. Nanstad and E. A. Little, Eds., American Society for Testing and Materials, Philadelphia (1993) p. 870.

41. M. Kodama, K. Fukuya and H. Kayano, "Influence of Impurities and Alloying Elements on IASCC in Neutron Irradiated Austenitic Stainless Steels," *Effects of Radiation on Materials: 16th International Symposium, ASTM STP 1175*, A. S. Kumar, D. S. Gelles, R. K. Nanstad and E. A. Little, Eds., American Society for Testing and Materials, Philadelphia (1993) p. 889.

42. A. J. Jacobs, "The Relationship of Grain Boundary Composition in Irradiated Type 304SS to Neutron Fluence and IASCC," *Effects of Radiation on Materials: 16th International Symposium, ASTM STP 1175*, A. S. Kumar, D. S. Gelles, R. K. Nanstad and E. A. Little, Eds., American Society for Testing and Materials, Philadelphia (1993) p. 902.

43. F. Garzarolli, D. Alter and P. Dewes, "Deformability of Austenitic Stainles Steels and Ni-Base Alloys in th Core of a Boiling and a Pressurized Water Reactor," *Proc. 2nd Int. Symp. on Env. Deg. of Mat. in Nucl. Pow. Systems-Water Reactors*, ANS, Monterey, CA (1985) p. 131.

44. F. Garzarolli, D. Alter, P. Dewes and J. L. Nelson, "Deformability of Austenitic Stainles Steels and Ni-Base Alloys in th Core of a Boiling and a Pressurized Water Reactor," *Proc. 3rd Int. Symp. on Env. Deg. of Mat. in Nucl. Pow. Systems-Water Reactors*, TMS, Traverse City, MI (1987) p. 657.

45. P. Dewes, D. Alter, F. Garzarolli, R. Hahn and J. L. Nelson, "Measurement of the Deformability of Austenitic Stainles Steels and Nickel-Base Alloys in Light Water Reactor Cores," *Slow Strain Rate Testing for the Evaluation of Environmentally Induced Cracking:*

Research and Engineering Applications, ASTM STP 1210, R. D. Kane, Ed., American Society for Testing and Materials, Philadelphia (1993) p. 83.

46. D. Weinstein, "Real Time, In-Reactor Monitoring of Double Cantilever Beam Crack Growth Sensors," *Proceedings of the Sixth International Symposium on Environmental Degradation of Materials in Nuclear Power Systems-Water Reactors*, TMS, San Diego, CA (1993) p. 645.

47. C. Vitanza and T. Karlsen, "In-Pile IASCC Test Programme in the Halden Reactor," *Proc. 6th Int. Symp. Env. Deg. Mat. Nucl. Pow. Syst.*, TMS, San Diego, CA (1993) p. 651.

48. P. S. Maiya and W. J. Shack, "Stress Corrosion Cracking Susceptibility of AISI 316 NG and 316 Stainless Steel in an Impurity Environment," *Corrosion*, 41 (November 1985) p. 630.

49. G. Buzzanca, E. Caretta, L. Meini, R. Pascali and C. Ronchetti, "A Contribution to the Interpretation of the Strain Rate Effect on Type 304 Stainless Steel Intergranular Stress Corrosion Cracking," *Corrosion Science*, 25, No. 8/9 (1985) p. 805.

50. P. L. Andresen, F. P. Ford, S. M. Murphy and J. M. Perks, "State of Knowledge of Radiation Effects on Environmental Cracking in Light Water Reactor Core Materials," *Proc. 4th Int. Symp. on Env. Deg. of Mat. in Nucl. Pow. Systems-Water Reactors*, NACE, Jekyll Island, GA (1989) p. 1-83.

51. L. G. Ljungberg, D. Cubicciotti and M. Trolle, "Effects of Some Seldom Noticed Water Impurities on Stress Corrosion Cracking of BWR Construction Materials," *Corrosion*, 45 (March 1989) p. 215.

52. P. L. Andresen, "Effects of Transients in Water Chemistry, Temperature, and Loading on Intergranular Stress Corrosion Cracking of AISI 304 Stainless Steel," *Corrosion*, 42 (March 1986) p. 169.

53. W. E. Ruther, W. K. Soppet and T. F. Kassner, "Effect of Temperature and Ionic Impurities at Very Low Concentrations on Stress Corrosion Cracking of AISI 304 Stainless Steel," *Corrosion*, 44 (November 1988) p. 791.

54. BWR Water Chemistry Guidelines-1993 Revision, Report TR-103515, Electric Power Research Institute, Palo Alto, CA (February 1994).

55. R. N. Parkins, "Development of Strain-Rate Testing and Its Implications," *Stress Corrosion Cracking-The Slow Strain-Rate Technique, ASTM STP 665*, G. M. Ugiansky and J. H. Payer, Eds., American Society for Testing and Materials, Philadelphia (1979) p. 5.

56. R. N. Parkins, "Slow Strain Rate Testing-25 Years Experience," *Slow Strain Rate Testing for the Evaluation of Environmentally Induced Cracking: Research and Engineering Applications, ASTM STP 1210*, R. D. Kane, Ed., American Society for Testing and Materials, Philadelphia (1993) p. 7.

57. J. L. Nelson and P. Andresen, "Review of Current Research and Understanding of Irradiation-Assisted Stress Corrosion Cracking," *Proc. 5th Int. Symp. on Env. Deg. of Mat. in Nucl. Pow. Systems-Water Reactors*, ANS, Monterey, CA (1991).

58. J. R. O'Donnell, "Design, Construction, and Commissioning of an In-Core Materials Testing Facility for Slow Strain Rate Testing," PhD Thesis, Department of Nuclear Engineering, Massachusetts Institute of Technology, Cambridge, MA (September 1994).

59. S. T. Boerigter, "An Investigation of Neutron-Irradiation Induced Segregation in Austenitic Stainless Steels," PhD Thesis, Department of Nuclear Engineering, Massachusetts Institute of Technology, Cambridge, MA (December 1992).

60. M. J. Driscoll, O. K. Harling, and G. E. Kohse, "In-Pile Loop Studies of the Effect of PWR Coolant pH on Corrosion Product Radionuclide Deposition," EPRI/ESEERCO Report TR-100156, Electric Power Research Institute and Empire State Electric Energy Research Corporation (February 1992).

61. M. J. Driscoll, O. K. Harling, and G. E. Kohse, "Development and Use of an In-Pile Loop for BWR Chemistry Studies," EPRI/ESEERCO Report TR-102248, Electric Power Research Institute and Empire State Electric Energy Research Corporation (September 1993).

CHAPTER 3

ELECTROCHEMICAL POTENTIAL (ECP) MEASUREMENTS FOR CHARACTERIZING RADIATION WATER CHEMISTRY ENVIRONMENTS

Electrochemical equivalents coincide, and are the same, with ordinary chemical equivalents. I think I cannot deceive myself in considering the doctrine of definite electrochemical action as of the utmost importance. It touches by its facts more directly and closely than any former fact, or set of facts, has done, upon the beautiful idea that ordinary chemical affinity is a mere consequence of the electrical attractions of different kinds of matter.

Michael Faraday
(1791-1867)

3.1 INTRODUCTION

Irradiation assisted stress corrosion cracking experience indicates the environment as a key parameter which contributes to this phenomenon. In other types of stress corrosion cracking where there is no radiation effect, the environment is believed to be sufficiently characterized by what is called the electrochemical potential (ECP) or corrosion potential. For in-core regions with neutron and gamma radiation flux, it is believed that the ECP also sufficiently characterizes the environment[1,2]. There has been considerable experience with in-flux ECP measurements in support of Hydrogen Water Chemistry implementation and surveillance[3-7] and substantial efforts in developing prediction methods based on engineering correlations or mixed potential theory[8-11]. The basis for any of the ECP prediction methods is an accurate estimation of the different chemical species' concentrations which result from water radiolysis. Hence, the predictive capability of ECP models implicitly depend on the reliability of the radiation water chemistry modeling. Because of these complex interdependencies and a significant number of additional complicating variables, direct measurement of ECP in radiation flux regions has been the industry standard for defining the environment's aggressiveness. The power of correlating IASCC with ECP is that the multitude of variables that otherwise would need to be quantified and are very difficult, if at all possible, to measure in the core region of a light water reactor can

be represented by a single measurable quantity. Although ECP measurement technology for LWR applications is well developed, it is not without its difficulties and uncertainties. Some areas that are of particular concern are the effects of radiation on the reference sensors and the different response for different radiation fields (i.e. gamma ray or neutron), the shift in equilibrium potential of the silver/silver-chloride reference under hydrogen over pressure conditions, and the effects of water radiolysis products compared to chemical species (e.g. oxygen, hydrogen peroxide, and hydrogen) in out-of-flux environments at the same ECP[12,13].

In order to characterize the in-flux environment that SSRT specimens would be subject to, ECP measurements of stainless steel were taken under a variety of conditions (with Ag/AgCl and Pt reference ECP sensors supplied by GE Nuclear Energy Company). The results of these tests are fully reported in O'Donnell[14] but are not without ambiguity. This section will present an analysis of these measurements with due attention given to the questions posed above.

3.2 ECP RIG MEASUREMENTS

Under a variety of thermal hydraulic, water chemistry and radiation field conditions, ECP measurements were made with an electrode fixture that contained six ECP reference sensors arranged in two clusters separated by an axial length of 228.6 mm (9 in). Each cluster consisted of one silver/silver-chloride (Ag/AgCl) reference, one platinum (Pt) reference, one stainless steel working electrode and a dual junction thermocouple. All ECP sensors were provided by General Electric and qualified for service in a radiation environment. For the tests conducted in this program, ECP measurements were made at two in-core positions (see Figure 3-1). In test position number 1, the lower cluster was located 304.8 mm (12 in) below the top of the core and the upper cluster was 76.2 mm (3 in) below the top of the core. In this position, the lower cluster is in the center of the MITR-II core which is the same axial position as the tensile specimens during SSRT testing. The ECP measurements made in test position number 1 were used to characterize the water chemistry environment relative to laboratory results and in-pile measurements made in some reactors. In test position number 2, the lower cluster was located 76.2 mm (3 in) below the top of the core and the upper cluster was 152.4 mm (6 in) above the top of the core. These ECP measurements also provided a comparison between the two clusters at the same conditions. All voltages were measured against ground with a high impedance digital voltmeter and the ECP of the stainless steel electrodes were corrected to the standard hydrogen electrode (SHE) by the

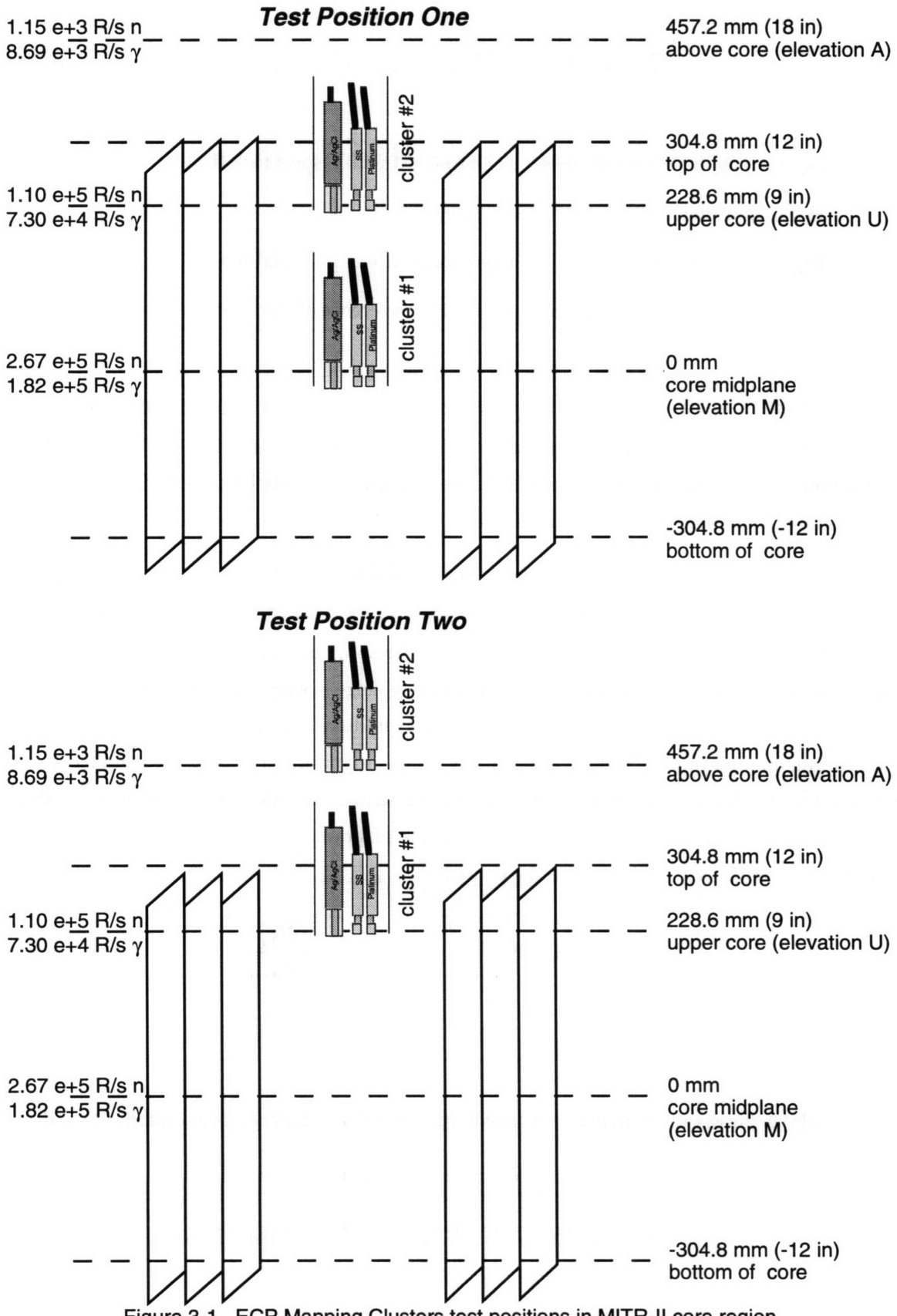

Figure 3-1. ECP Mapping Clusters test positions in MITR-II core region.

following expression:

$$E_{SS/SHE} = E_{SS/Gnd} - E_{Reference/Gnd} + E_{Reference/SHE}, \quad \text{(eq. 3-1)}$$

where

$E_{SS/SHE}$ is the ECP of stainless steel measured with respect to SHE,

$E_{SS/Gnd}$ is the measured stainless steel electrode potential,

$E_{Reference/Gnd}$ is the measured reference electrode potential and

$E_{Reference/SHE}$ is the correction for the ECP reference electrode (i.e. Ag/AgCl or Pt) to SHE.

Measurements with the Ag/AgCl reference sensor were made under both normal water chemistry and hydrogen water chemistry environments. The correction to SHE, governed by the Nernst equation, is expressed as a function of temperature only by substituting the temperature dependence of AgCl solubility. This is given below from Sawochka[12].

$$E_{Ag/AgCl/SHE} = 642.9mV - 1.645mV[T(^{\circ}C)] \quad \text{(eq. 3-2)}$$

The Pt reference sensor operates as a hydrogen reference electrode but only under hydrogen overpressure environments. For in-core SSR testing purposes, its signal to ground was also recorded during NWC operations. Although this voltage has no scientific meaning, it correlated with the ECP of stainless steel in oxidizing conditions and therefore provided a reliable engineering monitor of in-core chemistry. This was very important since only a single Pt reference electrode was utilized during the in-core SSR tensile tests (described in Section 4 of this thesis). Under a stoichiometric excess of hydrogen, the platinum electrodes reference potential with respect to SHE is given by the Nernst relation[12]:

$$E_{Pt/SHE} = 1.985 \times 10^{-4}\, T \left[pH + \frac{1}{2} \log \frac{(H_2)}{1000 K_{H_2}} \right], \quad \text{(eq. 3-3)}$$

where

T is the temperature in °K,

(H_2) is the dissolved hydrogen concentration (ppb) in excess of stoichiometric O_2 and

K_{H_2} is the hydrogen solubility coefficient (ppm/atm) given as[12]

$$K_{H_2} = 1.24 \times 10^{-4}[T(^{\circ}F)]^2 - 9.307 \times 10^{-2}[T(^{\circ}F)] + 21.298. \quad \text{(eq. 3-4)}$$

For discussion purposes the sensors in the lower cluster will be identified with the numeral one and the upper cluster sensors with the numeral two. For example, in the lower cluster the potential of stainless steel with respect to the Ag/AgCl reference will be identified as SS/Ag1.

3.2.1 Oxidizing Environment

The normal water chemistry of operating BWRs is a high purity, neutral pH, oxidizing environment. For these conditions, the measured dissolved oxygen concentration is ~200 ppb in the recirculation line and the ECP of 304 SS is between zero and +200 mV, SHE. Because of the difficulties in measuring oxygen concentration in-core and laboratory experience correlating ECP with environmental aggressiveness, the ECP was adopted for monitoring the chemistry in the SSR tests and a target ECP of 0-200 mV, SHE was chosen for simulating NWC conditions. The temperature and pressure were maintained at 12.1 MPa (1750 psig) and 277°C (531°F) except for one low temperature (200°C) run.

3.2.1.1 Reactor Power Effect

Most of the ECP measurements were made at 4.5MWt, MITR-II routine full power, and 0 MWt shutdown condition. Some tests were conducted with reactor power at 2.5 MWt to evaluate the dose rate effect on ECP. At full power, the neutron and gamma ray dose rates to the water in the MITR-II core at the midplane are estimated to be 2.67×10^5 Rad/s and 1.82×10^5 R/s, respectively. At 228.6 mm (9 in) above the midplane, the neutron and gamma ray dose rates to the water are estimated to be 1.10×10^5 R/s and 7.30×10^4 R/s and at 457.2 mm (18 in) above the midplane 1.15×10^3 R/s and 8.69×10^3 R/s, respectively.

For full power operation, the ECP (SS/Ag1) at the core midplane was 140-160 mV, SHE. No dose effect was seen at 2.5 MWt; the change in measured ECP (SS/Ag1) was less than 10 mV. At zero power , the ECP (SS/Ag1) decreased to 70 mV, SHE, but the letdown oxygen also fell from 400 ppb to 125 ppb during this test period while the feedwater concentration remained constant ~200±20 ppb. For this elevation (core midplane) , the radiation dose effect seems to saturate below 2.5 MWt (1.49×10^5 R/s and 1.01×10^5 R/s) and increases the corrosion potential by 70 mV compared to the zero dose condition.

The ECP at 228.6 mm (9 in) above the midplane, during 4.5 MWt full power operation, was 240 mV, SHE (SS/Ag1) and 65-80 mV, SHE (SS/Ag2). Both Ag/AgCl sensors showed no significant change in stainless steel ECP for a reactor power of 2.5 MWt. SS/Ag1 was 220 mV, SHE and SS/Ag2 was 95 mV, SHE. The two measurements at 228.6 mm were taken at different times so it is not certain whether the discrepancy reflects a physico-chemical difference or a bias

between the reference electrodes. There are no zero power results for SS/Ag1 at this core elevation, but zero power results for SS/Ag2 show a slight decrease in ECP to 55 mV, SHE. This change was considerably smaller than the change in ECP observed at the core midplane when the power was decreased to zero from 4.5 MWt and can be explained by the relative change in dose rates for the two positions.

Above core at the 457.2 mm position , the ECP of 304 SS was 290 mV, SHE (SS/Ag2) at MITR-II power of 4.5 MWt. At 2.5 MWt, the ECP did not change significantly (i.e. the potential was within 10 mV of the 4.5 MWt values) similar to the other core positions. Unfortunately, there are no zero power measurements under NWC for this elevation. According to the trend seen for the midplane and 288.6 mm above midplane position, the change in ECP between 4.5 MWt and zero power for the 457.2 mm position would be small (less than 10 mV).

3.2.1.2 Flowrate Effect

For SSRT operation, the experiment loop flowrate was 45,200 cc/min (12 gpm) which gave a superficial linear velocity past the specimen of 1.3 m/s (50.8 in/s) and a residence time from the top of the core to the specimen of 2.22 seconds. To study flowrate effects on ECP, the feedwater or refresh flowrate was decreased from 450 cc/min to 300 cc/min for one test and the recirculation rate was decreased from 45,200 cc/min (12 gpm) to 31,700 cc/min (8.4 gpm) for another test.

The reduced refresh rate test was conducted at 4.5 MWt. No effect on ECP was observed at the core midplane (SS/Ag1) or at the 288.6 mm position (SS/Ag2). The bulk chemistry is expected to dominate for such small refresh rates. The 30% change in refresh rates represented only a 0.3% change in the volumetric contribution to the total water inventory.

In contrast to reducing the refresh rate by 30%, decreasing the recirculation flowrate by 30% resulted in a marked change in the 304 SS ECP, at both the core midplane and the 288.6 mm position. At the midplane the ECP increased 120 mV to 260 mV, SHE (SS/Ag1) and at the 288.6 mm position the ECP increased 70mV to 150 mV, SHE (SS/Ag2). The decreased flowrate results in a longer irradiation residence time of 3.2 seconds compared to 2.2 seconds. This time change is significant for radiation water chemistry kinetics since nominal time constants are on the order of tenths of a second[15] . However the calculated ECP, correlated to oxidant concentrations as predicted by radiolysis modeling, does not reflect this large swing for a reduced flowrate.

3.2.2 Reducing Environment

3.2.2.1 Reactor Power Effect

Under reducing conditions that simulate hydrogen water chemistry (HWC) of BWR plants, both the Ag/AgCl and Pt reference sensors are expected to operate according to known thermodynamic relations. The BWR vendors have different strategies for implementing these two reference electrode types under HWC. GE prefers Pt as the reference of choice whereas the Studsvik Group in Sweden utilizes multiple Ag/AgCl reference sensors for continuous monitoring and a Pt reference electrode periodically for a secondary check[12]. The use of multiple reference electrode types is motivated because Ag/AgCl and or Pt performance have been observed to degrade under various conditions such as high hydrogen concentrations for Ag/AgCl and high copper levels for Pt reference. The measurement results for the hydrogen addition tests of the MIT ECP Rig are summarized in this section and a general discussion of the validity of the measurements is presented in the next section.

For full power operation and a hydrogen letdown concentration of 100 ppb, the ECP measured at the core midplane was -45 mV, SHE (SS/Ag1) and -340 mV, SHE (SS/Pt1). At zero power , the ECP decreased to -350 mV, SHE (SS/Ag1) and -445 mV, SHE (SS/Pt1). At a hydrogen letdown concentration of 200 ppb, the ECP was -30 mV, SHE (SS/Ag1) and -400 mV, SHE (SS/Pt1). For the core midplane elevation, there is a 300-400 mV discrepancy between the ECP measured by the Ag/AgCl sensor and the Pt sensor at full power. This difference decreases to 100 mV with the reactor shutdown.

During full power operation, the ECP measured at 230 mm (9 in) above the midplane and with 200 ppb hydrogen in the letdown line the ECP was -120 mV, SHE (SS/Ag1) and -350 mV, SHE (SS/Ag2). The ECP measured with the Pt sensors was -435 mV, SHE (SS/Pt1) and -375 mV, SHE (SS/Pt2). For cluster 1 (lower), there is still a 400 mV bias between the SS/Ag1 and SS/Pt1, whereas the bias for cluster 2 (upper) is only 25 mV.

At zero power, ECP was -410 mV, SHE (SS/Ag1) and -300 mV, SHE (SS/Ag2) compared to -480 mV, SHE (SS/Pt1) and -470 mV, SHE (SS/Pt2). The bias between SS/Ag1 and SS/Pt1 is the same for zero power at the core midplane. Whereas a negligible potential difference was observed between the SS/Ag2 and SS/Pt2 during full power operation, under zero power operation there is a 170 mV bias. Since the two measurements at 230 mm were taken at different times with slightly different arrangements, the bias could be explained by a number of factors.

Above core at the 460 mm position and with 200 ppb hydrogen in the letdown line, the ECP of 304 SS was -325 mV, SHE (SS/Ag2) and -500 mV, SHE (SS/Pt2) at MITR-II power of 4.5 MWt. This shows a ~200 mV bias which is much larger than the 25 mV difference observed at the 290 mm position. With the reactor shutdown, the ECP measured -225 mV, SHE (SS/Ag2) and

-500 mV, SHE (SS/Pt2), hence the trend in ECP change for the two sensors is very similar to that observed at 290 mm, but the bias is greater by 100 mV.

The measurements performed under hydrogen addition show inconsistencies and make it difficult to confidently characterize the water chemistry environment in-core. This characterization is very important for stress corrosion cracking testing because of the critical potential of -230 mV, SHE determined in laboratory tests. The Discussion section identifies the main ambiguities and some possible explanations for the behaviors observed.

3.3 ECP RIG MODELING CALCULATIONS

3.3.1 Introduction

The chemical species hydrogen, oxygen and hydrogen peroxide are believed to govern the ECP; hydrogen as a reducing agent and oxygen and hydrogen peroxide as oxidizing agents. Water radiolysis and thermal decomposition affects the concentrations of these three species as the coolant transits the Rig facility, resulting in corresponding changes in ECP. Hence, any methodology for predicting ECP requires *a priori* an accurate prediction of the concentration of these chemical species. A number of radiolysis computer codes exist which solve a set of simultaneous differential equations of chemical reactions. They are similar and were found to yield comparable results for the same given input set of reactants, chemical reactions and G-values. Computer calculations of the corrosion potential (ECP) are typically based on an empirical correlation of laboratory data or a "fundamental" development of mixed potential theory. The fundamental development actually requires assuming the value of certain constants, which are chosen to fit known data. Since both approaches essentially are derived from the same data (i.e. laboratory and in-plant measurements) and their predictive capability is similar when conditions are within correlation bounds, for simplicity the empirical correlation is employed for the comparisons discussed in this work.

3.3.2 Modeling Input Description

The RADICAL (RADIation Chemistry Analysis Loop) computer code, originally developed by the Massachusetts Institute of Technology NRL through the work of S. A. Simonson[16] and J. Chun[17] and further developed by EPRI[18], was used for the water chemistry simulation studies reported in this thesis. The code accepts input for BWR operating conditions and initial chemical concentrations, chemical reaction sets and radiolysis product, "G", values and

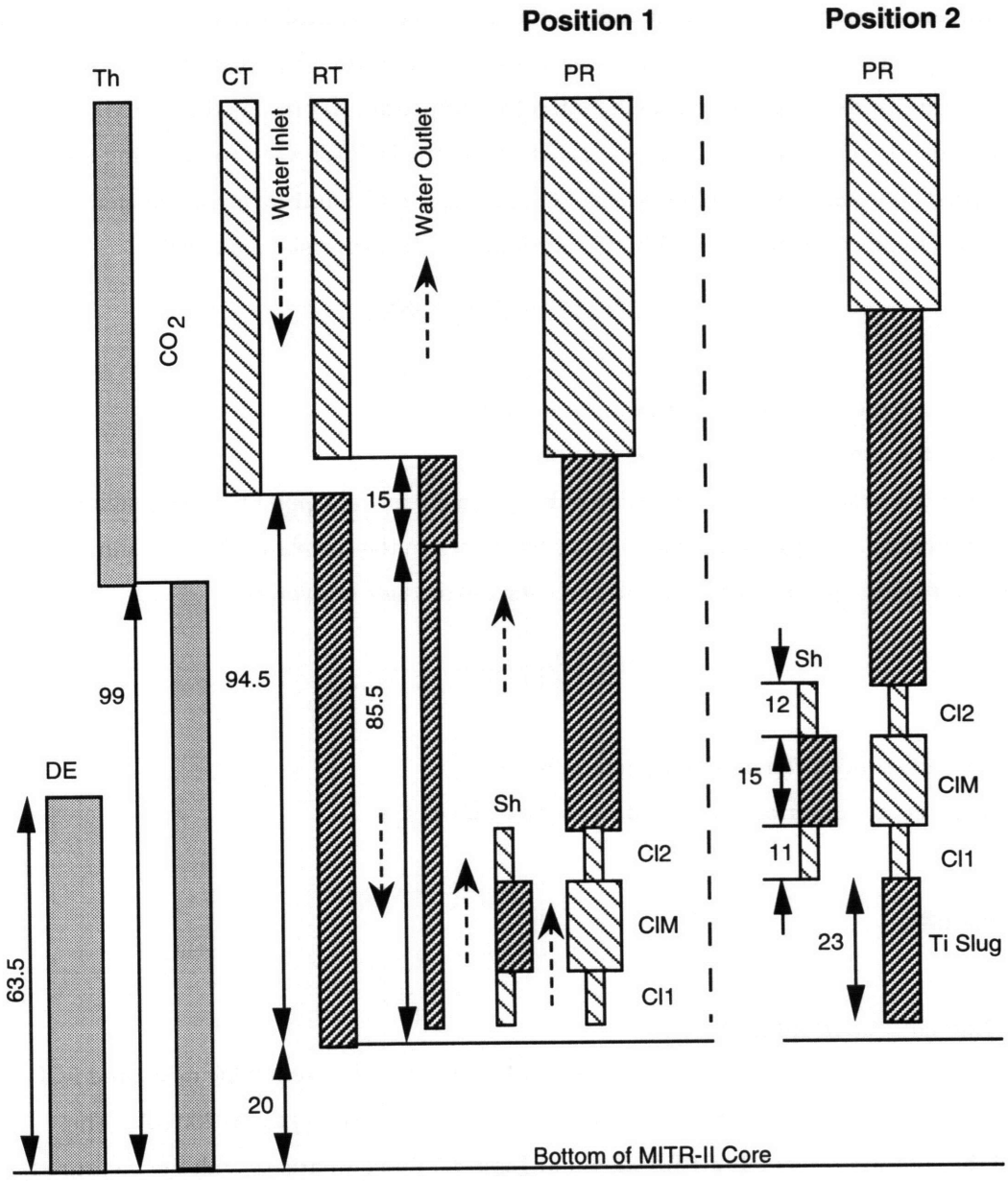

Legend: Dimensions in cm

DE ID = 5.08
DE OD = 7.34
Upper Th ID =10.03
Upper Th OD =11.40
Lower Th ID = 4.45
Lower Th OD = 5.08
Upper CT ID = 6.66
Upper CT OD = 8.69
Lower CT ID = 3.62
Lower CT OD = 4.13

Upper RT ID = 3.17
Upper RT OD = 6.23
Middle RT ID = 2.22
Middle RT OD = 3.18
Lower RT ID = 2.86
Lower RT OD = 3.18

Upper Sh ID = 2.54
Upper Sh OD = 2.70
Middle Sh ID = 1.27
Middle Sh OD = 2.70
Lower Sh ID = 2.54
Lower Sh OD = 2.70

Upper PR OD = 1.91
Lower PR OD = 1.60
Cl2 OD = 0.61
ClM OD = 0.64
Cl1 OD = 0.61
Ti Slug OD = 2.60

Al SS Ti

DE Dummy Element
Th Thimble
CT Containment Tube
RT Reaction Tube
Sh Shroud
Cl ECP Cluster

Figure 3-2. Schematic of ECP Mapping Rig for RADICAL Input.

runs a differential equation solver that outputs the calculated chemical species' concentrations as a function of position. In the version of RADICAL used in the work reported here, the reaction set and G-values were adopted from a GE matrix (see Appendix A) presented at the MIT radiolysis workshop[19]. Figure 3-2 shows a schematic of the ECP Rig used for defining the input. The ECP predictions are based on the work of C.C. Lin and F. R. Smith which correlated the logarithm of oxygen concentration with ECP according to the expression below[20]:

$$E_{SS/SHE} = 174 log[O_2] - 400, \quad \text{(eq. 3-5)}$$

where

$E_{SS/SHE}$ is the corrosion potential in mV (SHE) and

O_2 is the concentration of oxygen in ppb.

The uncertainties range from ±50 mV at 200 ppb O_2 to ±100 mV at 1 ppb O_2. For systems with hydrogen peroxide (H_2O_2), the net oxidant has been used in the correlation[8]. Assuming the H_2O_2 decomposition products are O_2 and H_2O, the net oxidant is given as

$$O_2 + {}^{8}/_{17} H_2O_2, \quad \text{(eq. 3-6)}$$

where

O_2 is the concentration of oxygen in ppb and

H_2O_2 is the concentration of hydrogen peroxide in ppb.

3.3.3 Results

3.3.3.1 Oxidizing Environment

Under oxidizing conditions, computer calculations underpredict the measured ECP values at all core elevations (i.e. mid-plane, upper core and above core) by 50-200 mV. The results of the computer calculations are shown in Table 3-1 for comparison with the measured values. Although this is a large discrepancy, the predicted ECP is still between 0-100 mV which is consistent with typical ECP values for normal water chemistry (NWC) operation in BWR plants.

The predicted stainless steel ECP trends slightly downward (~5 mV) for lower reactor power (2.5 MWt or 50% of rated power) which parallels the observed trend for ECP measurements. The small dependence of ECP on reactor power is essentially due to the ECP log dependence on oxidant concentration. Radiolytic production (i.e. oxidant increase) is linear with reactor power (i.e. energy deposition) whereas the corrosion potential depends on the logarithm of oxidant.

Contrary to the strong effect observed for flowrate on ECP, the computer simulation indicated a very weak effect. Essentially, the model predicted no change in ECP when the flowrate was decreased to 70% of its nominal value. Although the residence time increased by 50%, the enhanced radiolysis is only minor and consequently not strong enough to elevate the ECP by the 100-150 mV observed in the experiment. The reduction in flowrate ordinarily (i.e. without the consideration of radiolysis) may be expected to decrease ECP due to limited mass transport of oxidizing species, hence the experimentally observed increase is most confidently attributed to radiolysis. With this insight, it seems that either a) the basic reactions and G-values invoked in the radiolysis code under predict the net radiolysis or b) other short-lived species produced under radiolysis shift the ECP in a more positive direction.

Since differences in the geometry of the Rig during test position one and test position two may have influenced the ECP measurements, this was included in the RADICAL model. However, calculations show virtually no difference between the predicted ECP for position one and two geometries at the same core elevation. Whereas the difference between the measured ECP for position one and two geometries was 140 mV.

3.3.3.2 Reducing Environment

The predicted stainless steel ECP under reducing environments is typically between the value measured with the two different sensors in cluster 1 (i.e. SS/Ag1 and SS/Pt1) and higher than that measured with cluster 2 (i.e. SS/Ag2 and SS/Pt2). The calculated value is around -175 mV (SHE) for the in-core elevations. Above the core, the model predicts much lower ECP of ~-340 mV (SHE). Generally speaking, the code shows the ECP trending to lower values as the coolant moves up from the core midplane (i.e. 15 mV between the midplane and above core positions) and it predicts a significant decrease for regions out of the neutron field (e.g. above core elevation). The higher ECP corresponds to radiolytically generated hydrogen peroxide which quickly falls away after leaving the region subject to neutron radiation.

Model predictions were made for the various hydrogen addition concentrations used in the ECP Mapping Tests. The code predicts lower ECP for higher hydrogen concentrations showing about a 30 mV drop between 88 ppb and 190 ppb hydrogen and 5-10 mV drop between 190 and 239 ppb. However for these hydrogen concentrations, the ECP of in-core stainless steel is nominally predicted to be above the critical potential of -230 mV (SHE). But at such low oxidant concentrations, the uncertainty in the ECP correlation is 100 mV. Subtracting this uncertainty from the computer prediction moves the ECP below the critical potential, but is still 100-150 mV higher than that measured with the platinum reference. There is no clear explanation for these discrepancies. A number of possibilities do exist.

The calculated ECP may be higher than the measured values due to a different electrochemical state for hydrogen peroxide under hydrogen or a limited anodic current for the coolant velocities studied. First, for predicting ECP, hydrogen peroxide is assumed to behave as oxygen and the correlation uses total oxidant concentration for determining its response. In terms of mixed-potential theory, the similar response of stainless steel ECP to oxygen and hydrogen peroxide has been explained by the following oxidizing electrochemical reactions[9,20]:

$$O_2 + 4H^+ + 4e^- \Leftrightarrow 2H_2O, E^\circ_{298K} = 1.23V \qquad \text{(eq. 3-7)}$$

and

$$H_2O_2 + 2H^+ + 2e^- \Leftrightarrow 2H_2O, E^\circ_{298K} = 1.78V. \qquad \text{(eq. 3-8)}$$

But thermodynamically, there are equilibrium reactions for hydrogen peroxide at active potentials (i.e. under reducing conditions like HWC) which would explain the low ECP measured in the presence of hydrogen peroxide. One possible equilibrium reaction where hydrogen peroxide acts as a reducing agent is the following[21]:

$$H_2O_2 \Leftrightarrow O_2 + 2H^+ + 2e^-, E^\circ_{298K} = -0.68V \qquad \text{(eq. 3-9)}$$

Second, for the low oxidant concentrations considered here, a very low coolant velocity can lead to decreased ECP. The flowrate dependence of ECP has been observed in other experiments and is expected on fundamental grounds due to limited mass transport of oxidant[9,22]. The total volumetric flowrate for the SSR and ECP Mapping Tests is 45.2 lpm which is equivalent to a linear velocity at the point of action of 1.3 m/s and 0.15 m/s, respectively. Because of split flow through the ECP clusters and the gap between the clusters' shroud and the reaction tube, the ECP cluster region is expected to have only 10% of the total flow (this corresponds to the 0.15 m/s linear velocity). Even at such a low velocity, laboratory tests do not reflect a strong effect on ECP.

3.4 DISCUSSION

A summary of the results of the in-core ECP Mapping tests is displayed in Table 3-1 and in Figures 3-3 and 3-4. From the table it can be seen that there are inconsistencies between measurements made with the same type of reference electrode (SS/Ag1 and SS/Ag2 at position 230 mm above the core midplane) and discrepancies between measurements made with the two different types of reference electrode (SS/Ag1 compared to SS/Pt1 and SS/Ag2 compared to SS/Pt2 for all three measurement positions).

At the 290 mm position above the core midplane, SS/Ag1 ECP is between 70 and 200 mV higher than the SS/Ag2 ECP. This bias varies with reactor power and water chemistry. The SS/Pt ECP shows a bias of 60 mV at 4.5 MWt and at zero power, but the polarity is reversed from the SS/Ag bias. It should be noted that the 60 mV difference between SS/Pt2 and SS/Pt1 is approximately equal to the SS/Ag2 and SS/Ag1 bias observed during out of pile testing.

Since the SS/Ag1 and SS/Ag2 measurements for this axial position were taken at different times, the difference may be caused by some physico-chemical change. Perhaps the ECP differences for SS/Ag1 and SS/Ag2 can be attributed to a difference in water chemistry or material oxide film as explained by the following reasons:

1. Geometry that changes the flow path, the residence time and radiolysis products.

2. Titanium slug material (which was used to displace the water volume underneath the lower cluster during test position 2) may cause higher hydrogen peroxide concentrations and a corresponding elevated ECP[15].

3. The SS/Ag1 measurements were taken approximately two weeks after the SS/Ag2 measurements. Hence both measurements may be accurate; the higher ECP maybe due to changes in the metal oxide film which occurred over time[23]. However before in-core testing, the entire facility was pre-filmed for 500 hours at high oxygen concentrations which should minimize this drift in ECP measurements.

Table 3-1. Results of measurements and predictions[a] of 304 SS ECP in the MITR-II core .

Position[b] (mm)	MITR-II Power (MWt)	Inlet O2/H2 (ppb)	Letdown O2/H2 (ppb)	SS/Ag1 (mV, SHE)	SS/Ag2 (mV, SHE)	SS/Pt1 (mV, SHE)	SS/Pt2 (mV, SHE)
NWC							
0	4.5	205/2	410/36	150±10 (38)	•	86[c]	•
	2.5	•	375/26	140 (34)	•	74[c]	•
	0	•	125/2	175 (-35)	•	-34[c]	•
228.6	4.5	205/2	375±30/38	235 (36)	72±8 (33)	70[c]	94[c]
	2.5	205/2	360±20/40	220 (31)	95 (33)	77[c]	55[c]
	0	205/2	120/2	•	100 (-38)	•	-54[c]
457.2	4.5	200/5	360/45	•	290 (14)	•	69[c]
	2.5	200/5	340/40	•	300 (16)	•	73[c]
HWC							
0	4.5	6/88	8/100	-45 (-149)	•	-350	•
	0	6/88	8/100	-361 (-265)	•	-445	•
	4.5	6/195	7/205	-27 (-176)	•	-410	•
	0	6/195	7/205	-263 (-265)	•	-470	•
228.6	4.5	0/186	7/200	-123 (-192)	-350 (-201)	-435	-369
	0	0/186	0/185	-431 (-400)	-300 (-500)	-480	-433
	4.5	7/239	7/250	•	-465 (-205)	•	-408
	0	7/239	7/250	•	-310 (-253)	•	-433
457.2	4.5	0/200	0/200	•	-329 (-347)	•	-508
	0	0/180	0/180	•	-247 (-500)	•	-508

a Predictions shown in parentheses next to measured ECP.
b Measured from core midplane.
c For NWC, the signal cited is the potential difference between Ground and the Pt reference electrode (Gnd/Pt).

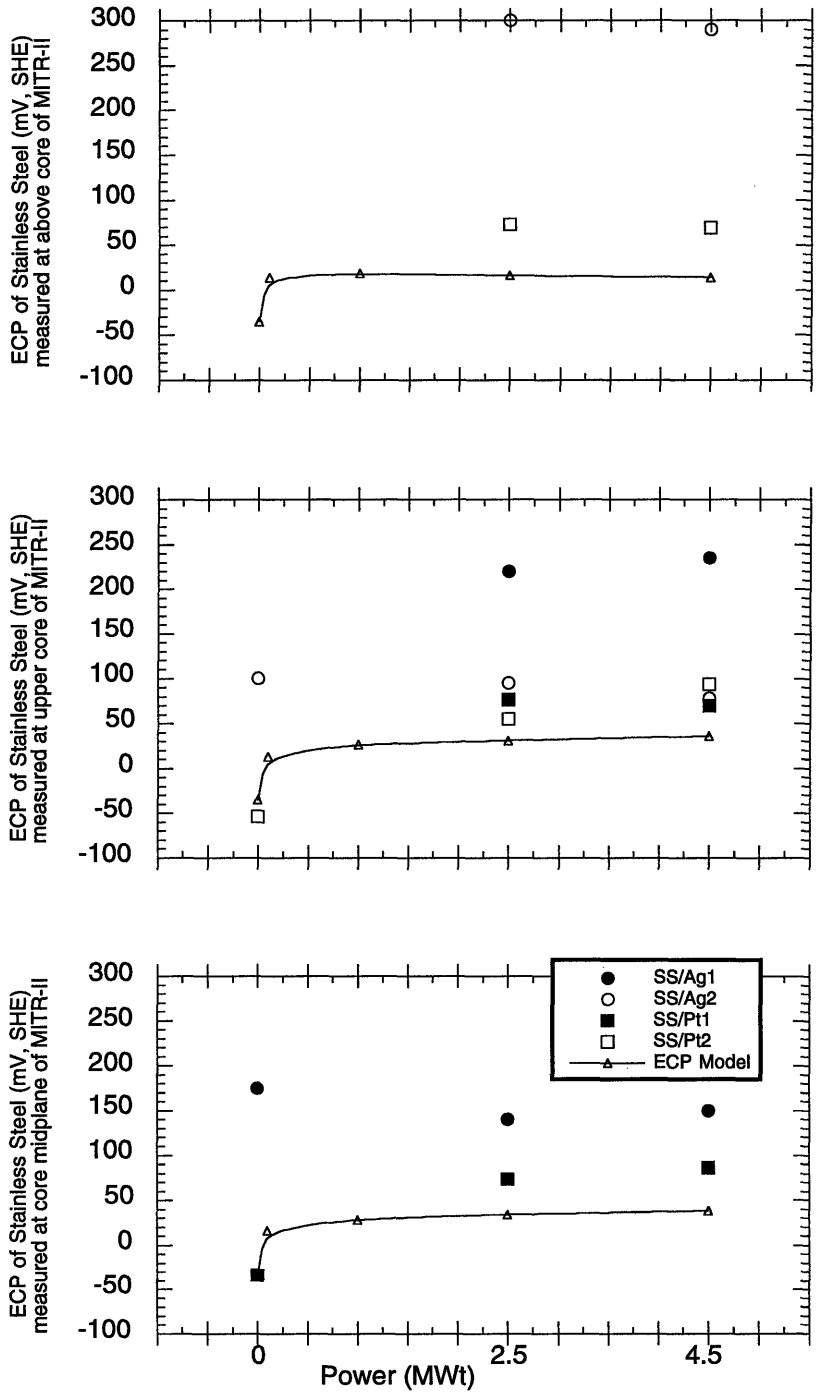

Figure 3-3. 304 SS ECP measurements made under NWC at three core elevations.

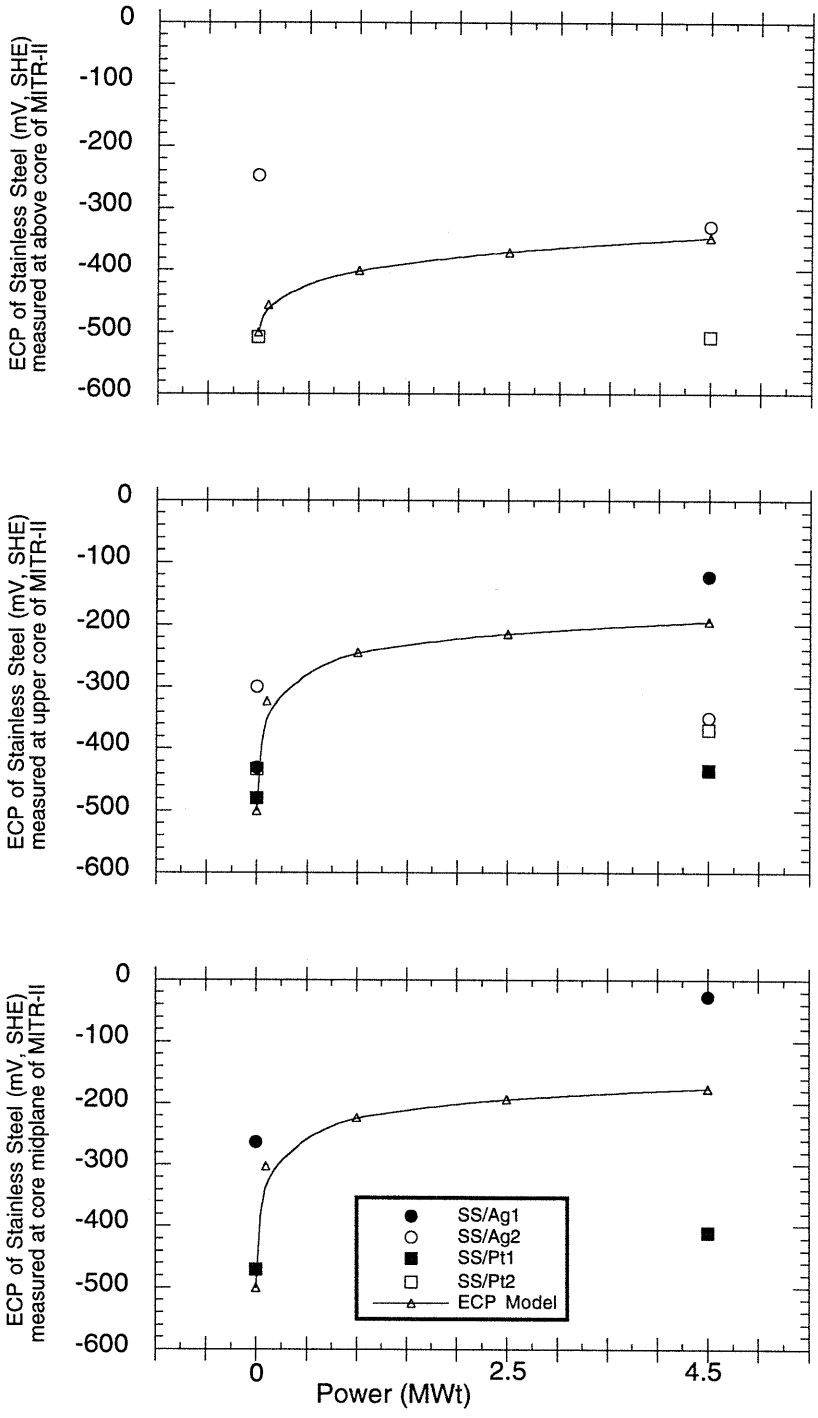

Figure 3-4. 304 SS ECP measurements made under HWC at three core elevations.

Besides these discrepancies between the ECP values determined by the Ag/AgCl electrodes in the two clusters, the ECP of SS/Ag was inconsistent with that measured with SS/Pt, but the behavior is not the same for clusters 1 (lower) and 2 (upper). The behavior of cluster 1 ECP will be evaluated first.

At the core midplane under 100 ppb hydrogen, SS/Ag1 exceeds SS/Pt1 by 300 mV at reactor power of 4.5 MWt and 210 mV at zero power. These can be compared with the data at 290 mm above the midplane. With 200 ppb hydrogen, SS/Ag1 is 310 mV higher than SS/Pt1 at 4.5 MWt and only 50 mV higher with the reactor shut down. According to cluster 1 data, it seems evident that the Ag/AgCl equilibrium potential shifts downward resulting in "falsely" high ECP readings for stainless steel. This behavior has been observed in BWR plant experience, but not to such a magnitude for these hydrogen concentrations. Experience from BWR plants indicate that Ag/AgCl reference electrodes do not degrade over a two month period with hydrogen concentrations ~550 ppb and for 200 ppb hydrogen, reliable performance is expected for 6 months[12]. The observed downward shift in Ag/AgCl equilibrium potential is due to a higher chloride concentration in the buffer solution attributed to enhanced solubility of the silver chloride. The increased solubility is postulated to be caused by chemical reduction of AgCl[23] and radiation enhanced reduction. Both of these are described by the following reaction,

$$AgCl + \frac{1}{2}H_2 \rightarrow Ag + H^+ + Cl^-. \qquad \text{(eq. 3-10)}$$

While this explanation could reconcile the discrepancies between SS/Ag1 and SS/Pt1, it does not explain the differences in cluster 1 and cluster 2 with respect to ECP measurements under hydrogen water chemistry. At the 290 mm elevation and under 200 ppb hydrogen, SS/Ag2 is only 20 mV higher than SS/Pt2 at 4.5 MWt, but it is 130 mV higher at zero power. This does not correspond to cluster 1 data. Furthermore the SS/Ag2 is 50 mV higher with the reactor at 0 MWt than at 4.5 MWt which does not fit the expected trend observed for cluster 1 and predicted by the explanation above. It is interesting that at the 460 mm position, the SS/Ag2 is 180 mV higher for full power and 260 mV higher for zero power operation. Hence the effect of radiation on the SS/Ag2 and SS/Pt2 bias remained the same for both core positions. For cluster 2, the bias is 80 mV greater at zero power compared to cluster 1 where the bias is 170-260 mV smaller at zero power. It is these inconsistencies that make it difficult to reach an unambiguous conclusion on the performance of the reference sensors used in the ECP Mapping Experiments.

Additional effects that may influence the ECP measurements are presence of transition metals such as copper and iron which affect water radiolysis and 304 SS ECP, heat generation by radiation attenuation in reference sensors which leads to higher local temperatures, and radiolysis of the reference sensor's electrolyte solution. Further analysis is necessary to evaluate

all these possible effects and their relative magnitudes. More measurements may help to identify the real trends and lead to definite conclusions about the ECP reference sensors' performance and the measurements made with them. However, some tentative conclusions regarding the aggressiveness of NWC environment and the suppression of ECP below -230 mV, SHE under HWC environment can be made with the caveat that more data and analysis is required to eliminate the large uncertainties that exist. At present, it seems reasonable to conclude that the Pt reference electrodes provided reliable ECP measurement under HWC conditions and that the Ag/AgCl reference electrodes gave a fair evaluation of the corrosive nature of the water chemistry under NWC. This being the case, then an environment similar to BWR NWC was achieved with 350-400 ppb oxygen in the letdown line and corresponded to in-core stainless steel ECP values greater than 0 mV, SHE. HWC conditions were achieved with hydrogen addition of 100 ppb in the feedwater which was sufficient to suppress 304 SS ECP values below -230 mV, SHE.

3.5 SUMMARY

This section presented an analysis of 304 SS ECP measurements made in an autoclave with a BWR simulated environment (12.1 MPa, 277 °C under normal water chemistry conditions ~ 400 ppb O_2 and hydrogen water chemistry conditions 100-200 ppb H_2 and ≤10 ppb O_2) subject to radiation fields at the core midplane ~2.67×10^5 R/s neutron and ~1.82×10^5 R/s gamma ray. A summary of the major findings and conclusions are listed below.

1. The 304 SS ECP was found to be slightly dependent on feedwater/refresh flowrate for a 30% reduction in refresh rate, but was strongly dependent on recirculation rate (i.e. increased 70-140 mV for a 30% reduction in flowrate under normal water chemistry).

2. In general, the dose rate effect on ECP seemed to saturate below 2.5 MWt (1.49×10^5 R/s neutron and 1.01×10^5 R/s gamma ray) since the ECP values at 2.5 MWt and 4.5 MWt were the same, within 20 mV.

3. Under excess hydrogen, the ECP data measured with the Pt reference electrodes is deemed more reliable. There appears to be a dose rate effect on the Ag/AgCl reference sensor under HWC.

3a. Suppression of 304 SS ECP below -230 mV, SHE was achieved with 100 ppb hydrogen addition in the feedwater.

3b. Hydrogen addition suppresses radiolysis throughout the core region which is indicated by the similar ECP for SS/Pt1 and SS/Pt2.

4. The ECP measured by SS/Ag1 and SS/Ag2 differed by ~±130 mV depending on the specific dose rate and oxygen/ hydrogen chemistry conditions. Because of these differences, it is assumed that one or both of the sensors was faulty.

3.6 REFERENCES

1. P. L. Andresen, F. P. Ford, S. M. Murphy and J. M. Perks, "State of Knowledge of Radiation Effects on Environmental Cracking in Light Water Reactor Core Materials," *Proc. 4th Int. Symp. Env. Deg. Mat. Nucl. Power Syst.-Water Reactors,* NACE, Jekyll Island, GA (1989) p. 1-83.

2. J. L. Nelson and P. L. Andresen, "Review of Current Research and Understanding of Irradiation-Assisted Stress Corrosion Cracking," *Proc. 5th Int. Symp. Env. Deg. Mat. Nucl. Power Syst.-Water Reactors,* ANS, Monterey, CA (1991) p. 10.

3. M. Indig, "Recent Advances in Measuring ECPs in BWR Systems," *Proc. 4th Int. Symp. Env. Deg. Mat. Nucl. Power Syst.-Water Reactors,* NACE, Jekyll Island, GA (1989) p. 4-111.

4. M. Ullberg, "On Corrosion Potential Measurement in BWRs," *Proc. 4th Int. Symp. Env. Deg. Mat. Nucl. Power Syst.-Water Reactors,* NACE, Jekyll Island, GA (1989).

5. A. Molander and G. Karlberg, "Hydrogen Water Chemistry Surveillance in a Boiling Water Reactor," *Proc. 4th Int. Symp. Env. Deg. Mat. Nucl. Power Syst.-Water Reactors,* NACE, Jekyll Island, GA (1989).

6. S. Ashida, J. Takagi, N. Ichikawa and Y. Morikawa, "First Experience of Hydrogen Water Chemistry at a Japanese BWR," *Proc. 6th Int. Conf. Water Chemistry Nucl. Reactor Syst., Vol. 2,* BNES, London (1992) p. 103.

7. M. E. Indig, J. S. Goldstein, A. J. Jarvis, R. Pathania and J. M. Burger, "Electrochemical Response to Hydrogen Water Chemistry at the J. A. Fitzpatrick BWR," *Proc. 6th Int. Symp. Env. Deg. Mat. Nucl. Power Syst.-Water Reactors,* TMS, San Diego, CA (1993) p. 897.

8. C. P. Ruiz, C. C. Lin, R. N. Robinson, W. G. Burns, J. Henshaw and R. Pathania, "Model Calculations of Water Radiolysis and Electrochemical Potentials in BWR Primary Coolant II," *Proc. 6th Int. Conf. Water Chemistry Nucl. Reactor Syst., Vol. 2,* BNES, London (1992) p. 141.

9. D. D. Macdonald, "Viability of Hydrogen Water Chemistry for Protecting In-Vessel Components of Boiling Water Reactors," *Corrosion,* 48 (March 1992) p. 194.

10. A. Bertuch, D. D. Macdonald, J. Pang, L. Kriksunov and K. Arioka, "Modeling the Corrosion Behaviors of the Heat Transport Circuits of Light Water Nuclear Reactors," *Proc. 6th Int. Symp. Env. Deg. Mat. Nucl. Power Syst.-Water Reactors,* TMS, San Diego, CA (1993) p. 905.

11. N. Ichikawa, Y. Hemmi and J. Takagi, "Estimation on Corrosion Potential of Stainless Steel in BWR Primary Circuit," *Proc. 6th Int. Conf. Water Chemistry Nucl. Reactor Syst., Vol. 2,* BNES, London (1992) p. 127.

12. S. Sawochka, "Corrosion Potential (ECP) Measurement Sourcebook," EPRI Report NP-7142, Electric Power Research Institute, Palo Alto, CA (January 1991).

13. D. F. Taylor, "Response of Electrochemical Sensors to Ionizing Radiation in High-Temperature Aqueous Environments," *Corrosion,* 47 (February 1991).

14. J. R. O'Donnell, "Design, Construction, and Commissioning of an In-Core Materials Testing Facility for Slow Strain Rate Testing," PhD Thesis, Department of Nuclear Engineering, Massachusetts Institute of Technology, Cambridge, MA (September 1994).

15. M. J. Driscoll, O. K. Harling, and G. E. Kohse, "Development and Use of an In-Pile Loop for BWR Chemistry Studies," EPRI/ESEERCO Report TR-102248, Electric Power Research Institute and Empire State Electric Energy Research Corporation (September 1993).

16. S. A. Simonson, "Modeling of Radiation Effects of Nuclear Waste Package Materials," PhD Thesis, Department of Nuclear Engineering, Massachusetts Institute of Technology, Cambridge, MA (September 1988).

17. J. Chun, "Modeling of BWR Water Chemistry," SM Thesis, Department of Nuclear Engineering, Massachusetts Institute of Technology, Cambridge, MA (September 1990).

18. J. Chun, R. Ballinger, D. Abdollahian, B. Sun, B. Chexal, and R. Pathania, "Modeling of BWR Water Chemistry and Thermal Hydraulics for Oxidizing Species Concentrations," EPRI Report TR-103366-V1, Electric Power Research Institute, Palo Alto, CA (November 1993).

19. Minutes of M. I. T. Radiolysis Workshop (August 1992).

20. C. C. Lin and F. R. Smith, "Electrochemical Potential Measurements Under Simulated BWR Chemistry Conditions," EPRI Report NP-6732, Electric Power Research Institute, Palo Alto, CA (March 1990).

21. W. M. Latimer, *The Oxidation States of the Elements and Their Potentials in Aqueous Solution, 2nd ed.*, Prentice Hall, Englewood Cliffs, NJ (1952).

22. Y.-J. Kim, C. C. Lin, and R. Pathania, "Electrochemical Corrosion Potential Measurement with a Rotating Cylinder Electrode in 288°C Water," *Proc. 6th Int. Conf. Water Chemistry Nucl. Reactor Syst., Vol. 1*, BNES, London (1992) p. 139.

23. "In-Plant Measurements of Electrochemical Potentials in BWR Water," Report NP-3521, Electric Power Research Institute, Palo Alto, CA (May 1984).

CHAPTER 4

SLOW STRAIN RATE (SSR) TESTING RESULTS

What we call results are beginnings.

Ralph Waldo Emerson
(1835-1882)

4.1 INTRODUCTION

Slow strain rate testing is an accelerated materials property test which combines the effects of an applied tensile stress and corrosive environment in evaluating the service behavior of a specific material that may or may not exhibit sensitivity (reduced life) to such an environment. The SSRT technique was first developed in the 1960s by Henthorne who adapted a constant load test to a constant strain rate test[1]. For industries with service components prone to environmentally assisted cracking (EAC), this technique is utilized extensively. Because failures of this nature occur premature to nominal life expectancy, they imply a loss of reliability that reduces safety and availability. The scientific merit of evaluating material properties for specific environments using the SSRT technique has been discussed by Parkins[2]. In reporting stress corrosion cracking (SCC) susceptibility, a number of measurable and quantifiable parameters can be used. Some of these are elongation to failure, reduction of area and maximum load. The measures of ductility may have large uncertainties which mask the comparative magnitudes, therefore a combination of the above factors (i.e. area under the stress strain curve) may provide a more accurate parameter. Since it has been observed that elongation varies with SCC severity, then for a constant extension rate test, the time to failure also shows a similar dependence on SCC severity. For evaluating SCC susceptibility with time to failure data, it is usually normalized by

dividing by the time to failure measured in SSRT tests for the same material at the same temperature but in an inert environment.

Another parameter considered important in irradiation assisted stress corrosion cracking (IASCC) is the yield strength. This property corresponds to the macroscopic effects of radiation hardening. Its exact role in IASCC is a point of discussion and is sometimes correlated with the susceptibility "threshold" to IASCC[3,4]. The effect of radiation on strain hardening or softening in the plastic region can be observed by changes in strain hardening behavior. These effects can be compared quantitatively via the strain hardening exponent. This parameter is used in mechanical metallurgy to develop phenomenological models describing the influences of cold work, alloying elements and heat treatments[5,6] and may be appropriate for describing radiation effects as well.

This chapter presents the mechanical properties results for the slow strain rate tensile tests performed as part of the MIT IASCC Research and Testing program. Specifically, figures displaying the stress versus strain data, the strain versus test time data, the 0.2% offset yield stress (on an expanded stress-strain view), and the strain hardening exponent (on a log-log plot of the plastic region of the stress-strain curve) are provided. The mechanical properties determined for the SSRT specimens and presented herein include the following: 0.2% offset yield strength, ultimate tensile strength, elongation to failure, reduction of area (determined by SEM, see Chapter 5), and strain hardening exponent.

4.2 ZERO FLUX SHAKEDOWN AND BASELINE TESTS

Prior to operating the SSR Test Rig in-core, proof tests were performed out of core which confirmed the working condition of all internal components. During these tests, the DC potential drop (DCPD) technique for strain measurement and in situ strain control was evaluated. Due to constraints on time and funding this method of strain control was temporarily abandoned for in-core tests and replaced by the constant elongation method. Details of the DCPD analysis and test program can be found in the thesis by O'Donnell[7] and report by P. Lidar[8]. The constant elongation rate for in-core tests was 0.0198 mm/hr which corresponded to strain rates ~2-6 x 10^{-7} s^{-1}. The zero flux tests were conducted at various constant extension rates (CER) (and corresponding strain rates) ranging between 1-100X that used for the in-core tests. The extension rates were varied because of test time and other facility and project considerations. Because of the observed variance in alloy performance for different heats, it was considered very important to compare the in-core results with out-of-core tests performed on alloys of the same heat. Such "baseline" mechanical properties were determined from data collected during SSRT

tests performed in support of the DCPD scoping studies[8]. The selected results from the DCPD scoping studies are presented as baseline data for the test alloys in the unirradiated condition tested at temperature in highly oxygenated water. As part of the development and commissioning of the in-core tensile test rig, three zero flux tests were performed: two out-of-pile and one in-pile with the reactor (MITR-II) at zero power. This sub-section will present the results from the out-of-pile SSRT tests including the shakedown phase of the in-core test facility and baseline from preliminary DCPD studies. The effect of *in situ* radiation damage on mechanical properties is discussed in Chapter 6. The contribution of these parameters to irradiation assisted stress corrosion cracking is examined in Chapter 7.

4.2.1 Specimen 2005

Specimen 2005 was made from commercial purity alloy 304 (heat AJ9139) stainless steel and tested in the unirradiated, solution annealed, and 30% cold worked condition. The cold work condition was employed to simulate the long lasting hardening effects of neutron irradiation on the pre-irradiated tensile specimens that were tested in-core.

The test was conducted out of core and the ramp rate used was 0.457 mm/hr until failure. Figure 4-1 shows the stress-strain plot for the SSR test. There was no foot correction. The 0.2% offset yield strength was determined with respect to an elastic modulus of 171 GPa "best-fit" to the linear portion of the stress-strain curve (see Figure 4-3). The nominal yield stress was 562 MPa (81.5 ksi) and yield strain was 0.5%. The ultimate tensile strength was 865 MPa (125.5 ksi) at 3.9% strain. The nominal strain to failure was 11% (calculated assuming uniaxial tensile stress). The specimen showed little strain until yield at about 2.1×10^4 seconds (see Figure 4-2). In the same figure, the calculated strain rate shows a small amount of scatter due to the sensitivity of rig compliance on applied stress, but indicates an average strain rate of $4.0 \times 10^{-6}\ s^{-1}$ during uniform elongation and $1.5 \times 10^{-5}\ s^{-1}$ after ultimate stress. A good correlation (R=0.970) of the strain-hardening exponent was fit by the relation $\sigma = A\varepsilon^{\alpha}$ to the true stress-strain curve in the plastic region (from 1% beyond the yield strain to strain at ultimate stress) as seen in Figure 4-4. It was determined to be 0.20 and the reduction of area was 30%.

4.2.2 Specimen 2012

Specimen 2012 was made from commercial purity alloy 304 (heat AJ9139) stainless steel and tested in the unirradiated, furnace sensitized, and 30% cold worked condition. As with specimen 2005, the cold work on specimen 2012 was to simulate radiation hardening effects. A

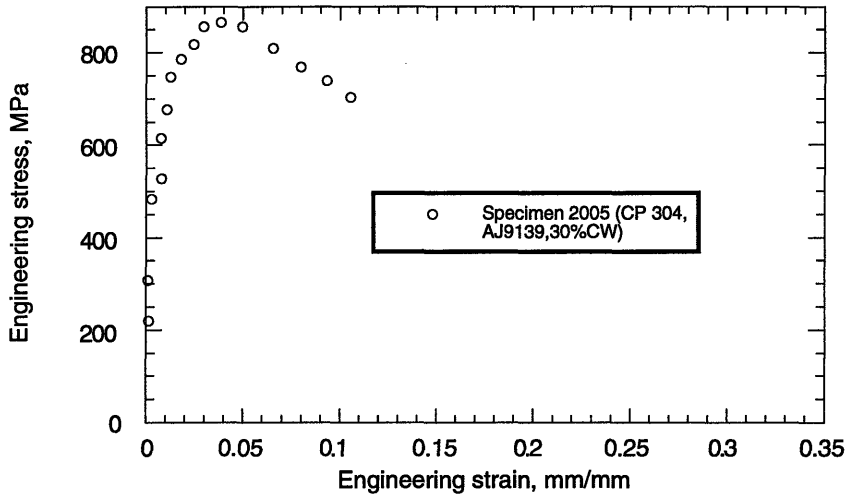

Figure 4-1. Stress-strain plot for specimen 2005 (CP 304,AJ9139,30%CW,0 n/m^2).

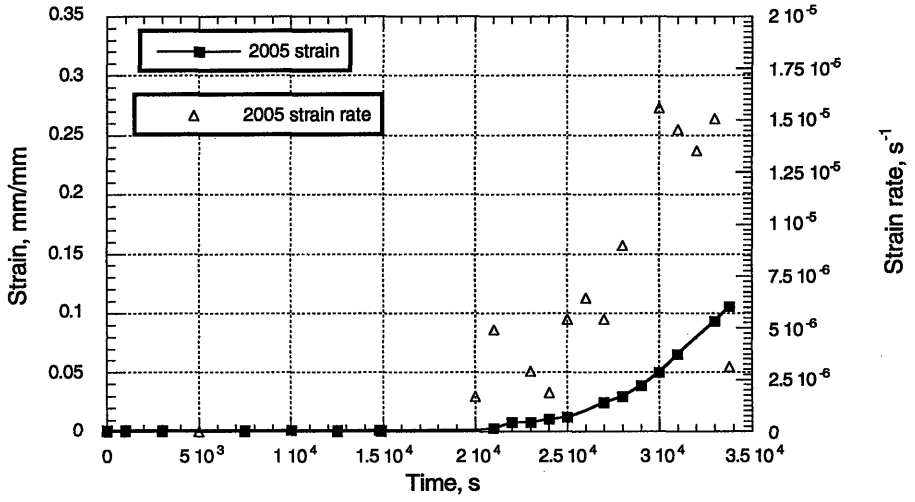

Figure 4-2. Strain-time plot for specimen 2005 (CP 304,AJ9139,30%CW,0 n/m^2).

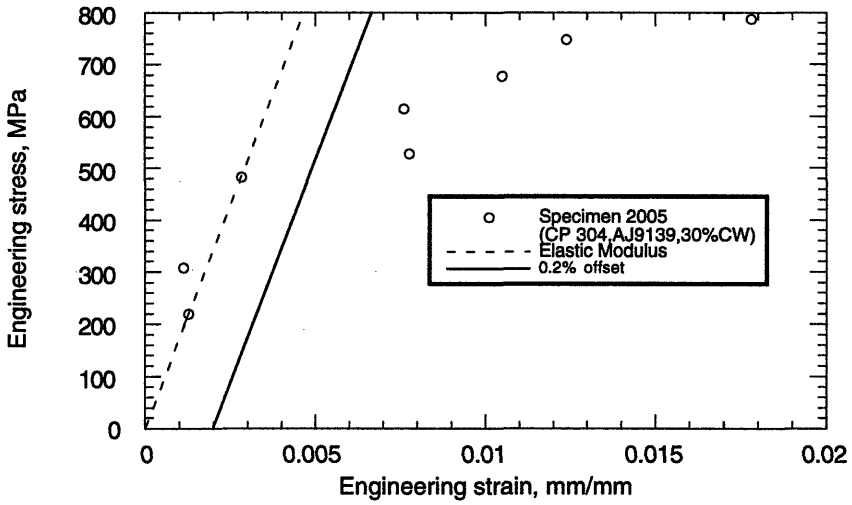

Figure 4-3. Yield stress for specimen 2005 (CP 304,AJ9139,30%CW,0 n/m^2).

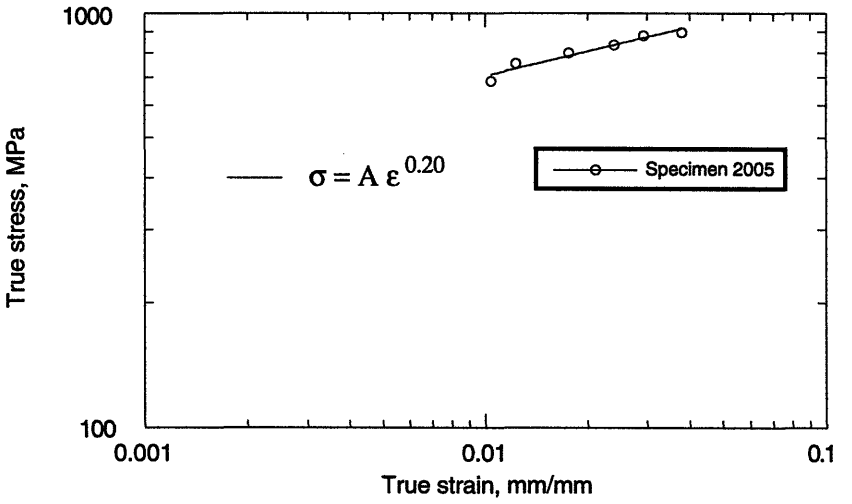

Figure 4-4. Strain-hardening exponent for specimen 2005 (CP 304,AJ9139,30%CW,0 n/m^2).

furnace heating at 650°C for 10 hours was employed to precipitate chromium carbides on the grain boundaries, thereby inducing thermal sensitization. The percentage of intergranular failure mode would verify that the strain rate was appropriate for investigating stress corrosion cracking.

Figure 4-5 shows the stress-strain plot for the SSR test. There was no foot correction. The 0.2% offset yield strength was determined with respect to an elastic modulus of 171 GPa "best-fit" to the linear portion of the stress-strain curve (see Figure 4-7). The nominal yield stress was 632 MPa (91.7 ksi) and yield strain was 0.6%. The ultimate tensile strength was 860 MPa (124.7 ksi) at 3.6% strain. The nominal strain to failure was 6% (calculated assuming uniaxial tensile stress). The specimen strain shows a straight line dependence on time (see Figure 4-6) indicative of the constant extension rate employed. In the same figure, the calculated strain rate shows a small amount of scatter due to the sensitivity of rig compliance on applied stress, but indicates an average strain rate of $3.3 \times 10^{-7}\ s^{-1}$. A good correlation (R=0.940) of the strain-hardening exponent was fit by the relation $\sigma = A\varepsilon^{\alpha}$ to the true stress-strain curve in the plastic region (from 1% beyond the yield strain to strain at ultimate stress) as seen in Figure 4-8. It was determined to be 0.21 and the reduction of area was 10%.

4.2.3 Specimen 2021

Specimen 2021 was made from alloy 347L (heat K12) stainless steel and tested in the unirradiated, solution annealed condition. This alloy belongs to the class of stabilized austenitic stainless steels which are supposed to have superior mechanical properties under conditions that produce IASCC in other commercial purity alloys like 304.

The reactor was shut down for the entire test. The ramp rate used was 0.0198 mm/hr for the initial nine hours of testing then increased to 1.98mm/hr for the remainder of the test. Time constraints mandated that the test be abandoned or modified to quickly reach failure. After nine hours of slow strain at 0.0198 mm/hr, the test had accomplished its primary focus which was verifying the capability of the facility to conduct such material tests while situated in a MITR-II core position.

Figure 4-9 shows the stress-strain plot for the SSR test. The foot correction was -0.9%. The 0.2% offset yield strength was determined with respect to an elastic modulus of 16.6 GPa "best-fit" to the linear portion of the stress-strain curve (see Figure 4-11). The nominal yield stress was 231 MPa (34.0 ksi) and yield strain was 1.7%. The ultimate tensile strength was 446 MPa (64.7 ksi) at 22.6% strain. Since the test was not completed while applying a slow strain rate, the strain to failure and reduction of area properties (which are measured after failure) are not comparable with other specimens' properties determined in this program. Hence, they are not presented in this discussion. The specimen strain shows a straight line dependence on time (see

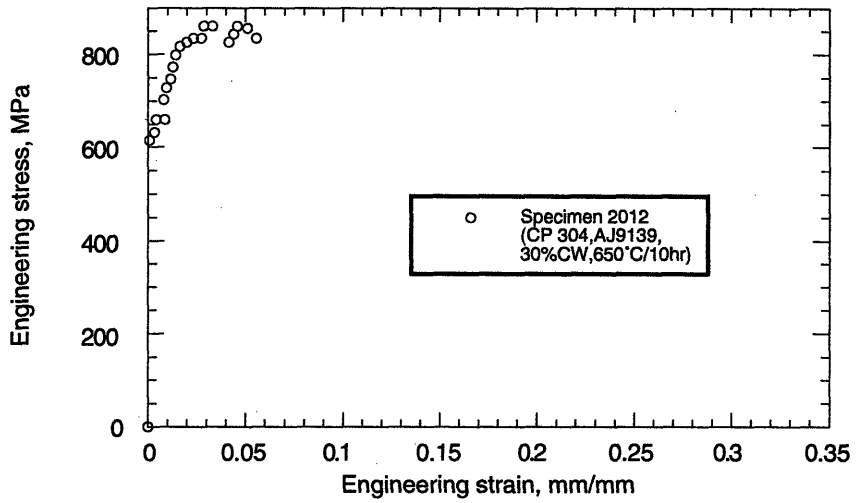

Figure 4-5. Stress-strain plot for specimen 2012 (CP 304,AJ9139,30%CW,furnace sensitized at 650°C/10hr,0 n/m^2).

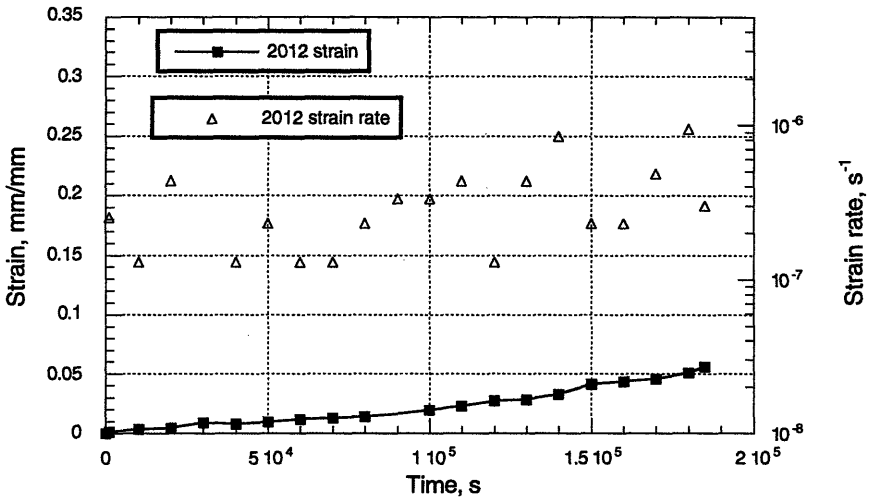

Figure 4-6. Strain-time plot for specimen 2012 (CP 304,AJ9139,30%CW,furnace sensitized at 650°C/10hr,0 n/m^2).

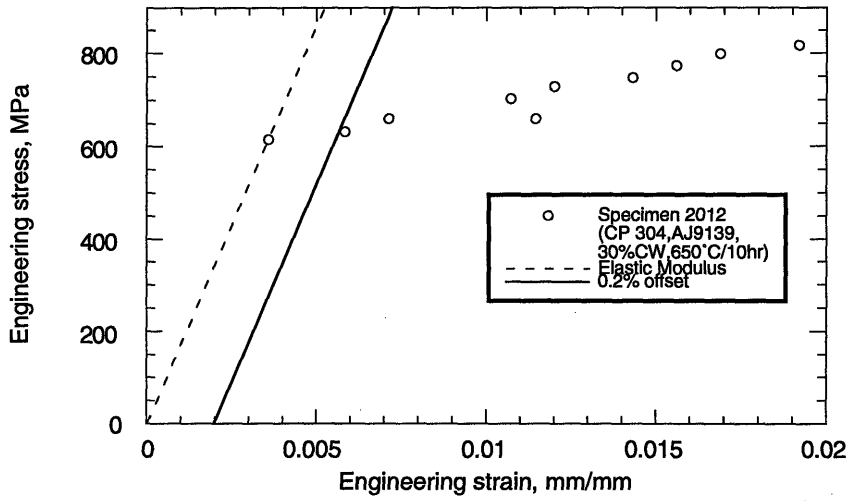

Figure 4-7. Yield stress for specimen 2012 (CP 304,AJ9139,30%CW,furnace sensitized at 650°C/10hr,0 n/m^2).

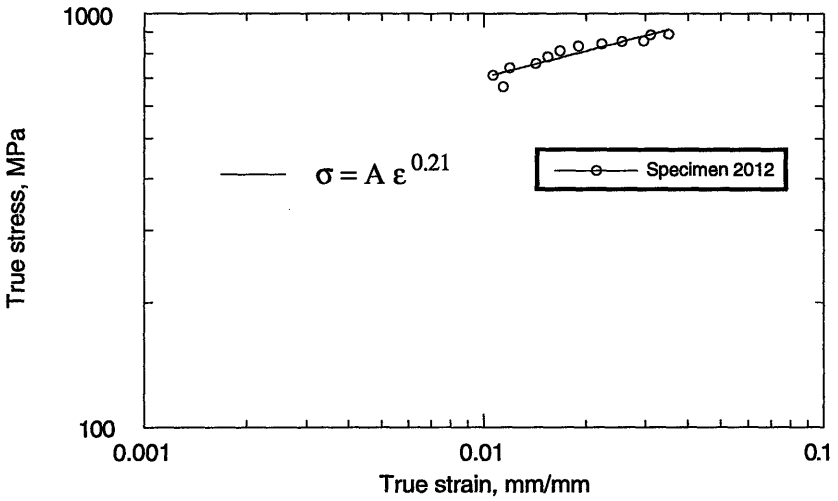

Figure 4-8. Strain-hardening exponent for specimen 2012 (CP 304,AJ9139,30%CW,furnace sensitized at 650°C/10hr,0 n/m^2).

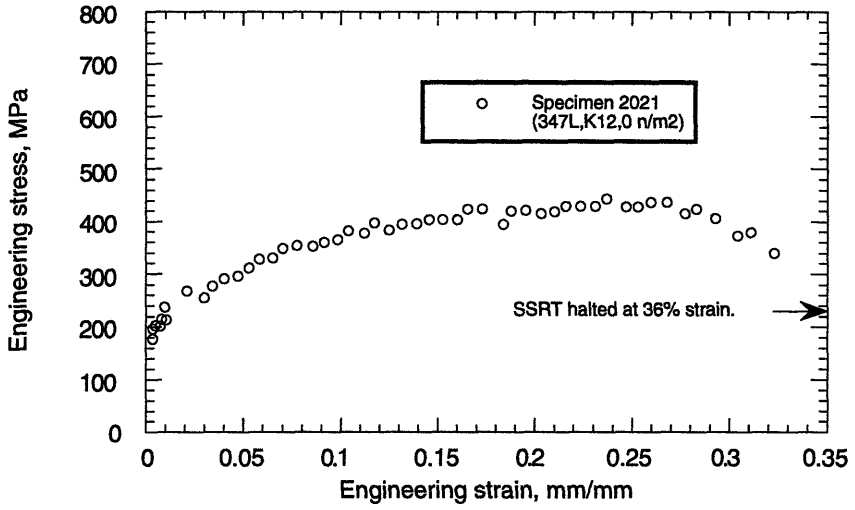

Figure 4-9. Stress-strain plot for specimen 2021 (347L, K12, 0 n/m^2).

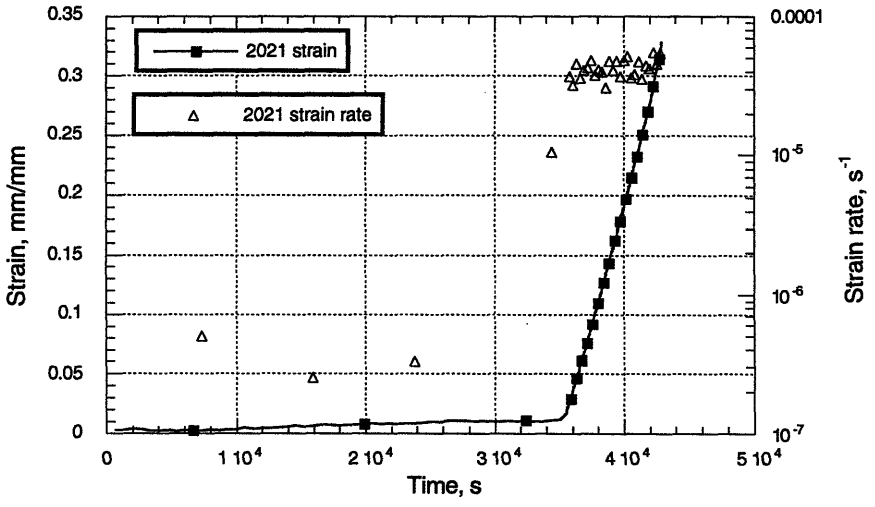

Figure 4-10. Strain-time plot for specimen 2021 (347L, K12, 0 n/m^2).

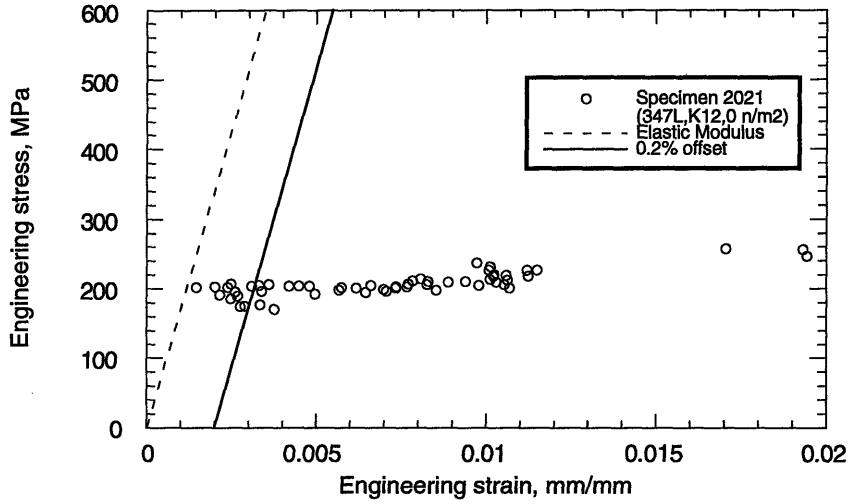

Figure 4-11. Yield stress for specimen 2021 (347L, K12, 0 n/m^2).

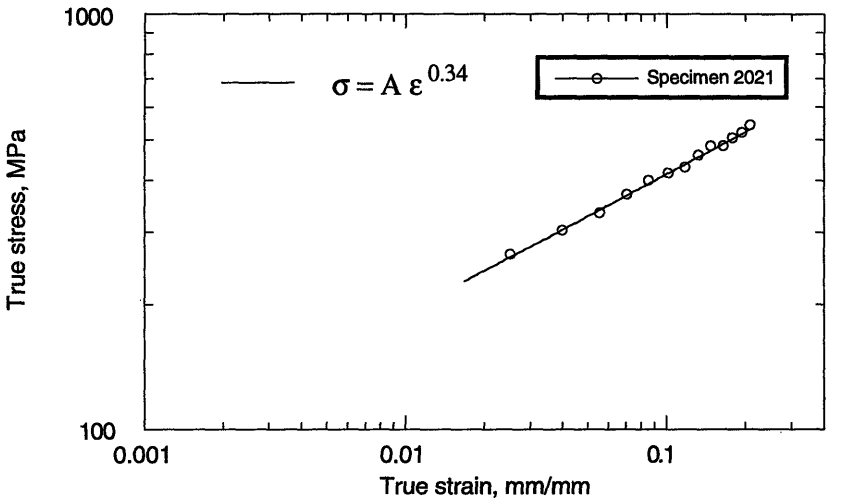

Figure 4-12. Strain-hardening exponent for specimen 2021 (347L, K12, 0 n/m^2).

Figure 4-10) indicative of the constant extension rate employed. In the same figure, the calculated strain rate shows an initial value of 3.3×10^{-7} s^{-1} and the higher value of 4.2×10^{-5} s^{-1} after the extension rate was increased. A good correlation (R=0.981) of the strain-hardening exponent was fit by the relation $\sigma = A\varepsilon^{\alpha}$ to the true stress-strain curve in the plastic region (from 1% beyond the yield strain to strain at ultimate stress) as seen in Figure 4-12. It was determined to be 0.34.

4.2.4 Specimen 89

Specimen 89 was made from commercial purity alloy 304 (heat AJ9139) stainless steel and tested in the unirradiated, solution annealed condition. It was tested in support of the DCPD scoping studies; therefore, it represents a baseline sample which can be used in comparisons with the specimens tested in the MITR-II core. The SSR test was performed in an out-of-pile autoclave and loading rig that were different than those employed for the in-core SSR testing. However, mechanical properties determined from different rigs are equivalent since the compliance of the rigs is known. In order to eliminate scaling concerns, the tensile specimen geometry was exactly the same as all other specimens (see description in section 2.4.1). The SSR test was conducted at a slightly higher constant extension rate of 8.47×10^{-4} mm/sec (0.002 in/min) and in the equivalent chemistry environment; in high temperature and pressure water test conditions that simulated BWR primary coolant (10.3 MPa, 288°C, 8 ppm dissolved O_2). No pauses occurred during the test.

Figure 4-13 shows the stress-strain plot for the SSR test. The foot correction was -0.9%. The 0.2% offset yield strength was determined with respect to an elastic modulus of 16.6 GPa "best-fit" to the linear portion of the stress-strain curve (see Figure 4-15). The nominal yield stress was 253 MPa (36.7 ksi) and yield strain was 1.7%. The ultimate tensile strength was 504 MPa (73.0 ksi) at 46% strain. The nominal strain to failure was 53% (calculated assuming uniaxial tensile stress). The specimen strain shows a straight line dependence on time (see Figure 4-14) indicative of the constant extension rate employed. In the same figure, the calculated strain rate displays a constant value of 8×10^{-5} s^{-1}. A good correlation (R=0.981) of the strain-hardening exponent was fit by the relation $\sigma = A\varepsilon^{\alpha}$ to the true stress-strain curve in the plastic region (from 1% beyond the yield strain to strain at ultimate stress) as seen in Figure 4-16. It was determined to be 0.42 and the reduction of area was not measured.

4.2.5 Specimen 17

Specimen 17 was made from alloy 316L (heat K5) stainless steel and tested in the unirradiated, solution annealed condition. It was tested in support of the DCPD scoping studies along with specimen 89. The SSR test was conducted at a constant extension rate of 8.47×10^{-4}

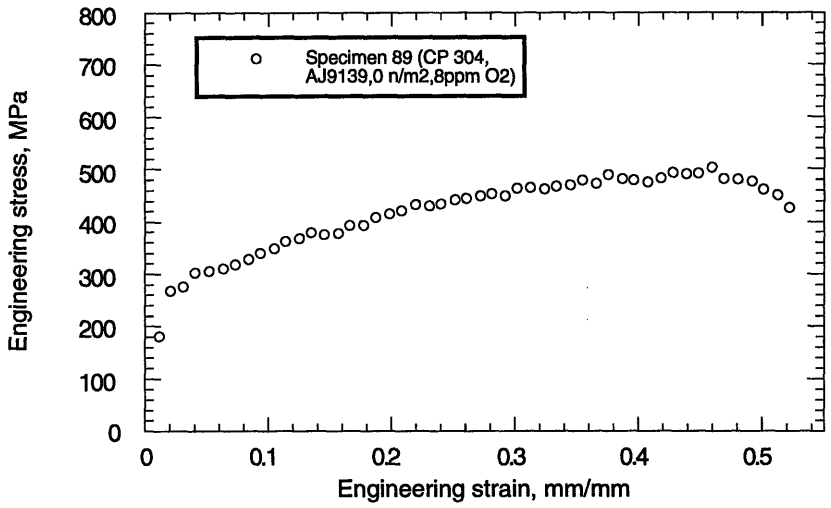

Figure 4-13. Stress-strain plot for specimen 89 (CP 304,AJ9139,0 n/m^2,8 ppm O_2 H_2O).

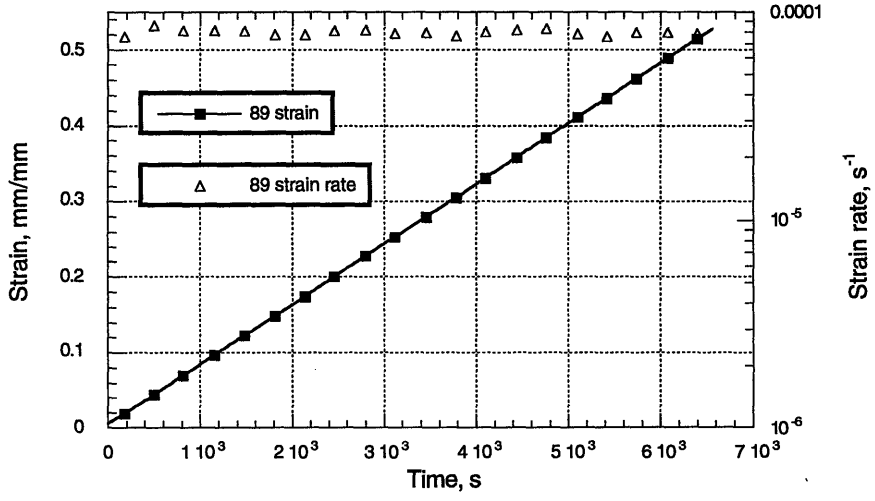

Figure 4-14. Strain-time plot for specimen 89 (CP 304,AJ9139,0 n/m^2,8 ppm O_2 H_2O).

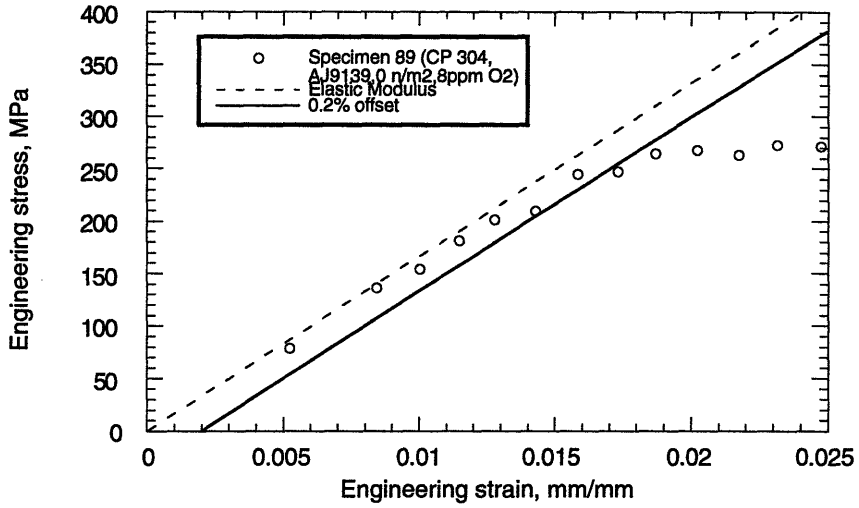

Figure 4-15. Yield stress for specimen 89 (CP 304,AJ9139,0 n/m^2,8 ppm O_2 H_2O).

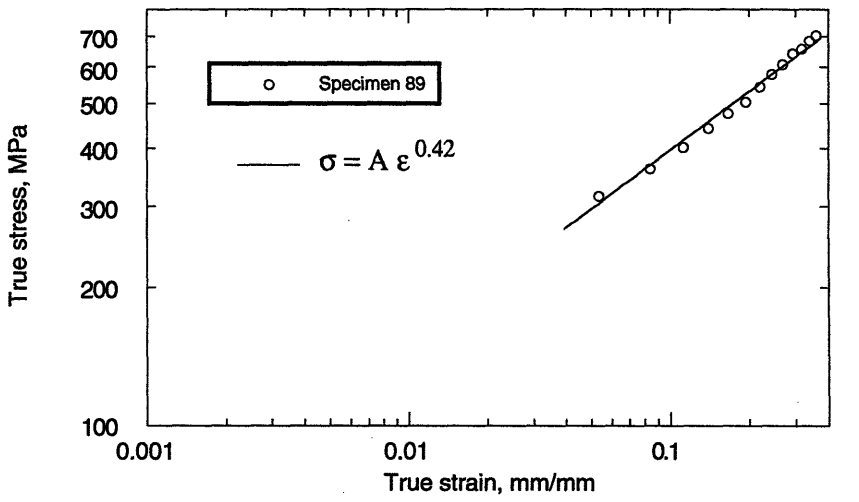

Figure 4-16. Strain-hardening exponent for specimen 89 (CP 304,AJ9139,0 n/m^2,8 ppm O_2 H_2O).

mm/sec (0.002 in/min) in high temperature and pressure water test conditions that simulated BWR primary coolant (10.3 MPa, 288°C, 8 ppm dissolved O_2). No pauses occurred during the test.

Figure 4-17 shows the stress-strain plot for the SSR test. The foot correction was -0.4%. The 0.2% offset yield strength was determined with respect to an elastic modulus of 16.6 GPa "best-fit" to the linear portion of the stress-strain curve (see Figure 4-19). The nominal yield stress was 213 MPa (30.9 ksi) and yield strain was 1.6%. The ultimate tensile strength was 440 MPa (63.8 ksi) at 35.6% strain. The nominal strain to failure was 45% (calculated assuming uniaxial tensile stress). The specimen strain shows a straight line dependence on time (see Figure 4-20) indicative of the constant extension rate employed. In the same figure, the calculated strain rate displays a constant value of 8×10^{-5} s^{-1}. A good correlation (R=0.981) of the strain-hardening exponent was fit by the relation $\sigma = A\varepsilon^{\alpha}$ to the true stress-strain curve in the plastic region (from 1% beyond the yield strain to strain at ultimate stress) as seen in Figure 4-21. It was determined to be 0.40 and the reduction of area was not measured.

4.2.6 Specimen 32

Specimen 32 was made from alloy 347L (heat K12) stainless steel and tested in the unirradiated, solution annealed condition. It was tested in support of the DCPD scoping studies along with specimens 89 and 17. The SSR test was conducted at a constant extension rate of 2.96×10^{-3} mm/sec (0.007 in/min) in high temperature and pressure water test conditions that simulated BWR primary coolant (10.3 MPa, 288°C, 8 ppm dissolved O_2). This extension rate was 3.5 times greater than that employed in the other out-of-pile SSR tests, but still within the range of strain rates utilized for environmentally assisted cracking tests. No pauses occurred during the test.

Figure 4-21 shows the stress-strain plot for the SSR test. The foot correction was -0.3%. The 0.2% offset yield strength was determined with respect to an elastic modulus of 16.6 GPa "best-fit" to the linear portion of the stress-strain curve (see Figure 4-23). The nominal yield stress was 230 MPa (33.4 ksi) and yield strain was 1.6%. The ultimate tensile strength was 440 MPa (63.8 ksi) at 32.2% strain. The nominal strain to failure was 41% (calculated assuming uniaxial tensile stress). The specimen strain shows a straight line dependence on time (see Figure 4-22) indicative of the constant extension rate employed. In the same figure, the calculated strain rate displays a constant value of 3×10^{-4} s^{-1}. A good correlation (R=0.981) of the strain-hardening exponent was fit by the relation $\sigma = A\varepsilon^{\alpha}$ to the true stress-strain curve in the plastic region (from 1% beyond the yield strain to strain at ultimate stress) as seen in Figure 4-24. It was determined to be 0.38 and the reduction of area was not measured.

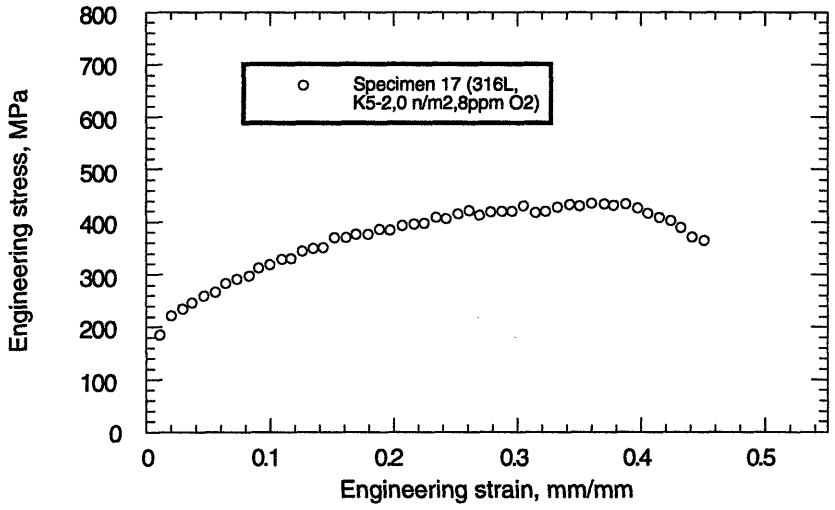

Figure 4-17. Stress-strain plot for specimen 17 (316L,K5,0 n/m^2,8 ppm O_2 H_2O).

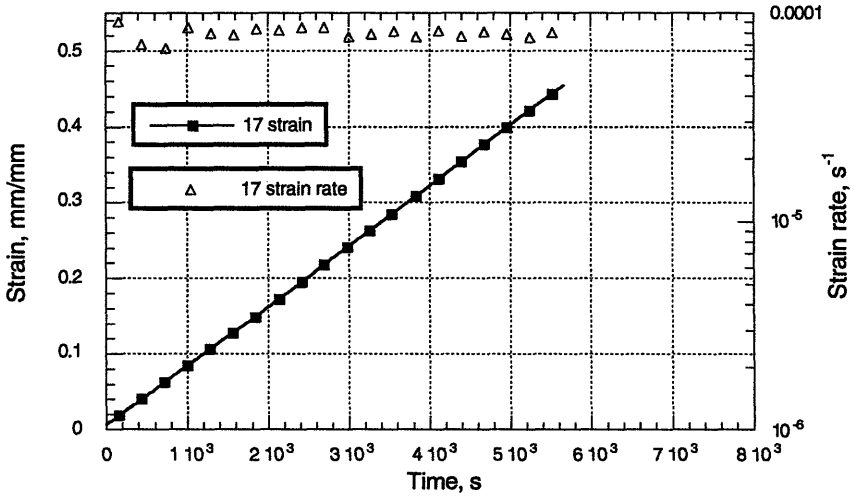

Figure 4-18. Strain-time plot for specimen 17 (316L,K5,0 n/m^2,8 ppm O_2 H_2O).

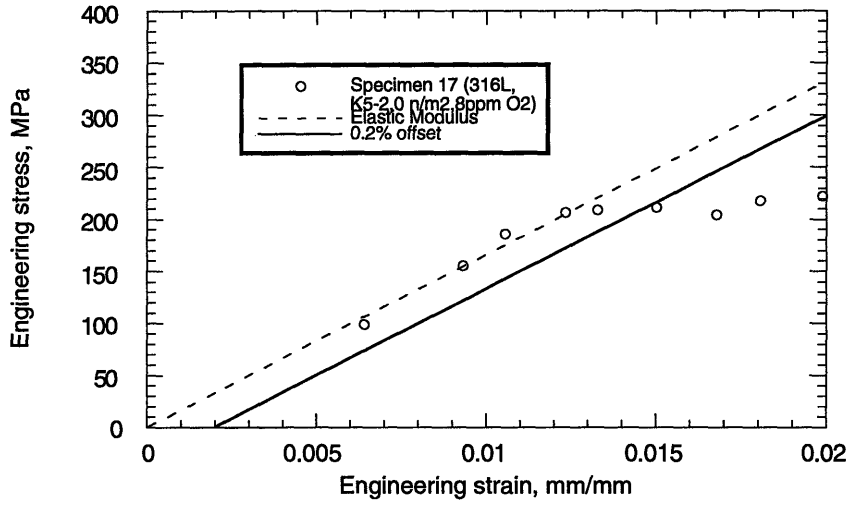

Figure 4-19. Yield stress for specimen 17 (316L,K5,0 n/m^2,8 ppm O_2 H_2O).

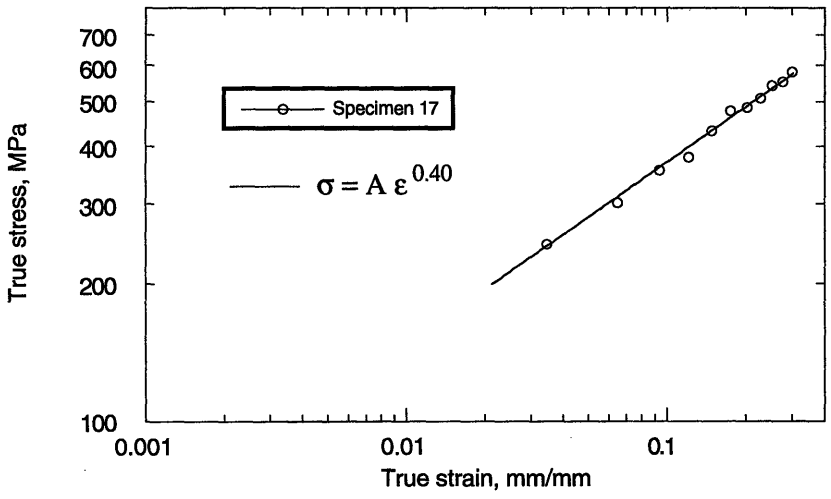

Figure 4-20. Strain-hardening exponent for specimen 17 (316L,K5,0 n/m^2,8 ppm O_2 H_2O).

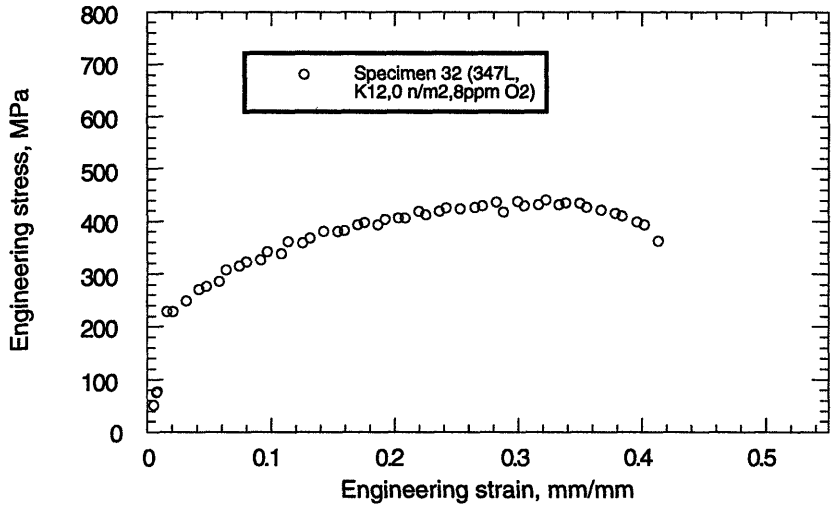

Figure 4-21. Stress-strain plot for specimen 32 (347L,K12,0 n/m^2,8 ppm O_2 H_2O).

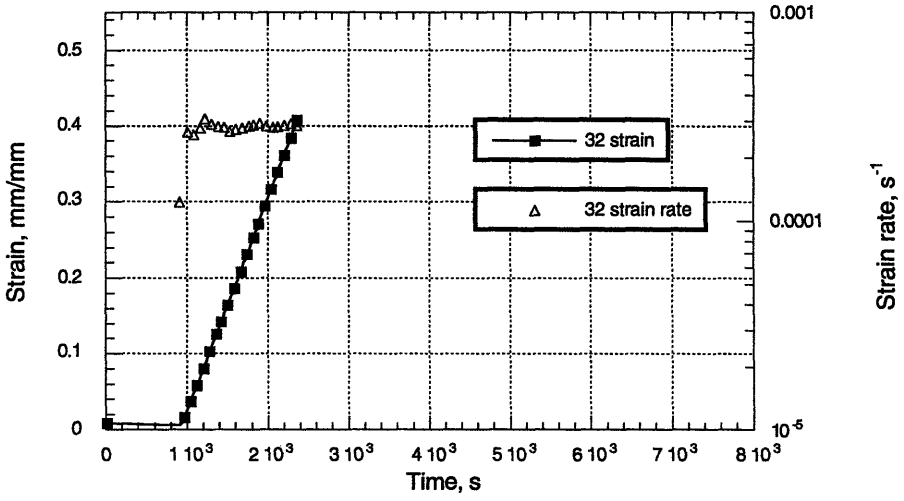

Figure 4-22. Strain-time plot for specimen 32 (347L,K12,0 n/m^2,8 ppm O_2 H_2O).

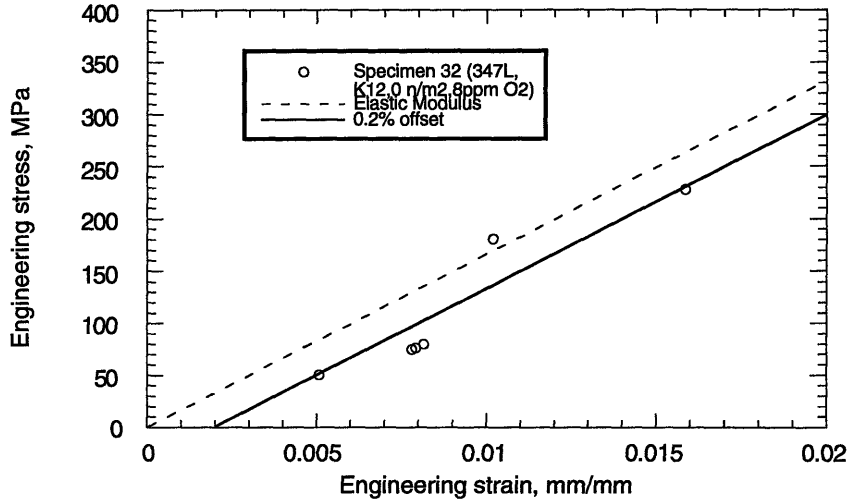

Figure 4-23. Yield stress for specimen 32 (347L,K12,0 n/m^2,8 ppm O_2 H_2O).

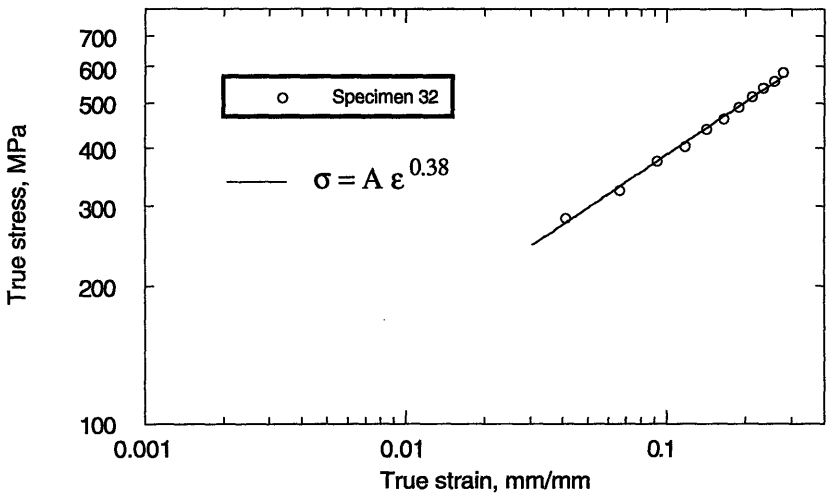

Figure 4-24. Strain-hardening exponent for specimen 32 (347L,K12,0 n/m^2,8 ppm O_2 H_2O).

4.3 IN-FLUX TESTS

The in-core slow strain rate tensile testing of pre-irradiated specimens performed at the MIT Nuclear Reactor Laboratory was the first of its kind performed throughout the world. It represented the culmination of an intensive research and development effort over the six year MIT IASCC program. As a result of the technology which has been developed, there now exists a facility and the necessary infrastructure for in-core SSRT tests on various materials of interest to the sponsor and to the nuclear power industry more generally. For this series of in-core SSRT tests, seven tensile specimens were tested. Of these seven specimens only five were pre-irradiated in the MITR-II, hence they made up less than 10% of the total inventory of 64 which were irradiated in the Dry Irradiation Facility. Because of the finite time and resources required to conduct the in-core SSR testing, a matrix (which essentially prioritized the tensile specimens available) was developed to provide a logical sequence for chronologically testing the specimens, based on successive test results.

4.3.1 Test Matrix

The test matrix for in-core SSR tests embodied guiding principles for conducting the most relevant research investigation of irradiation assisted stress corrosion cracking. The proposed and completed test matrices are shown in Figure 4-25. As the top matrix in the figure shows, three alloys from the family of austenitic stainless steels were proposed for study in this program: commercial purity 304 (heat AJ9139), 316L (heat K5), and ultra-high purity (UHP) 304L (heat V945). These alloys were chosen because of their relevance to the nuclear power industry and the sponsors' interests. These alloys are currently employed as structural components' materials or are being considered as replacement or future materials. The first alloy, CP 304, represents the material most generally employed as structural members within reactor vessels (e.g. top guide, core support plate, neutron monitoring guide tubes, and the core shroud). The alloy 316L is used less frequently because of its higher cost. It is considered more resistant to corrosion related failures and particularly stress corrosion cracking, and is, therefore a candidate for more general use in future if it shows greater resistance to IASCC as it has to SCC. The research alloy UHP 304L is not used in current LWR primary vessels, but is of scientific and engineering interest for comparison with the commercial purity 304 alloy. The lower carbon and impurity concentrations, particularly phosphorus of UHP 304L alloy, suggest it will behave favorably relative to the CP 304 material.

The test matrix outline follows the logical sequence with CP 304 material tested first, followed by 316L, and lastly UHP 304L. Of these alloys, the specimens pre-irradiated to the

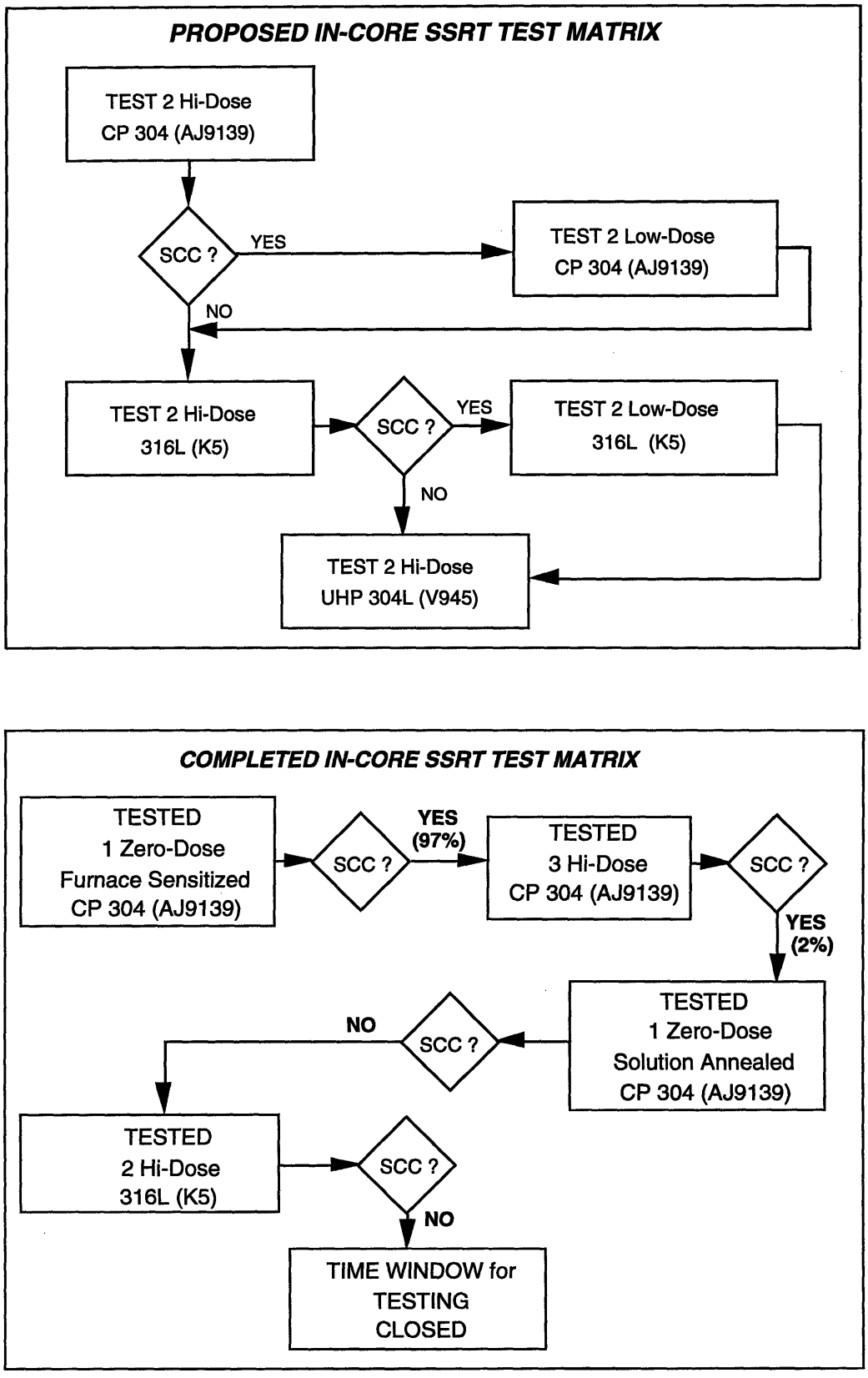

Figure 4-25. Proposed and completed test matrices for MIT IASCC program.

highest fluence or damage level were of primary interest because of the highest likelihood for irradiation assisted stress corrosion cracking susceptibility. Secondary interest was given to lower fluence specimens, but they would be tested only on the condition that SCC was observed for the hi-dose tensile specimens that failed. This research path would be used to determine a correlation between fluence level and IASCC susceptibility. If, on the other hand, no SCC was observed, then the next alloy of interest was tested.

The completed test matrix indicates that this general approach was indeed followed. Three CP 304 (heat AJ9139) samples, pre-irradiated to the highest fluence of 0.8×10^{25} n/m^2, were tested instead of just two because one SSR test was not completed due to an equipment failure. Because only a small percentage of intergranular cracking (SCC) was observed on the fractured surfaces (see Chapter 5), an unirradiated CP 304 specimen was tested in the place of a low-fluence level CP 304 in order to have a more distinct comparison. The unirradiated sample test also provided data for distinguishing the long term (fluence) and instantaneous radiation effects. Following the tests on CP 304 two 316L specimens, pre-irradiated to a fluence of 0.74×10^{25} n/m^2, were evaluated by SSR testing and compared to the results of CP 304 specimen pre-irradiated to a comparable fluence of 0.8×10^{25} n/m^2. Further testing on the third alloy was omitted because of time constraints. The following subsections present summaries of the SSR tests and results for the mechanical properties determined from the SSRT data.

4.3.2 Unirradiated CP 304 (heat AJ9139) Stainless Steel

4.3.2.1 Specimen 2003

Specimen 2003 was fabricated from commercial purity alloy 304 (heat AJ9139) and tested in the unirradiated, furnace sensitized condition. The furnace heat treatment at 650°C for 10 hours was more than adequate to produce a sensitized microstructure susceptible to stress corrosion cracking. The EPR ratio for this specimen was 16.5, showing this specimen to be highly sensitized. The Vickers hardness number was 263. The SSR test results for specimen 2003 provided secondary verification that the oxidizing conditions employed in the in-core SSR tests were sufficiently aggressive to initiate and propagate stress corrosion cracking. This evidence was critical since IASCC requires a similarly aggressive environment as that which causes SCC for a thermally sensitized material. A major thrust of the program was to evaluate the susceptibility to IASCC for materials that had varying levels of radiation damage. Therefore the results for this sensitized specimen (defined by heat treatment and EPR measurements) revealed the susceptibility to intergranular attack in the same physico-chemical environment used in all in-core tests. These test results substantiate that maintaining the letdown oxygen concentration

between 200 and 550 ppb provided an adequately oxidizing water chemistry as the electrochemical potential (ECP) measurements indicated.

The reactor was operated at 4.2 MW. At the completion of this test the specimen appeared bent. Further investigations lead to the conclusion that the specimen was improperly positioned in the grips when load was first applied. Specimen loading procedures were modified for subsequent tests to prevent this from recurring.

Figure 4-26 shows the stress-strain plot for the SSR test. The foot correction was -0.15%. The 0.2% offset yield strength was determined with respect to an elastic modulus of 171 GPa "best-fit" to the linear portion of the stress-strain curve (see Figure 4-28). The nominal yield stress was 182 MPa (26.4 ksi) and yield strain was 0.3%. The ultimate tensile strength was 336 MPa (48.7 ksi) at 8.0% strain. The nominal strain to failure was 15% (calculated assuming uniaxial tensile stress). The specimen strain shows a straight line dependence on time (see Figure 4-27) indicative of the constant extension rate employed except for the times during test pauses (plateau regions with constant strain). In the same figure, the calculated strain rate shows considerable scatter due to the sensitivity of rig compliance on applied stress, but indicates an average strain rate of $4.9 \times 10^{-7}\ s^{-1}$. A good correlation (R=0.977) of the strain-hardening exponent was fit by the relation $\sigma = A\varepsilon^{\alpha}$ to the true stress-strain curve in the plastic region (from 1% beyond the yield strain to strain at ultimate stress) as seen in Figure 4-29. It was determined to be 0.26 and the reduction of area was less than 5%. Note that all of these results were calculated without correction for the bending of the specimen and should therefore be viewed as qualitative indicators only.

4.3.2.2 Specimen 98

Specimen 98 was fabricated from commercial purity alloy 304 (heat AJ9139) and tested in the unirradiated, solution annealed condition. In order to discriminate between the long-term radiation effects such as hardening and instantaneous effects which might include hardening by defect production and enhanced creep, this unirradiated tensile specimen was tested in the in-core SSRT Rig.

Testing was done with the reactor operating at 4.0 MW. Testing was paused three times during the test. At a specimen strain of 9.5% and a load of 432 MPa, the SSR test was paused and the load reduced to 136 MPa., during reactor power maneuvers. After reactor power was returned to 4.0 MW and all temperature and chemical conditions stabilized, specimen stress was increased to 402 MPa and the SSR testing was resumed. At a specimen strain of 11.5% and a load of 469 MPa, the reactor had a temporary shut down, the SSR test was paused and the load reduced to 136 MPa. After reactor power was returned to 4.0 MW and all temperature and chemical conditions stabilized, specimen stress was increased to 424 MPa and the SSR testing was

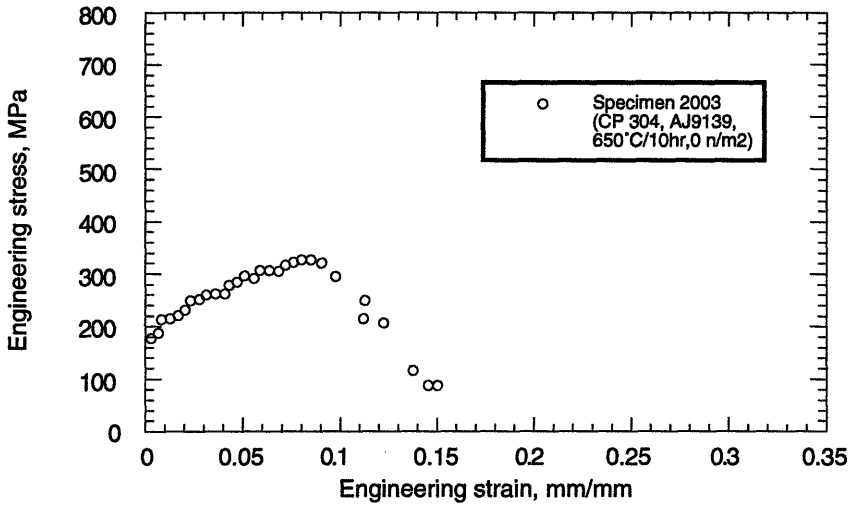

Figure 4-26. Stress-strain plot for specimen 2003 (CP 304, AJ9139, furnace sensitized at 650°C/10hr, 0 n/m^2).

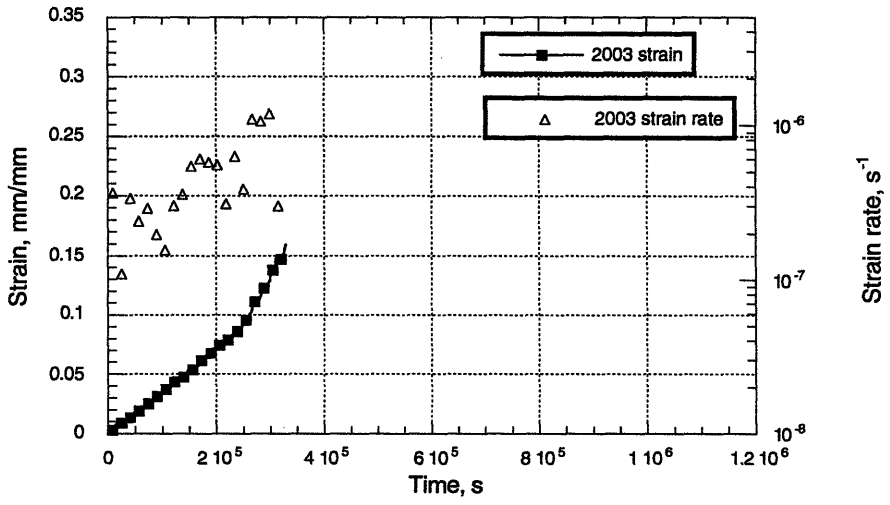

Figure 4-27. Strain-time plot for specimen 2003 (CP 304, AJ9139, furnace sensitized at 650°C/10hr, 0 n/m^2).

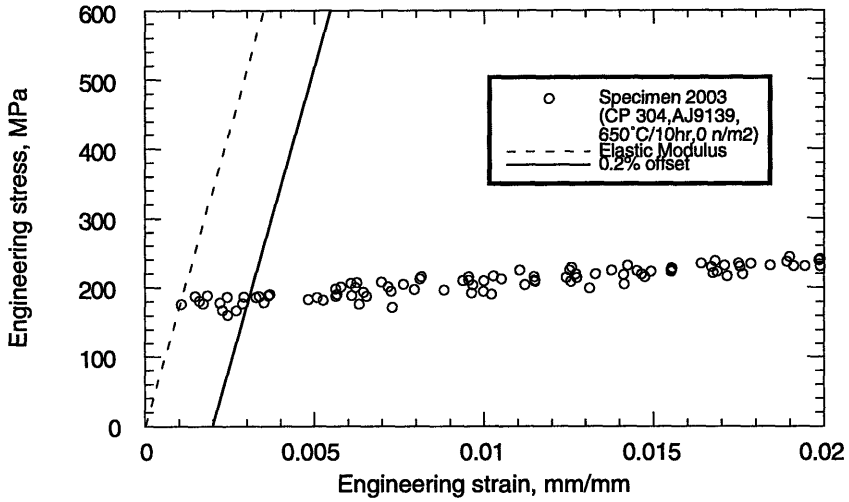

Figure 4-28. Yield stress for specimen 2003 (CP 304, AJ9139, furnace sensitized at 650°C/10hr, 0 n/m^2).

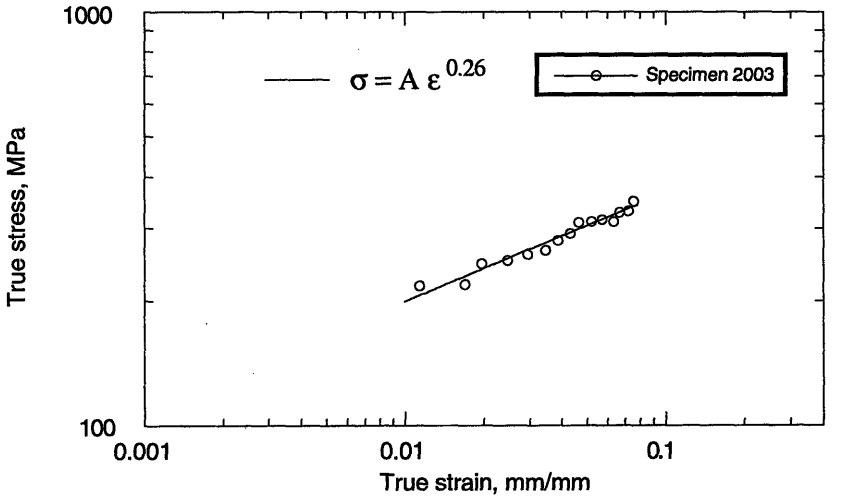

Figure 4-29. Strain-hardening exponent for specimen 2003 (CP 304, AJ9139, furnace sensitized at 650°C/10hr, 0 n/m^2).

resumed. At a specimen strain of 18% and a load of 510 MPa, the reactor had a temporary shut down. The SSR test was paused and the load reduced to 136 MPa. After reactor power was returned to 4.0 MW and all temperature and chemical conditions stabilized, specimen stress was increased to 470 MPa and the SSR testing was resumed. These pauses experienced in this test were well managed by the instrumentation and operators of the SSRT Rig.

Figure 4-30 shows the stress-strain plot for the SSR test. The foot correction was 0.45%. The 0.2% offset yield strength was determined with respect to an elastic modulus of 171 GPa "best-fit" to the linear portion of the stress-strain curve (see Figure 4-32). The nominal yield stress was 316 MPa (45.8 ksi) and yield strain was 0.4%. The ultimate tensile strength was 563 MPa (81.7 ksi) at 26.5% strain. The nominal strain to failure was 36% (calculated assuming uniaxial tensile stress). The specimen strain shows a straight line dependence on time (see Figure 4-31) indicative of the constant extension rate employed except for the times during test pauses (plateau regions with constant strain). In the same figure, the calculated strain rate shows considerable scatter due to the sensitivity of rig compliance on applied stress, but indicates an average strain rate of 9 x (10^{-7} s^{-1}). A good correlation (R=0.985) of the strain-hardening exponent was fit by the relation $\sigma = A\varepsilon^{\alpha}$ to the true stress-strain curve in the plastic region (from 1% beyond the yield strain to strain at ultimate stress) as seen in Figure 4-33. It was determined to be 0.31 and the reduction of area was 73%.

4.3.3 Pre-irradiated CP 304 (heat AJ9139) Stainless Steel

4.3.3.1 Specimen 80

Specimen 80 was fabricated from CP alloy 304 (heat AJ9139), solution annealed and tested after pre-irradiation to a fluence of 0.8 x 10^{25} n/m^2. Testing was done with the reactor operating at 4.0 MW. At 15% strain the main loop recirculation pump failed. The test was halted and the specimen pulled to failure at room temperature using a fast strain rate. The premature ending of the SSR test provides some interesting data that will be discussed in Chapter 5.

Figure 4-34 shows the stress-strain plot for the SSR test which was halted at 15% strain. The foot correction was -0.2%. The 0.2% offset yield strength was determined with respect to an elastic modulus of 39 GPa "best-fit" to the linear portion of the stress-strain curve (see Figure 4-36). The nominal yield stress was 520 MPa (75.4 ksi) and yield strain was 1.5%. The ultimate tensile strength was 605 MPa (87.8 ksi) at 13.7% strain. The nominal strain to failure was 32% (calculated assuming uniaxial tensile stress). The yield stress and ultimate stress for specimen 80 is 12% less than specimens 81 and 82 (discussed below) which is within the experimental error of

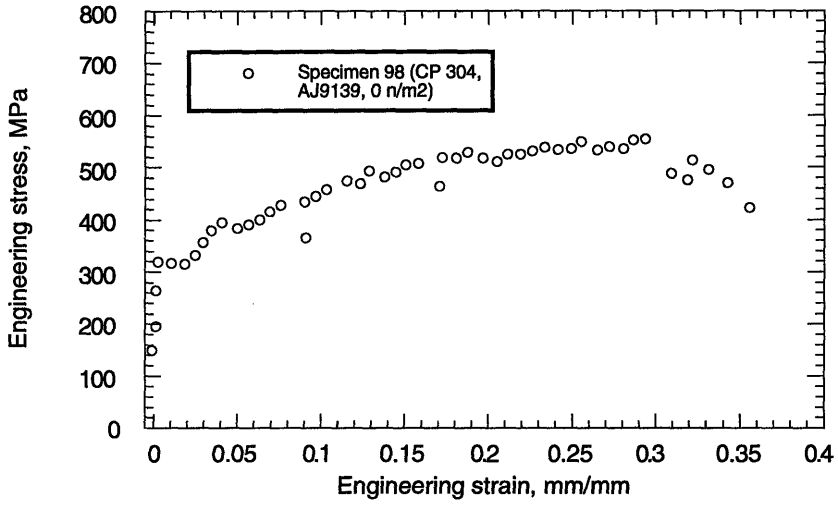

Figure 4-30. Stress-strain plot for specimen 98 (CP 304, AJ9139, 0 n/m^2).

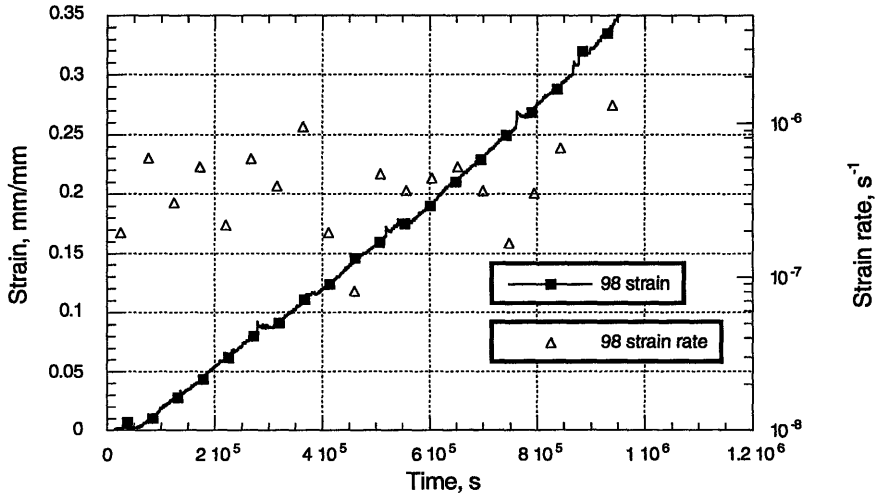

Figure 4-31. Strain-time plot for specimen 98 (CP 304, AJ9139, 0 n/m^2).

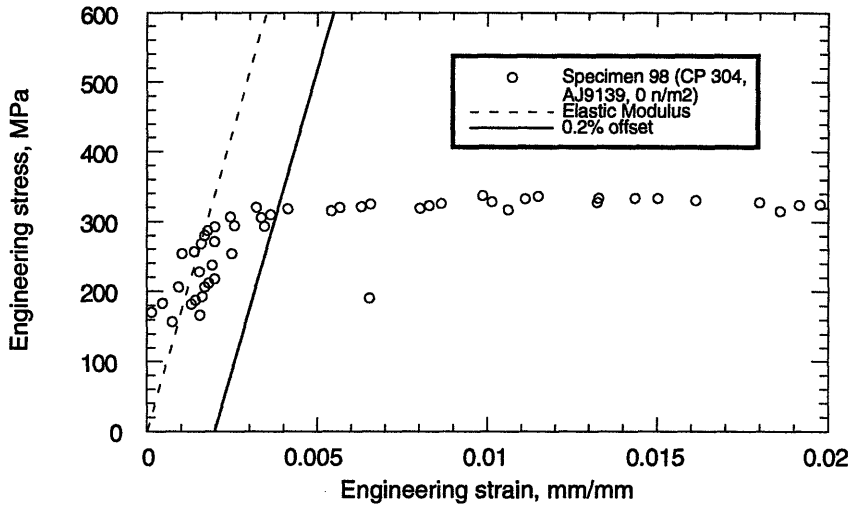

Figure 4-32. Yield stress for specimen 98 (CP 304, AJ9139, 0 n/m^2).

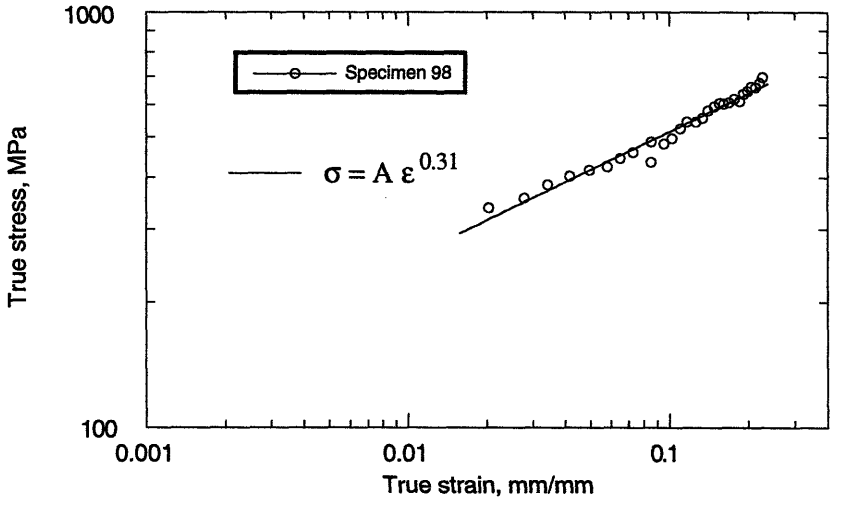

Figure 4-33. Strain-hardening exponent for specimen 98 (CP 304, AJ9139, 0 n/m^2).

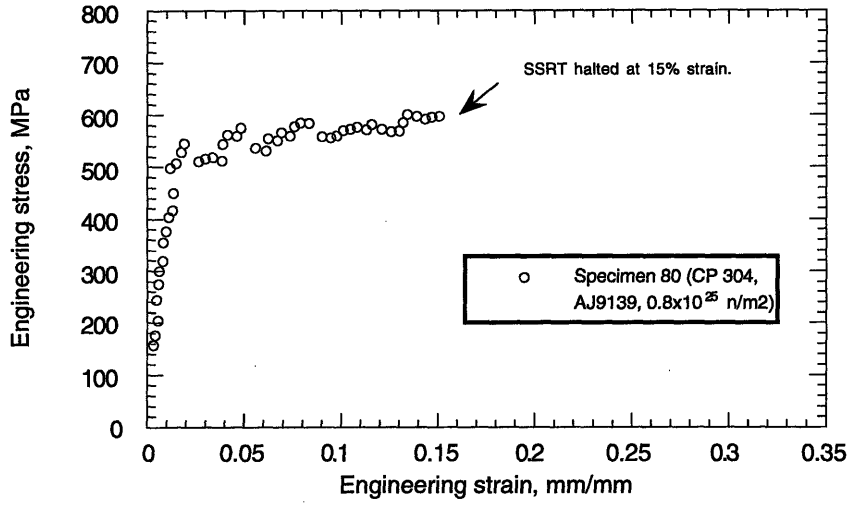

Figure 4-34. Stress-strain plot for specimen 80 (CP 304, AJ9139, 0.8 x 10^{25} n/m^2). SSRT halted at 15% strain.

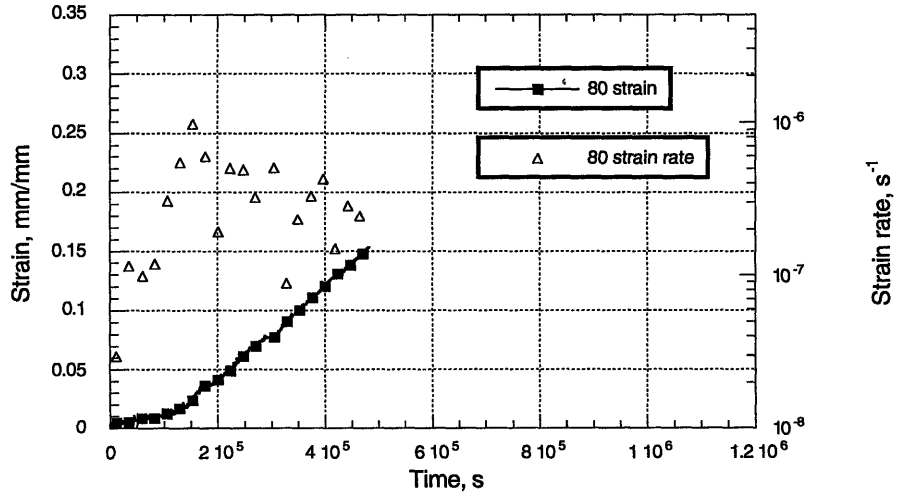

Figure 4-35. Strain-time plot for specimen 80 (CP 304, AJ9139, 0.8 x 10^{25} n/m^2). SSRT halted at 15% strain.

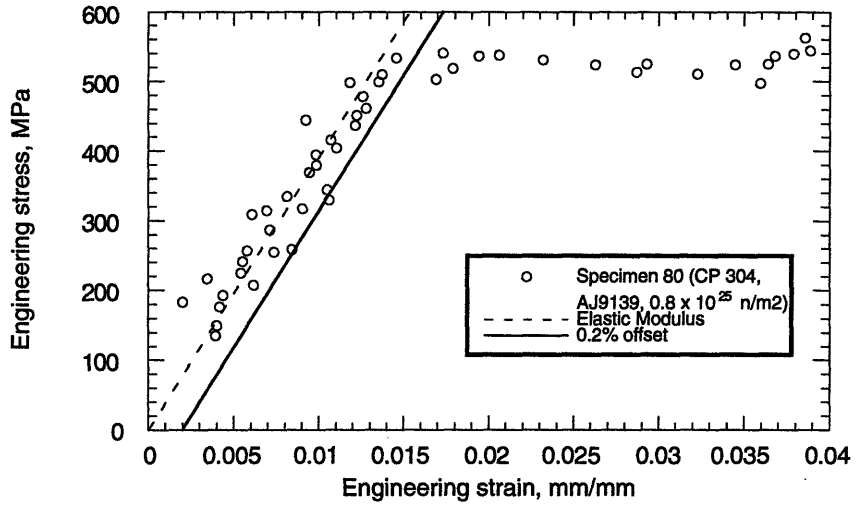

Figure 4-36. Yield stress for specimen 80 (CP 304, AJ9139, 0.8 x 10^{25} n/m^2).

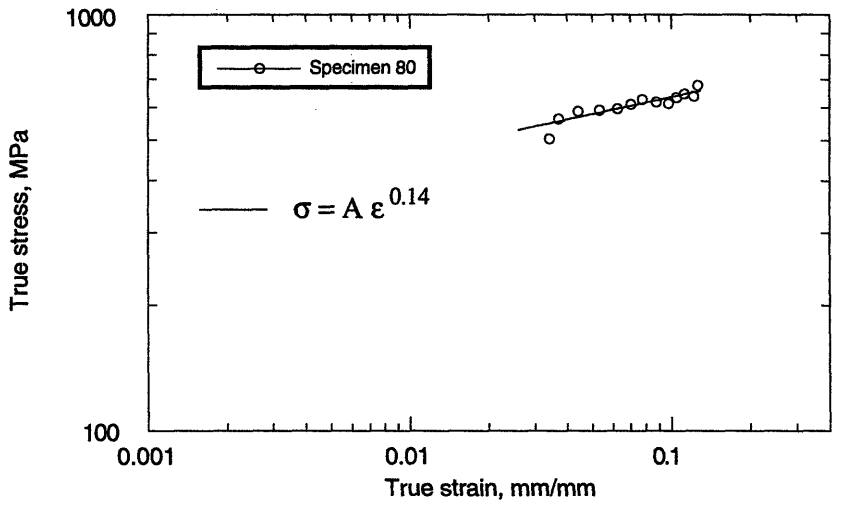

Figure 4-37. Strain-hardening exponent for specimen 80 (CP 304, AJ9139, 0.8 x 10^{25} n/m^2).

the apparatus, but it should be noted that the elastic modulus determined is 4.5 times lower than for specimens 81 and 82. The specimen strain shows a straight line dependence on time (see Figure 4-35) indicative of the constant extension rate employed except for the times during test pauses (plateau regions with constant strain). The change in the slope at 1.2×10^5 sec corresponds to the onset of yielding. In the same figure, the calculated strain rate shows considerable scatter due to the sensitivity of rig compliance on applied stress, but indicates an average strain rate of 3.4×10^{-7} s^{-1}. A good correlation (R=0.923) of the strain-hardening exponent was fit by the relation $\sigma = A\varepsilon^{\alpha}$ to the true stress-strain curve in the plastic region (from 1% beyond the yield strain to strain at ultimate stress) as seen in Figure 4-37. It was determined to be 0.14.

4.3.3.2 Specimen 81

Specimen 81 was fabricated from commercial purity alloy 304 (heat AJ9139), solution annealed and tested after pre-irradiation to a fluence of 0.8×10^{25} n/m^2. Testing was done with the reactor operating at 4.0 MW. Testing was paused two times during the test. At a specimen strain of 2% and a load of 578 MPa, the reactor had a temporary shut down, the SSR test was paused and the load reduced to 136 MPa. After reactor power was returned to 4.0 MW and all temperature and chemical conditions stabilized, specimen stress was increased to 554 MPa and the SSR testing was resumed. At a specimen strain of 19% and a load of 636 MPa, the reactor had a temporary shut down, the SSR test was paused and the load reduced to 136 MPa. After reactor power was returned to 4.0 MW and all temperature and chemical conditions stabilized, specimen stress was increased to 490 MPa and the SSR testing was resumed.

Figure 4-38 shows the stress-strain plot for the SSR test. The foot correction was 0.2%. The shift in the elastic portion at ~350MPa is attributed to slip and deformation in the wet seals of the rig. The 0.2% offset yield strength was determined with respect to an elastic modulus of 171 GPa "best-fit" to the linear portion of the stress-strain curve (see Figure 4-40). The nominal yield stress was 570 MPa (84.0 ksi) and yield strain was 0.5%. The ultimate tensile strength was 677 MPa (98.2 ksi) at 12.8% strain. The nominal strain to failure was 22% (calculated assuming uniaxial tensile stress). The specimen strain shows a straight line dependence on time (see Figure 4-39) indicative of the constant extension rate employed except for the times during test pauses (plateau regions with constant strain). Changes in the slope correspond to yielding (1.3×10^5 sec) and necking (~6×10^5 sec). The calculated strain rate shows considerable scatter due to the sensitivity of rig compliance on applied stress, but indicates an average strain rate of $3.7 \times 10^{-7} s^{-1}$. A good correlation (R=0.967) of the strain-hardening exponent was fit by the relation $\sigma = A\varepsilon^{\alpha}$ to the true stress-strain curve in the plastic region (from 1% beyond the yield strain to strain at

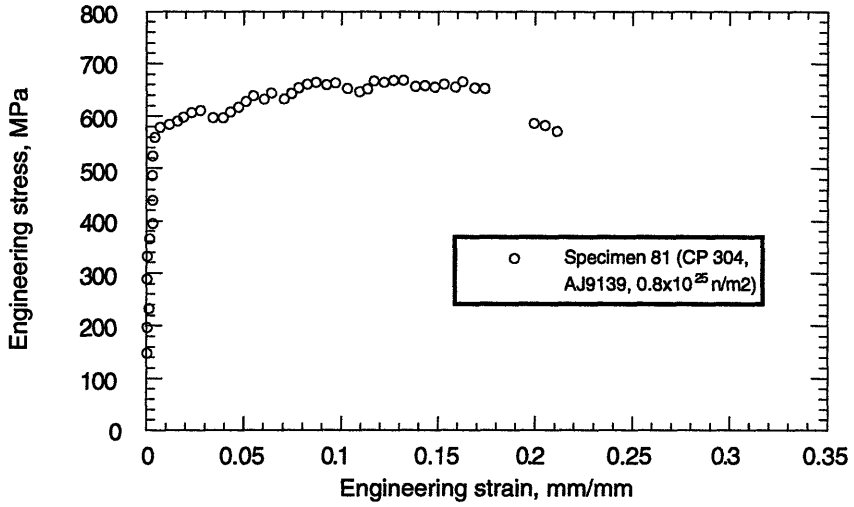

Figure 4-38. Stress-strain plot for specimen 81 (CP 304, AJ9139, 0.8 x 10^{25} n/m^2).

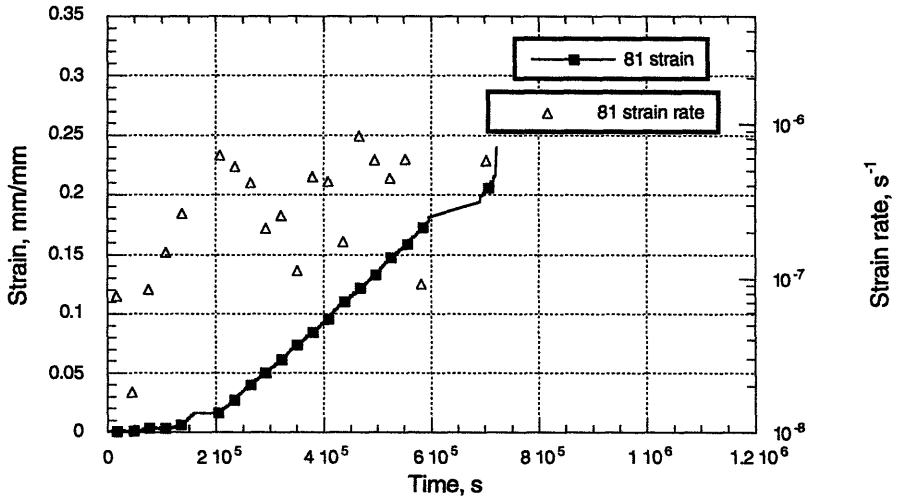

Figure 4-39. Strain-time plot for specimen 81 (CP 304, AJ9139, 0.8 x 10^{25} n/m^2).

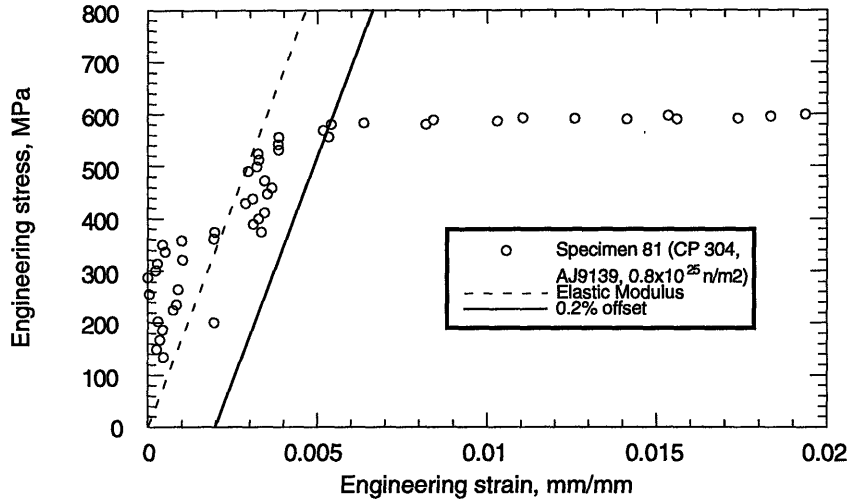

Figure 4-40. Yield stress for specimen 81 (CP 304, AJ9139, 0.8 x 10^{25} n/m^2).

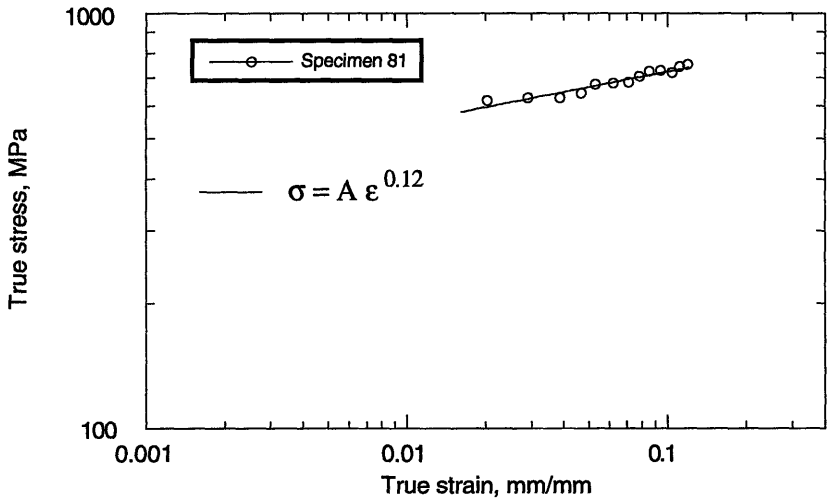

Figure 4-41. Strain-hardening exponent for specimen 81 (CP 304, AJ9139, 0.8 x 10^{25} n/m^2).

ultimate stress) as seen in Figure 4-41. It was determined to be 0.12 and the reduction of area was 59%.

4.3.3.3 Specimen 82

Specimen 82 was fabricated from commercial purity alloy 304 (heat AJ9139), solution annealed and tested after pre-irradiation to a fluence of 0.8×10^{25} n/m^2. It was taken from the same pre-irradiation capsule as specimens 80 and 81. Since the test for specimen 80 was halted before failure occurred under slow strain rate conditions, a third SSR test for this alloy and material condition was considered valuable to confirm the properties measured in the initial tests and indicate the reproducibility of results obtained from the SSRT Rig.

The reactor was operated at 4.0 MW. Testing was paused three times during the test. Prior to specimen yielding the reactor scrammed. Load was lowered from 420 MPa to 136 MPa and held there in load control until the reactor power was raised to 4.0 MW and temperature and chemistry conditions stabilized. To resume the test, load was raised to 420 MPa and the SSR test was restarted. The second pause occurred at a specimen strain of 4.5%. The loading machine was off for nearly 18 hours due to a problem with the loading machine control and data acquisition system. For this period load was nearly constant, 600±20 MPa. The third and final pause occurred at a specimen strain of about 15%. A reactor shut down was required. Specimen load was lowered and held at 136MPa. After reactor power was returned to 4.0 MW and all temperature and chemical conditions stabilized, specimen stress was increased to 520 MPa and the SSR test was resumed.

Figure 4-42 shows the stress-strain plot for the SSR test. The foot correction was -0.2%. The shift in the elastic portion at ~350MPa (similar to that observed for specimen 81) is attributed to deformation of the seals. The 0.2% offset yield strength was determined with respect to an elastic modulus of 171 GPa "best-fit" to the linear portion of the stress-strain curve (see Figure 4-44). The nominal yield stress was 536 MPa (77.7 ksi) and yield strain was 0.5%. The ultimate tensile strength was 706 MPa (102.4 ksi) at 13.2% strain. The nominal strain to failure was 21% (calculated assuming uniaxial tensile stress). The specimen strain shows a straight line dependence on time (see Figure 4-43) indicative of the constant extension rate employed except for the times during test pauses (plateau regions with constant strain). In the same figure, the calculated strain rate shows considerable scatter due to the sensitivity of rig compliance on applied stress, but indicates an average strain rate of 3.5×10^{-7} s^{-1}. A good correlation (R=0.981) of the strain-hardening exponent was fit by the relation $\sigma = A\varepsilon^{\alpha}$ to the true stress-strain curve in the plastic region (from 1% beyond the yield strain to strain at ultimate stress) as seen in Figure 4-45. It was determined to be 0.13 and the reduction of area was 48%.

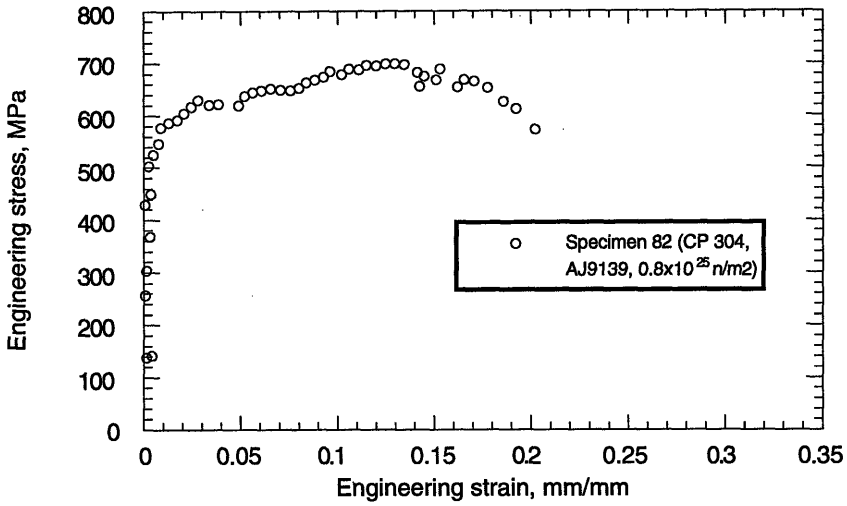

Figure 4-42. Stress-strain plot for specimen 82 (CP 304, AJ9139, 0.8 x 10^{25} n/m^2).

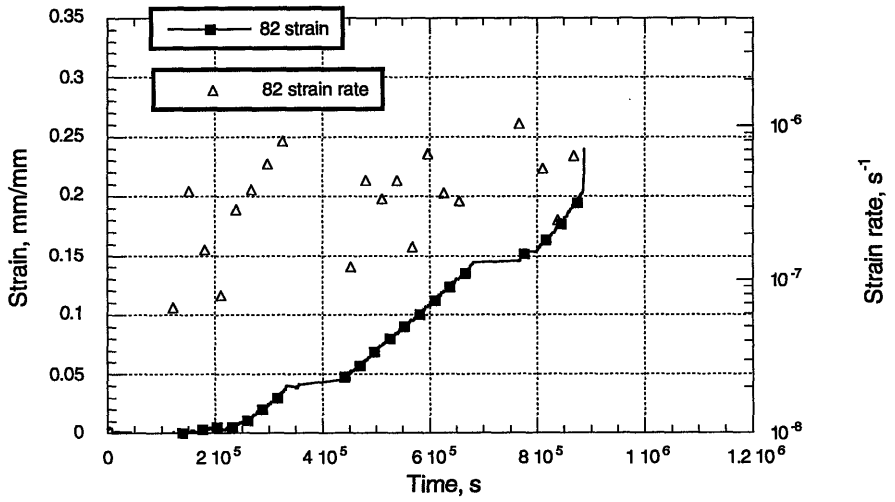

Figure 4-43. Strain-time plot for specimen 82 (CP 304, AJ9139, 0.8 x 10^{25} n/m^2).

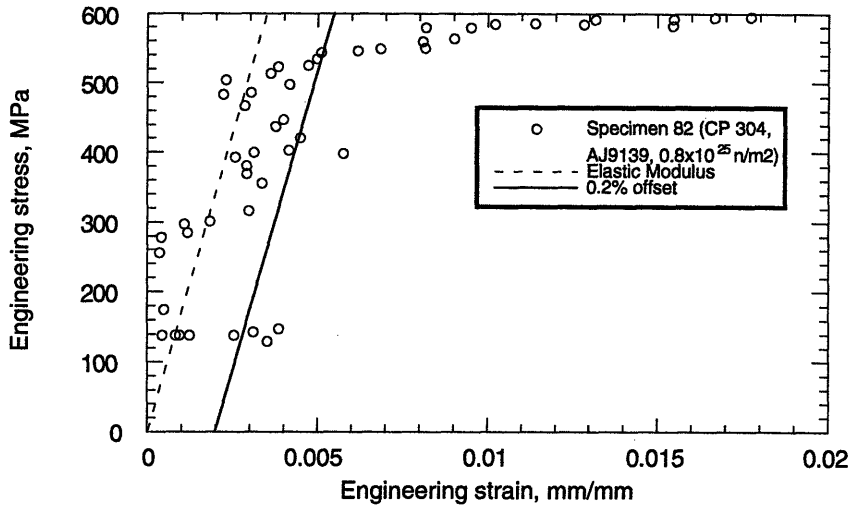

Figure 4-44. Yield stress for specimen 82 (CP 304, AJ9139, 0.8 x 10^{25} n/m^2).

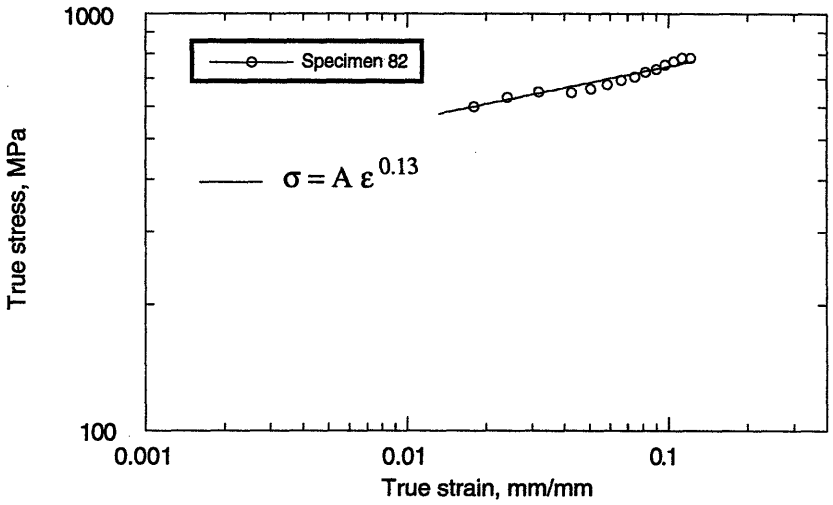

Figure 4-45. Strain-hardening exponent for specimen 82 (CP 304, AJ9139, 0.8 x 10^{25} n/m^2).

4.3.4 Pre-irradiated 316L (heat K5) Stainless Steel

4.3.4.1 Specimen 10

Specimen 10 was fabricated from alloy 316L (heat K5), solution annealed and tested after pre-irradiation to a fluence of 0.74×10^{25} n/m^2. This fluence level was the second highest available for the 316L specimens pre-irradiated under the IASCC program. The neutron fluence is comparable to the CP 304 alloy samples that were pre-irradiated to 0.8×10^{25} n/m^2. This comparison provides data that shows the similarities and/ or differences in mechanical properties of these materials when subject to conditions sufficiently aggressive to cause IASCC. This comparison is valuable since 316L is considered a more corrosion-resistant alloy that may provide more reliable long term service. Therefore, the increase in capital expense could be offset by the longer service life and reduced maintenance of key in-core components.

Testing was done with the reactor operating at 4.0 MW. Testing was paused five times during the test. At a specimen strain of 1.5% and load of 314 MPa, the test was paused and load reduced to 136 MPa for maintenance on a reactor ventilation pump. After reactor power was returned to 4.0 MW and all temperature and chemical conditions stabilized, specimen stress was increased to 249 MPa and the SSR testing was resumed. At a specimen strain of 5% and load of 374 MPa, the test was paused and load reduced to 136 MPa due to a problem with the loading machine control and data acquisition system. After reactor power was returned to 4.0 MW and all temperature and chemical conditions stabilized, the specimen was loaded to 272 MPa and the SSR test resumed. The third pause occurred at 6.7% strain and a load of 432 MPa, which was reduced to 136 MPa while the reactor was shut down for sample unloading. After reactor power was returned to 4.0 MW and all temperature and chemical conditions stabilized, specimen stress was increased to 306 MPa and the SSR test was resumed. The fourth pause was due to a reactor scram. The specimen strain was 13.7% at a stress of 533 MPa. The load was reduced to 136 MPa until the test was resumed at a stress of 408 MPa. At 22.2% strain and a 536 MPa load, a short pause occurred due to a problem with the computer/data acquisition system. The load was held constant at 536 MPa for one hour then the test resumed from this load.

Figure 4-46 shows the stress-strain plot for the SSR test. There was no foot correction. The 0.2% offset yield strength was determined with respect to an elastic modulus of 83 GPa "best-fit" to the linear portion of the stress-strain curve (see Figure 4-48). The nominal yield stress was 310 MPa (45.0 ksi) and yield strain was 0.6%. The ultimate tensile strength was 564 MPa (81.8 ksi) at 22.1% strain. The nominal strain to failure was 32% (calculated assuming uniaxial tensile stress). The specimen strain shows a straight line dependence on time (see Figure 4-47) indicative of the constant extension rate employed except for the times during test pauses (plateau regions with constant strain). In the same figure, the calculated strain rate shows considerable scatter due

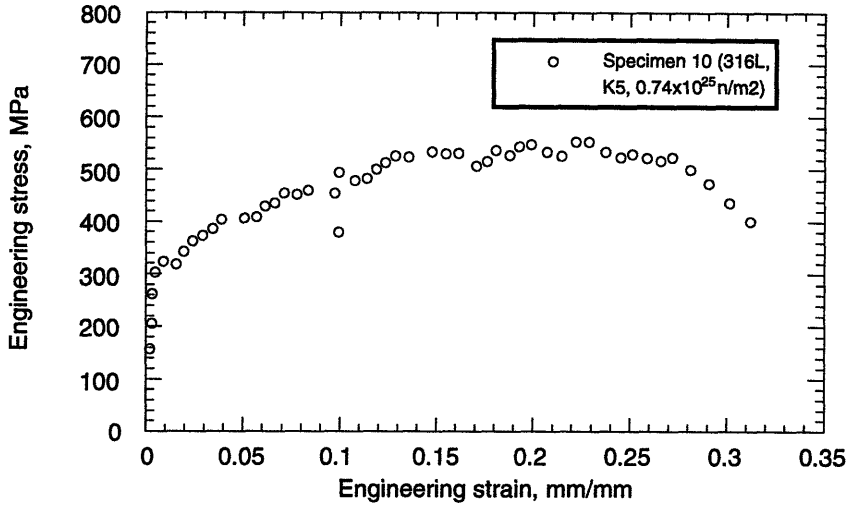

Figure 4-46. Stress-strain plot for specimen 10 (316L, K5, 0.74 x 10^{25} n/m^2).

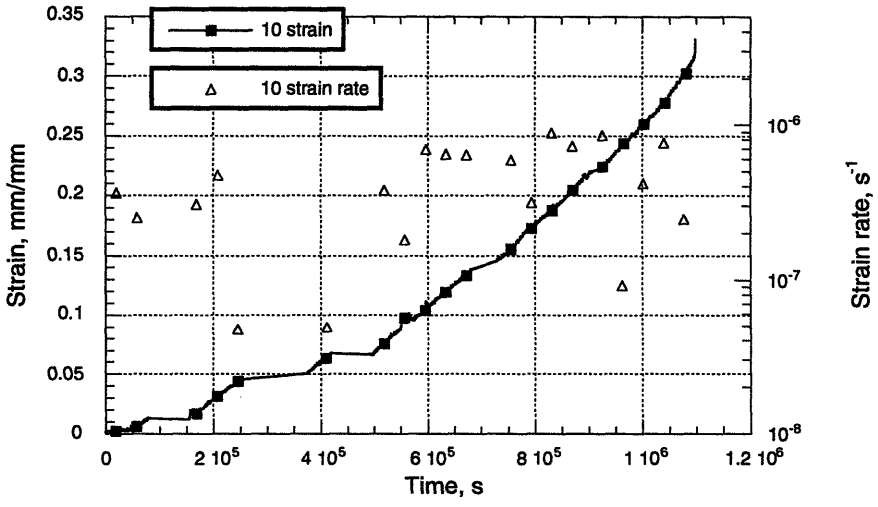

Figure 4-47. Strain-time plot for specimen 10 (316L, K5, 0.74 x 10^{25} n/m^2).

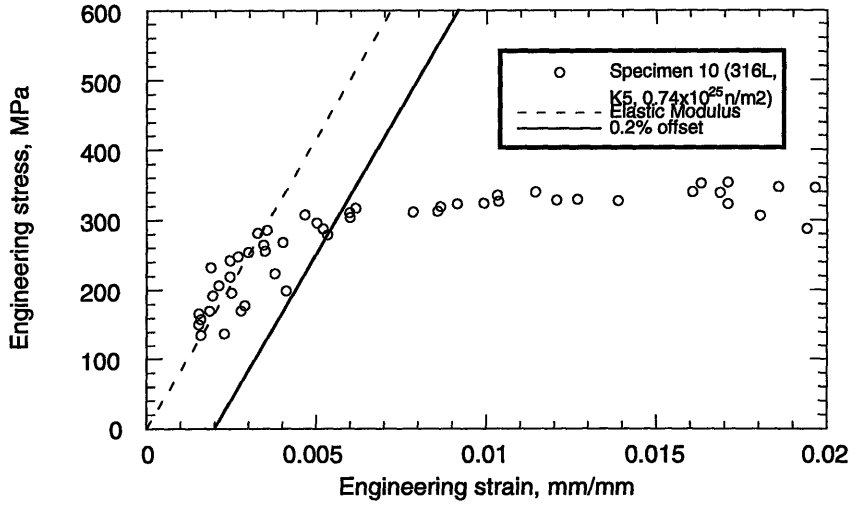

Figure 4-48. Yield stress for specimen 10 (316L, K5, 0.74 x 10^{25} n/m^2).

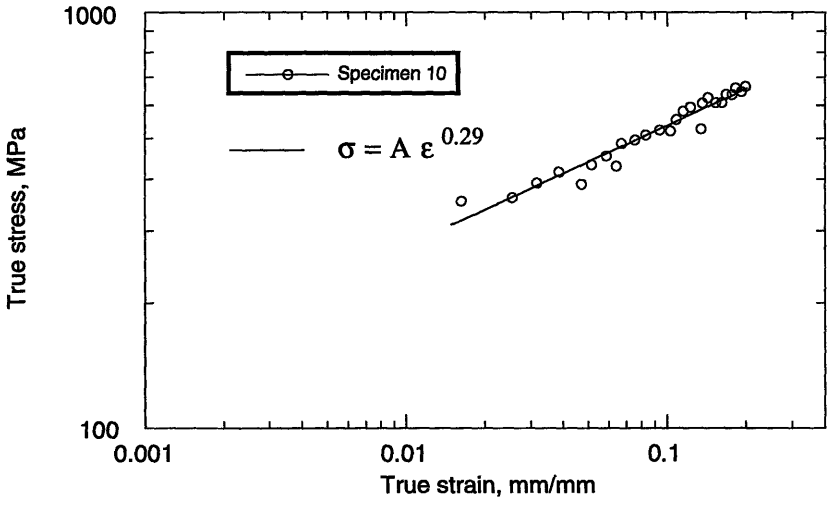

Figure 4-49. Strain-hardening exponent for specimen 10 (316L, K5, 0.74 x 10^{25} n/m^2).

to the sensitivity of rig compliance on applied stress, but indicates an average strain rate of 4.1 x 10^{-7} s^{-1}. A good correlation (R=0.981) of the strain-hardening exponent was fit by the relation $\sigma = A\varepsilon^{\alpha}$ to the true stress-strain curve in the plastic region (from 1% beyond the yield strain to strain at ultimate stress) as seen in Figure 4-49. It was determined to be 0.29 and the reduction of area was 84%.

4.3.4.2 Specimen 11

Specimen 11 was fabricated from alloy 316L (heat K5), solution annealed and tested after pre-irradiation to a fluence of 0.74 x 10^{25} n/m^2. It came from the same pre-irradiation capsule as specimen 10. Hence, it provided a second 316L alloy sample with the same physical characteristics before SSR testing and variations must be attributed to the test procedure or the stochastic nature of the cracking process.

Testing was done with the reactor operating at 4.2 MW. Testing was paused five times during the test. At a specimen strain of 3.8% and load of 407 MPa, the test was paused and load reduced to 136 MPa due to a problem with the loading machine control and data acquisition system. After reinitializing the data acquisition program, specimen stress was increased to 356 MPa and the SSR testing was resumed. At a specimen strain of 16% and load of 472 MPa, the test was paused and load reduced to 352 MPa during reactor power changes necessitated by a medical experiment. After reactor power was returned to 4.2 MW and all temperature and chemical conditions stabilized, the specimen was loaded to 466 MPa and the SSR test resumed. The third pause occurred at 25.2% strain and a load of 513 MPa due to a problem with the loading machine control and data acquisition system. After reinitializing the data acquisition program, specimen stress was increased to 508 MPa and the SSR test was resumed. The fourth pause at a specimen strain of 26.1% at a stress of 517 MPa and the fifth pause at a specimen strain of 27.9% at a stress of 501 MPa were also necessitated by reactor power changes for a medical experiment. In both cases, the load was reduced to 136 MPa. The test was resumed at 435 MPa and 471 MPa for the fourth and fifth pauses, respectively.

Figure 4-50 shows the stress-strain plot for the SSR test. The foot correction was 0.21% strain. The 0.2% offset yield strength was determined with respect to an elastic modulus of 83 GPa "best-fit" to the linear portion of the stress-strain curve (see Figure 4-52). The nominal yield stress was 335 MPa (48.6 ksi) and yield strain was 0.6%. The ultimate tensile strength was 543 MPa (78.8 ksi) at 26.3% strain. The nominal strain to failure was 31% (calculated assuming uniaxial tensile stress). The specimen strain shows a straight line dependence on time (see Figure 4-51) indicative of the constant extension rate employed except for the times during test pauses (plateau regions with constant strain). In the same figure, the calculated strain rate shows considerable scatter due to the sensitivity of rig compliance on applied stress, but indicates an

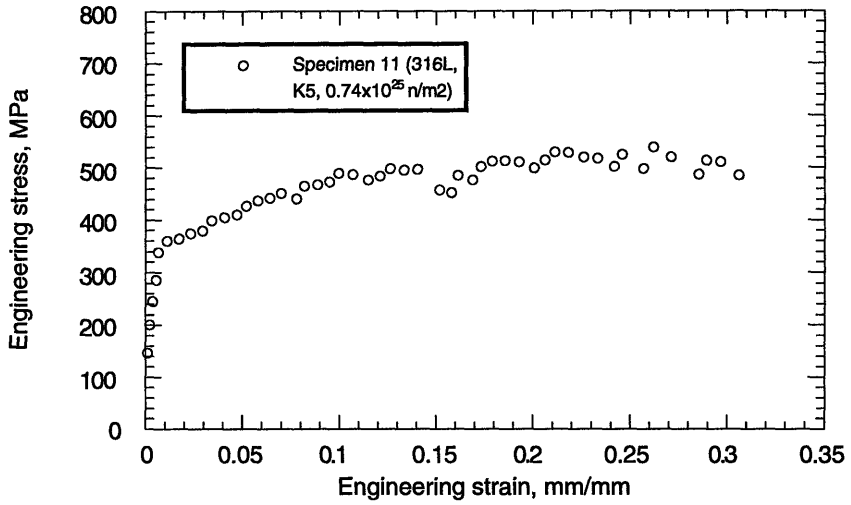

Figure 4-50. Stress-strain plot for specimen 11 (316L, K5, 0.74 x 10^{25} n/m^2).

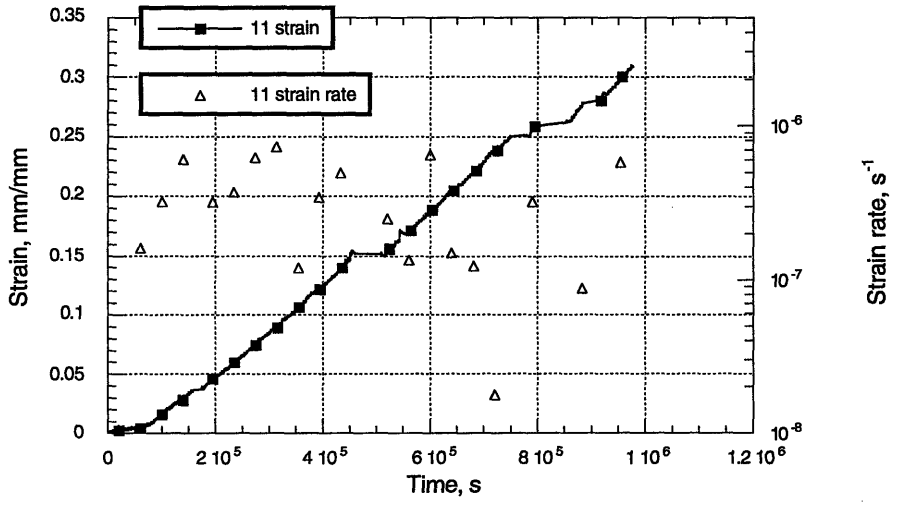

Figure 4-51. Strain-time plot for specimen 11 (316L, K5, 0.74 x 10^{25} n/m^2).

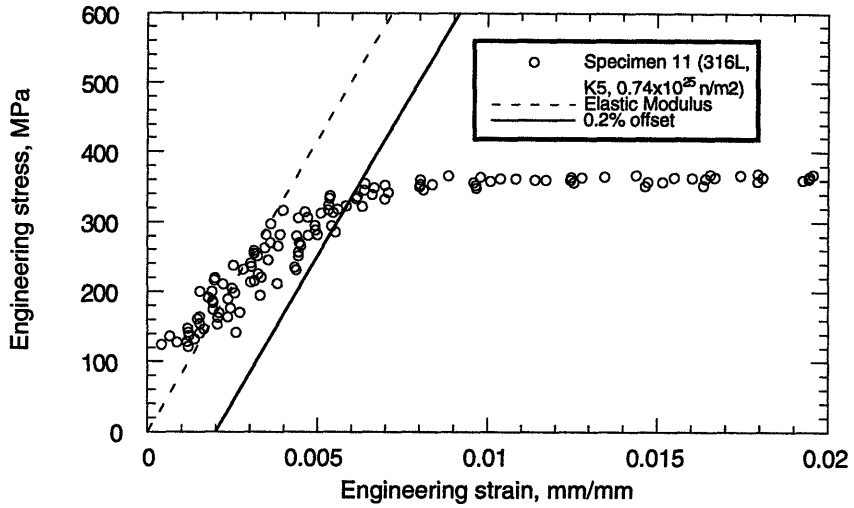

Figure 4-52. Yield stress for specimen 11 (316L, K5, 0.74 x 10^{25} n/m^2).

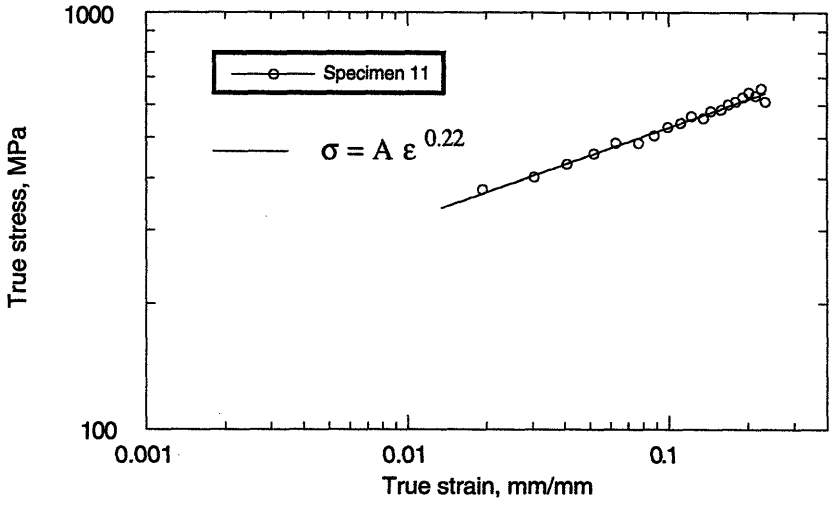

Figure 4-53. Strain-hardening exponent for specimen 11 (316L, K5, 0.74 x 10^{25} n/m^2).

average strain rate of 4.1×10^{-7} s^{-1}. A good correlation (R=0.981) of the strain-hardening exponent was fit by the relation $\sigma = A\varepsilon^{\alpha}$ to the true stress-strain curve in the plastic region (from 1% beyond the yield strain to strain at ultimate stress) as seen in Figure 4-53. It was determined to be 0.22 and the reduction of area was 84%.

4.4 SUMMARY

In this sub-section trends in the mechanical behavior observed for the in-core specimens tested by SSRT are summarized. Significant differences were seen between the irradiated CP 304 and 316L alloys and a noticeable trend was observed between the unirradiated and pre-irradiated CP 304 specimens. A discussion of these results and their implications is presented in Chapters 6 and 7 in the context of other data.

Tables 4-1 and 4-2 show the mechanical properties for the specimens tested in zero flux and in-flux in the MITR-II core. Table 4-3 shows the normalized mechanical properties for the specimens tested in-core relative to the same properties determined for unirradiated specimens tested out-of-pile in oxygenated water. Since a significant focus of this research was to compare out-of-pile SSR tests with in-flux SSR tests, the normalizing specimens were tested in BWR simulated water in out-of-pile autoclaves. This comparison differs from the standard practice for stress corrosion studies that normalize the properties to specimens tested in inert environments at the same temperature[2]. From these tables, the first thing that can be noticed for these tests is the reproducibility of the results. For similarly prepared specimens (i.e. the CP type 304 group of 80, 81, 82 and the type 316L group of 10, 11), the deviation of the measured mechanical properties is typically less than 10%. This is an important consideration when determining trends since some specimens were only tested once. The reproducibility of results, therefore leads to high confidence in the results reported here. A point of caution with respect to trends observed in the data presented in Table 4-3. The SSRT data obtained for unirradiated specimens tested out-of-pile in oxygenated water utilized a different facility than that for the in-core experiments. Experimental differences in mechanical properties determined with these two SSRT autoclave facilities have not been quantified but are expected to be less than 10%.

For the CP 304 alloy, a 20 % increase in the yield strength was observed for the unirradiated specimen tested in-flux compared to out-of-flux testing. Because there is only one data point it is with great caution that conclusions are drawn about the general behavior of metals subject to radiation flux and load. Because the author is aware of the uncertainty involved

Table 4-1. Mechanical properties for zero flux SSRT specimens.

Specimen No.	Heat Treatment	Fluence ($x10^{25}$ n/m^2)	Yield Stress (MPa)	Ultimate Stress (MPa)	Strain to Failure (%)	Hardening Exponent (n)
CP 304						
89 (a)	SA	0	253	503	53	0.42
2005	SA, CW	0	562	865	11	0.20
2012	SA, CW, f.sensitized	0	204	860	6	0.21
316L						
17 (b)	SA	0	213	440	45	0.40
347L						
32 (c)	SA	0	230	440	41	0.38
2021	SA	0	204	446	• (d)	0.34

a) Specimen 89 mechanical properties used to normalize CP 304 (heat AJ9139) data in Table 4-3.
b) Specimen 17 mechanical properties used to normalize 316L (heat K5) data in Table 4-3.
b) Specimen 32 mechanical properties can be used to normalize 347L (heat K12) data.
d) Specimen 2021 SSR test was halted at 36% strain so no strain to failure reported.

Table 4-2. Mechanical properties for in-flux SSRT specimens.

Specimen No.	Heat Treatment	Fluence ($x10^{25}$ n/m^2)	Yield Stress (MPa)	Ultimate Stress (MPa)	Strain to Failure (%)	Hardening Exponent (n)
CP 304						
98	SA	0	316	563	36	0.31
2003	SA, f.sensitized	0	182	336	16	0.26
80	SA	0.8	520	605	• (a)	0.14
81	SA	0.8	570	677	22	0.12
82	SA	0.8	536	706	21	0.13
316L						
10	SA	0.74	310	564	32	0.29
11	SA	0.74	335	543	31	0.23

a) Specimen 80 SSR test was halted at 15% so no strain to failure reported.

Table 4-3. Normalized mechanical properties for in-flux SSRT specimens.

Specimen No.	Heat Treatment	Fluence ($x10^{25}$ n/m^2)	S_y / S_y^o	S_u / S_u^o	e_f / e_f^o	n / n^o
CP 304						
98	SA	0	1.25	1.12	0.68	0.74
2003	SA, f.sensitized	0	0.72	0.668	0.30	0.62
80	SA	0.8	2.06	1.2	•	0.33
81	SA	0.8	2.25	1.35	0.42	0.29
82	SA	0.8	2.12	1.40	0.40	0.31
316L						
10	SA	0.74	1.46	1.28	0.71	0.73
11	SA	0.74	1.57	1.23	0.69	0.58

S_y / S_y^o ratio of yield strengths of in-core specimen test divided by unirradiated out-of-flux specimen.
S_u / S_u^o ratio of ultimate tensile strengths of in-core specimen test divided by unirradiated out-of-flux specimen.
e_f / e_f^o ratio of strain to failure of in-core specimen test divided by unirradiated out-of-flux specimen.
n / n^o ratio of strain hardening exponents of in--core specimen test divided by unirradiated out-of-flux specimen.

in this test and the significance of the observed trend, any discussion must proceed with the understanding that more data are necessary to verify the observed trend. Subject to these considerations, the observed effect of radiation flux on the tensile loaded specimens is discussed in Chapter 6 along with some physical arguments explaining the behavior. The yield stress increase for pre-irradiated CP type 304 was 200%. This magnitude increase in yield stress is typical of CP type 304 at this dose[3].

The mechanical properties for #2003, furnace sensitized at 650°C for 10 hours, are much degraded, although part of the reduction in yield and ultimate stresses may be attributed to the misalignment of the tensile specimen[9]. Misalignment can cause non-uniform stresses applied across the cross sectional area, thereby producing local stresses which exceed the average stress. While recognizing this technical concern, there is an expected degradation in mechanical strength and ductility due to the thermal sensitization and resulting intergranular attack of the stressed specimen. Because this specimen showed almost complete intergranular failure, it represents another reference point in comparison to the 0.8×10^{25} n/m^2 pre-irradiated CP type 304 specimens.

The hardening effect of radiation does not continue indefinitely, but reduces the materials ability to strain harden after plastic deformation begins. For all CP type 304 specimens tested there is a decrease in strain hardening, as depicted by the relative strain hardening exponent values. There is still some available hardening beyond yield for the high-dose CP type 304, but it is reduced to 30% of the value for unirradiated material. The trend is similar to that seen in out-of-pile tests[10] where the yield strength saturates for fluences $\geq 1.5 \times 10^{25}$ n/m^2 and no further hardening occurs.

It is seen that although hardening in the unirradiated CP type 304 (#98) is mild, there is still a 30% reduction in ductility. There is a considerably greater loss in ductility for the pre-irradiated CP type 304 specimens (#80, 81, 82) which was around 60% and almost equal to that observed for the furnace sensitized specimen (70% loss of ductility).

For the pre-irradiated 316L alloy, a 50% increase in yield strength was observed relative to the unirradiated out-of-flux test specimen. This is considerably lower than the factor of two increase seen for the pre-irradiated CP type 304 but higher than that observed for the unirradiated CP type 304. The SSR data reported in the literature for pre-irradiated 316L alloy is sparse for the fluence levels ($\sim 0.8 \times 10^{25}$ n/m^2) studied in this test. But Kodama et al.[11] have reported a decrease in fracture strain less than 1% for a fluence level of 0.53×10^{25} n/m^2. This decrease in total elongation is smaller than the 30% observed for the in-core tests, but the trend is comparable. Moreover, the differences between the mechanical properties of CP type 304 and type 316L observed for these in-core tests were qualitatively the same as observed by Kodama et al.[11] Hence from these SSR tests and for these fluences ($\sim 0.8 \times 10^{25}$ n/m^2), alloy 316L shows

improved mechanical properties performance compared to the standard commercial purity alloy 304 that is more commonly found in reactor vessel structural components.

The in-flux mechanical properties measured for the austenitic stainless steel alloys CP 304 (heat AJ9139), 316L (heat K5) pre-irradiated to ~0.8×10^{25} n/m^2 were presented in this section. Out-of-pile zero flux data for the same alloys and heats were recorded and comparative properties discussed. These tests were performed at BWR simulated conditions with high oxygen and were used to identify differences and similarities between instantaneous flux effects and the accumulated radiation damage. The changes in mechanical behavior of CP type 304 are greater than the changes of type 316L for similar doses (0.8×10^{25} n/m^2 and 0.74×10^{25} n/m^2, respectively). This increased resistance to radiation damage may be true for greater fluences or it may only indicate different radiation damage "thresholds" for the two alloys. SSR tests on specimens irradiated to higher fluences are necessary in order to further investigate these long term property changes.

4.5 REFERENCES

1. M. Henthorne, PhD Thesis, Dept. Met. Eng. Mat., University of Newcastle upon Tyne, England (1965).

2. R. N. Parkins, "Development of Strain-Rate Testing and Its Implications," *Stress Corrosion Cracking-The Slow Strain-Rate Technique, ASTM STP 665*, G. M. Ugiansky and J. H. Payer, Eds., American Society for Testing and Materials, Philadelphia (1979) p. 5.

3. S. W. Bruemmer, J. I. Cole, J. L. Brimhall, R. D. Carter and G. S. Was, "Radiation Hardening Effects on Localized Deformation and Stress Corrosion Cracking of Stainless Steels," *Proc. 6th Int. Symp. Env. Deg. Mat. Nucl. Power Syst.-Water Reactors*, TMS, San Diego, CA (1993) p. 537.

4. K. Fukuya, S. Shima, K. Nakata, S. Kasahara, A. J. Jacobs. G. P. Wozadlo, S. Suzuki and M. Kitamura, "Mechanical Properties and IASCC Susceptibility in Irradiated Stainless Steels," *Proc. 6th Int. Symp. Env. Deg. Mat. Nucl. Power Syst.-Water Reactors*, TMS, San Diego, CA (1993) p. 565.

5. G. E. Dieter, *Mechanical Metallurgy*, 2nd Edition, McGraw-Hill, Inc., New York (1976).

6. F. A. McClintock and A.S. Argon, *Mechanical Behavior of Materials*, Addison-Wesley Publishing Company, Inc., Reading, Massachusetts (1966).

7. J. R. O'Donnell, "Design, Construction, and Commissioning of an In-Core Materials Testing Facility for Slow Strain Rate Testing," PhD Thesis, Department of Nuclear Engineering, Massachusetts Institute of Technology, Cambridge, MA (September 1994).

8. P. Lidar, "D. C. Potential Drop System Development," MIT Department of Nuclear Engineering, Cambridge, MA (1991).

9. *Tensile Testing*, ASM 440, P. Han, Ed., ASM International, Materials Park, OH (1992).

10. H. M. Chung, W. E. Ruther, J. E. Sanecki, A. G. Hins and T. F. Kassner, "Stress Corrosion Cracking Susceptibility of Irradiated Type 304 Stainless Steels," *Effects of Radiation on Materials: 16th International Symposium, ASTM STP 1175*, A. S. Kumar, D. S. Gelles, R. K. Nanstad, and E. A. Little, Eds., American Society for Testing and Materials, Philadelphia (1993) p. 851.

11. M. Kodama, K. Fukuya and H. Kayano, "Influence of Impurities and Alloying Elements on IASCC in Neutron Irradiated Austenitic Stainless Steels," *Effects of Radiation on Materials: 16th International Symposium, ASTM STP 1175*, A. S. Kumar, D. S. Gelles, R. K. Nanstad, and E. A. Little, Eds., American Society for Testing and Materials, Philadelphia (1993) p. 889.

CHAPTER 5

SCANNING ELECTRON MICROSCOPY (SEM) ANALYSIS OF SSRT SPECIMENS

No man ever looks at the world with pristine eyes. He sees it edited by a definite set of customs and institutions and ways of thinking.

Ruth Fulton Benedict
(1887-1948)

5.1 INTRODUCTION

The study and analysis of fracture surfaces has developed into an integral part of failure analysis. Symposia[1-4] have been solely dedicated to the field of fractography. An encyclopedia of failure modes and accompanying micrographs of the failed surfaces has been compiled and published in the Metals Handbook[5,6]. Investigation of irradiation assisted stress corrosion cracking requires application of this specialization in order to describe the failure mode of fractured SSRT specimens. Fracture maps which identify the various topologies (e.g. ductile void coalescence, brittle cleavage, intergranular and transgranular) are commonly used and the areal fraction identified as intergranular (IG) is reported[7-9].

For this investigation, a Topcon ABT-150T Two stage Scanning Electron Microscope (SEM) was employed for analyzing the fractured specimens. Photographs made on a positive/negative instant sheet film were later electronically scanned for use in quantifying the fraction of intergranular cracking. This areal fraction was determined by weighing the various areas cut from a single picture. In this chapter the results of the SEM analysis are presented.

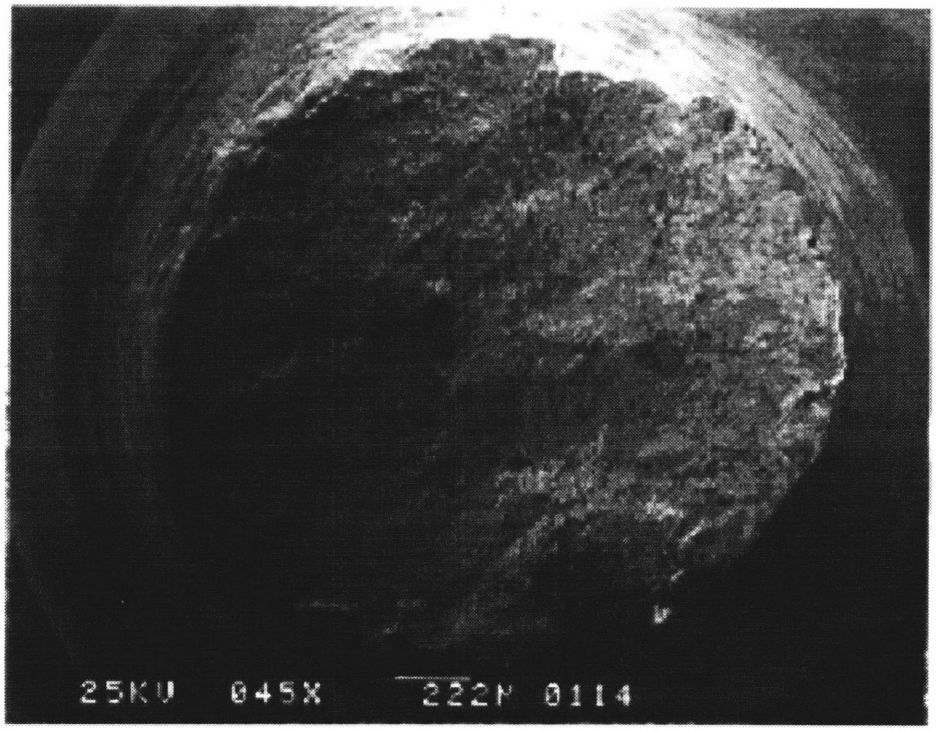

Figure 5-1. Fracture surface of specimen 2005 (CP 304,AJ9139,30%CW,0 n/m^2).

5.2 ZERO FLUX SHAKEDOWN TESTS

SEM analysis was conducted on the out-of-core shakedown specimens, but not the unirradiated specimens tested as part of the DCPD strain measurement study. Since the purpose of testing these specimens was primarily to evaluate the SSR Test Rig, the SEM analysis was given cursory attention. Hence, the fractographs presented are few and the discussion brief for these specimens.

5.2.1 Specimen 2005

Specimen 2005 was made from commercial purity alloy 304 (heat AJ9139) stainless steel and tested in the unirradiated, solution annealed, and 30% cold worked condition. Figure 5-1 shows the fracture surface of #2005 which exhibited 30% reduction of area (RA). There was no intergranular failure observed for this specimen.

5.2.2 Specimen 2012

Specimen 2012 was made from commercial purity alloy 304 (heat AJ9139) stainless steel and tested in the unirradiated, furnace sensitized, and 30% cold worked condition. Its fracture

surface is displayed in Figure 5-2. This specimen had a lower RA, determined to be 10%, than #2005 . This further loss of ductility beyond the imparted cold work was attributed to the furnace sensitization heat treatment. There are regions identified as intergranular and a magnified view of one region is shown in Figure 5-3.

5.2.3 Specimen 2021

Specimen 2021 was made from alloy 347L (heat K12) and tested in the unirradiated, solution annealed condition. Because the test was halted prematurely and other operational time constraints, no SEM analysis was conducted on this specimen. During the SSRT the strain rate was increased 100X after 9 hours of testing (at ~0.01% strain) to expedite failure. However, failure did not occur before the test was terminated at a strain of 36%. Therefore in all likelihood, the fracture mode would have been purely ductile and the fracture surface would have shown cup and cone features indicative of microvoid coalescence.

5.3 IN-FLUX TEST SPECIMENS

Results of the SEM analysis are reported for all seven specimens tested in-core. Since these specimens were radioactive (due to pre-irradiation and/or irradiation during the tensile test), appropriate measures for protecting investigators during the handling and analysis were instituted for the SEM work (see O'Donnell[10] for details). The analysis of these failed specimens, pulled to failure while subject to a radiation flux comparable to that in a power reactor core, represents a significantly unique work that can be used to qualify and quantify the behavior of similar materials employed in power reactors today.

5.3.1 Unirradiated CP 304 (heat AJ9139)

5.3.1.1 Specimen 2003

Specimen 2003 was fabricated from commercial purity alloy 304 (heat AJ9139) and tested in the unirradiated, furnace sensitized condition. As reported in section 4.3.2.1, the furnace treatment at 650°C for 10 hours induced an adequately sensitized microstructure verified by EPR measurement. Figure 5-4 is the fracture surface of #2003. The extent of intergranular cracking is evident from the fractograph and was calculated to be 97% of the total fracture area. A closer look at the lower right region is shown in Figure 5-5 and shows the smooth intergranular facets with a small fraction with ribs identified as granulated in the paper by Solomon[9]. For reporting purposes, the %IG is the sum of the areas with purely intergranular and granulated facets.

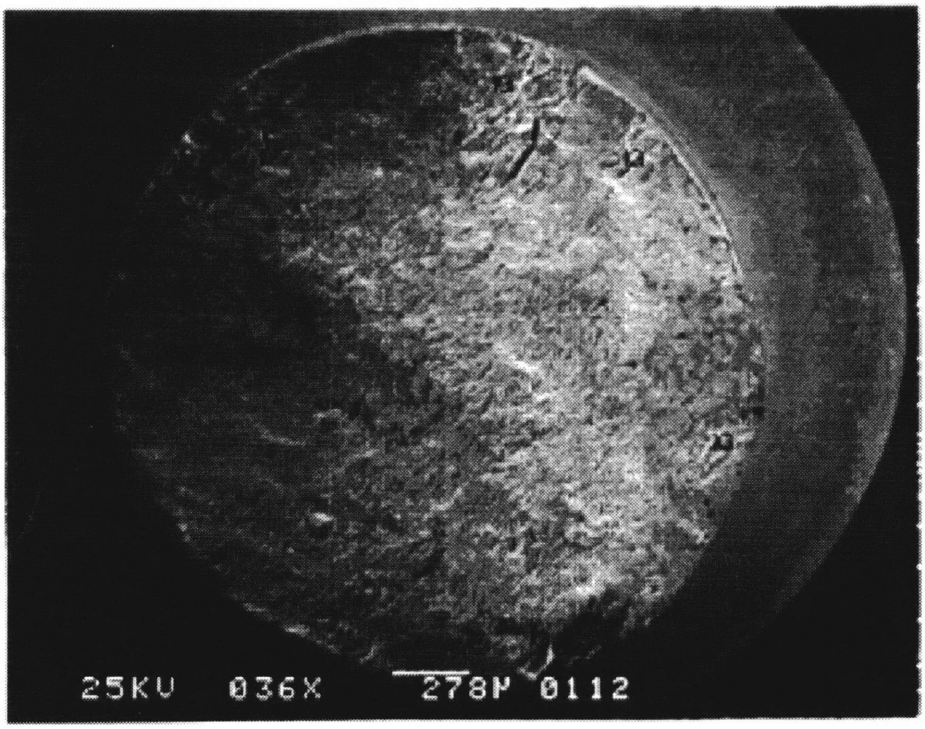

Figure 5-2. Fracture surface of specimen 2012 (CP 304,AJ9139,30%CW,furnace sensitized at 650°C/10hr,0 n/m^2).

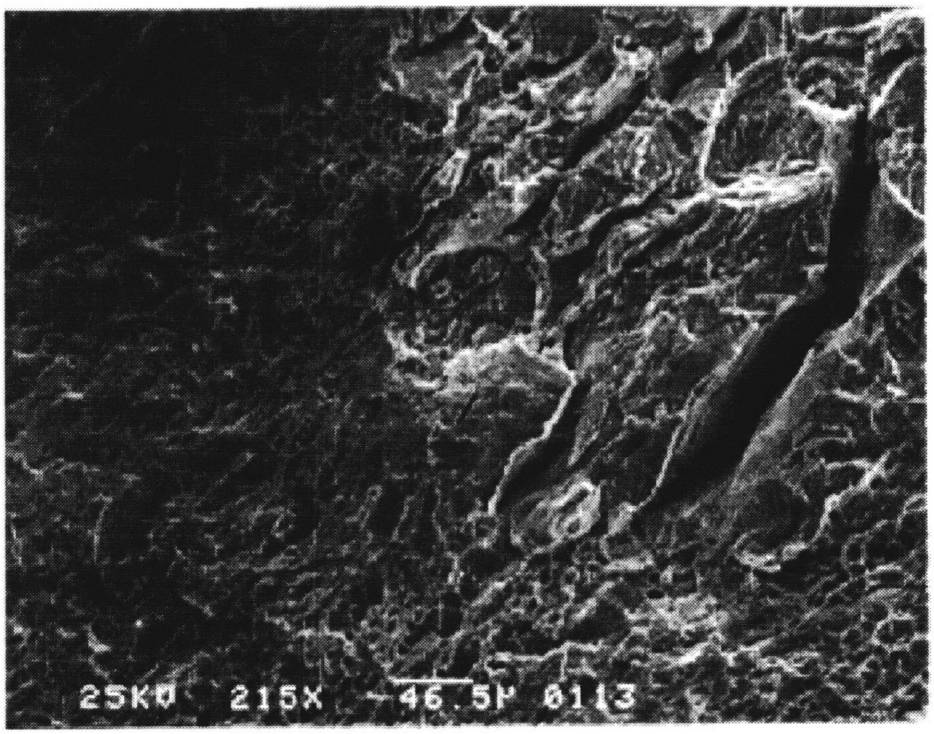

Figure 5-3. Intergranular and ductile fracture morphology on surface of specimen 2012 (CP 304,AJ9139,30%CW,furnace sensitized at 650°C/10hr,0 n/m^2).

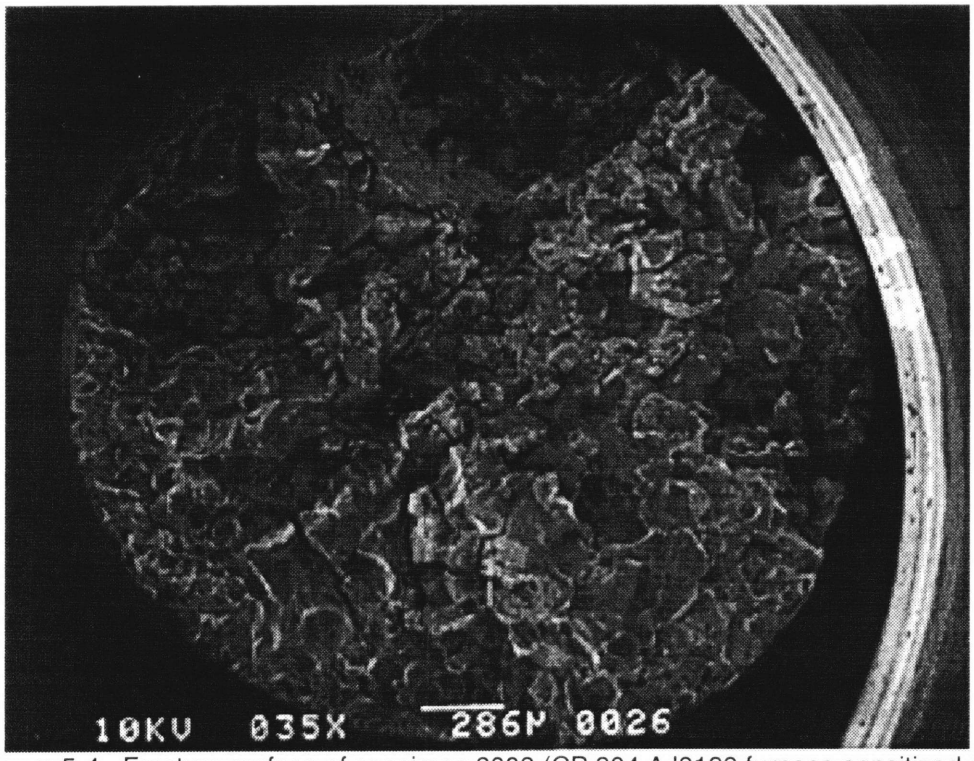

Figure 5-4. Fracture surface of specimen 2003 (CP 304,AJ9139,furnace sensitized at 650°C/10hr,0 n/m^2).

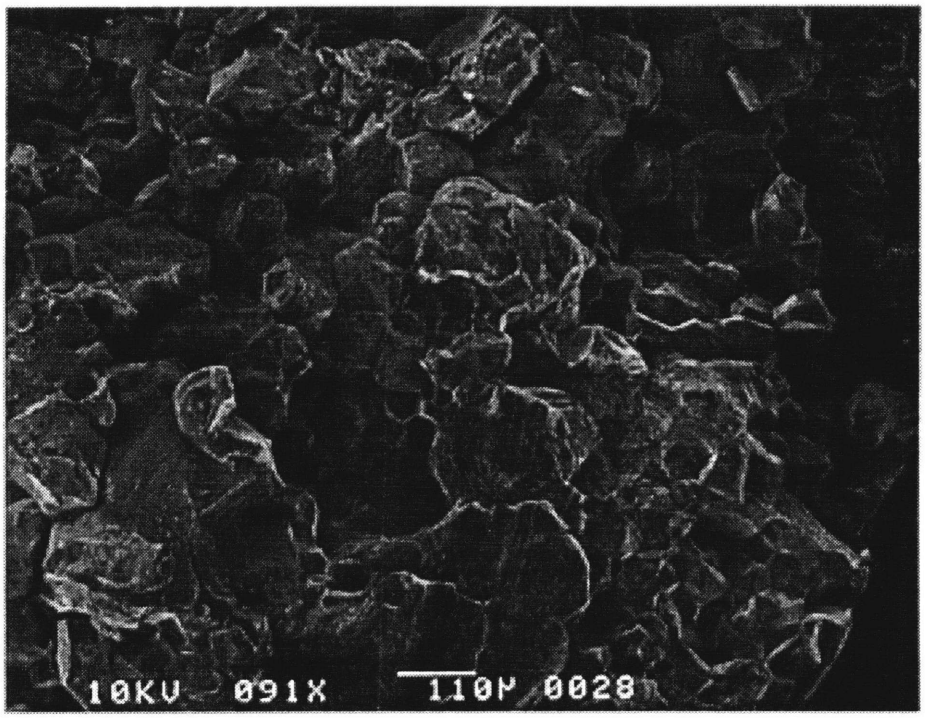

Figure 5-5. Lower right of Figure 5-4 depicting intergranular and granulated facets on fracture surface of specimen 2003 (CP 304,AJ9139,furnace sensitized at 650°C/10hr,0 n/m^2).

Although this specimen was bent during testing (see Figure 5-6), its susceptibility to SCC was not considered affected by this mechanical complication. The 97% IG on the fracture surface and <5% RA are indicative of a very high susceptibility to SCC. This supports the conclusion that the in-core environment is sufficiently aggressive to promote SCC in a sensitized material and therefore provides a proper environment to evaluate material sensitization to IASCC for the pre-irradiated specimens tested in this investigation. The high susceptibility of #2003 to SCC is also seen by examination of the gage section. Figure 5-7 shows extensive cracking through the gage section independent of the crack that caused ultimate failure. A higher magnification view (Figure 5-8) of the large crack in Figure 5-7, shows that the crack morphology on the surface is intergranular which is expected for a material with a high degree of microstructure sensitization. Figure 5-9 shows a crack in its beginning stages. The crack opening measures ~ 60 μm wide and 1-3 μm high. This high aspect ratio suggests that crack propagation proceeds readily after initiation. These observations for the unirradiated, furnace sensitized specimen significantly differ from those for the pre-irradiated specimens.

5.3.1.2 Specimen 98

Specimen 98 was fabricated from commercial purity alloy 304 (heat AJ9139) and tested in the unirradiated, solution annealed condition. Figure 5-10 depicts the fracture surface and the large reduction of area. The RA is 73% and no IG was observed on the fracture surface. A close-up of the fracture surface showing evidence of the ductile failure mechanism of microvoid coalescence is shown in Figure 5-11. The gage profile micrograph of #98 (see Figure 5-12) exhibits a homogeneous array of dimples on the fracture surface, typical of ductile failures, and a large amount of necking that took place before fracture. Examination of the gage section near the fracture surface (see Figure 5-13) displays wavy slip spread throughout the section and possibly grouping of slip lines by grains (see Figure 5-14). There is one region in Figure 5-14 that exhibits a lower density of slip lines, but not to such an extent as in the pre-irradiated CP 304 specimens (see Figures 5-29, 5-37). An interesting point of the SEM analysis of #98 is insight into the in-flux deformation mechanism for LWR stainless steels.

Dislocation channeling is the main deformation mode of metals observed in post-irradiation tensile tests conducted at temperatures below one half the melting point[11]. This type of deformation has also been traditionally reported for stainless steels, but at temperatures and fluence slightly higher than LWR structures[12]. Recent work by Gorynin et al.[13] and Bruemmer et al.[14] have documented dislocation channels in stainless steels at LWR conditions (~300°C and ~1 dpa) and dislocation channeling has been suggested as a significant deformation mechanism influencing IASCC behavior[14]. Regarding the MIT results, no *definite* conclusions can be

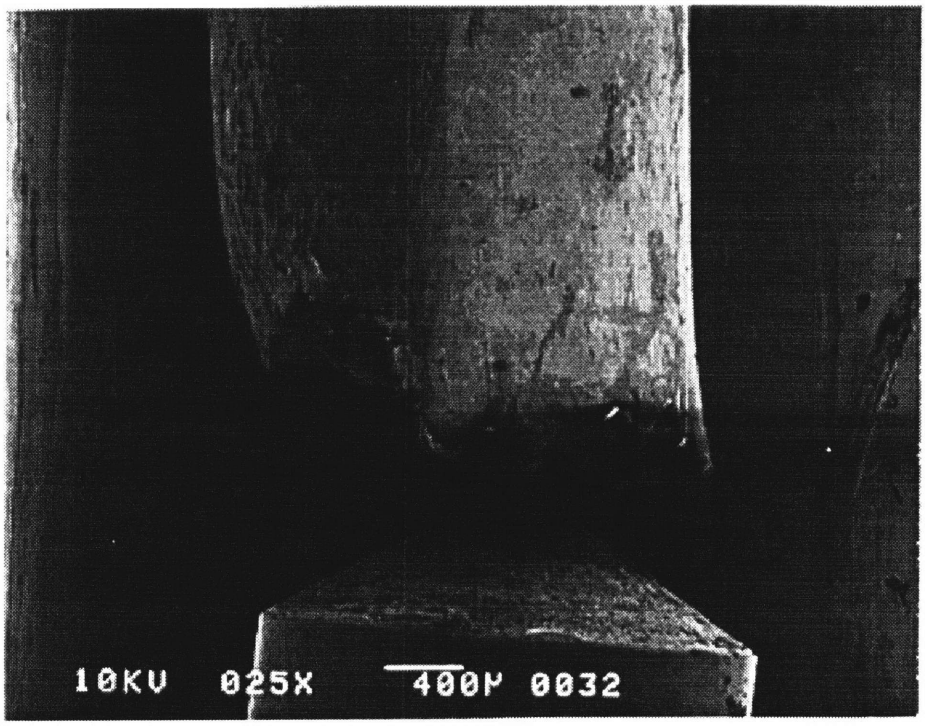

Figure 5-6. Side of specimen 2003 (CP 304,AJ9139,furnace sensitized at 650°C/10hr,0 n/m^2).

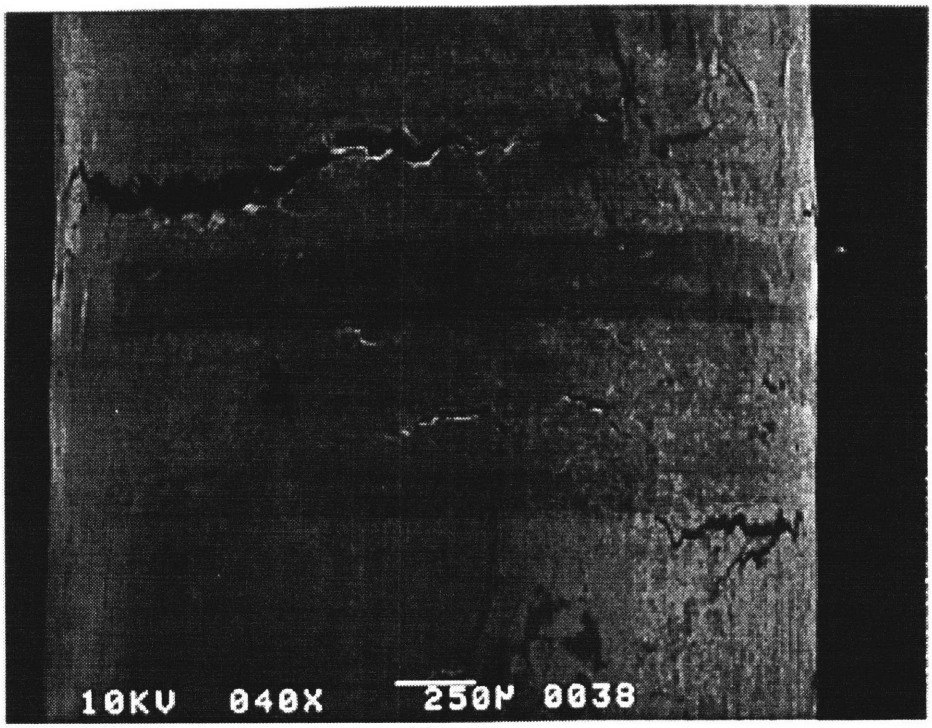

Figure 5-7. Side of specimen 2003 (CP 304,AJ9139,furnace sensitized at 650°C/10hr,0 n/m^2) away from the fracture surface depicting extensive cracking.

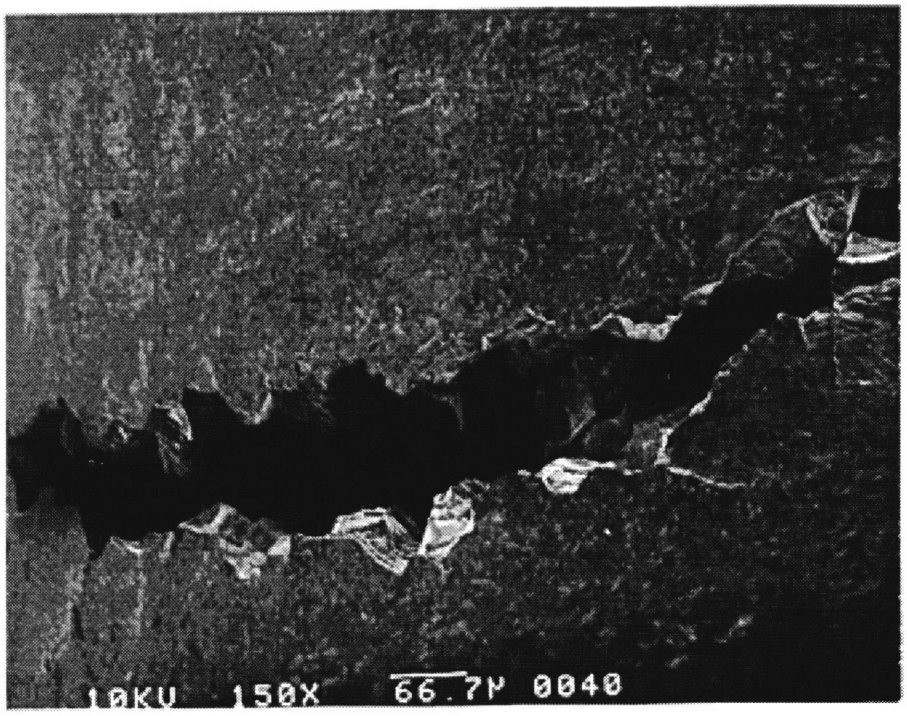

Figure 5-8. Higher magnification of crack located in upper left of Figure 5-7.

Figure 5-9. Side of specimen 2003 (304CP,AJ9139,furnace sensitized at 650°C/10hr,0 n/m^2) away from the fracture surface depicting cracks with high aspect ratio.

Figure 5-10. Fracture surface of specimen 98 (CP 304,AJ9139,0 n/m^2).

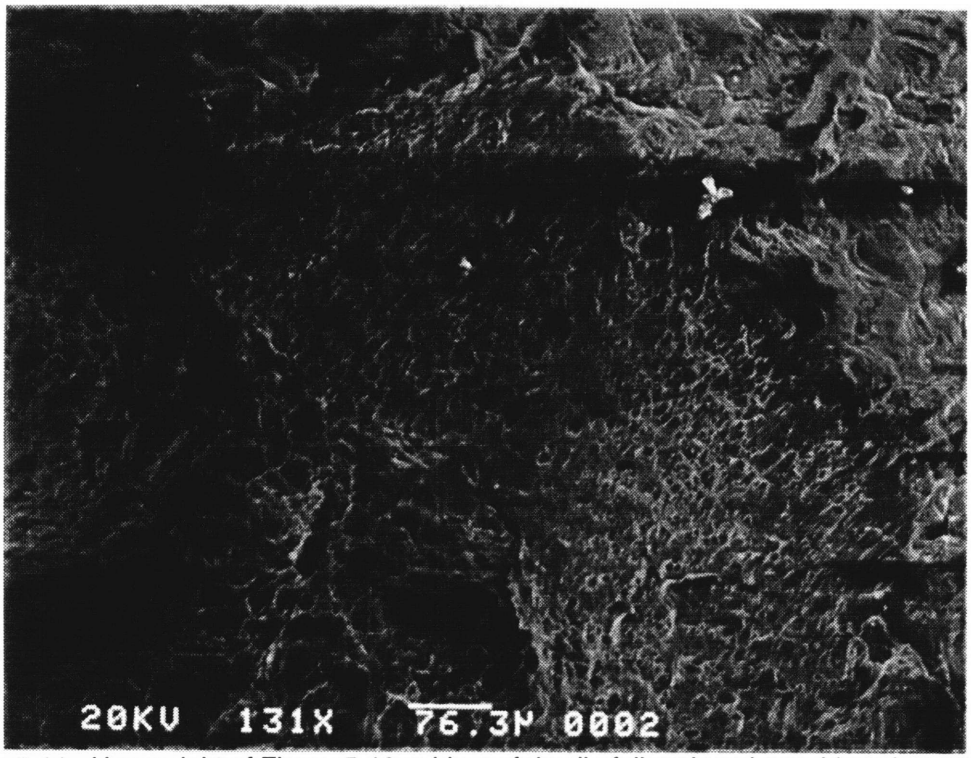

Figure 5-11. Upper right of Figure 5-10 evident of ductile failure by microvoid coalescence on fracture surface of specimen 98 (CP 304,AJ9139,0 n/m^2).

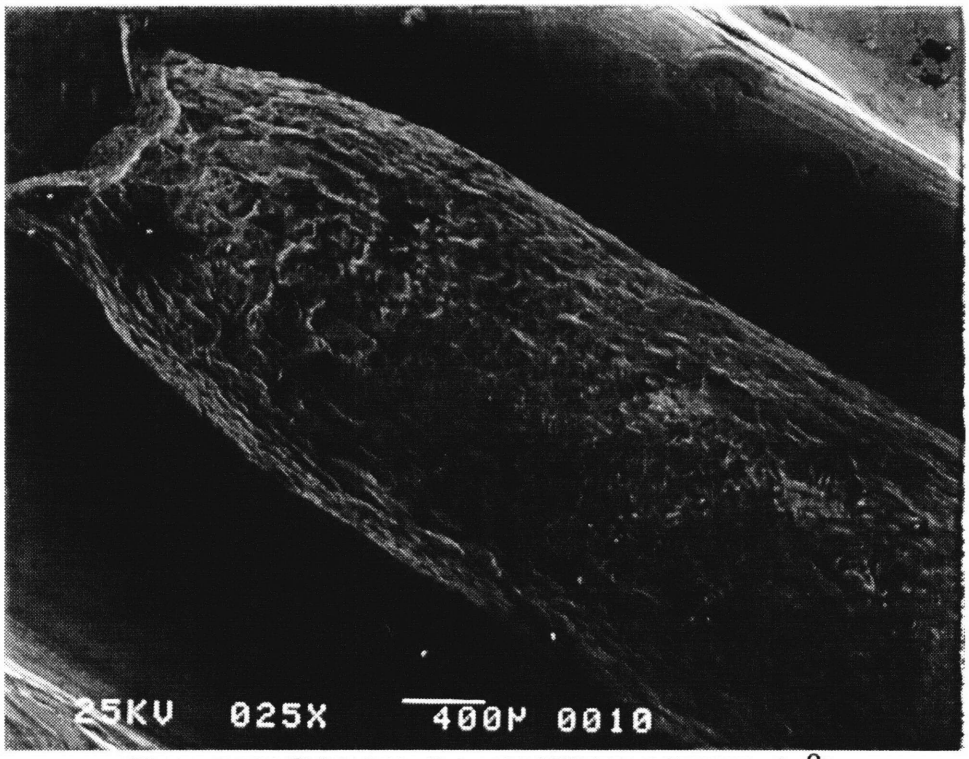

Figure 5-12. Side of specimen 98 (CP 304,AJ9139,0 n/m^2).

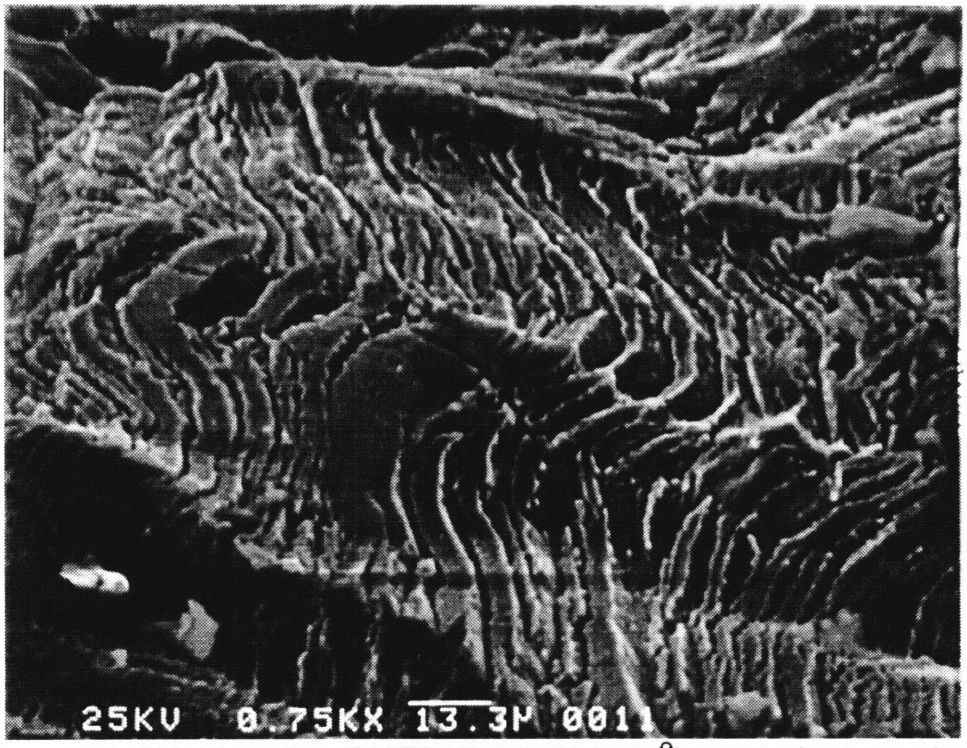

Figure 5-13. Side of specimen 98 (CP 304,AJ9139,0 n/m^2) near the fracture surface.

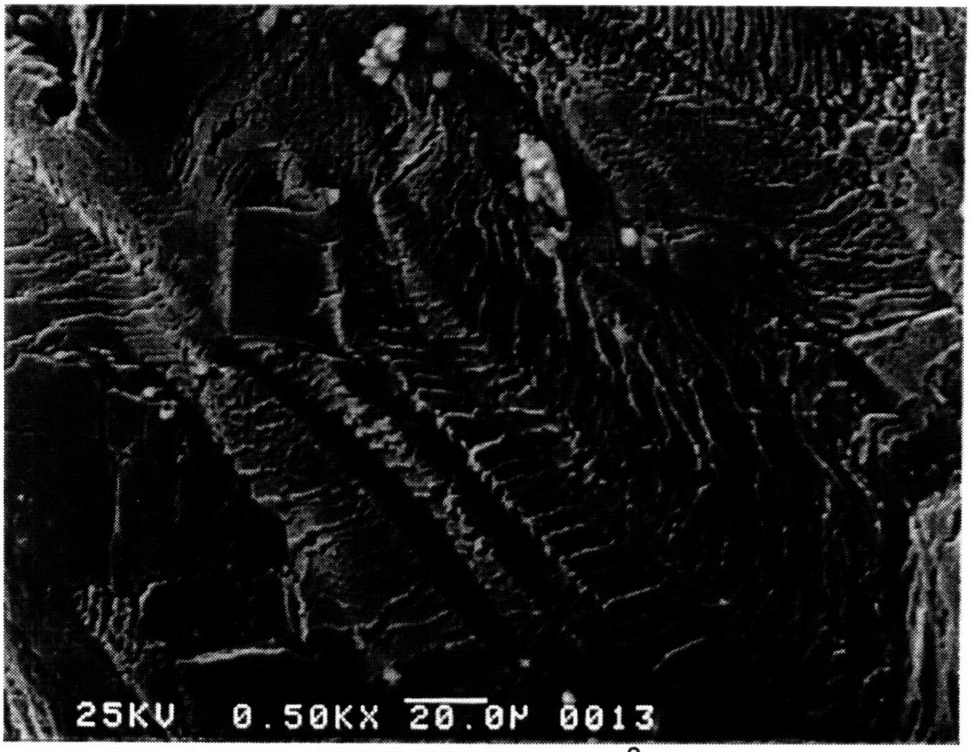

Figure 5-14. Side of specimen 98 (CP 304,AJ9139,0 n/m^2) away from the fracture surface depicting slip lines in regions. One region with lower density.

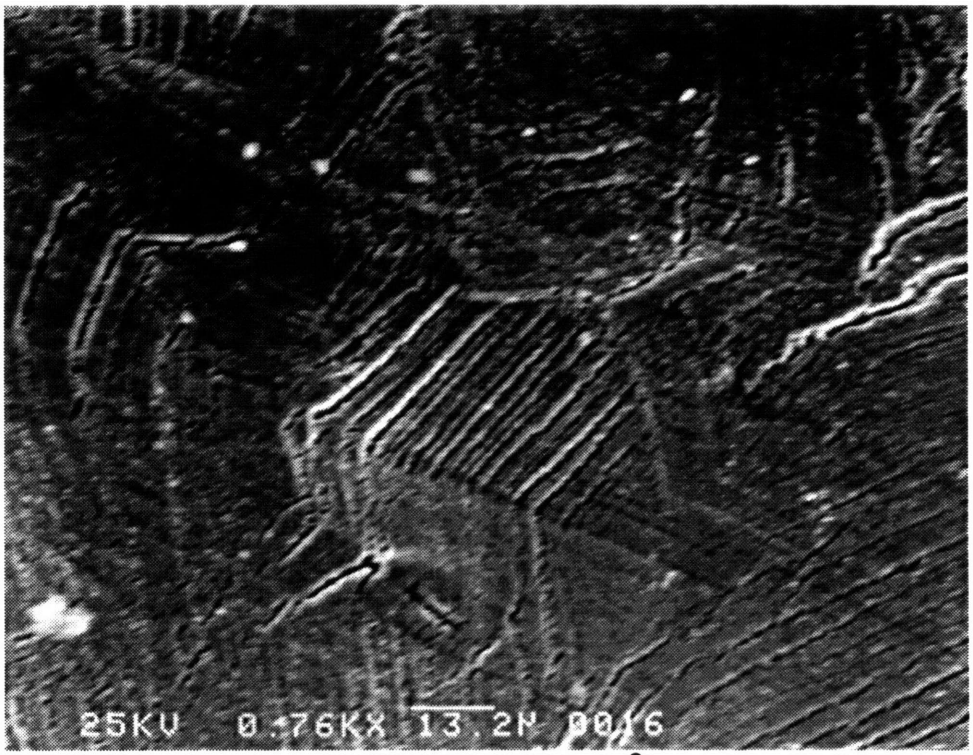

Figure 5-15. Side of specimen 98 (CP 304,AJ9139,0 n/m^2) away from the fracture surface depicting slip lines oriented in preferred directions in neighboring regions.

determined since TEM was not performed, but comparison of #98 (unirradiated 304 alloy) slip formations with the slip formations on an unirradiated and pre-irradiated 304 alloy that exhibited dislocation channeling can provide some *preliminary* indications. Figure 5-15 is a micrograph of the gage section away from the fracture surface. The slip lines are arranged in patterns suggestive of grains and in preferred directions oriented to the stress axis. Furthermore the apparent depth of the slip steps indicates that a large amount of slip has occurred on certain planes. Compared with in-laboratory SSRT results reported by Cookson et al.[15], the surface image of the unirradiated 304 alloy tested in-flux at MIT is more similar to the SEM micrograph of a pre-irradiated (1 dpa by protons at 400°C) 304 alloy than an unirradiated specimen. Figure 5-16, from Cookson et al.[15], displays the gage section profiles of an unirradiated speciment tested in argon, a 1 dpa pre-irradiated specimen tested in argon and a 1 dpa pre-irradiated specimen tested in high temperature water . TEM analyses performed on these same materials by Bruemmer et al.[14] clearly showed evidences of dislocation channeling in the pre-irradiated specimen (see Figure 5-17). Hence, based on a comparison of slip formations at the surface of unirradiated and pre-irradiated strained specimens dislocation channeling occurs in unirradiated slow straining stainless steels under a neutron flux. Although the SEM evidence is far from conclusive, the loss of ductility and work hardenability observed for the unirradiated 304 alloy tested in flux (cf. section 4.3.2.2) is consistent with an inhomogeneous deformation mechanism, i.e. dislocation channeling, that leads to premature plastic instability.

5.3.2 Pre-irradiated CP 304 (heat AJ9139) Stainless Steel

5.3.2.1 Specimen 80

Specimen 80 was fabricated from commercial purity alloy 304 (heat AJ9139), solution annealed and tested after pre-irradiation to a fluence of 0.8×10^{25} n/m^2. Although the SSRT was halted at a specimen strain of 15% and the specimen subsequently pulled to failure at a fast strain rate at room temperature, the SEM analysis provided some important insights into IASCC susceptibility and crack propagation. Close examination of the fracture surface shown in Figure 5-18 revealed small areas of transgranular (TG) cracking (~3% TG). The greater percentage of the fracture was ductile as seen by the remnants of void coalescence (Figure 5-19). An expanded view of the bottom edge that exhibited transgranular cracking is shown in Figure 5-20. Because the SSR test was halted at 15% strain and then loaded to failure at a *rapid* strain rate, it is logical to assume that any stress corrosion cracking observed on the fracture surface occurred prior to 15% strain. This being the case then the SEM analysis of #80 effectively evaluates an intermediate stage of crack development. The amount of SCC for #80 can be compared with %IG

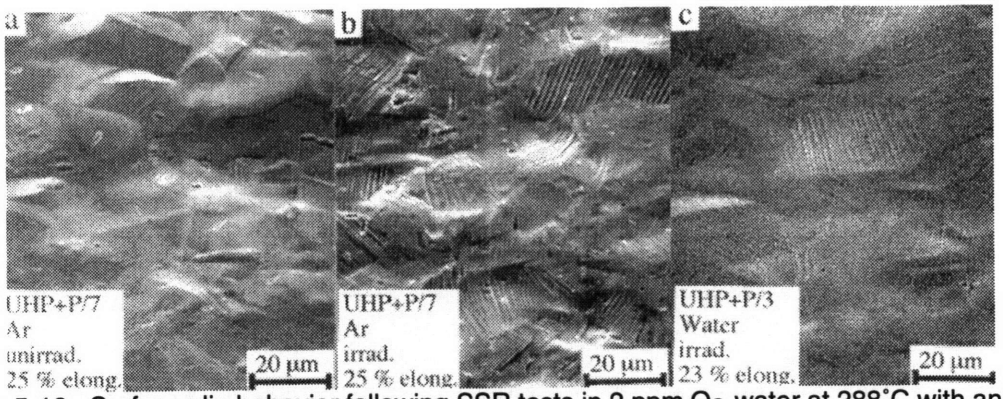

Figure 5-16. Surface slip behavior following SSR tests in 2 ppm O_2 water at 288°C with an initial strain rate of 3.6×10^{-7} s^{-1}; a) unirradiated 304 in argon, e_f=25%; b) irradiated 304 in argon, e_f=25%; c) irradiated 304 in water, e_f=23% (Cookson et al.[15]).

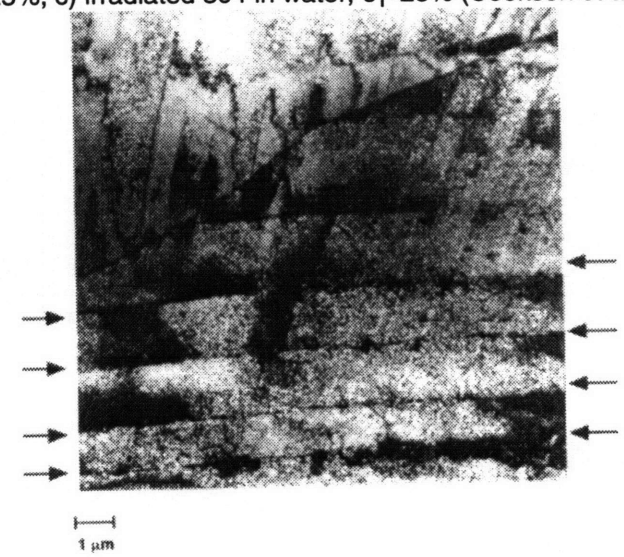

(a)

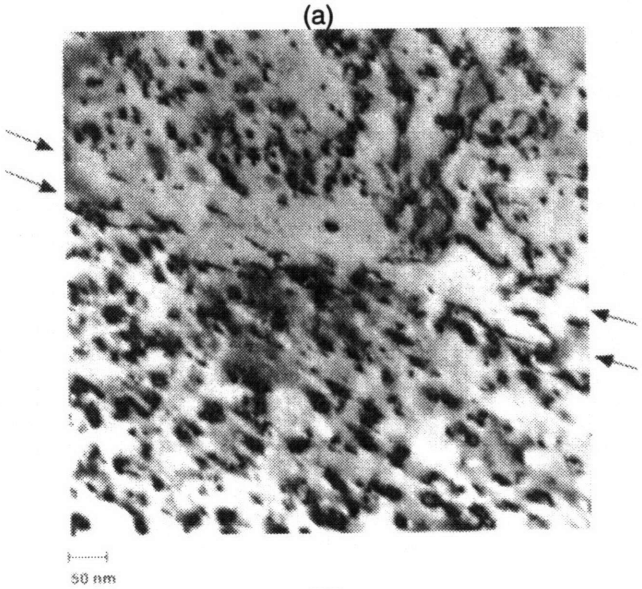

(b)

Figure 5-17. a) TEM microstructure and b) dislocation channel of 304L after 9% strain at 288°C (Bruemmer et al.[14]).

Figure 5-18. Fracture surface of specimen 80 (CP 304,AJ9139,0.8 x 10^{25} n/m^2).

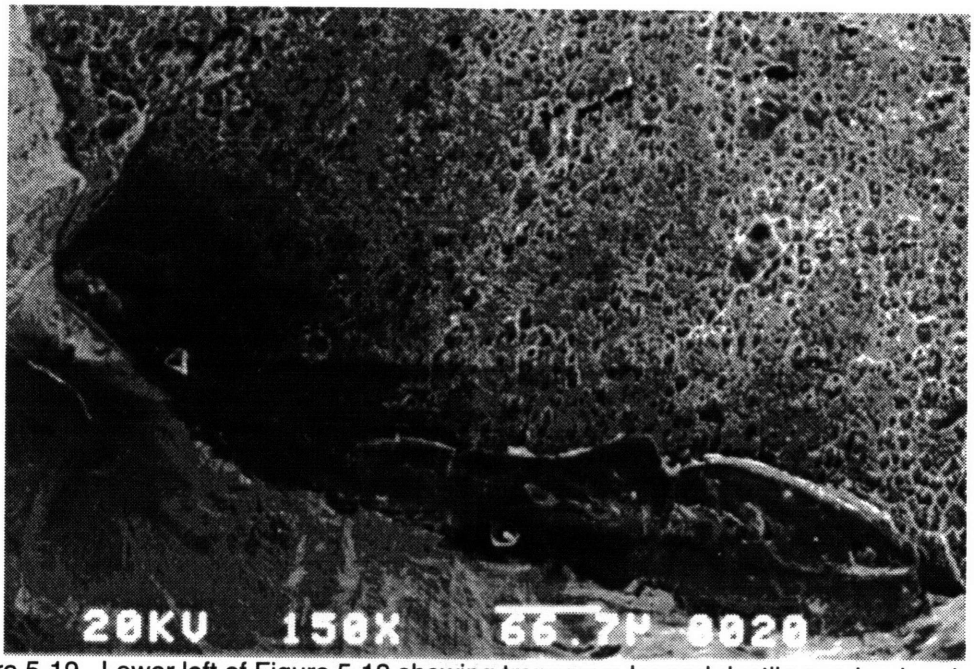

Figure 5-19. Lower left of Figure 5-18 showing transgranular and ductile overload region on fracture surface of specimen 80 (CP 304,AJ9139,0.8 x 10^{25} n/m^2).

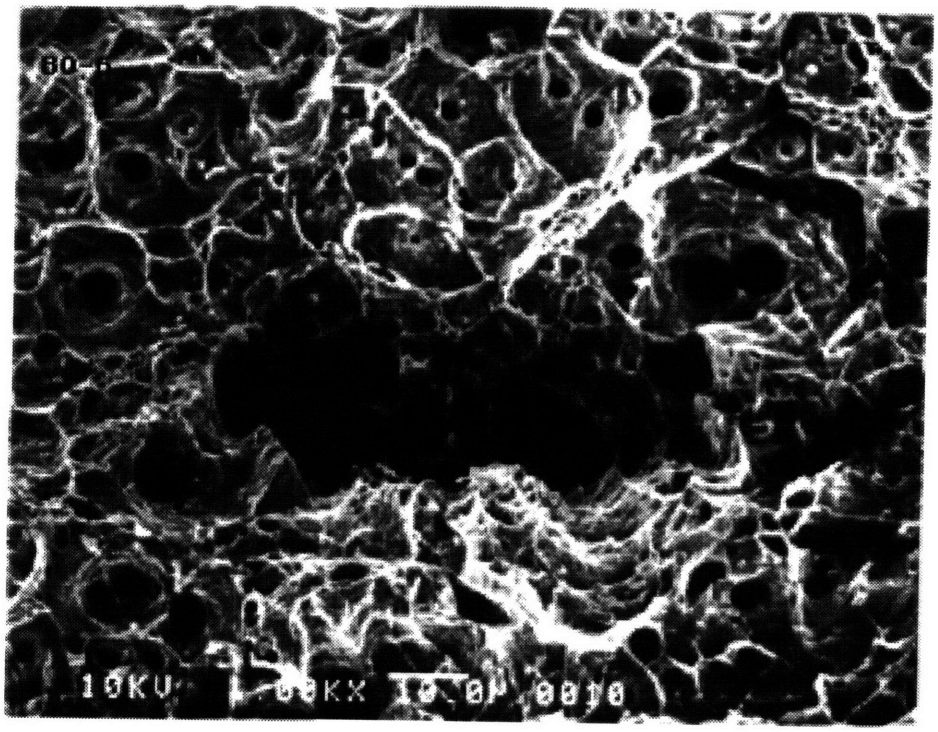

Figure 5-20. Higher magnification of Figure 5-18 ductile region showing evidence of microvoid coalescence on fracture surface of specimen 80 (CP 304,AJ9139,0.8 x 10^{25} n/m^2).

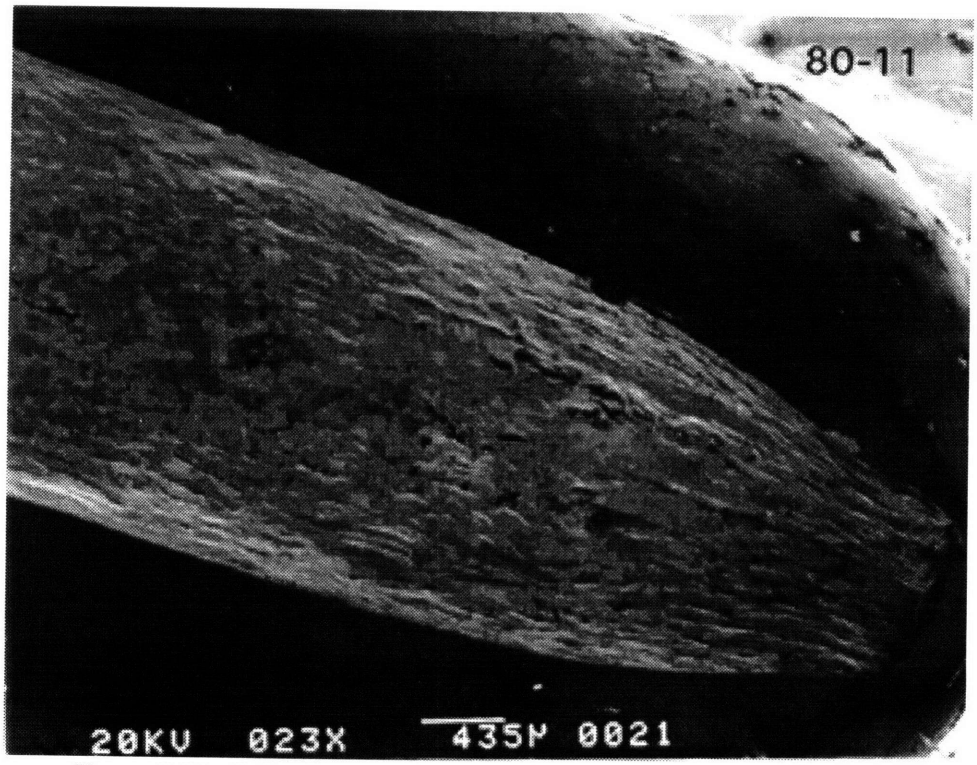

Figure 5-21. Side of specimen 80 (CP 304,AJ9139,0.8 x 10^{25} n/m^2).

measurements for the type CP 304 specimens dynamically loaded at slow strain rate until failure (specimens 81 and 82).

The gage profile of #80 is displayed in Figure 5-21. Many blunt cracks, like that in Figure 5-22, were observed on the side. The one shown in Figure 5-22 measured 55 μm wide and 10 μm high. In an area farther away from the fracture surface (Figure 5-23), the observed cracks are smaller but show indications of opening up. These cracks have a relatively low aspect ratio compared to the cracks observed for the furnace sensitized specimen. These observations suggest that cracks initiate readily in the CP 304 alloy pre-irradiated to 0.8×10^{25} n/m^2, whereas cracks propagate at a modest rate.

5.3.2.2 Specimen 81

Specimen 81 was fabricated from commercial purity alloy 304 (heat AJ9139), solution annealed and tested after pre-irradiation to a fluence of 0.8×10^{25} n/m^2. Figure 5-24 shows the fracture surface. The areas identified as intergranular were determined to cover 12% of the total area. The morphology displayed on a higher magnification micrograph of the lower brittle region (Figure 5-25) indicates that the crack initiation and propagation is by transgranular cleavage. Figure 5-26 shows the right SCC region has a transgranular crack ~60-100 μm from the surface that then changes to an intergranular fracture mode. There is a transition back to TG and then ductile where the stress corrosion crack meets the ductile fracture. The initial transgranular fracture and transition to intergranular fracture is readily seen in Figure 5-27 on the matching region of the opposite face of the fractured specimen.

The gage profile is shown in Figure 5-28 and a higher magnification of the area near the fracture surface shown in Figure 5-29. This combined view of cracking regions on the side surface shows few slip indications. However, the regions, possibly grains, adjacent to the cracking exhibit intense slip markings. A closer look at the enhanced slip steps near a crack opening is displayed in Figure 5-30. The initiation point of the crack was not determined from these SEM slides, hence there is no information on the relationship between deformation and crack initiation. Examination of the side of #81 on the opposite fracture face (see Figure 5-31) showed the intergranular region approximately at the center of the slip-bare region and not near to the boundary of the intense slip-limited slip regions. This suggests that the intense slip deformation does not play a role in crack initiation or perhaps the corollary, that this type of slip sufficiently relieves the stress to *preclude* crack initiation. The former opinion was espoused by Cookson et al.[15] from their work on proton irradiated high purity (HP) 304 stainless steels. Their post-irradiation laboratory IASCC studies showed a negative correlation between slip step deformation and cracking incidence. This was considered indirect evidence that dislocation channeling was not directly involved in the irradiation assisted stress corrosion cracking

Figure 5-22. Side of specimen 80 (CP 304,AJ9139,0.8 x 10^{25} n/m^2) away from the fracture showing typical blunt crack (55µm wide by 10 µm high).

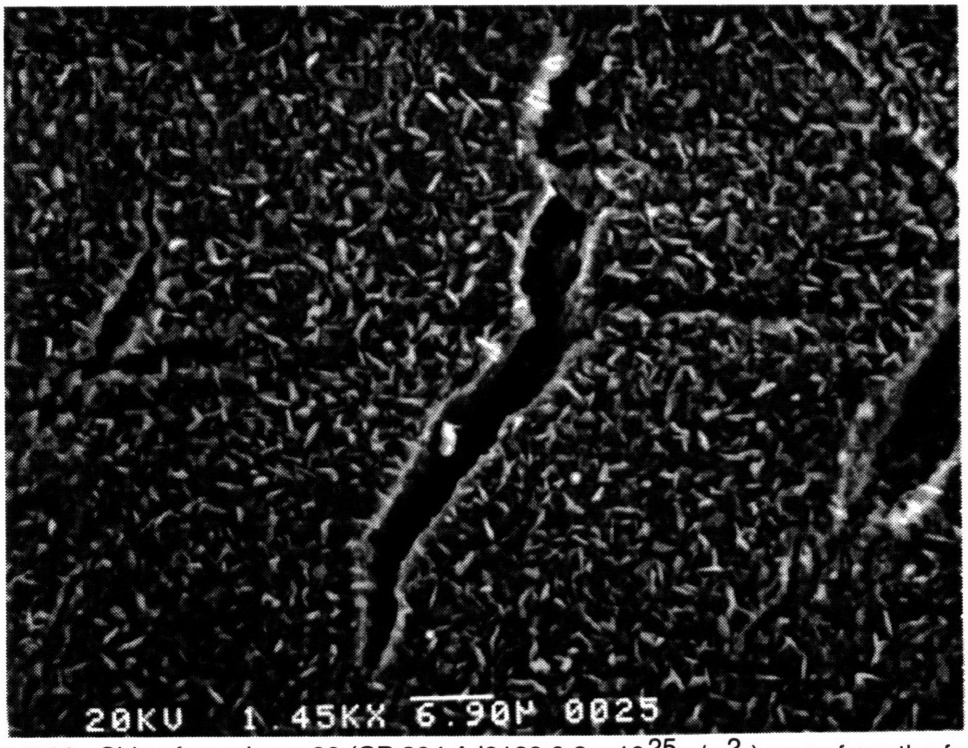

Figure 5-23. Side of specimen 80 (CP 304,AJ9139,0.8 x 10^{25} n/m^2) away from the fracture surface depicting cracks in early stage of development beginning to open up.

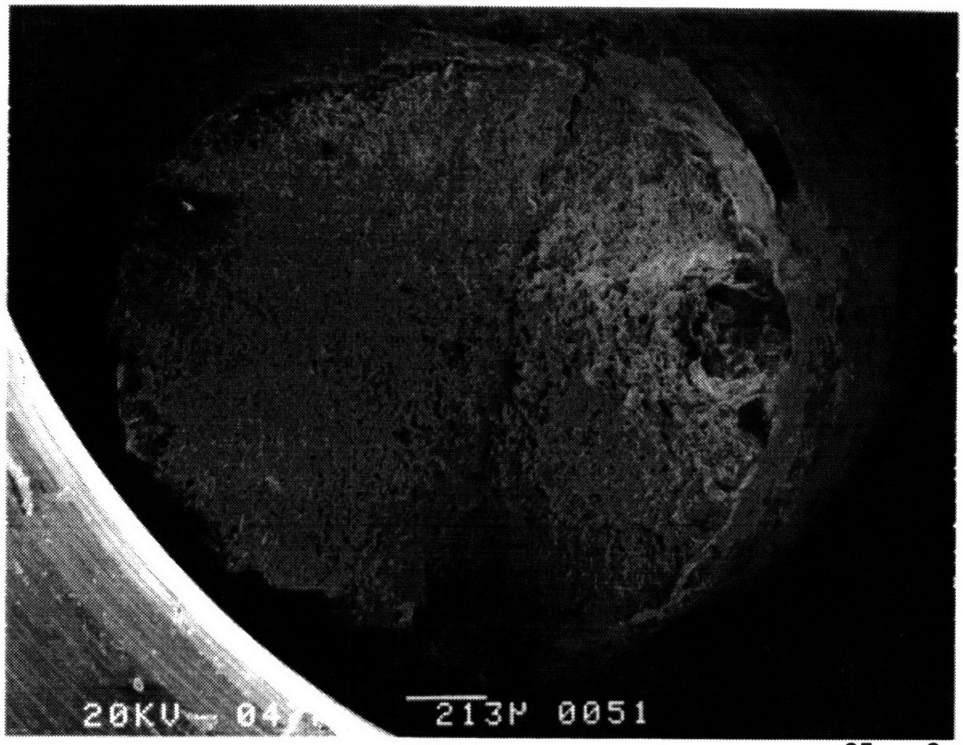

Figure 5-24. Fracture surface of specimen 81 (CP 304,AJ9139,0.8 x 10^{25} n/m^2).

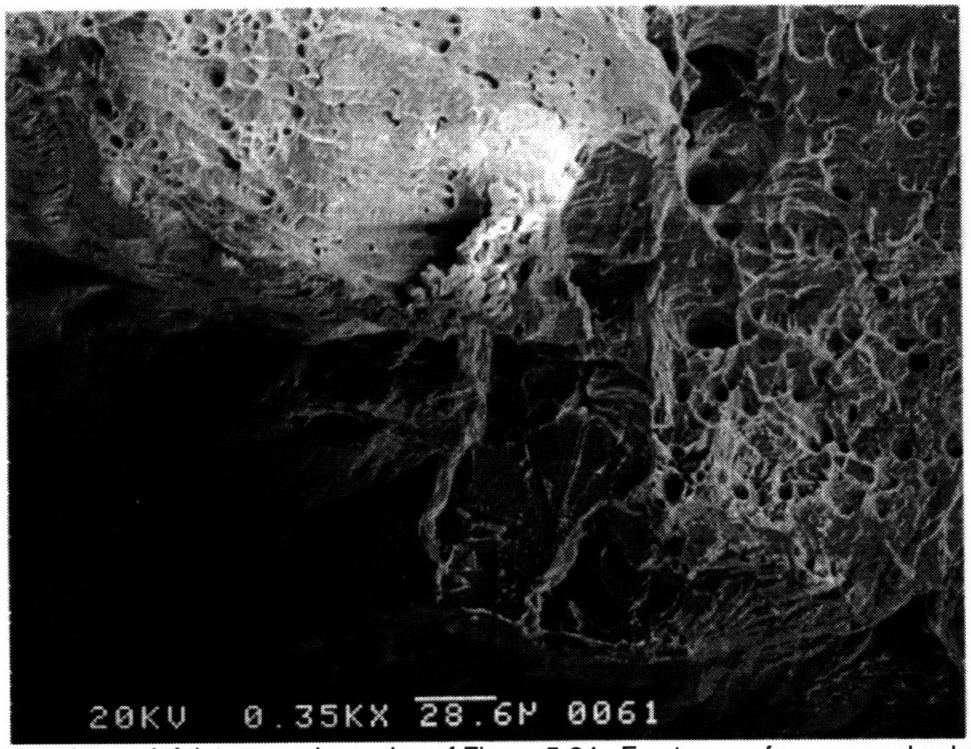

Figure 5-25. Lower left intergranular region of Figure 5-24. Fracture surface near edge begins in transgranular mode and changes to intergranular.

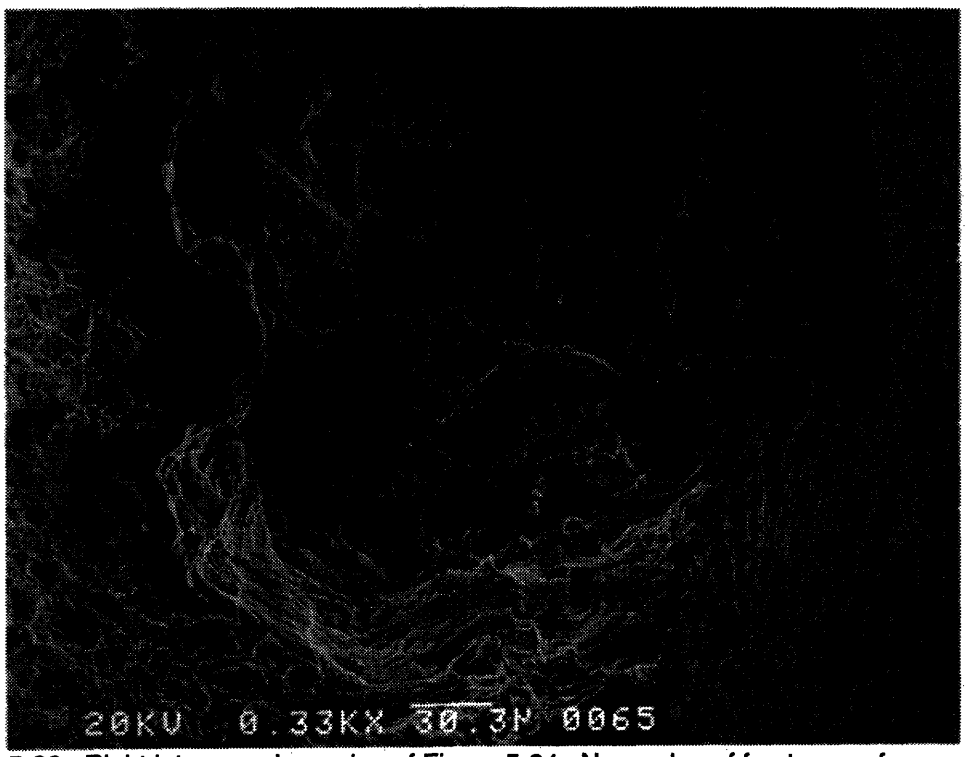

Figure 5-26. Right intergranular region of Figure 5-24. Near edge of fracture surface appears transgranular with transition to intergranular after 60-100 μm.

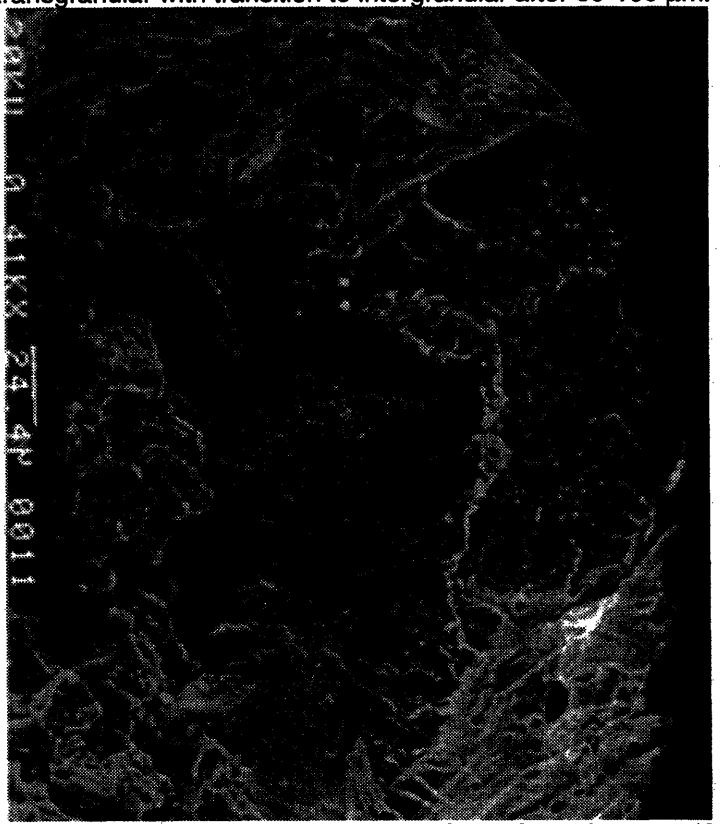

Figure 5-27. Matching SCC region on other fracture surface of specimen 81 (CP 304,AJ9139,0.8 x 10^{25} n/m^2) depicting transition from transgranular to intergranular fracture path.

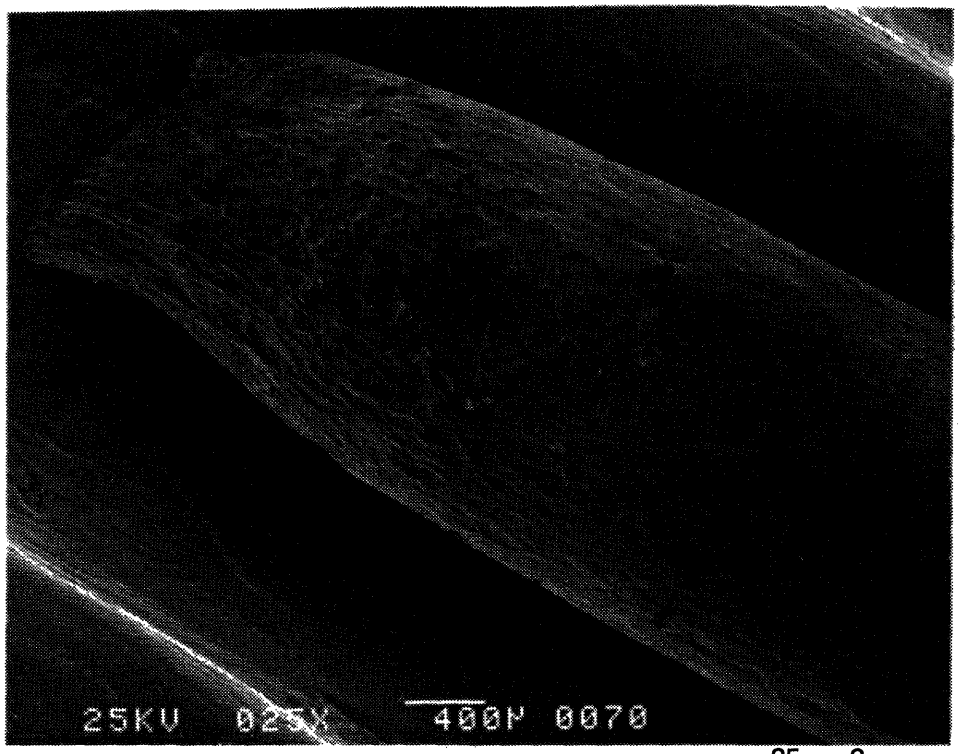

Figure 5-28. Side of specimen 81 (CP 304,AJ9139,0.8 x 10^{25} n/m^2).

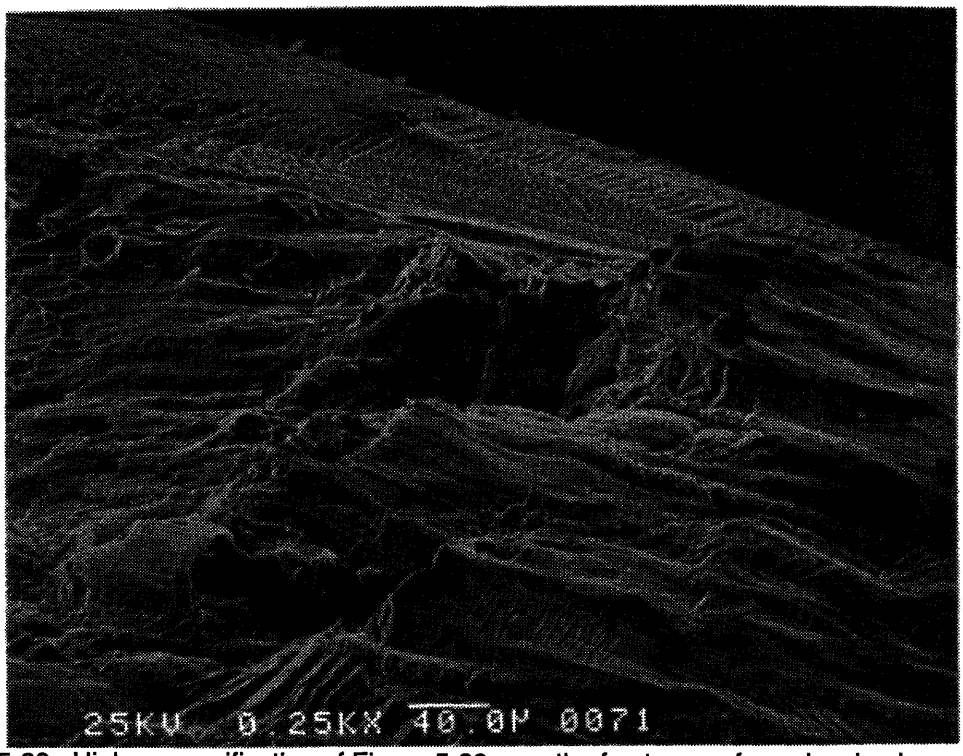

Figure 5-29. Higher magnification of Figure 5-28 near the fracture surface showing low and high intensity slip regions corresponding to SCC and ductile fracture surfaces, respectively.

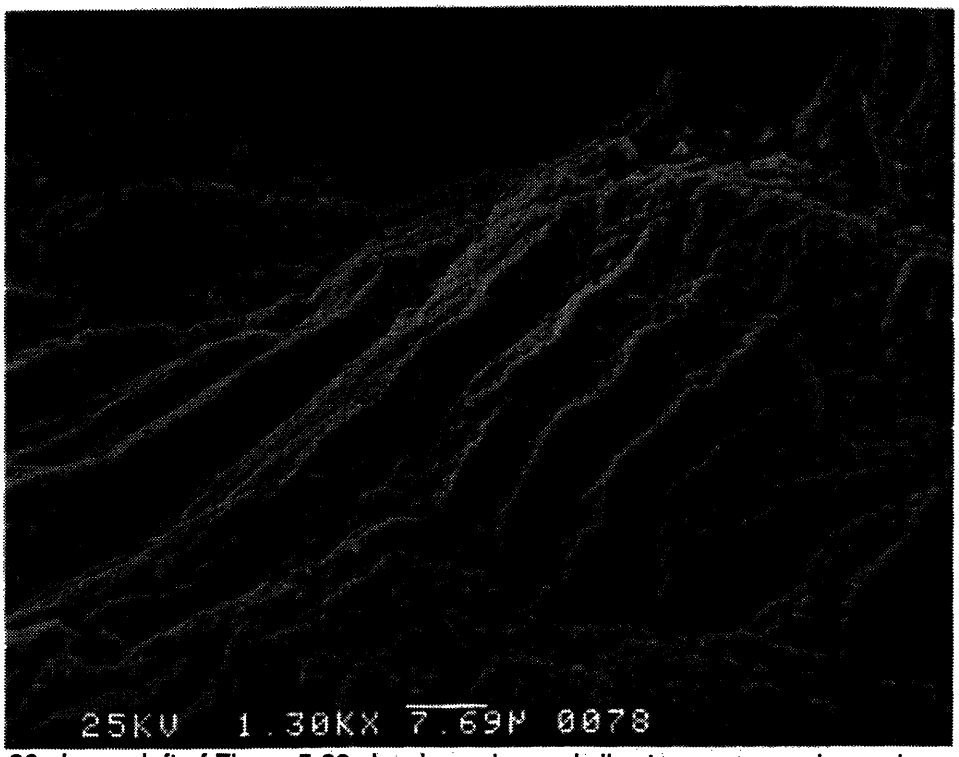

Figure 5-30. Lower left of Figure 5-29 showing enhanced slip steps near crack opening on side of specimen 81 (CP 304,AJ9139,0.8 x 10^{25} n/m^2).

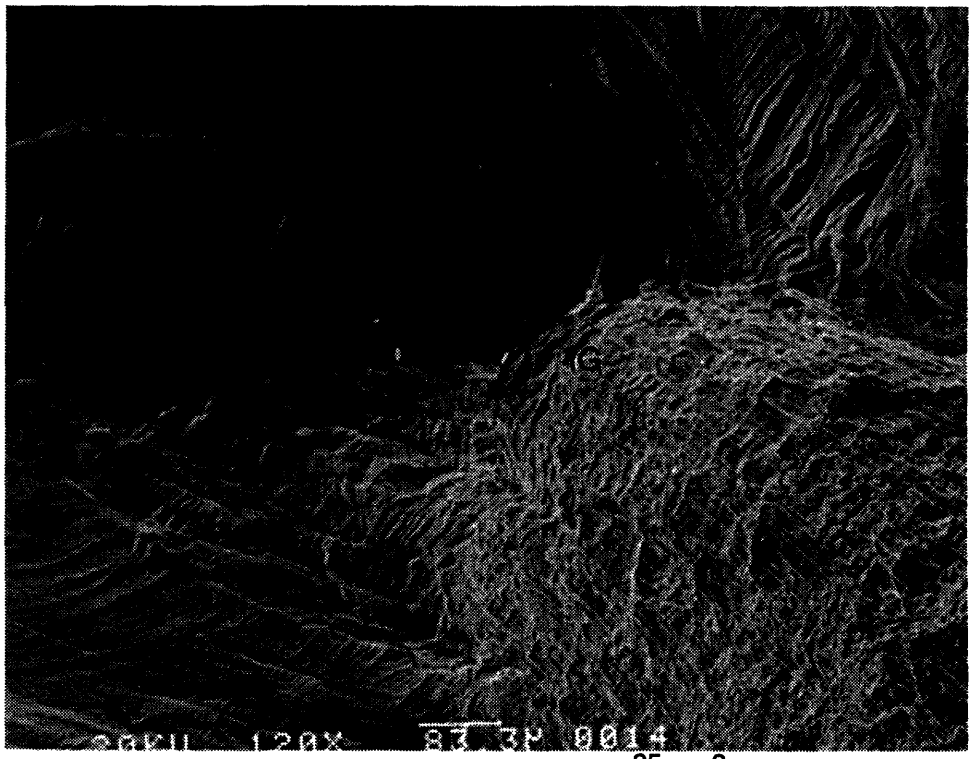

Figure 5-31. Side of specimen 81 (CP 304,AJ9139,0.8 x 10^{25} n/m^2) near fracture surface with IG fracture centered in region of limited slip (bounding regions show intense slip bands).

mechanism. The surface analysis of pre-irradiated CP 304 alloy tested by in-flux SSRT also supports this conclusion.

5.3.2.3 Specimen 82

Specimen 82 was fabricated from commercial purity alloy 304 (heat AJ9139), solution annealed and tested after pre-irradiation to a fluence of 0.8×10^{25} n/m^2. The fracture surface is displayed in Figure 5-32. There is 9% intergranular mode on the surface and 48% RA. The total amount of IG compares very well with #81, which was the other type CP 304 specimen pre-irradiated to 0.8×10^{25} n/m^2 and pulled at a slow strain rate until failure. Higher magnification micrographs of the lower IG surface (Figure 5-33) and upper IG surface (Figure 5-34) do not show very clearly the transgranular cracking mode near the surface edge. For the upper IG surface on #81 transgranular fracture is a very small percentage with intergranular paths beginning after a TG traverse of 60 μm. Evaluation of the gage profile (see Figure 5-35) away from the fracture surface also indicated that cracks proceeded along transgranular and intergranular paths (Figure 5-36). On the gage section near the fracture surface, there were regions displaying an abundance of slip adjacent to regions with minimal slip indications (Figure 5-37). The less deformed zones on the side corresponded to intergranular areas on the fracture surface. This observation corroborates the conclusion that dislocation channeling does not directly affect IASCC.

5.3.3 Pre-irradiated 316L (heat K5) Stainless Steel

5.3.3.1 Specimen 10

Specimen 10 was fabricated from alloy 316L (heat K5), solution annealed and tested after pre-irradiation to a fluence of 0.74×10^{25} n/m^2. Its fracture surface (see Figure 5-38) shows no evidence of intergranular cracking. There is only ductile fracture by void coalescence and an overload region. The high degree of necking (RA was 84%) is consistent with this observation and contrasts greatly with the evaluation of pre-irradiated CP 304 alloy. Analysis of the gage profile (Figure 5-39) showed evidence of intense slip band formation (see Figure 5-40 for an expanded view) which is associated with dislocation channeling. Figure 5-41 shows the slip lines pattern away from the fracture surface. The slip patterns are also similar to the patterns on the unirradiated type CP 304 specimen tested in-flux (Figure 5-15). The pre-irradiated 316L and CP 304 alloys had comparable fluence, but showed very different IASCC behavior. The 316L alloy showed no %IG and the type CP 304 alloy showed slight susceptibility (~10% IG). Hence, the

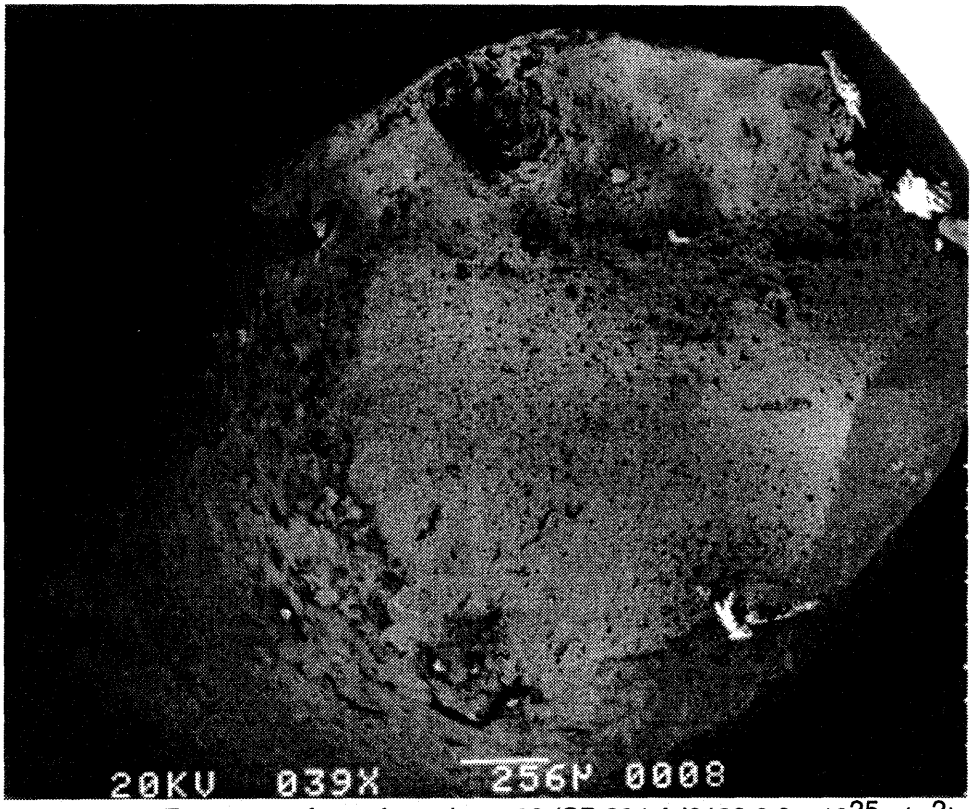

Figure 5-32. Fracture surface of specimen 82 (CP 304,AJ9139,0.8 x 10^{25} n/m^2).

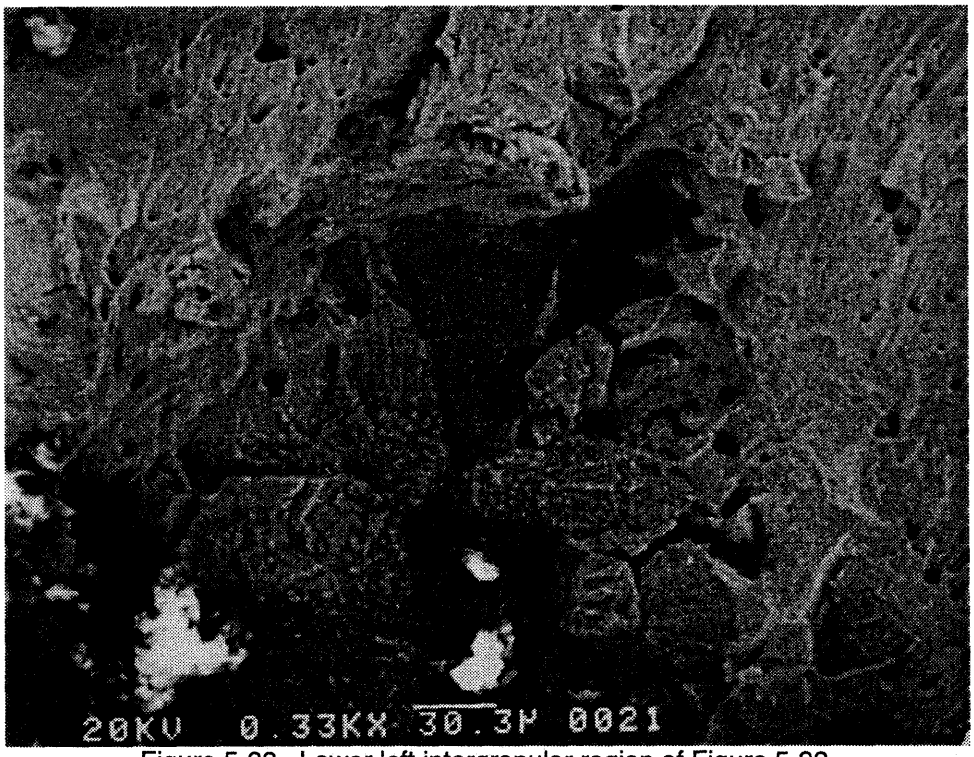

Figure 5-33. Lower left intergranular region of Figure 5-32.

Figure 5-34. Upper intergranular region of Figure 5-32. Fracture surface near edge appears to begin in transgranular mode and changes to intergranular.

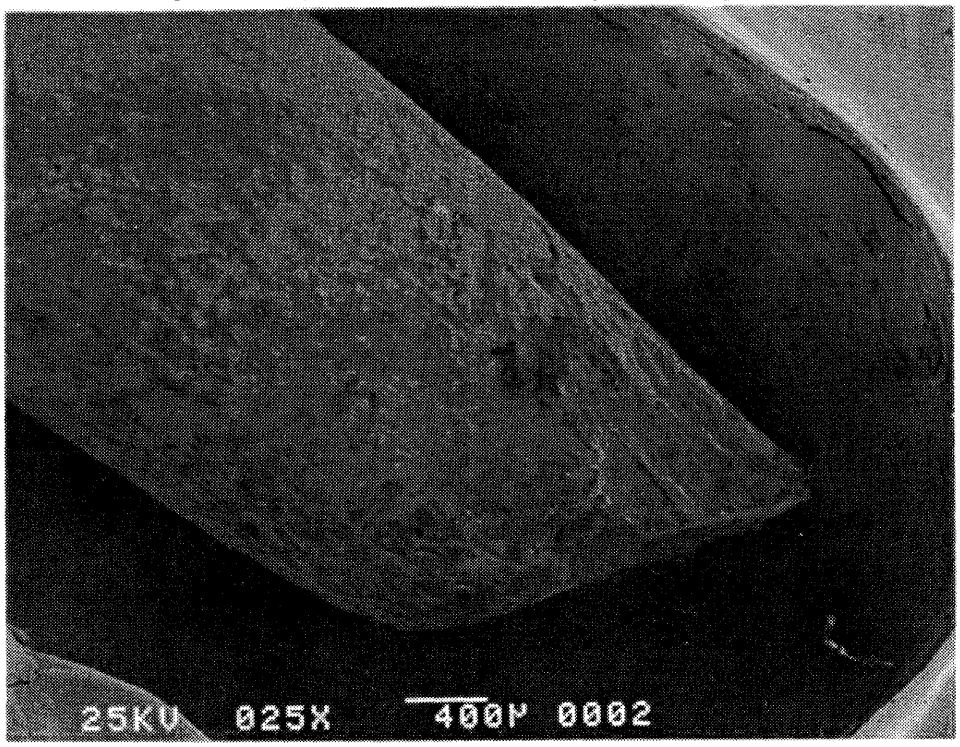

Figure 5-35. Side of specimen 82 (CP 304,AJ9139,0.8 x 10^{25} n/m^2).

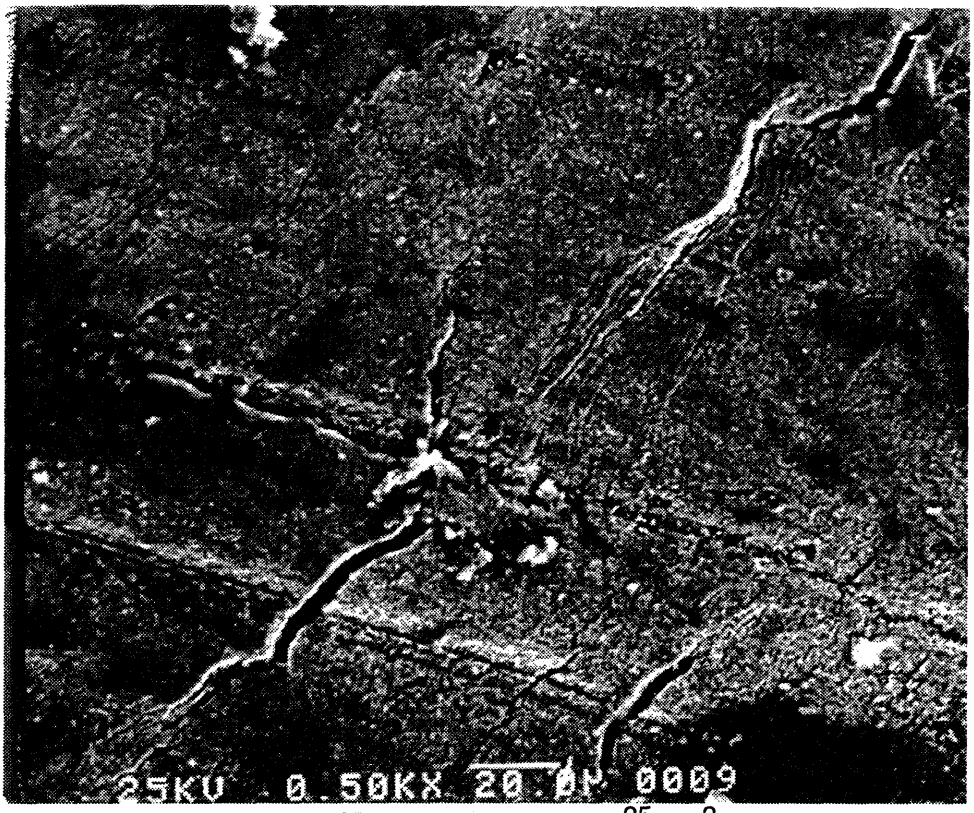

Figure 5-36. Side of specimen 82 (CP 304,AJ9139,0.8 x 10^{25} n/m^2) away from fracture surface showing cracks with transgranular and intergranular modes.

Figure 5-37. Higher magnification of Figure 5-35 showing adjacent regions with intense slip band deformation and an absence of slip.

Figure 5-38. Fracture surface of specimen 10 (316L,K5,0.74 x 10^{25} n/m^2) displaying large reduction of area and cup and cone morphology indicative of ductile failure.

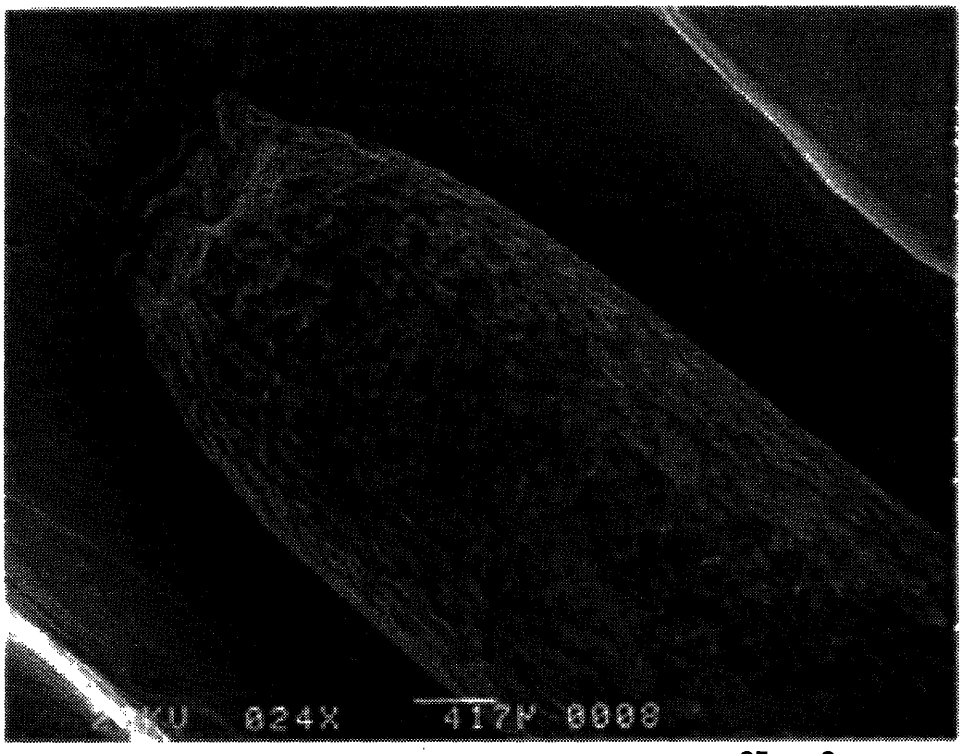

Figure 5-39. Side of specimen 10 (316L,K5,0.74 x 10^{25} n/m^2).

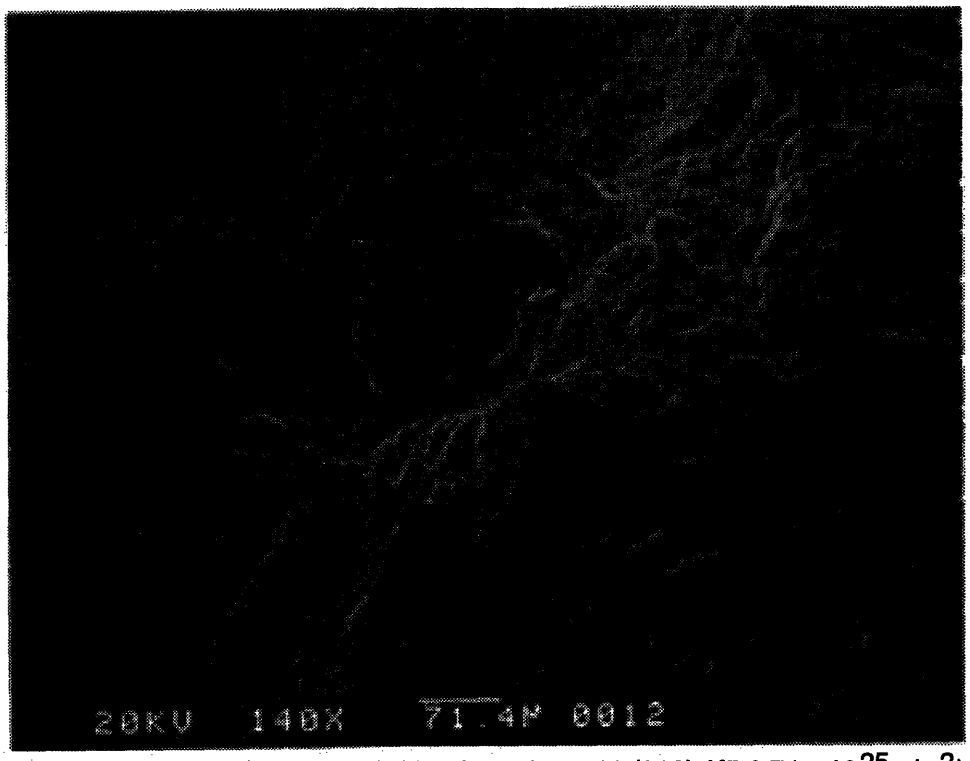

Figure 5-40. Higher magnification of side of specimen 10 (316L,K5,0.74 x 10^{25} n/m^2) near fracture surface. The fracture surface typical of ductile failure.

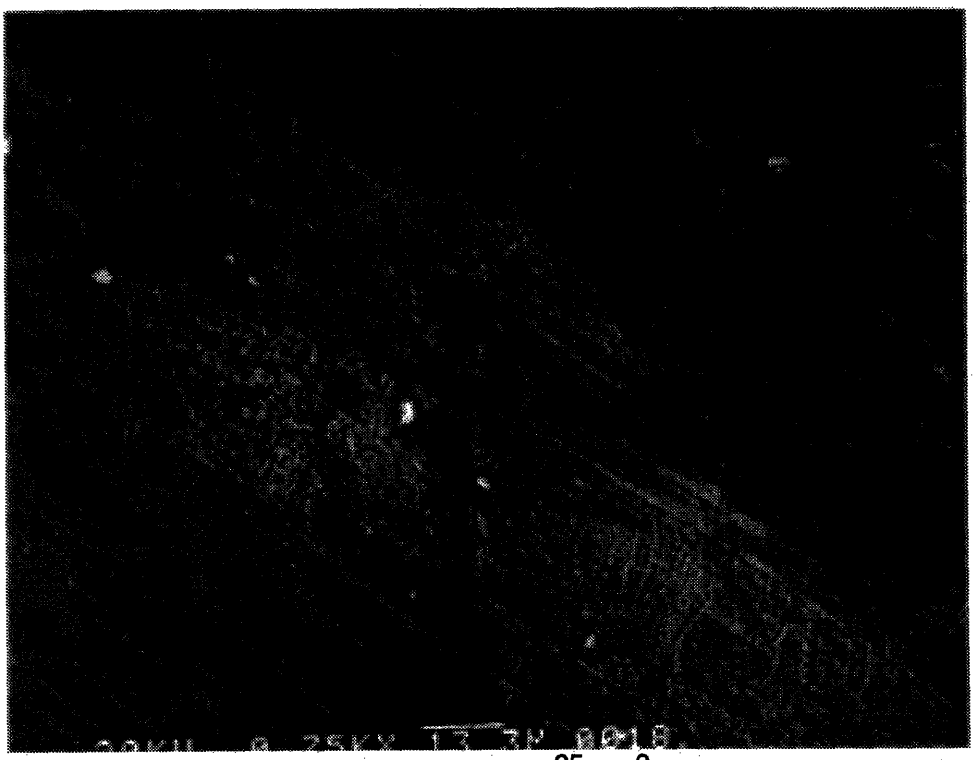

Figure 5-41. Side of specimen 10 (316L,K5,0.74 x 10^{25} n/m^2) away from fracture surface. Slip lines similar to markings on unirradiated CP 304 tested in-flux (see Figure 5-15).

Figure 5-42. Side of specimen 11 (316L,K5,0.74 x 10^{25} n/m^2) near fracture surface. Slip deformation appears uniform throughout cross section. Compare with localized regions of specimen 81 (CP 304, 0.8 x 10^{25} n/m^2) seen in Figure 5-29.

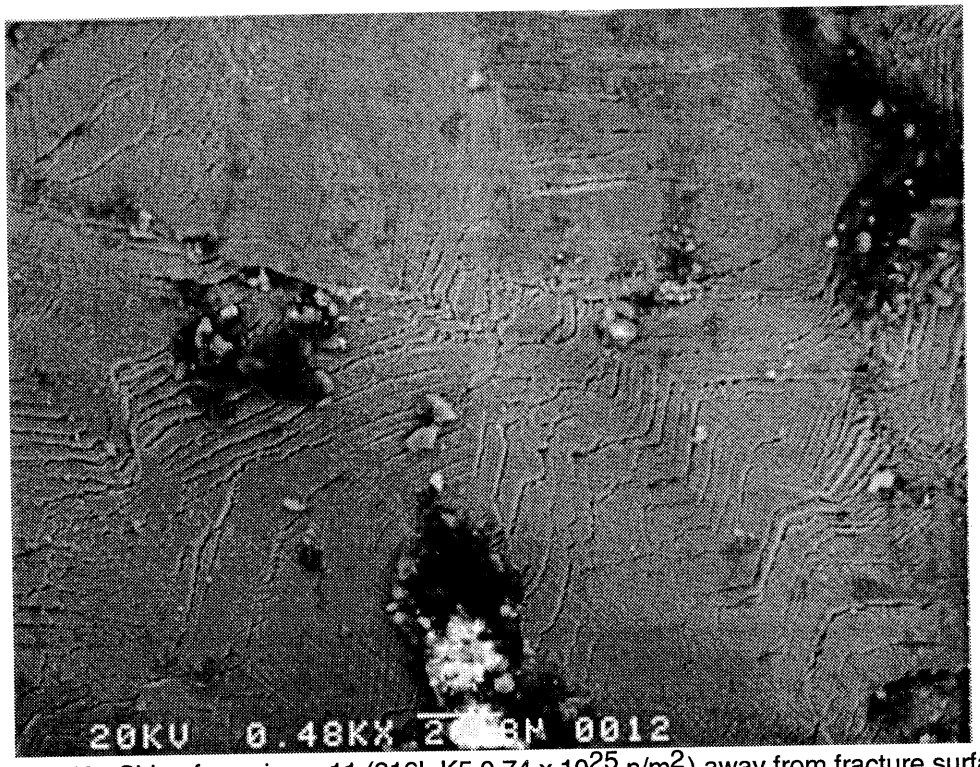

Figure 5-43. Side of specimen 11 (316L,K5,0.74 x 10^{25} n/m^2) away from fracture surface.

fluence threshold for IASCC to occur in 316L is higher than it is for CP 304 alloy. Results from specimen 11, discussed in the next section, support this conclusion.

5.3.3.2 Specimen 11

Specimen 11 was fabricated from alloy 316L (heat K5), solution annealed and tested after pre-irradiation to a fluence of 0.74×10^{25} n/m^2. SEM analysis was hindered by gross contamination of the fractured specimen incurred during handling. A number of cleaning rinses (de-ionized water, ethanol, and an inhibited HCl solution) in an ultrasonic bath were performed but were ineffective in removing all of the debris. Because of the large RA observed (84% which is the same as specimen 10) and zero %IG around the perimeter analyzed by SEM, there is high degree of confidence that no IG occurred on the fracture surface. The gage profile micrograph was also distorted by the surface contamination. The slip line deformation pattern (Figure 5-42) is similar to that observed on the other 316L and CP 304 alloys, except that it is not limited to localized regions. Rather, the slip appears uniformly spread throughout the cross section. This result is somewhat fortuituous since no IG was observed on the 316L specimens and the regions of low intensity slip for the CP 304 alloy corresponded to cracking areas on the fracture surface. Away from the fracture surface (see Figure 5-43), slip markings which are similar to those on the other pre-irradiated 316L specimen 10 (see Figure 5-41) were observed.

5.4 DISCUSSION

A number of observations made from the scanning electron microscope surface analysis merit a brief discussion in light of the fracture mechanism of IASCC. Specifically, insights about dislocation channeling, fracture mode and susceptibility measures are discussed.

Indirect evidence of dislocation channeling was observed on the in-flux SSRT specimens by comparing in-flux strained surfaces with unirradiated and pre-irradiated stainless steel which were tested out-of-flux and documented to have and not have dislocation channeling, respectively[15]. Based on observation limited by the resolution of conventional SEM, there is a negative correlation with cracking and intense slip deformation as observed in laboratory experiments. However on a smaller scale, very high resolution microscopy may reveal intense slip deformation near the grain boundary that initiates IASCC behavior. Observations on the failure morphology of the stress corrosion cracked specimens follows.

Of the alloys and fluence examined in this work, only the pre-irradiated CP 304 alloy showed SCC. The unirradiated CP 304 and pre-irradiated type 316L stainless steel specimens failed in a ductile manner. The fracture surfaces of the pre-irradiated CP type 304 showed

intergranular and transgranular regions. Some SCC regions showed transgranular cleavage with secondary intergranular cracks. Generally the deepest cracks initiated as transgranular, propagated transgranularly a short distance (~60-100 μm) and then propagated intergranularly. This fracture mode is similar to that observed on stainless steel lightly sensitized by thermal treatment and tested in laboratory high temperature, oxygenated water[16]. The film rupture/slip dissolution model does not explain crack morphology changes as observed for in-flux SSRT. Earlier research on thermally sensitized stainless steel[17] showed fracture path changes as a function of oxygen and corrosion potential, but observations and explanations indicated cracks that initiated intergranularly changed to transgranular for mid-range oxygen levels (~1-2 ppm) and higher strain rates (~$2 \times 10^{-6} s^{-1}$). It has been suggested that fatigue damage incurred during unexpected unload-load cycles of some of the SSRTs may have influenced the failure behavior.

This seems highly doubtful for several reasons. There were two in-flux SSRTs of pre-irradiated CP type 304; one test was completed with two pauses and one with three pauses. Similar fracture features, %IG and total elongation were observed for both specimens. Results from out-of-pile SSRTs reported by Andresen[18] showed no significant variation in fracture behavior of specimens tested with one to many unload-load cycles. Hence, a comparison of specimens that experienced multiple unload cycles and control specimens that were strained continuously to failure indicates that fatigue damage has no measurable effect on the fracture characteristics. The predicted effect of fatigue damage based on the very low number of loading cycles is negligible. Work hardening, which has been observed in fully reversed loaded single crystals in the first few cycles, is not significant until 20-100s of cycles. Surface roughening caused by extrusions of persistent slip bands (PSBs) has been identified as a crack initiation mechanism, but typically does not occur before 1000s of cycles. Furthermore, the SEM examination of the TG regions on the type 304 fracture surface was inconsistent with crack initiation by fatigue. The number of observed striation markings greatly exceeded the number of pauses incurred during in-flux SSRTs. Finally, if fatigue damage affected cracking initiation then the type 316L specimens should have shown some transgranular cracking because the SSRTs were paused around six times. But as reported in the above sections in this chapter, the pre-irradiated type 316L specimens failed in a completely ductile manner. Based on the similar in-flux and out-of-flux performance of specimens strained with unload cycles and continously to failure, the negligible predicted effect of very low cycle (1-5) fatigue, and the inconsistency between the number of striation markings and load cycles, the fracture morphology and failure characteristics of the in-flux SSRT specimens were not influenced by the unload-load cycles incurred during testing.

Transgranular stress corrosion cracking has been observed in both lightly sensitized (by thermal treatment and irradiation) and solution annealed stainless steel alloys tested by SSR

in high temperature, oxygenated (288°C, 8-32 ppm DO) water environments. The fact that the initiating fracture mode (transgranular) changes (to an intergranular mode) after some amount of crack growth indicates one or more of the SCC variables (microstructure, stress, environment) has changed. The radiation damage from the fast neutron fluence of 0.8×10^{25} n/m^2 is expected to be uniform throughout the volume of the specimen although it may be anisotropic. The nucleation and growth of faulted loops depends on the orientation of preferred slip planes and radiation induced segregation at grain boundaries has been suggested to vary with type and alignment. Observations from the SEM fractographs do not support the supposition of grain to grain variation causing the transition to IG fracture. At the point where fracture changes morphology it is evident that more than one grain is being "sampled". The likelihood of multiple adjacent grains having preferred alignments and hence susceptible microstructures is incongruous with the initial premise, therefore microstructure is not considered the differentiating variable. The stress will certainly change with crack growth. As the load supporting area is reduced by the fractured ligament and as the material strain hardens, the stress will increase at the crack tip. The change in stress intensity can certainly alter the rate limiting fracture path, furthermore IGSCC susceptibility has been observed to increase with yield stress. On the other hand, a higher stress results in a faster strain rate which generally moves the fracture path into a transgranular regime rather than intergranular regime. The third variable, environment, will certainly change within the crack enclave (at 60-100 μm) which might alter the SCC growth. Under no irradiation, acidification at the crack tip, higher dissolution rates and ionic migration driven by the potential difference between the bulk coolant and the crack solution have been put forward to explain crack growth. This chemistry change can occur under irradiation, but unfortunately it does not explain the change from transgranular to intergranular fracture. Perhaps the change in fracture mode is indicative of a change in fracture mechanism. It is conceivable that transgranular cracks initiate by dissolution and proceed along preferred planes until crack growth proceeds far enough that the crack tip chemistry changes and a hydrogen induced cleavage mechanism becomes rate limiting at the crack front. With the present data, no definite conclusions on IASCC mechanism can be drawn. Insights into susceptibility measures of IASCC are discussed next.

As mentioned in section 2.3.4, the percentage intergranular fracture (%IG) has been used extensively as a susceptibility index for SSRTs and particularly for IASCC investigations. Another index that utilizes SEM analysis of the fracture surface is the average crack propagation rate calculated from the maximum crack depth length and test time to failure. Some alternative methods for calculating average crack velocity have been suggested by Congleton et al.[19], but in this work the maximum crack depth length on the fracture surface and time between yield and failure are adopted. Although primarily reported because of the utility in correlating

susceptibility[20], average crack propagation rates have been observed to usually be in good agreement with *in situ* crack velocity measurements[21] and have, on occasion, been used in evaluating deterministic prediction models[22]. The relevance of such calculations is more tenable provided two conditions are met: 1) cracking initiates early and 2) few secondary cracks occur during SSR testing. Actual initiation strains have been estimated by Andresen[18] to be 3±0.6% for furnace sensitized specimens tested by SSR, thus the initiation at yield assumption is not too far off. The low aspect ratio cracks observed on pre-irradiated CP 304 alloy are also consistent with early crack initiation. Cracks observed on the side of the gage section were shallow compared to the fracture surface cracks and on the fracture surface there was typically only one or two stress corrosion cracks. Hence, these conditions are satisfied for the in-flux SSRTs and average crack propagation rates are a relevant susceptibilty measure. However, there is a complication for determining the test time to failure which is discussed below.

Some of the SSR tests were paused due to scheduled and unscheduled events. The total time to failure needed to be adjusted for these pauses to estimate the time during which the crack propagated. Crack propagation was assumed to cease during these unloading periods because the driving energy for crack growth was removed. A psuedo-continuous time was calculated by subtracting the time during pauses (time while unloaded and reloading to the stress prior to the pause) from the test time between yield and failure.

The results for these average crack propagation rate calculations are presented in Table 5-1. It is seen that the average crack growth rates for the sensitized CP type 304 specimens are comparable to one another. These data are close (~3 times lower) to values reported by Shoji et al.[23] for the same CP type 304 (heat AJ9139) similarly sensitized and tested out-of-pile in highly oxygenated (8 ppm oxygen) 288°C water. A factor of three difference is small compared to experimental variation and could very likely be explained by the same magnitude difference in strain rates (i.e. ~4×10^{-7} s^{-1} for this work and 1.33×10^{-6} s^{-1} for Shoji et al.'s tests). It is important to recognize that one sensitized specimen (#2012) was tested out-of-pile and the other (#2003) was tested in-flux. The similarity of propagation rates suggests that the degree of sensitization results in equivalent susceptibilities for the two environments. This could mean that the two environments are equivalent or at least that both environments are sufficiently aggressive for intergranular cracking in a highly sensitized microstructure.

The crack growth rates of the furnace sensitized specimens are much greater (~6X) than those of the pre-irradiated specimens. Susceptibility as measured by crack growth rates is consistent with susceptibility trends determined by %IG and grain boundary microstructure changes as measured by STEM-EDX. The large difference in crack growth rates for the furnace

Table 5-1. Summary of SEM analysis of zero-flux and in-flux SSRT specimens.

Specimen Description	Pretreatment	l_{max} (mm)	Test Time (sec)	e_f (%)	RA (%)	IG (%)	TG (%)	v_{avg} (mm/sec)	Comment
#2005, CP304	SA+CW+SEN	•	$1.13x10^4$	11	30	0		•	out of core
#2021, 347L	SA	•	$7.81x10^3$	•	•	0	0	•	0 MW,end SSR @36%
#98, CP304	SA	•	$8.42x10^5$	36	73	0	0	•	4 MW
#2012, CP304	SA+CW+SEN	0.537	$1.75x10^5$	6	10	12		$3.07x10^{-6}$	out of core
#2003, CP304	SA + SEN	1.27	$3.21x10^5$	15	5	97	0	$3.96x10^{-6}$	4.2 MW
#80, CP304	SA + 0.8 dpa	0.041	$3.64x10^5$	•	•	0	0.3	$1.13x10^{-7}$	4 MW,end SSR @15%
#81, CP304	SA + 0.8 dpa	0.255	$4.58x10^5$	22	59	1.8	1.9	$5.57x10^{-7}$	4 MW
#82, CP304	SA + 0.8 dpa	0.341	$5.15x10^5$	21	48	2.7	2.0	$6.62x10^{-7}$	4 MW
#10, 316L	SA + 0.74 dpa	•	$7.33x10^5$	32	84	0	0	•	4 MW
#11, 316L	SA + 0.74 dpa	•	$7.30x10^5$	31	84	0	0	•	4.5 MW

l_{max} - maximumum crack depth
e_f - strain to failure
v_{avg} - average crack growth rate

sensitized and radiation sensitized specimens displays the high sensitivity to susceptibility of this parameter which is one reason it is favored as a susceptibility index. Comparing the crack velocities of the pre-irradiated CP type 304 specimens reveals that #80's is lower than that of both #81 and #82 by a factor of five. This trend is consistent with the other SCC susceptibility measures (strain to failure, reduction in area and percentage intergranular fracture). However, specimens with a similar microstructure, i.e. #80, #81 and #82, and subject to the same environment are expected to exhibit similar crack growth dependencies. This anomalous behavior suggests that the crack velocity is strongly influenced by another variable. Differences in the stress or fracture mode may explain the crack velocity behavior. Since specimen 80 was strained to 15%, whereas #81 and #82 were strained to failure (~21%), the latter specimens would have experienced a higher stress because of strain hardening. But due to radiation hardening, work hardening was reduced and the stress strain curves of these specimens (cf. section 4.3.3) exhibited only a small difference (~25%) in yield and ultimate stresses compared to the five fold difference in average crack velocities. The fracture mode of #80 SCC region was pure TG, but the SCC areas of specimens 81 and 82 exhibited TG and IG fracture. Transgranular crack velocities are considerably less than those of IG cracking, therefore the stress dependence is considered a secondary effect to the fracture mode. Hence, the five fold difference in average crack growth rates between #80 and #81, #82 is attributed to the SCC fracture mode differences which were pure TG and combined TG + IG, respectively. It should be noted that the factor of five difference represents an even greater difference between pure TG and pure IG crack velocities. A TG crack

velocity for the 0.8×10^{25} n/m^2 pre-irradiated CP type 304 can be estimated from the #80 SEM data, since the SCC was pure transgranular. It is possible to estimate the IG crack velocity using the TG crack velocity from #80 and the lengths of IG and TG fracture along the deepest cracks identified for #81 and #82. However, this estimate of the intergranular crack velocity is not tenable due to uncertainties in the TG initiation time, effect of crack geometry and the high sensitivity to the estimated TG crack velocity.

Since the SCC on #80 was determined to be only transgranular, then its average crack growth rate represents pure TG crack velocity. The measured value can be compared with Ford et al.'s[16] predicted value based on laboratory SSRT data. Assuming crack growth proceeded in cleavage steps (equal to striation spacings measured on SEM fractographs) at a critical fracture strain, a simple algorithm for predicting TG crack velocities is given as a function of strain rate:

$$v_{TG} = \dot{\varepsilon}, [mms^{-1}]. \qquad \text{(eq. 5-1)}$$

For the in-core SSRT, the strain rate was ~3.4×10^{-7} s^{-1}. Substituting this into Eq. 5-1 gives the predicted crack velocity as 3.4×10^{-7} mms^{-1} which compares very well with the measured crack velocity of 1.13×10^{-7} mms^{-1}. In summary, average crack propagation rates calculated for the specimens with SCC areas on the fracture surface trended similarly with other susceptibility measures of IASCC. The average crack growth rates of the furnace sensitized specimens compared well with other data reported in the literature. The transgranular crack velocity in pre-irradiated CP type 304 was estimated based on SEM analysis of the interrupted SSRT specimen. The measured estimate was within a factor of three of the predicted value based on out-of-flux SSRT data.

5.5 SUMMARY

SEM analyses of the fractured specimens tested as part of the MIT IASCC program were presented in this chapter. The major findings and observations are summarized below.

Localized regions of slip deformation were observed on the pre-irradiated CP 304 and 316L alloys and the unirradiated CP type 304 specimen tested in-flux. These intense slip bands were believed to be evidence of dislocation channeling, based on surface patterns comparisons. There was no correlation between the intense slip bands and cracking. SCC areas on the fracture surface were associated with a lower density of slip markings on the side relative to the ductile failure areas. For the specimens that did not exhibit any SCC on the fracture surface (unirradiated CP 304 and pre-irradiated 316L alloys), slip markings appeared uniformly across the cross section.

A significant difference in crack initiation and growth morphology was observed between the furnace sensitized CP type 304 specimen (#2003) and the pre-irradiated CP type 304 specimens (#s80, 81, and 82). For the furnace sensitized specimen, crack initiation occurred quite easily and so did crack propagation as indicated by the large number of high aspect ratio cracks. The pre-irradiated CP type 304 specimens showed a fair number of low aspect ratio cracks that were blunted. This is explained by susceptibility to crack initiation, but with low probability of continued crack growth. This difference is probably due to the degree of sensitization (high degree correlates with high probability of crack growth).

Although the susceptibility to initiate cracking was similar for furnace sensitized and radiation sensitized material, crack evolution differed. Cracks initiated along grain boundaries and propagated intergranularly in the furnace sensitized specimen. In contrast, the pre-irradiated CP 304 alloy crack growth began transgranularly with a transition after ~60 μm into an intergranular fracture mode. This fracture morphology is similar to that observed in out-of-flux SSRTs for CP type 304 lightly sensitized by thermal treatment. It is considered evidence of the low level of sensitization induced by radiation, rather than a fracture path unique to the in-flux radiation environment.

Average crack propagation rates, calculated from maximum crack depth measurements and test time from yield to failure, trended with %IGSCC. The calculated crack velocity of the furnace sensitized CP 304 alloy was similar to estimates derived from out-of-flux laboratory SSR tests. An average IG crack velocity in the pre-irradiated CP type 304 was not determined because of the initial TG fracture mode. On the pre-irradiated CP type 304 specimen (#80) halted at 15% strain, the SCC region was only transgranular. Data from the SEM analysis of #80 was used to estimate an average TG crack propagation rate for the pre-irradiated CP type 304. This estimate was consistent with a predicted TG crack velocity, calculated from Ford et al.'s[16] algorithm developed for out-of-flux data. The similarities between the average crack velocities (i.e. for heavily sensitized, furnace sensitized #2003, and lightly sensitized, #80) suggests that the SCC mechanism is similar for in-flux and out-of-flux SSRTs.

With respect to IASCC susceptibility, there is a significant difference between CP 304 and 316L stainless steels pre-irradiated to ~0.8 x 10^{25} n/m^2 fluence. The CP 304 alloy with radiation damage showed modest susceptibility with ~2% of the fracture surface area intergranular mode; whereas there was no intergranular cracking observed on the 316L alloy. Neither was there any intergranular fracture on the unirradiated CP 304 alloy. This suggests that flux effects causing instantaneous radiation damage to the metal and radiolysis of the water coolant did not change the material or environment sufficiently to induce IASCC. Although IASCC susceptibility measured by in-flux and out-of-flux SSRTs were comparable for low dose stainless steel alloys, there may be other differences which were not manifested in this test matrix.

5.6 REFERENCES

1. *Symposium on Fractography-Microscopic Cracking Processes, ASTM STP 600,* Philadelphia (1976).

2. *Symposium on Fractography in Failure Analysis, ASTM STP 645,* Philadelphia (1978).

3. *Symposium on Fractography and Material Science, ASTM STP 733,* Philadelphia (1981).

4. *Symposium on Fractography of Ceramic and Metal Failures, ASTM STP 827,* Philadelphia (1984).

5. *Failure Analysis and Prevention,* Metals Handbook, 9th Edition, Vol. 11, American Society of Materials, Metals Park, OH (1986).

6. *Fractography,* Metals Handbook, 9th Edition, Vol. 12, American Society of Materials, Metals Park, OH (1987).

7. A. J. Jacobs, R. E. Clausing, L. Heatherly and R. M. Kruger, "Irradiation-Assisted Stress Corrosion Cracking and Grain Boundary Segregation in Heat Treated Type 304 SS," *Effects of Radiation on Materials: 14th International Symposium, Vol. I, ASTM STP 1046,* N. H. Packan, R. E. Stoller, and A. S. Kumuar, Eds., American Society for Testing and Materials, Philadelphia (1989) p. 424.

8. H. M. Chung, W. E. Ruther, J. E. Sanecki, A. G. Hins and T. F. Kassner, "Stress Corrosion Cracking Susceptibility of Irradiated Type 304 Stainless Steels," *Effects of Radiation on Materials: 16th International Symposium, ASTM STP 1175,* A. S. Kumuar, D. S. Gelles, R. K. Nanstad, and E. A. Little, Eds., American Society for Testing and Materials, Philadelphia (1993) p. 851.

9. H. D. Solomon, "Transgranular, Granulated, and Intergranular Stress Corrosion Cracking in AISI 304 SS," *Corrosion,* 40 (September 1984) p. 493.

10. J. R. O'Donnell, "Design, Construction, and Commissioning of an In-Core Materials Testing Facility for Slow Strain Rate Testing," PhD Thesis, Department of Nuclear Engineering, Massachusetts Institute of Technology, Cambridge, MA (September 1994).

11. A. L. Bement, Jr., "Fundamental Materials Problems in Nuclear Reactors," *Proceedings Second Int. Conf.erence on the Strength of Metals and Alloys, Vol. II,* ASM, Pacific Grove, CA (1970) p. 693.

12. E. E. Bloom, "Irradiation Strengthening and Embrittlement," *Radiation Damage in Metals,* N.L. Peterson and S. D. Harkness, Eds., American Society for Metals, Metals Park, Ohio (1975) p. 295.

13. I. V. Gorynin, O. A. Kozhevnikov, K. A. Nikishina, A. M. Parsh and V. M. Sedov, "Effect of Radiation and Chemical Action on Corrosion Cracking of Austenitic Chromium-Nickel Alloys," *Fiizika Radiatsionnykh i Povrezhdenii Radiatsionnoe Materialovedenie,* 3, no. 26 (1983) p. 45.

14. S. W. Bruemmer, J. I. Cole, J. L. Brimhall, R. D. Carter and G. S. Was, "Radiation Hardening Effects on Localized Deformation and Stress Corrosion Cracking of Stainless Steels," *Proc. 6th Int. Symp. Env. Deg. Mat. Nucl. Power Syst.-Wat. Reactors,* TMS, San Diego, CA (1993) p. 537.

15. J. M. Cookson, R. D. Carter Jr., D. L. Damcott, M. Atzmon and G. S .Was, "Irradiation Assisted Stress Corrosion Cracking of Controlled Purity 304L Stainless Steels," *J. Nucl. Mat.*, 202 (1993) p. 104.

16. F. P. Ford, D. F. Taylor, P. L. Andresen and R. G. Ballinger, "Corrosion-Assisted Cracking of Stainless and Low-Alloy Steels in LWR Environments," EPRI Report NP-5064S , Electric Power Research Institute, Palo Alto, CA (February 1987).

17. F. P. Ford and M. J. Povich, "The Effect of Oxygen Temperature Combinations on the Stress Corrosion Susceptibility of Sensitized Type 304 Stainless Steel in High Purity Water," *Corrosion*, 35 (December 1979) p. 569.

18. P. Andresen, "Crack Initiation in CERT Tests on Type 304 Stainless Steel in Pure Water," *Corrosion*, 38 (January 1982) p. 53.

19. J. Congleton, H. C. Shih, T. Shoji and R. N. Parkins, "The Stress Corrosion Cracking of Type 316 Stainless Steel in Oxygenated and Chlorinated High Temperature Water," *Corrosion Science*, 25, No. 8/9 (1985) p. 769.

20. R. N. Parkins, "Develpment of Strain-Rate Testing and Its Implications," *Stress Corrosion Cracking-The Slow Strain-Rate Technique, ASTM STP 665*, G. M. Ugiansky and J. H. Payer, Eds., American Society for Testing and Materials, Philadelphia (1979) p. 5.

21. R. N. Parkins and B. S. Greenwell, *Metal Science*, 11, p. 405.

22. P. Maiya, "Prediction of Environmental and Strain-Rate Effects on the Stress Corrosion Cracking of Austenitic Stainless Steels," *Predictive Capabilities in Environmentally Assisted Cracking, PVP- Vol. 99*, American Society of Mechanical Engineers, Miami Beach, FL (November 1985) p. 39.

23. T. Shoji, K. Yamaki, R. G. Ballinger and I. S. Hwang, "Grain Boundary Segregation and Intergranular Stress Corrosion Cracking Susceptibility of Austenitic Stainless Steels in High Temperature Water," *Proc. 5th Int. Symp. Env. Deg. Mat. Nucl. Power Syst.-Water Reactors*, ANS, Monterey, CA (1991) p. 827.

CHAPTER 6

IN-FLUX MATERIALS EFFECTS THAT INFLUENCE IRRADIATION ASSISTED STRESS CORROSION CRACKING

A hypothesis or theory is clear, decisive and positive but it is believed by no one but the man who created it. Experimental findings, on the other hand, are messy , inexact things which are believed by everyone except the man who did the work.

Harlow Shapley
(1885-1972)

6.1 INTRODUCTION

Radiation effects on materials were recognized as a significant area of concern even during the initial development stage of nuclear reactor technology[1]. Research efforts have concentrated on evaluating both microstructural and mechanical property effects with the motivation of quantifying the relationship between the two. A well developed understanding of the fundamental principles governing microstructural evolution during irradiation has been achieved; theoretical predictions have been verified, refined or stimulated by direct physical observation using AEM and computational simulation. These tools have provided the means of studying accumulated damage (i.e. post-irradiation) and instantaneous damage (i.e. *in situ* irradiation) to the microstructure. Mechanical properties investigations have relied largely on post-irradiation tests, leaving an uncertainty of the instantaneous radiation effect on the material performance. Some work in high resolution electron microscopes has been used to bridge this gap, but many questions remain as to the similitude to in-core components. A series of proceedings addressing these issues have significantly contributed to understanding the microstructural, microchemical and mechanical property behavior on a fundamental level[2-10]. The contribution of *in situ* radiation effects on materials to irradiation assisted stress corrosion cracking, however is not as well understood.

A number of mechanisms have been postulated as influencing IASCC behavior of LWR structural materials like stainless steels, but no conclusions have been made because of a paucity of data that addresses the microscopic influences on the macroscopic mechanical properties[11]. As discussed in the introduction (cf. section 1.2), different radiation-induced effects are still a matter of debate, partly due to a lack of relevant data. *In situ* radiation damage studies can help eliminate some of the uncertainties and assist in determining the relationship between microstructural and mechanical properties. A theoretical evaluation of the mechanisms can be made on the basis of representative time constants for the individual process compared to the time constant of the macroscopic behavior. This section provides the results of these calculations, comparisons with the microstructure, microchemistry, hardening and relaxation time constants and the predicted impact on the mechanical properties. The material property data determined for the SSR specimens tested under a fast neutron flux of ~5 x 10^{13} n/cm^2s provides some uniquely relevant data that can be compared with the theoretical predictions of *in situ* material behavior subject to a radiation flux.

6.2 MICROSTRUCTURE EVOLUTION ON A SHORT TIME SCALE

The microstructural evolution of austenitic stainless steels under irradiation shows a complex dependence on temperature and fluence. These dependencies are particularly difficult to quantify for LWR conditions because of observed transitions at the temperatures and fluences of interest for LWR in-vessel components. In a review by Maziasz[12] the temperature dependence was categorized by low and high temperature behavior with the transition temperature at ~300°C. The dependence of microstructure development on fluence has been noted in irradiation creep and swelling research[13-16]. The transition between low fluence and high fluence behavior is observed at ≈1 x 10^{25} n/m^2 to 1 x 10^{26} n/m^2 (E> 1.0 MeV).

It should be noted that transitions of microstructural dependence occur at temperatures and fluence levels typical of LWR in-vessel components, hence extrapolation of results from high temperature or high dose experiments may not be valid. This emphasizes the complex radiation-induced interactions that occur for LWR structural materials and the importance of conducting material tests at the particular conditions to further clarify the contribution of low and high regime processes.

Under fast neutron irradiation, material damage occurs in the form of damage cascades induced by interaction of the neutron with an atom of the host matrix which is then denoted the primary knock-on atom (PKA). The PKA then moves through the matrix forming interstitial-vacancy pairs in the nascent cascade. This interaction time is estimated to be on the order of

10^{-11} to 10^{-10} seconds[17,18]. Next, a short period of diffusional movement, on the order of 10^{-7} to 10^{-6} seconds[18], occurs which results in annihilation of some fraction of point defects and the development of defect clusters and interstitial loops. Following which the nascent cascade is completed.

Over longer periods of time, singular point defects migrate to sinks where they are annihilated or to like defects to agglomerate. The results are voids and bubbles from vacancy agglomeration and interstitial loops from interstitial-interstitial interactions or vacancy emission from existing interstitial loops. It is the nucleation and growth of interstitial loops (faulted with a burger's vector, b, equal to $^{a}o/3<111>$) that is considered the dominant microstructure effect in post-irradiation studies of austenitic stainless steels[13].

Since the in-flux SSR test results for the solution annealed type 304 specimen showed a 20% higher yield stress compared to out-of-flux SSR tests for the same material and condition(cf. section 4.4), it was suggested that "instantaneous" radiation damage increased the material's resistance to plastic deformation. The plausibility of this in-flux effect can be examined by physical arguments and by comparing the representative time constants estimated for radiation-induced processes and deformation processes. In irradiated materials, the development of microstructural features has been correlated with changes in the macroscopic behavior. The three main microstructural features of stainless steels which contribute to resistance to dislocation glide and consequently an increase in the yield stress are: voids, dislocation networks and dislocation loops[19].

6.2.1 *Time Characteristic for Dislocation Loop Nucleation*

The time characteristic for point defect creation can be assumed to be equivalent to that of the nascent cascade, i.e. ~10^{-12} seconds, and an initial population of voids can be considered to be created on a time scale equivalent to the defect cluster development, i.e. 10^{-6} seconds. The time characteristic for dislocation loop development is not so readily apparent. There have been numerous studies which modeled the microstructural development of metals, but most assumed a quasi-steady state behavior where the loop nucleation and growth stages were completed. However, to study the material behavior in-flux, the initial transient for loop nucleation and growth is the critical time characteristic. Determining this transient response requires the solution of a set of differential equations of the form below[20] which follow the development of defect clusters, e.g. dislocation loops, voids and gas containing voids.

$$dn_j/dt = \dot{n}_j + \sum_i k_{i\to j} n_j - \sum_i k_{j\to i} n_j - l_j \qquad \text{(eq. 6-1)}$$

In this expression, n_j is the concentration of defect clusters (e.g. dislocation loops), $\dot{n}_j$ is the rate at which clusters are created directly (e.g. di-interstitials from the nascent cascade), $k_{i\rightarrow j}$ is the rate constant for the probability that a cluster type j is *created* from a different cluster type (e.g. voids or gas containing voids), $k_{j\rightarrow i}$ is the rate constant denoting the probability that a cluster type j is *converted* into a different type of cluster, and l_j is the loss of type j defect clusters to sinks other than the clusters explicitly modeled in the third term.

Hayns has reported the solution to Eq. 6-1 for the austenitic stainless steel M316 for a number of temperatures and dose rates[21]. Since the microstructural development of different stainless steel alloys is very similar[13], the results for M316 stainless steel can be used for the evaluation of the 304 and 316L alloys tested in this work.

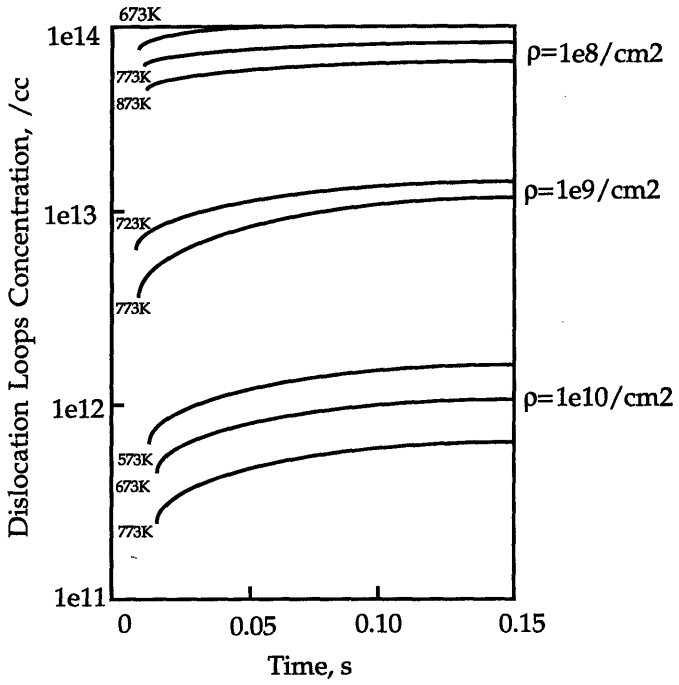

Figure 6-1. Total loop concentrations for M316 as a function of time (from Hayns[21])

Figure 6-1, from Hayns' paper, shows the initial transients for dislocation network densities of 10^{12} m^{-2} and 10^{14} m^{-2} as reported for a dose rate of 1 x 10^{-6} dpa/s at temperatures between 573°K and 773°K. As seen in the figure, the dislocation loop concentrations saturate in less than 0.2 seconds for both dislocation network densities. The dislocation network densities are representative of solution annealed and 1 dpa pre-irradiated stainless steel[12,22]. These are the material conditions of the specimens tested in the MIT in-core SSR facility, but the dose rate and temperature differ from the environmental conditions of the in-flux SSR specimens. For the SSR specimens loaded in the MITR-II, the fast neutron flux is ~5 x 10^{13} n/cm^2s which

corresponds to a dose rate of 0.7×10^{-7} dpa/s by the Norgett-Robinson-Torrens (NRT) displacement model[23] and a temperature of 553°K. Hayns' predicted dislocation loop concentrations must be extrapolated to the temperature and dose rate conditions representative of the MIT in-core SSR tests. Saturation times change very slightly with dose rates and temperatures; they increase with lower dose rate and decrease with lower temperatures which tends to diminish the net changes. For the above reasons, the saturation time of 0.2 seconds is adopted for the stainless steels tested in the present work. According to Hayns' calculation, there is a weak temperature dependence in the temperature range studied, such that loop concentrations slightly increase with decreasing temperatures. Extrapolating the results to 553°K increases the saturation concentrations of Figure 6-1 by a factor of 1.5.

Hayns also examined the dose rate influence on loop nucleation and growth and reported the saturation concentrations versus temperature for two dose rates, 10^{-3} dpa/s and 10^{-6} dpa/s. At the temperature of interest, the saturated loop concentration decreases by a factor of 12 per decade reduction in dose rate. Extrapolating to the lower dose rate in this research (0.7×10^{-7} dpa/s), which is typical of LWRs in general, the saturation loop concentrations in Figure 6-1 will be reduced by a factor of 15.

6.2.2 *Interaction Time for Loops and Mobile Dislocations*

The characteristic time for irradiation induced microstructural development of loops can be compared with the interaction time between mobile dislocations and the obstacles in their path (i.e. dislocation loops). This interaction time for deformation is related to the dislocation velocity which depends on the applied strain rate. The velocity-strain rate relationship is given in Eq. 6-2[24]:

$$\dot{\varepsilon} = \tfrac{1}{2}\rho b\bar{v} = \frac{\rho b l^*}{2t^*}, \qquad \text{(eq. 6-2)}$$

where

$\dot{\varepsilon}$ is the true strain rate,

1/2 is an approximate Schmid factor,

ρ is the mobile or glissile dislocation density (i.e. dislocation network density),

b is the burger's vector, and

$\bar{v}$ is the average dislocation velocity.

The average dislocation velocity can be calculated as the quotient of the mean inter-obstacle spacing, l^*, and the interaction time, t^*, since the interaction time is much greater than the time for the dislocation to travel between obstacles. For the present situation of stainless steels subject to a

radiation flux, the obstacles are the dislocation loops which have a mean spacing inversely proportional to the square root of the loop concentration, N_l, and loop diameter, $2R_l$[18]:

$$l^* = (2R_l N_l)^{-½}. \qquad \text{(eq. 6-3)}$$

Substituting the expression for the mean loop spacing, l^*, into Eq. 6-2 and solving for the characteristic time of deformation, t^*, yields the following:

$$t^* = \frac{\rho b}{2\dot{\varepsilon}\sqrt{2R_l N_l}}. \qquad \text{(eq. 6-4)}$$

From TEM examination[25] of type 304 (heat AJ9139) pre-irradiated to 0.8 x 10^{25} n/m^2 and from calculations[26] for solution annealed type 304 stainless steel, the mean loop radius is estimated to be ~5 nm. The loop concentration for the solution annealed specimen is the saturated loop concentration estimated from Hayns' work, 1 x 10^{19} m^{-3}, as described above. The pre-irradiated specimen will have a pre-existing distribution of dislocation loops[22] of concentration ~5 x 10^{21} m^{-3}, which is much larger than the marginal increase of loops, i.e. 2 x 10^{17} m^{-3}, produced during in-flux slow strain rate tests. For the in-flux SSR tests, the average true strain rates were ~4 x 10^{-7} s^{-1}, the burger's vector for the dislocation network is $a_o/2$<110> which is 0.24 nm, the dislocation network density is 10^{12} m^{-2} for solution annealed stainless steel and 10^{14} m^{-2} for ~0.7 x 10^{25} n/m^2 pre-irradiated stainless steel. Finally substituting these values into Eq. 6-4, the characteristic times of deformation interactions for the solution annealed and pre-irradiated conditioned material are given below.

$$t^*_{SA} = \frac{(10^{12} m^{-2})(0.24nm)}{2(4x10^{-7} s^{-1})\sqrt{2(5nm)(1x10^{19} m^{-3})}} = 950\,\text{sec} \qquad \text{(eq. 6-4a)}$$

$$t^*_{PI} = \frac{(10^{14} m^{-2})(0.24nm)}{2(4x10^{-7} s^{-1})\sqrt{2(5nm)(5x10^{21} m^{-3})}} = 4240\,\text{sec} \qquad \text{(eq. 6-4b)}$$

From the above calculations, the characteristic time for dislocation network-loop interaction is found to be much greater than the saturation time of 0.2 seconds for dislocation loop nucleation and initial growth. Hence, for *slow strain rate conditions* a field of interstitial loops due to the fast neutron flux is expected to be fully developed with respect to deformation induced dislocation motion. Consequently, this distribution of dislocation loops can act as an obstacle to dislocation glide and therefore increase the flow stress of the metal. The predicted affect on the yield stress and comparison with the in-flux tensile properties will be discussed in section 6.4.1.

Now according to this analysis, at sufficiently high strain rates the dislocations will sweep through the material during dislocation loop nucleation or at least before the initial development. With Eq. 6-2, one can estimate the limiting strain rate at which instantaneous damage effects will occur on the same time scale as mechanical deformation by substituting the

saturation time of ~0.2 seconds for the loop-dislocation interaction time. The estimated limiting strain rates, 2.5×10^{-3} s^{-1} and 8.5×10^{-3} s^{-1} for solution annealed and 1 dpa pre-irradiated material, respectively, are in the range of conventional tensile testing[27] which means that the dominant microstructure feature under irradiation will change from dislocation loops for slow strain rate conditions to nascent cascade damage (e.g. point defects and voids) for strain rates employed in general material property testing. The transition strain rate is predicted to be ~5×10^{-3} s^{-1} for stainless steel components in LWR core regions.

6.3 IRRADIATION CREEP OF STAINLESS STEELS IN LWR SERVICE

A critical question for structural materials subject to radiation is the effect of irradiation enhanced creep strains. Although generally considered detrimental due to bulk deformation, i. e. geometry changes, creep strains can have a positive effect by relaxing high localized stresses that occur near stress raisers (e.g. notches, corners, and cracks). The influence of irradiation creep compared to other deformation processes active for a particular component depends on its relative contribution to the total strain, accrued over a small time interval and over the life of the component. An evaluation of the time characteristics of irradiation creep relative to other deformation processes for irradiation assisted stress corrosion cracking will be presented in this sub-section.

For the case of IASCC, the local stress field ahead of the crack tip is the region of action. Since the stress field develops in time as the crack propagates, the impact of the creep strain depends on how quickly it develops relative to the crack tip moving forward. And according to the slip dissolution model, the crack velocity depends on the strain rate. The time measure of comparison for creep is simply then the rate at which the material flows by creep (creep rate) compared to the rate at which plastic strain is mechanically put into the material (applied strain rate). For conventional applications of structural materials creep strains and strain rates become significant only at high temperatures (i.e. $\approx> 0.5T_m$ which is one half the melting temperature or around 900°K for stainless steel); however, under irradiation low temperature creep rates are enhanced by orders of magnitude. The relative contribution of irradiation enhanced creep to the nominal strain rate may be non-negligible under the slow strain rate conditions which are employed in constant extension rate or constant load tests and are characteristic of nuclear vessel internal structural components.

6.3.1 Review of Functional Dependencies

Comprehensive reviews of irradiation creep, describing trends, functional dependencies and mechanisms have been written by Garner[28], Matthews and Finnis[29], Ehrlich[30], Harries[14], and Gilbert[31]. These reviews indicate that data comes most frequently from experimental conditions relevant to the liquid metal fast reactor technology (e.g. in the temperature range 400°C-700°C and at high damage levels >10 dpa), but require extrapolation to the temperatures and fluence levels representative of light water reactor (LWR) technology (e.g. 250-350°C and 1-2 dpa). Results from a number of papers which have reported experimentally and computationally determined irradiation creep strain rates for stainless steels at low temperature and low fluence can further benchmark the extrapolated results.

An empirical representation of irradiation induced creep in LWR structural materials includes the effects of flux, stress, temperature and fluence. According to most formulations, irradiation creep rates of stainless steels show a linear dependence on flux and stress and a weak temperature dependence. Fluence effects, often modeled by including a swelling-coupled term[28,30,32], $\dot{\varepsilon}_{irr}^{sw}$, also show an approximately linear dependence. Analogous to thermal creep, the swelling-independent part of irradiation creep has a primary or transient component, $\dot{\varepsilon}_{irr}^{tr}$, and a steady state component[33], $\dot{\varepsilon}_{irr}^{ss}$. The formulation of transient and steady state contributions was first suggested by Hesketh[34] and that of the swelling-coupling by Foster[35] and Straalsund[32]. The irradiation creep rate, represented by the sum of the three terms, is usually expressed as given below:

$$\dot{\varepsilon}_{irr} = \dot{\varepsilon}_{irr}^{tr} + \dot{\varepsilon}_{irr}^{ss} + \dot{\varepsilon}_{irr}^{sw} = \frac{A\phi\sigma}{F}\exp(-\frac{\phi t}{F}) + B\phi\sigma + D\dot{S}\sigma, \qquad \text{(eq. 6-5)}$$

where

A, B, D and F are material constants that vary with temperature and fluence,

ϕ is the damage rate (flux),

ϕt is the accumulated damage (fluence),

$\dot{S}$ is the swelling rate and

σ is the applied stress.

Some representative values for the constants are listed in Table 6-1. According to the table, A is ~3×10^{-7} MPa^{-1}, F is ~0.1-0.7 dpa, B is ~$0.5\text{-}2 \times 10^{-6}$ $MPa^{-1}dpa^{-1}$ and D is ~$0.2\text{-}12 \times 10^{-3}$ s^{-1}. The data reveals the similar behavior of different types (304, 304L, 316, 321 and 347) and materials conditions (solution annealed and 20% cold worked) of stainless steels. However, differences in the coefficient values may be more than experimental uncertainty since the experiments were conducted at different damage rates (10^{-8} - 10^{-6} dpa/s), fluences (0.1-100 dpa) and temperatures (70°K-800°K). Based upon a literature review and some simplifying physical arguments, Eq. 6-5

Table 6-1. Irradiation creep rate coefficients for austenitic stainless steels.

Type	*A* MPa^{-1}	*D* s^{-1}	*F* dpa	*B* $MPa^{-1}\ dpa^{-1}$	*B1* MPa^{-1} - $(dpa\ s)^{-1/2}$	Comments	Reference
J316				2.2e-4	9.02e-8	335K in ORR, 1.68e-7 dpa/s, <8 dpa	Grossbeck et al.[36]
J316				1.4e-4	6.18e-8	605K in ORR, 1.95e-7 dpa/s	Ibid.
J316				1.4e-4	6.18e-8	675K in ORR	Ibid.
Ni				1.23e-5	2.88e-9	80K in Herald,	Hesketh[37]
321 (En58B)				6.20e-6	1.45e-9	315K in Herald	Ibid.
304				2.80e-6	6.29e-10	450K in K R	Bement et al.[38]
304				1.05e-6	4.06e-10	640K in K R	Ibid.
304, 316				1.41e-6	1.21e-9	525K in DFR, 7.0e-7 dpa/s	Mosedale et al.[39,40]
304, 316	2.6e-7		0.698	5.70e-7		525K	Leggett[41]
304, 316	2.9e-7						Gilbert[31]
M316	0		~0.1	1.13e-6	7.99e-10	555K in DFR, 5e-7 dpa/s,	Mosedale et al.[42]
321 (En58B)	3.4e-6			1.5e-6		555K in DFR	Ibid.
				3.53e-5	1.14e-8	560K in BR-10	Kruglov et al.[43]
304				1.75e-6	2.96e-10	575K in NRU, 2.86e-8 dpa/s, >0.286 dpa	Causey et al.[44]
304L				2.0e-6	1.55e-9	580K in EBR-II, 6.0e-7 dpa/s, <45 dpa	Walters et al.[45]
316 20%CW				6.0e-7		650K in EBR-II, extrapolated to 1 dpa	Chin, Gilbert[46]
347		6.3-12e-3		1.0e-6	1.12e-9	625K in BOR-60 <60 dpa	Neustroev, Shamardin[47]
304L		2.7e-3		9.2e-7	8.4e-10	673K in EBR-II	Weiner[48]
304, 316		~3e-3		7.2e-7	5.6e-10	700K in EBR-II, >10 dpa	Straalsund[32]
				2.53e-5	2.65e-8	773K in EBR-II	Hudson et al.[49]
304, 316, 321, 347				2e-6		555K-825K, <20 dpa	Ehrlich[30]
		~6e-3		~1e-6			Garner, Porter[50]

All stainless steels in the solution annealed condition unless otherwise specified.
dpa is determined by the NRT damage correlation[23].

and the coefficient values were adapted to the specific application of austenitic stainless steels as LWR structural components. A discussion of the simplifications and modified functional dependencies follows.

6.3.2 *Simplified Expression for LWR Environment*

The creep rate equation was first simplified by omitting the transient term. The magnitude of the transient term ($A\phi/F$) is negligibly small compared to the steady state term (B), so in general and for the case of high fluence in particular, it can be ignored relative to the steady state and swelling-coupled creep rate terms. A further simplification can be made for in-vessel structural components like the top guide and core shroud in a BWR, that have end-of-life accumulated doses, ≈1-2 dpa, which are below the incubation dose (~5-10 dpa) for swelling. Consequently, the swelling-coupled term is not significant for LWR structural materials and can also be neglected. Neglecting the transient and swelling contributions leaves only the steady state, swelling-independent term with its material and temperature dependence implicitly included in the coefficient, B. The temperature dependence of stainless steel's steady state irradiation creep rate is complex, but can be modeled as the product of a temperature-dependent function multiplied by a temperature-independent material coefficient, B_0. For a quantitative analysis of irradiation creep rates, the functional dependencies of stress, temperature and flux need to be determined. The creep coefficient and functions adopted for the case of LWR in-vessel stainless steels are presented below.

6.3.2.1 Stress dependence

The commonly adopted linear stress dependence of irradiation creep was noted previously. This is a significant distinction between irradiation induced creep rates and thermal creep rates. Thermally activated creep rates follow a power law dependence with exponents of ~6 for stainless steel, whereas the linear stress dependence of irradiation creep rates is equivalent to a power law exponent of ~1. This difference in stress dependence helps distinguish the two mechanisms. Although some researchers[51] have observed a transition stress for irradiation creep rates, above which the linear dependence changes to a power law dependence with an exponent of ~2. At high temperatures (>700°K) this transition stress can be attributed to a mixed response of thermal and irradiation creep contributions. At lower temperatures the explanation is not so clear. Nevertheless for conditions appropriate to LWR materials, the linear stress dependence is considered more representative of data in the literature.

In establishing a quantitative relationship for irradiation creep strain rate, effective strain and effective stress are used. Typically, the Soderberg formalism[52] for constant volume

processes is adopted to convert data from the three different stress states employed in creep tests [e.g. tensile (uniaxial), shear (helical coils), and hoop or biaxial (pressurized tubes)]. However in the case of non-conservative volume creep, the Soderberg formalism does not apply and the effective stress and strain relationships can be expressed after Gilbert and Straalsund's formulation[53]. The effective stress-strain formalisms for constant volume and non-conservative volume creep are shown in Eq. 6-6 and 6-7, respectively:

$$\bar{\varepsilon}/\bar{\sigma} = \varepsilon/\sigma = \gamma/3\tau = 4\varepsilon_h/3\sigma_h \text{ and} \qquad \text{(eq. 6-6)}$$

$$\bar{\varepsilon}/\bar{\sigma} = \varepsilon/6\sigma = \gamma/3\tau = 4\varepsilon_h/33\sigma_h, \qquad \text{(eq. 6-7)}$$

where

$\bar{\varepsilon}/\bar{\sigma}$ are effective,

ε/σ are tensile,

γ/τ are shear and

ε_h/σ_h are hoop strain per unit stress ratios, respectively.

With the functional stress dependence and the use of effective strain and stress, irradiation creep rates from different experiments can be normalized and a single quantitative relationship developed. First, the effects of flux and temperature also need to be defined. These two parameters are often inter-dependent in experiments which makes it difficult to characterize their individual effects on irradiation creep rates. To distinguish and quantify the individual effects of the temperature and flux, the two parameters are discussed in parallel.

6.3.2.2 Temperature and flux dependence

The first thing to note for temperatures typical of LWR conditions (i.e. $<0.3T_m$), is that irradiation enhanced creep rates far exceed thermal creep rates. Not until temperatures reach around 900°K do thermally activated creep rates become significant. Despite the experimental inter-dependence of flux and temperature, investigations of stainless steel's temperature dependence on irradiation creep have resulted in fairly well defined functions, at least for temperatures greater than 550°K. At lower temperatures, the creep rate is described qualitatively as increasing with decreasing temperatures and having a minimum between 300°K and 550°K[15,54].

As the temperature increases above 550°K the irradiation creep rate exhibits initially a weak temperature dependence regime and at higher temperatures a strong temperature dependence regime. The functional dependence is exponential (Arrhenius) for both regimes and the transition temperature is ~850°K. For temperatures between 550°K and 850°K, the small

temperature dependence of irradiation creep has been observed by a number of researchers[32,45,49]. The Arrhenius dependence was quantified by Wassilew et al.[55] to have an activation energy of 0.13eV below 850°K and 1.16eV above 850°K. The temperature dependence transition in creep rate was attributed to the rate controlling species changing from interstitials to vacancies.

In contrast to the higher temperature results, research at very low temperatures (<550°K) have shown creep rates increase as the temperature decreases. McElroy, Dahl and Gilbert[56] defined a semi-empirical exponential function based on data from Hesketh[37], Bement[38] and Mosedale[39]. For the correlation, the data was normalized according to a linear flux model and non-conservative volume creep. The import of the normalization will be discussed later. More recent work on fusion reactor material applications by Grossbeck et al.[36] showed creep rates increase by a factor of ~4-7 when the temperature was lowered from ~650°K to 330°K, which was ~2-3 times greater than McElroy et al.'s temperature correlation. Besides having a larger temperature gradient response, Grossbeck et al.'s normalized creep rates were also an order of magnitude higher. Such large discrepancies between normalized creep rates determined with different experiments suggest that one, or at least one, of the normalizing parameters is in error. This is not related to the experimental inter-dependence of flux and temperature, but rather to the functional dependencies assumed in normalizing data. As stated above, the irradiation creep rate is generally considered to vary linearly with stress and flux. Since the linear stress dependence is considered well supported, experimental evidence for the linear flux dependence seems to merit serious re-evaluation.

Although a linear flux dependence is most commonly applied to normalize irradiation creep rate data, a square root dependence on flux, based on both experimental evidence and theoretical arguments, has been reported in a number of papers[42,55,57,58]. Why there is this discrepancy is an interesting question. Two observations can help reconcile this difference: 1) the linear flux dependence is valid over a small range but increases in error beyond this range and 2) the experiment facilities make it difficult to evaluate the flux effects independent of other variables. The first observation will be true for the case of a square root dependence since the range of fluxes applied in irradiation creep experiments is 10^{-6} to 10^{-8} dpa/s. A factor of ten difference in flux (dpa/s) results in a factor of ~3.5 in normalized creep rate which is on the same order as the experimental scatter. But the difference between a fast reactor flux (10^{-6} dpa/s) and a power reactor flux (10^{-8} dpa/s) results in a factor of 10 difference which is comparable to the difference observed in the low temperature fusion work and others. Touching on the second observation, Garner[28] noted that flux effects have been difficult to assess because, in most experiments, the flux can not be varied independently of the temperature. As an example, work by Kruglov et al.[43] indicated that irradiation creep varies linearly with flux, but the data was not

measured at constant temperature. In fact, the temperature increased from 560°K to 765°K for fluxes between 0.95 x 10^{14} n/cm^2s and 9.5 x 10^{14} n/cm^2s. Over this temperature range, irradiation creep rates are expected to increase by a factor ~2 which suggests that the true flux dependence is less than linear. In experiments where flux effects were studied at constant temperature, the irradiation creep rate actually showed a square root dependence on flux[42,55,57]. This square root dependence is explained by increased recombination of point defects due to a higher density of damage cascades[58]. Reanalysis of Kruglov et al.'s data is also consistent with a square root flux dependence. By adjusting the data to a constant temperature reference (using Wassilew et al.'s results), the irradiation creep rate dependence on damage rate (i.e. flux) was determined. Figure 6-2 shows Kruglov et al.'s original data which fits a linear flux dependence and the temperature normalized data which compares very well with a square root flux dependence. Fitting, by least squares method, the temperature normalized data to a power law function with exponent 1/2 resulted in a correlation factor of 0.974 which is indicative of the good agreement observed in Figure 6-2.

The swelling-independent creep rate coefficients normalized by the square root of the damage rate have been calculated for a number of temperatures and are included in Table 6-1 under the column *B1*. Based on the range of damage rates (1 x 10^{-8} dpa/s to 6 x 10^{-6} dpa/s) and temperatures (80K - 773K) sampled in Table 6-1, the square-root normalization, fits no better than the conventional linear flux coefficient, *B*. Apparently, the square root damage rate dependence can not wholly reconcile the range of irradiation creep rates observed by different researchers. However for low temperatures (<0.3 T_m or ~550°K for stainless steel), typical of LWRs, it is concluded that the swelling-independent irradiation creep rate is best modeled as a square root dependence on flux. With the flux dependence defined, the temperature dependence in the range below 550°K can be evaluated.

Rather than adopt McElroy et al.'s correlation, which used a linear flux and non-conservative volume formalism for normalizing the data, the original data and Grossbeck et al.'s results will be analyzed using a constant volume formalism and square root flux dependence. Using an exponential function to fit the data, Grossbeck's and the other data gave similar values for the exponential coefficient, ~-0.003 K^{-1}. The magnitude of irradiation creep rates was chosen to match the data used by McElroy since this corresponded better with measurements made in the middle and higher temperature regimes. For the normalized irradiation creep rate, the temperature dependence can be divided into three regimes (less than 550°K, between 550°K and 850°K, and greater than 850°K) or described by three functions that dominate the creep rate behavior within the specified temperature range. Figure 6-3 displays the temperature dependence of stainless steel's irradiation creep rate over the three regimes and the respective

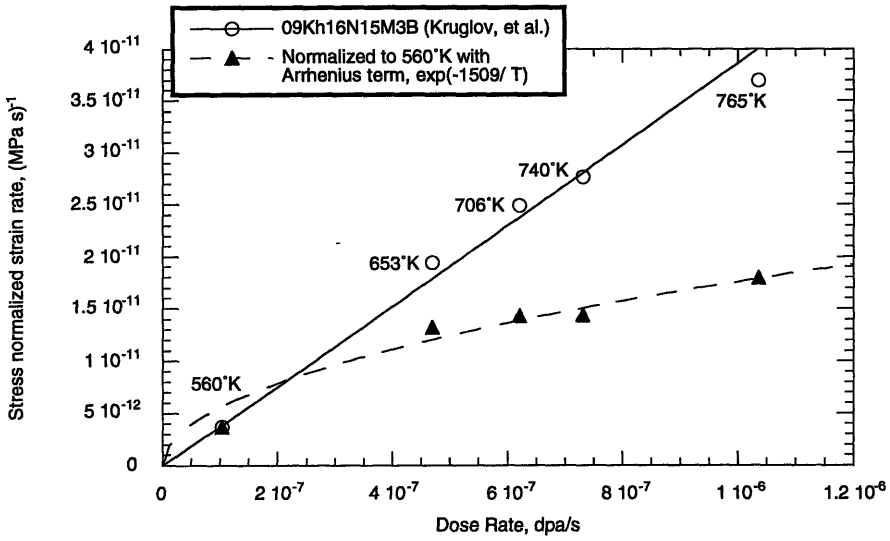

Figure 6-2. Re-analysis of Kruglov et al.'s[43] irradiation creep rate data showing square root dependence on damage rate.

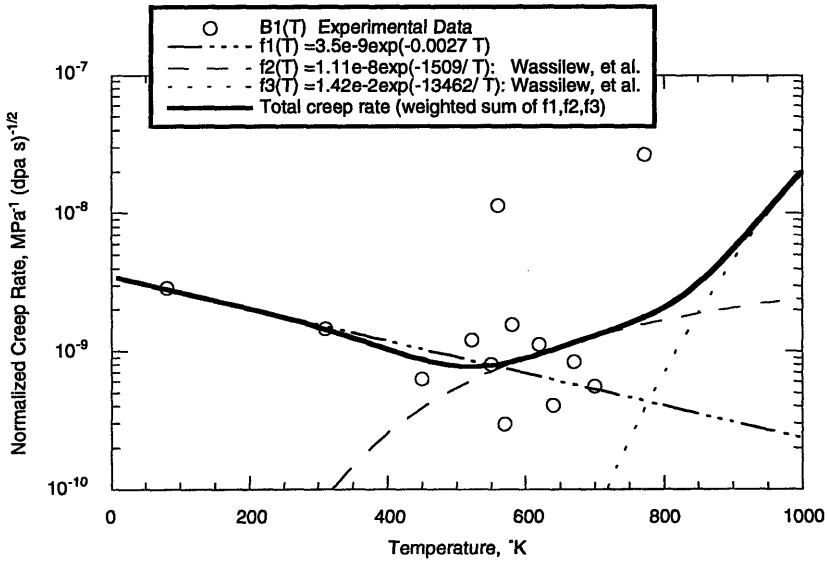

Figure 6-3. Temperature dependence of irradiation creep rate.

governing relationships. The temperature dependent function for the creep coefficient, $f_B(T)$, is expressed as a weighted sum of the three temperature regime functions normalized to unity at 573°K:

$$f_B(T) = W_1(T)f_{1,B}(T) + W_2(T)f_{2,B}(T) + W_3(T)f_{3,B}(T), \qquad \text{(eq. 6-8)}$$

where

$$W_1(T)f_{1,B}(T) = 4.31\exp(-0.0027T),$$
$$W_2(T)f_{2,B}(T) = 137\tanh(T/220 - 2.5)\exp(-1509/T),$$
$$W_3(T)f_{3,B}(T) = 5.17x10^7\tanh(T/220 - 3.18)\exp(-13462/T).$$

An expression for the irradiation creep rate of austenitic stainless steels employed as LWR in-vessel structures can be formulated from Equation 6-6 and 6-8, according to the simplifications and modifications discussed above. The resulting expression, Eq. 6-9, is the product of the steady state, swelling- and temperature- independent coefficient, *B1*, the temperature function, $f_B(T)$, the stress raised to the power ~1, σ^1, and the square root of the damage rate (i.e. flux), $\sqrt{\phi}$:

$$\dot{\varepsilon}_{irr} = B1 f_B(T)\sigma\phi^{1/2} = 8.12x10^{-10} f_B(T)\sigma\phi^{1/2}. \qquad \text{(eq. 6-9)}$$

6.3.3 Comparison of Irradiation and Thermal Creep Rates and Applied Strain Rates

Setting the value of *B1* equal to the average normalized irradiation creep rate at 573°K, 8.12 x 10^{-10} MPa (dpa s)$^{-1/2}$, reproduces the experimental data within an order of magnitude. The predicted irradiation creep rates at LWR operating temperature of 573°K can be compared with the applied strain rate, for the case of SSR tests, and predictions for the thermal creep rates and crack tip strain rates. Formulations for thermal creep rates can be extrapolated from high temperature correlations using the activation energy in the Arrhenius function. Data from Bernard et al.[59] indicated that types 304 and 316 stainless steels have slightly different thermal creep properties. Creep rates at 622°C and 722°C are higher for type 304 than for type 316. Type 304 has a lower activation energy, but both types show a power law stress dependence with exponent 6.9:

$$\dot{\varepsilon}_{th}^{304} = (3.58 \pm 1.22)x10^{-35}\sigma^{6.9}\exp(76.4 - 43780/T), [MPa, ^\circ K]; \qquad \text{(eq. 6-10)}$$

$$\dot{\varepsilon}_{th}^{316} = (1.23 \pm 0.82)x10^{-43}\sigma^{6.9}\exp(121 - 69280/T), [MPa, ^\circ K]. \qquad \text{(eq. 6-11)}$$

Formulations for crack tip strain rates under different loading conditions (e.g. SSR, constant and cyclic load) have been given by Ford et al.[60,61,62]. The semi-empirical expressions are derived from fracture mechanics and in-plant and laboratory crack growth data measured at LWR operating conditions. For SSR conditions, the crack tip strain rate depends on the fracture morphology and density of secondary cracks, but is between 1 and 10 times the applied strain rate for transgranular and intergranular cracks in stainless steel. The constant load expression (for long, i.e. >1mm, cracks) is given as a function of stress intensity, *K:*

$$\dot{\varepsilon}_{ct} = 4.1x10^{-14}K^4 \cong 4.1x10^{-14}\sigma^4(\pi a)^2, [MPa\sqrt{m}, MPa, m]. \qquad \text{(eq. 6-12)}$$

Figure 6-4 displays the average strain rates for the applied, irradiation creep and thermal creep contributions and the calculated crack tip strain rates for SSR and constant load conditions as a function of stress at 300°C. For comparison purposes a crack length of 1 mm is assumed. Note that the crack tip strain rate calculation is sensitive to the assumed crack length because of the square dependence and would be 100 times greater for a crack length of just 1 cm (typical of cracks found in BWR core shrouds[63]). A similar plot by Andresen et al.[62] predicts irradiation and thermal creep rates 1-4 orders of magnitude greater than the current estimate. Andresen et al. applied Straalsund's[32] irradiation creep rate expression derived from high

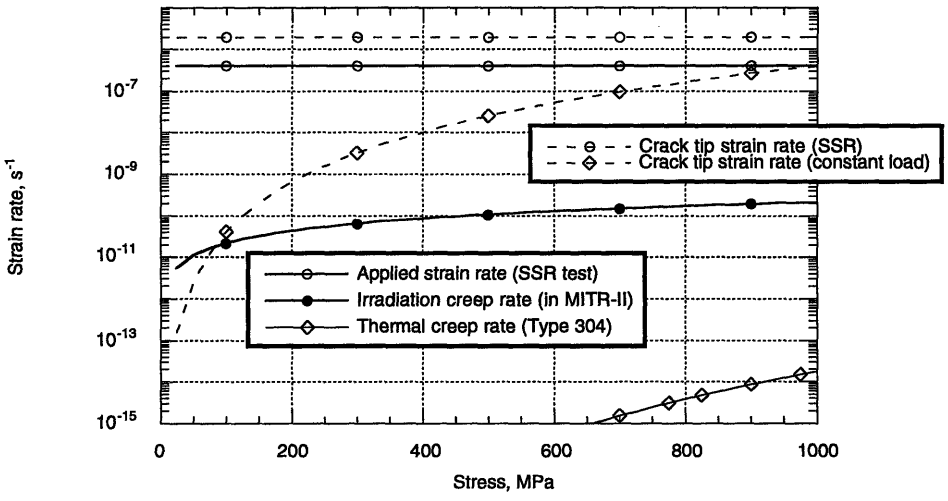

Figure 6-4. Comparison of irradiation and thermal creep strain rates with applied strain rates for type 304 stainless steel at 300°C in MITR-II.

fluence specimens and recognized that the predicted rate could be as much as ~10 times greater than the strain rate typical for LWR components. The thermal strain rate expression employed by Andresen et al. is for transient or primary creep, whereas Bernard et al.'s[59] expression is for steady state creep. Although the transient stage is the dominant contributor to thermal creep at low temperatures, the secondary, or steady state, creep rate provides a more consistent comparison with the steady state irradiation creep rate. Some interesting observations can be made from Figure 6-4.

The first point to observe is that irradiation creep rates are insignificant compared to the applied strain rate employed during the in-flux SSR test. This justifies neglecting its effect on the IASCC material performance determined in this series of tests and for in-flux SSR tests in general. An equally significant observation is the difference between the predicted strain rates for constant load conditions and for slow strain rate conditions and their magnitude relative to irradiation creep. The applied strain rate (average and crack tip) for the in-flux SSR test is 3-4 orders of magnitude greater than the strain rate attributed to irradiation-induced creep. In contrast, the irradiation creep rate is comparable to the constant load crack tip strain rate at low stresses, but becomes insignificant at stresses higher than ~300 MPa. It should be remembered however that this comparison is approximate and very sensitive to the assumed crack length. Even for a modest crack length of 1cm (1mm was assumed in Figure 6-4), the crack tip strain rate is predicted to be 100 times greater which would make the irradiation creep contribution insignificant at stresses above ~100 MPa. Despite the uncertainties inherent in the calculation, it seems evident that the effect of irradiation creep can always be neglected for SSR tests, but should be included for constant load tests performed at low stresses. This also suggests that constant load tests should be preferred for investigating IASCC in a fast neutron flux environment, like the MITR-II. The possible impact of irradiation creep rates on the crack tip stresses is evaluated in the next section.

6.4 IMPACT OF NEUTRON FLUX ON *IN SITU* MECHANICAL BEHAVIOR

The two in-flux mechanisms evaluated here with respect to mechanical behavior are hardening due to radiation produced defects and stress relaxation caused by irradiation induced creep strains. The motivation for understanding microstructural evolution is to predict the corresponding macroscopic changes. This subsection presents the analyses for making this connection and comparison with experiment where data is available.

6.4.1 Hardening and Increased Yield Stress

Three types of radiation induced defects (faulted loops, network dislocations and voids) have traditionally been considered the most significant for increased resistance to dislocation glide or slip[19]. With higher resolution electron microscopy, other microstructural changes like cavity formation and metal-carbide precipitation were also incorporated as strengthening components[64]. Traditional strengthening mechanisms incorporating these microstructural changes successfully predict yield stress increases at higher temperatures and fluences (≥400°C and ≥10 dpa), but underpredict the increases at lower temperatures[65,66]. The discrepancy at lower temperatures has often been attributed to "invisible" microstructure which is below the resolution limit of TEM[67,68]. Garner et al.[69] were able to reconcile the difference by considering the faulted loop component as part of the dislocation network. A more recent paper by Simons and Hulbert[70] adopted Garner et al.'s loop treatment and made reasonable predictions by including the strength contribution of the "unresolvable" black spot microstructure. It seems evident that an accurate strengthening model needs to include the contribution of the "unresolvable" as well as observable microstructure. For low fluence LWR conditions, precipitate and void formation can be ignored and the microstructure features to be considered are faulted Frank loops, network dislocations, cavities and black spot loops. The increased yield strength due to these features is described below.

The dislocation network interaction with glissile dislocations is a long range force which means the moving dislocation feels the influence of more than the nearest neighboring part of the dislocation network. The large Frank loops (≥10 nm diameter) are considered to interact similarly because of their geometry and size (on the order of the inter-loop spacing). The yield stress increase due to network dislocations can be correlated by the Hall-Petch relationship with a constant of ~0.33 for 304 and 316 stainless steel. The faulted Frank loops are modeled in the same manner where the dislocation loops density is given as the product of the loop concentration and mean loop circumference.

$$\Delta\tau_{NW} = 0.33Gb\sqrt{\rho}$$
$$\Delta\tau_{loops} = 0.33Gb\sqrt{2\pi R_l N_l} \qquad \text{(eq. 6-13a)}$$

The strengthening contributions of the cavities and black dot microstructure are formulated as short range particles, after Fleischer's analysis for tetragonal defects[71]. The reported coefficient, 0.33, was assumed for the cavities, whereas the black dot coefficient was set to 0.4 to provide a better fit to post-irradiation data. The number density of cavities was reduced by one half since the minimum size for interaction is approximately equal to the average size of ~4 nm. The hardening due to short range obstacles is given in Eq. 6-13b.

$$\Delta\tau_{cav} = 0.33Gb/l' = 0.33Gb\sqrt{R_c N_c}$$
$$\Delta\tau_{bd} = 0.4Gb/l = 0.4Gb\sqrt{2R_{bd}N_{bd}} \qquad \text{(eq. 6-13b)}$$

The combined strengthening effect of obstacles with similar range is calculated as a quadratic sum (i.e. the square root of the sum of the squares) and that of obstacles with dissimilar range is considered simply additive. Here the loops and network dislocations exert long range forces and cavities and black dots interact on a short range.

$$\Delta\tau_{total} = \sqrt{\Delta\tau_{NW}^2 + \Delta\tau_{loops}^2} + \sqrt{\Delta\tau_{cav}^2 + \Delta\tau_{bd}^2} \qquad \text{(eq. 6-14)}$$

The shear stress is converted to a yield stress by multiplying by $\sqrt{3}$, according to von Mises criterion. Applying this multiplier and substituting Eqs. 6-13 into 6-14 then results in an expression for the irradiation hardening due to dislocations (faulted loops and network), cavities and black dots, in terms of the increased yield stress observed under uniaxial tension:

$$\Delta\sigma_{total} = 0.572Gb(\sqrt{\rho + 2\pi R_l N_l} + \sqrt{R_c N_c + 2.94 R_{bd} N_{bd}}), \qquad \text{(eq. 6-15)}$$

where

$\Delta\sigma_{total}$ is the total increase in yield stress observed under uniaxial tension,

G is the shear modulus,

b is the burger's vector,

ρ is the dislocation network concentration,

R_l and N_l, R_c and N_c, R_{bd} and N_{bd}, are the mean radii and defect concentrations for dislocation loops, cavities and black dots, respectively.

For slow strain rate conditions, a field of dislocation loops was determined to have nucleated and developed in a time much shorter than the typical interaction time between one loop obstacle and a moving dislocation (cf. section 6.2.2). Hence the concentration of dislocation loops is given by the initial saturation concentration calculated by Hayns and is expected to have the largest effect on the observed macroscopic mechanical behavior. It is predicted that as the strain rate increases the most significant microstructure changes from dislocation loops to point defects produced during the nascent damage cascade; the transition strain rate is on the order of that employed in conventional tensile tests (e.g. ~10^{-3} - 10^{-2} s^{-1}). The predicted increase in yield stress due to *in situ* radiation damage is displayed in Figure 6-5 for strain rates ranging from those applied in SSR tests to those applied in conventional mechanical property tests. According

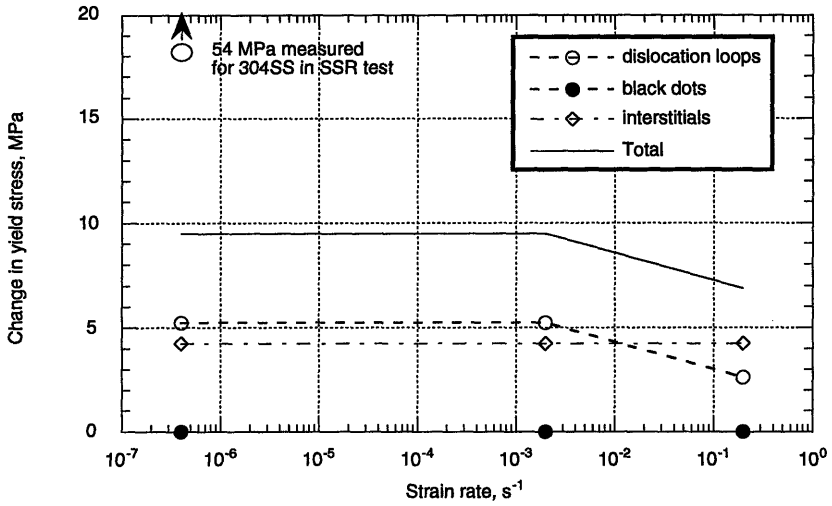

Figure 6-5. Contribution of irradiation induced microstructures to the increased yield stress for in-flux material tests at different strain rates.

to this simplistic model, *in situ* hardening decreases by 30% over the range of strain rates as the dominant obstacle to plastic flow changes from loops to nascent point defects and clusters. It is not surprising that the predicted change in yield stress is lower than the observed quantity. A number of modifications to the model would help reconcile the difference. First, the loop nucleation and growth calculation by Hayns considered a zero stress state, whereas the specimens in the SSR tests are under load which is known to enhance loop nucleation and growth rates[72,73,74]. This would increase the short term saturation loop concentrations and correspondingly the hardening contribution. Second, the black dot and cavity populations were not considered in the calculation by Hayns and so their contribution to instantaneous hardening are not included in this treatment. Despite the discrepancy, it is encouraging that prediction and measurement show the same trend and are of the same magnitude. According to these evidences, the supposition of *instantaneous radiation hardening* is supported by theory and experiment. The impact of irradiation creep on the mechanical state of a structural component is discussed next.

6.4.2 Stress Relaxation by Irradiation Creep

For constrained components, irradiation creep strains, and thermal creep for that matter, are expected to relax the applied stress. Stress relaxation by creep is a well known

phenomenon and in fact is used as an experimental technique for measuring creep strains. Irradiation creep has been suggested as an important phenomenon affecting irradiation assisted SCC although there has been no rigorous quantitative analysis or experimental program to investigate this effect[11,62,75]. The purpose of this section is to examine in semi-quantitative terms the influence of irradiation creep strains on IASCC. Although the treatment here is also simplistic in nature, the insights gleaned can help bridge the current understanding of irradiation creep effects on IASCC to future more detailed analyses.

Only the constant load case will be analyzed since the applied strain rate for the MIT in-flux SSR tests is many orders of magnitude greater than the irradiation creep rate. Combining the irradiation creep rate, Eq. 6-9, and Hooke's law for a bent beam, the elastic stress relaxation for constant load conditions is described by[44]:

$$\sigma = \sigma_{appl} \exp[-B1 f_B(T) E \phi^{1/2} t], \qquad \text{(eq. 6-15)}$$

where the initial transient relaxation has been neglected, σ_{appl} is the applied stress at time $t = 0$, E is Young's Modulus and the rest of the terms are the same as in Eq. 6-9. The actual stress decays away exponentially with time resulting in relaxed loads. The time dependence for either the average or crack tip stresses is the same if expressed as the fractional relaxation. For austenitic stainless steels employed in LWRs, the creep coefficient, $B1\, f_B(T)$ is 8.12×10^{-10} MPa^{-1}(dpa s)$^{-1/2}$, E is 171 GPa and ϕ is $\sim 3 \times 10^{-8}$ dpa/s. Substituting these values into Eq. 6-15 gives a time constant of 4.16×10^7 s (~1.32 years). Operating cycles for LWRs are ~1.5 years which means an upper bound for stress relaxation for in-vessel components will be 63%. For constant load tests which typically last ~3 months (7.8×10^6 s) the maximum fractional relaxation would be 17%. Assuming Andresen et al.'s[62] estimate of 10^5 s for creep growth reactivation intervals (due to temperature and pressure transients) is accurate then the stress relaxation will be less than 1%. The impact on the crack tip stress can range from insignificant to considerable. Since the time constant for irradiation creep induced stress relaxation is fairly large and temperature and pressure changes will reinitiate the creep process, the overall effect will depend on the operational history of the component in question.

6.5 SUMMARY

The characteristic times for irradiation induced microstructural evolution and creep were evaluated in regard to *in situ* radiation damage. The nucleation and initial growth of dislocation loops was determined to have a characteristic time of ~0.2 seconds which is much shorter than the interaction time between a loop obstacle and moving dislocation under slow

strain rates (~4 x 10^{-7} s^{-1}). It was concluded that during in-flux SSR tests a field of dislocation loops numbering the saturation concentration would exist and inhibit slip by dislocation motion.

An irradiation creep rate expression, neglecting transient and swelling-coupled components, was tailored for stainless steels in LWR vessel service. The expression included a linear stress dependence and a square root flux dependence observed in low temperature (<0.3 T_m) experiments. The temperature dependence was formulated by incorporating three functions descriptive of low, mid-range and high temperature regimes (<500°K, between 500°K and 850°K, and >850°K). Using the simplified expression, the irradiation creep rate at 300°C was evaluated for different stresses and compared with applied strain rates and predicted crack tip strain rates. The irradiation creep rate was found to be negligible compared to applied and crack tip strain rates in SSR tests, but was significant, at least for low stresses (<100-350 MPa), compared to crack tip strain rates under constant load conditions.

The impact of in-flux microstructural development and irradiation creep on the mechanical behavior pertinent to IASCC was estimated. The increased yield stress due to *in situ* fast neutron flux was estimated with a modified Orowan stress relationship. Hardening contributions from dislocation loops, network dislocations, black spots, cavities and supersaturation of interstitials were modeled. The predicted increase in yield strength was less than the measured value which was partly explained by some model assumptions. Nevertheless, the higher yield stress observed for solution annealed type 304 stainless steel (on the order of 30-55 MPa) during the in-core SSR tests was consistent with predictions for *in situ* irradiation hardening.

A brief evaluation of exponential stress relaxation by irradiation creep was also presented. Under LWR conditions, the time constant was determined to be ~1.3 years (4.13 x 10^7 s). The maximum stress relaxation calculated with this time constant was 63% of the applied stress for an 18 month fuel cycle. The calculated range of more realistic estimates was from less than 1% to 17% for steady state operation over 10^5 s and 7.8 x 10^6 s, respectively.

The in-flux material effects discussed in this section indicate that *in situ* radiation damage is significant and can alter the physical behavior of materials under stress which will impact its general performance as a LWR structural material and specifically its susceptibility to IASCC.

6.6 REFERENCES

1. E. P. Wigner, "Theoretical Physics in the Metallurgical Laboratory of Chicago," *J. Applied Phys.*, 17 (1946) p. 857.

2. *Effects of Radiation on Materials: 16th International Symposium, ASTM STP 1175*, A. S. Kumar, D. S. Gelles, R. K. Nanstad and E. A. Little, Eds., American Society for Testing and Materials, Philadelphia (1993).

3. *Effects of Radiation on Materials: 15th International Symposium, ASTM STP 1125*, R. E. Stoller, A. S. Kumar and D. S. Gelles, Eds., American Society for Testing and Materials, Philadelphia (1992).

4. *Effects of Radiation on Materials: 14th International Symposium, Volumes I and II, ASTM STP 1046*, N. H. Packan, R. E. Stoller and A. S. Kumar, Eds., American Society for Testing and Materials, Philadelphia (1989).

5. *Radiation-Induced Changes in Microstructure: 13th International Symposium, ASTM STP 955*, F. A. Garner, N. H. Packan and A. S. Kumar, Eds., American Society for Testing and Materials, Philadelphia (1987).

6. *Influence of Radiation on Material Properties: 13th International Symposium, ASTM STP 956*, F. A. Garner, C. H. Henager and N. Igata, Eds., American Society for Testing and Materials, Philadelphia (1987).

7. *Effects of Radiation on Materials: 12th International Symposium, ASTM STP 870*, F. A. Garner, and J. S. Perrin, Eds., American Society for Testing and Materials, Philadelphia (1985).

8. *Effects of Radiation on Materials: 11th International Symposium, ASTM STP 782*, H. R. Brager and J. S. Perrin, Eds., American Society for Testing and Materials, Philadelphia (1982).

9. *Effects of Radiation on Materials: 10th International Symposium, ASTM STP 725*, D. Kramer, H. R. Brager and J. S. Perrin, Eds., American Society for Testing and Materials, Philadelphia (1981).

10. *Effects of Radiation on Structural Materials: 9th International Symposium, ASTM STP 683*, J. A. Sprague and D. Kramer, Eds., American Society for Testing and Materials, Philadelphia (1979).

11. J. L. Nelson and P. L. Andresen, "Review of Current Research and Understanding of Irradiation-Assisted Stress Corrosion Cracking," *Proc. Fifth Int. Symp. Env. Deg. of Mat. in Nucl. Pow. Systems-Water Reactors*, ANS, Monterey, CA (1991) p. 10.

12. P. J. Maziasz, "Temperature Dependence of the Dislocation Microstructure of PCA Austenitic Stainless Steel Irradiated in ORR Spectrally-tailored Experiments," *J. Nucl. Mat.*, 191-194 (1992) p. 701.

13. P. J. Maziasz, "Overview of Microstructural Evolution in Neutron-Irradiated Austenitic Stainless Steels," *J. Nucl. Mat.*, 205 (1993) p. 118.

14. D. R. Harries, "Irradiation Creep in Non-Fissile Metals and Alloys," *J. Nucl. Mat.*, 65 (1977) p. 157.

15. E. R. Gilbert, J. L. Straalsund and G. L. Wire, "Irradiation Creep Data in Support of LMFBR Core Design," *J. Nucl. Mat.*, 65 (1977) p. 266.

16. *Mechanical Behaviour and Nuclear Applications of Stainless Steel at Elevated Temperatures*, The Metals Society, London (1982).

17. J. Yu, "Interstitial Dislocation Loop Nucleation and Growth and Swelling Produced By High-Energy Cascades," *Radiation-Induced Changes in Microstructure: 13th International Symposium, ASTM STP 955*, F. A. Garner, N. H. Packan and A. S. Kumar, Eds., American Society for Testing and Materials, Philadelphia (1987) p. 393.

18. D. R. Olander, *Fundamental Aspects of Nuclear Reactor Fuel Elements*, TID-26711-P1 (1976) p. 407.

19. J. J. Holmes, R. E. Robbins, J. L. Brimhall and B. Mastel, *Acta Metall.* 16, (1968) p. 955.

20. H. Wiedersich, "Theory of Defect Clustering and Void Formation," *Radiation Damage in Metals*, N. L. Peterson and S. D. Harkness, Eds., American Society for Metals, Metals Park, OH (1975) p. 157.

21. M. R. Hayns, "The Nucleation and Early Growth of Interstitial Dislocation Loops in Irradiated Materials," *J. Nucl. Mat.*, 56 (1975) p. 267.

22. J. M. Cookson, R. D. Carter Jr., D. L. Damcott, M. Atzmon and G. S. Was, "Irradiation Assisted Stress Corrosion Cracking of Controlled Purity 304L Stainless Steels," *J. Nucl. Mat.*, 202 (1993) p. 104.

23. M. J. Norgett, M. T. Robinson and I. M. Torrens, "A Proposed Method of Calculating Displacement Dose Rates," *Nucl. Eng. & Des.*, 33 (1975) p. 50.

24. R. E. Reed-Hill and R. Abbaschian, *Physical Metallurgy Principles, 3rd Ed.*, PWS-Kent Publishing Co., Boston (1992) p. 163.

25. H. Mansoux, "Experimental Determination of Radiation Induced Segregation Susceptibility in Austenitic Stainless Steels," SM Thesis, Department of Nuclear Engineering, Massachusetts Institute of Technology, Cambridge, MA (June 1994).

26. C. H. Henager, Jr. and E. P. Simonen, "Critical Assessment of Low-Fluence Irradiation Creep Mechanisms," *Effects of Radiation on Materials: 12th International Symposium, Vol. I, ASTM STP 870*, F. A. Garner and J. S. Perrin, Eds., American Society for Testing and Materials, Philadelphia (1985) p. 75.

27. *Tensile Testing*, ASM 440, P. Han, Ed., ASM International, Materials Park, OH (1992).

28. F. A. Garner, "Irradiation Performance of Cladding and Structural Steels in Liquid Metal Reactors," *Nuclear Materials*, B. R. T. Frost, Ed., Vol. 10 Mat. Sci. Tech., VCH, NY (1992) p. 481.

29. J. R. Matthews and M. W. Finnis, "Irradiation Creep Models-An Overview," *J. Nucl. Mat.*, 159 (1988) p. 257.

30. K. Ehrlich, "Irradiation Creep in Austenitic Stainless Steels," *Mechanical Behaviour and Nuclear Applications of Stainless Steel at Elevated Temperatures*, The Metals Society, London (1982) p. 149.

31. E. R. Gilbert, "In-Reactor Creep of Reactor Materials," *Reactor Technology*, 14, no. 3 (1971) p. 258.

32. J. L. Straalsund, "Irradiation Creep in Breeder Reactor Structural Materials," *Int. Conf. Rad. Effects in Breeder Reactor Struct. Mat.*, M. L. Bleiberg and J. W. Bennett, Eds., The Metallurgical Society of AIME, New York, NY (1977) p. 191.

33. B. M. Ma, "Irradiation Swelling, Creep, Thermal Shock and Thermal Cycling Fatigue Analysis of Cylindrical Controlled Thermonuclear Reactor First Wall," *Nucl. Eng. & Des.* 28 (1974) p. 1.

34. R. V. Hesketh, "A Transient Irradiation Creep in Non-Fissile Metals," *Phil. Mag.*, (1963), p. 1321.

35. J. P. Foster, W. G. Wolfer, A. Biancheria and A. Boltax, "Analysis of Irradiation-Induced Creep of Stainless Steel in Fast Spectrum Reactors," *Proc. Conf. on Irradiation Embrittlement and Creep in Fuel Cladding and Core Components*, BNES, London (November 1972) p. 273.

36. M. L. Grossbeck, L. K. Mansur and M. P. Tanaka, "Irradiation Creep in Austenitic Stainless Steels at 60 to 400°C with a Fusion Reactor Helium to dpa Ratio," *Effects of Radiation on Materials: 14th International Symposium, Vol. II, ASTM STP 1046*, N. H. Packan, R. E. Stoller and A. S. Kumar, Eds., American Society for Testing and Materials, Philadelphia (1989) p. 537.

37. R. V. Hesketh, "Collapse of Vacancy Cascades to Dislocation Loops," *Proc. Int. Conf. Solid State Physics Research with Accelerators*, BNL-50083 (C-52), Brookhaven National Laboratory (1967) p. 389.

38. A. L. Bement, G. J. Dau, E. A. Evans and R. E. Nightingale, Quarterly Progress Report, January, February, March 1970, Reactor Fuels and Materials Branch of USAEC Division of Reactor Development and Technology, BNWL-1349-1, Battelle-Northwest, Richland, WA (May 1970).

39. D. Mosedale, G. W. Lewthwaite, G. O. Leet, and W. Sloss, "Irradiation Creep in the Dounreay Fast Reactor," *Nature*, 224 (December 1969) p. 1301.

40. G. W. Lewthwaite, D. Mosedale and I. R. Ward, "Irradiation Creep in Several Metals and Alloys at 100°C," *Nature*, 216 (1967) p. 472.

41. R. D. Leggett, "Plutonium Fuels for LMFBR-an Extrapolation," WHAN-SA-51 (October 1970).

42. D. Mosedale, D. R. Harries, J. A. Hudson, G. W. Lewthwaite and R. J. McElroy, "Irradiation Creep in Fast Reactor Core Component Materials," *Int. Conf. Rad. Effects in Breeder Reactor Struct. Mat.*, M. L. Bleiberg and J. W. Bennett, Eds., The Metallurgical Society of AIME, New York, NY (1977) p. 209.

43. A. S. Kruglov, M. G. Bul'kanov, V. N. Bykov and Yu. M. Pevchikh, "Investigation of Radiation Creep of Steel 09Kh16N15M3B in the BR-10 Reactor," *Soviet Atomic Energy*, 48, No. 4 (1980) p. 266.

44. A. R. Causey, G. J. C. Carpenter and S. R. MacEwen, "In-Reactor Stress Relaxation of Selected Metals and Alloys at Low Temperatures," *J. Nucl. Mat.*, 90 (1980) p. 216.

45. L. C. Walters, G. L. McVay and G. D. Hudman, "Irradiation-Induced Creep in 316 and 304L Stainless Steels," *Int. Conf. Rad. Effects in Breeder Reactor Struct. Mat.*, M. L. Bleiberg and J. W. Bennett, Eds., The Metallurgical Society of AIME, New York, NY (1977) p. 277.

46. B. A. Chin and E. R. Gilbert, "Influence of a Temperature Change on In-Reactor Creep," *Effects of Radiation on Materials: 12th International Symposium, Vol. I, ASTM STP 870*, F. A. Garner and J. S. Perrin, Eds., American Society for Testing and Materials, Philadelphia (1985) p. 38.

47. V. S. Neustroev and V. K. Shamardin, "Radiation Creep and Swelling of Austenitic 16Cr-15Ni-3Mo-Nb Steels Irradiated in the Reactor BOR-60 at 350 and 420 C," *Effects of Radiation on Materials: 16th International Symposium, ASTM STP 1175*, A. S. Kumar, D. S. Gelles, R. K. Nanstad and E. A. Little, Eds., American Society for Testing and Materials, Philadelphia (1993) p. 816.

48. R. A. Weiner, J. P. Foster and A. Boltax, "Irradiation Creep-Swelling Coupling: Microstructural Modeling and Data Analysis," *Int. Conf. Rad. Effects in Breeder Reactor Struct. Mat.*, M. L. Bleiberg and J. W. Bennett, Eds., The Metallurgical Society of AIME, New York, NY (1977) p. 865.

49. J. A. Hudson, R. S. Nelson and R. J. McElroy, "The Irradiation Creep of Nickel and AISI 321 Stainless Steel During 4 MeV Proton Bombardment," *J. Nucl. Mat.*, 65 (1977) p. 279.

50. F. A. Garner and D. L. Porter, "Irradiation Creep and Swelling of AISI 316 to Exposures of 130dpa at 385-400C," *J. Nucl. Mat.*, 155-157 (1988) p. 1006.

51. L. K. Mansur and T. C. Reiley, "Irradiation Creep by Dislocation Glide Enabled by Preferred Absorption of Point Defects-Theory and Experiment," *J. Nucl. Mat.*, 90 (1980) p. 60.

52. C. R. Soderberg, *Trans. ASME*, 58, (1936), p. 733; I. Finnie and W. R. Heller, *Creep of Engineering Materials*, New York, McGraw-Hill (1959).

53. E. R. Gilbert and J. L. Straalsund, "A Relationship for Non-Conservative -Volume Creep under Different States of Stress," *Nucl. Eng. & Des.*, 12 (1970) p. 421.

54. I. Shibahara, S. Ukai, S. Onose and S. Shikakura, "Irradiation Performance of Modified 316 Stainless Steel for Monju Fuel," *J. Nucl. Mat.*, 204 (1993) p. 131.

55. C. Wassilew, K. Ehrlich and H-J. Bergmann, "Analysis of the In-Reactor Creep and Rupture Life Behavior of Stabilized Austenitic Stainless Steels and the Nickel-Base Alloy Hastelloy-X," *Radiation-Induced Changes in Microstructure: 13th International Symposium, ASTM STP 955*, F. A. Garner, N. H. Packan and A. S. Kumar, Eds., American Society for Testing and Materials, Philadelphia (1987) p. 30.

56. W. N. McElroy, R. E. Dahl and E. R. Gilbert, "Neutron Energy-Dependent Damage Function for Analysis of Austenitic Steel Creep Data," *Nucl. Eng. & Des.*, 14 (1970) p. 319.

57. W. Barmore, A. Ruotola, E. Raymond and A. Mukherjee, "Effects of 14 MeV Neutron Irradiation on Creep of Nickel and Niobium," *J. Nucl. Mat.*, 117 (1983) p. 258.

58. G. W. Lewthwaite and D. Mosedale, "The Effects of Temperature and Dose-Rate Variations on the Creep of Austenitic Stainless Steels in the Dounreay Fast Reactor," *J. Nucl. Mat.*, 90 (1980) p. 205.

59. L. Bernard, E. Campo and S. Quaranta, "Creep Behaviour of AISI 304 and 316 Stainless Steels and Influence of Cold Working," *Mechanical Behaviour and Nuclear Applications of Stainless Steel at Elevated Temperatures*, The Metals Society, London (1982) p. 88.

60. F. P. Ford, D. F. Taylor, P. L. Andresen and R. G. Ballinger, "Corrosion-Assisted Cracking of Stainless and Low-Alloy Steels in LWR Environments," EPRI Report NP-5064S, Electric Power Research Institute, Palo Alto, CA (February 1987).

61. P. L. Andresen and F. P. Ford, "Life Prediction by Mechanistic Modeling and System Monitoring of Environmental Cracking of Iron and Nickel Alloys in Aqueous Systems," *Mater. Sci. E.*, A103 (1988) p. 167.

62. P. Andresen, F. P. Ford, S. M. Murphy and J. M. Perks, "State of Knowledge of Radiation Effects on Environmental Cracking in Light Water Reactor Core Materials," *Proceedings of the Fourth International Symposium on Environmental Degradation of Materials in Nuclear Power Systems-Water Reactors*, NACE, Jekyll Island, GA (1989) p. 1-83.

63. NRC Information Notice 94-42, Supplement I: Cracking in the Lower Region of the Core Shroud in Boiling-Water Reactors, U. S. Nuclear Regulatory Commission Office of Nuclear Reactor Regulation (July 19, 1994).

64. G. D. Johnson, F. A. Garner, H. R. Brager and R. L. Fish, "A Microstructural Interpretation of the Fluence and Temperature Dependence of the Mechanical Properties of Irradiated AISI 316," *Effects of Radiation on Materials: Tenth International Symposium, ASTM STP 725*, D. Kramer, H. R. Brager and J. S. Perrin, Eds., American Society for Testing and Materials, Philadelphia (1981) p. 393.

65. A. L. Bement, Jr., "Fundamental Materials Problems in Nuclear Reactors," *Proceedings Second Int. Conference on the Strength of Metals and Alloys, Vol. II*, American Society for Metals, Pacific Grove, CA (1970) p. 693.

66. E. E. Bloom and J. O. Stiegler, "Effects of Fast Neutron Irradiation on the Tensile Properties of Austenitic Stainless Steels," *Proceedings Second Int. Conf. on the Strength of Metals and Alloys*, American Society for Metals, Pacific Grove, CA (1970) p. 768.

67. M. J. Makin, "The Obstacles Responsible for the Hardening of Neutron Irradiated Copper Crystals," *Philos. Mag.*, 18 (1968) p. 1245.

68. N. F. Panayotou, "The Use of Microhardness to Determine the Strengthening and Microstructural Alterations of 14 MeV Neutron Irradiated Metals," *J. Nucl. Mat.*, 108-109 (1982) p. 456.

69. F. A. Garner, M. L. Hamilton, N. F. Panayotou and G. D. Johnson, "The Microstructural Origins of Yield Strength Changes in AISI 316 During Fission or Fusion Irradiation," *J. Nucl. Mat.*, 103-104 (1981) p. 803.

70. R. L. Simons and L. A. Hulbert, "Correlation of Yield Strength with Irradiation-Induced Microstructure in AISI Type 316 Stainless Steel," *Effects of Radiation on Materials: 12th International Symposium, Vol. I, ASTM STP 870*, F. A. Garner and J. S. Perrin, Eds., American Society for Testing and Materials, Philadelphia (1985) p. 820.

71. R. L. Fleischer, "Solution Hardening by Tetragonal Distortions: Application to Irradiation Hardening in F. C. C. Crystals," *Acta Met.*, 10 (1962) p. 835.

72. H. R. Brager, F. A. Garner, E. R. Gilbert, J. E. Flinn and W. G. Wolfer, "Stress-Affected Microstructural Development and the Creep-Swelling Interrelationship," *Int. Conf. Rad. Effects in Breeder Reactor Struct. Mat.*, M. L. Bleiberg and J. W. Bennett, Eds., The Metallurgical Society of AIME, New York, NY (1977) p. 727.

73. R. W. Powell, "Theoretical Prediction of Microstructural Development During Irradiation," *Int. Conf. Rad. Effects in Breeder Reactor Struct. Mat.*, M. L. Bleiberg and J. W. Bennett, Eds., The Metallurgical Society of AIME, New York, NY (1977) p. 757.

74. Y. Katoh, Y. Kohno and A. Kohyama, "Effects of Applied Stress on Microstructural Evolution in 316SS under Ion Irradiation," *Effects of Radiation on Materials: 16th International Symposium, ASTM STP 1175*, A. S. Kumar, D. S. Gelles, R. K. Nanstad and E. A. Little, Eds., American Society for Testing and Materials, Philadelphia, (1993) p. 978.

75. P. Scott, "A Review of Irradiation Assisted Stress Corrosion Cracking," *J. Nucl. Mat.*, 211 (1994) p. 101.

CHAPTER 7

SERVICE PERFORMANCE INDICATORS OF IASCC SUSCEPTIBILITY

Haste still pays haste, and leisure answers leisure;
Like doth quit like, and Measure still for Measure.

William Shakespeare
(1564-1616)

7.1 MOTIVATION

Irradiation assisted stress corrosion cracking is a real engineering problem experienced in materials employed in operating nuclear reactors. It is a complex scientific phenomenon described by the influence of radiation on parameters that encompass the environment-material-stress triad of stress corrosion cracking. IASCC is both a basic and an applied topic that challenges our scientific mettle to understand the fundamental mechanisms and our engineering savvy to design practical mitigation technologies. The combined motivations of scientific discovery and practical application for investigating IASCC is eloquently captured in the words of Sir Alan Cottrell[1],

> *"...We have all the playthings of the basic materials scientist- vacancies, dislocations, grain boundaries, foreign atoms- interacting in the most fascinating of ways, and setting innumerable problems for fundamental science. And yet, at the same time, the performances of the materials are of the most profound importance for practical reactor engineering and must be understood and mastered if we are to build good reactors. I doubt whether there has ever been such a fortunate and intimate combination of fundamental scientific problems and practical needs."*

The fundamental scientific problem of IASCC requires practical, economical solutions. The discovery of basic mechanisms that contribute to susceptibility and development of engineering solutions that imbue resiliency are the motivations for IASCC research. Numerous

parameters have been identified or suggested as influencing IASCC, but no universal mechanism has been verified. In this section correlations between four types of service performance yardsticks and irradiation assisted stress corrosion cracking susceptibility are presented using data from the MIT IASCC program and data for similar materials reported in the literature. Implications of the correlations on currently proposed mechanisms are discussed and the major findings are summarized.

7.2 FLUENCE

The first paper, by Clarke and Jacobs[2], that reported an increased cracking susceptibility of irradiated austenitic materials noted a threshold fluence of 5×10^{24} n/m^2 (E> 1 MeV) below which no intergranular failures were observed. Traditionally, then, fluence has been considered a fundamental parameter to correlate IASCC susceptibility. Because it is relatively simple to measure or calculate and relates to the overall radiation damage that occurs on a microscopic level (e.g. segregation, hardening, transmutation) it is a good engineering candidate for correlating IASCC susceptibility.

The susceptibility measure of SCC adopted in this thesis was the percentage intergranular failure (%IG) observed on the fracture surface of tensile specimens dynamically loaded at slow strain rate. Laboratory SSR tests with pre-irradiated specimens is a research technique extensively used in estimating irradiation assisted SCC susceptibility. Pre-irradiated specimens, cut from BWR components or fabricated from samples placed in test or power reactors, are tested to examine long lasting irradiation effects (i.e. determined by the fluence). To simulate the excess oxidant produced in-core by radiolysis, out-of-flux laboratory SSR tests are typically conducted at very high oxygen concentrations (8-32 ppm) although some researchers[3] use much lower oxygen levels (0.3 ppm) that are similar to concentrations measured in the recirculation line. Although laboratory data correspond quite well with in-plant data[4], the influence of *in situ* radiation effects on material behavior and water chemistry on IASCC susceptibility remain unquantified. Because of the uncertainties of *in situ* radiation effects on material behavior and water chemistry, in-flux SSR tests were conducted on samples of types 304 and 316L stainless steel pre-irradiated to a fluence of ~0.8×10^{25} n/m^2. The performance of types 304 and 316 stainless steel is of particular interest to the nuclear power industry since many in-vessel structural components are fabricated from these two alloys.

Figure 7-1 displays the in-flux SSR results (MIT) and the out-of-flux laboratory data[2,3,5-10] for percentage intergranular failure (%IG) plotted against fluence (E> 1 MeV). The results for commercial purity types 304 and 304L were consistent with a threshold fluence of

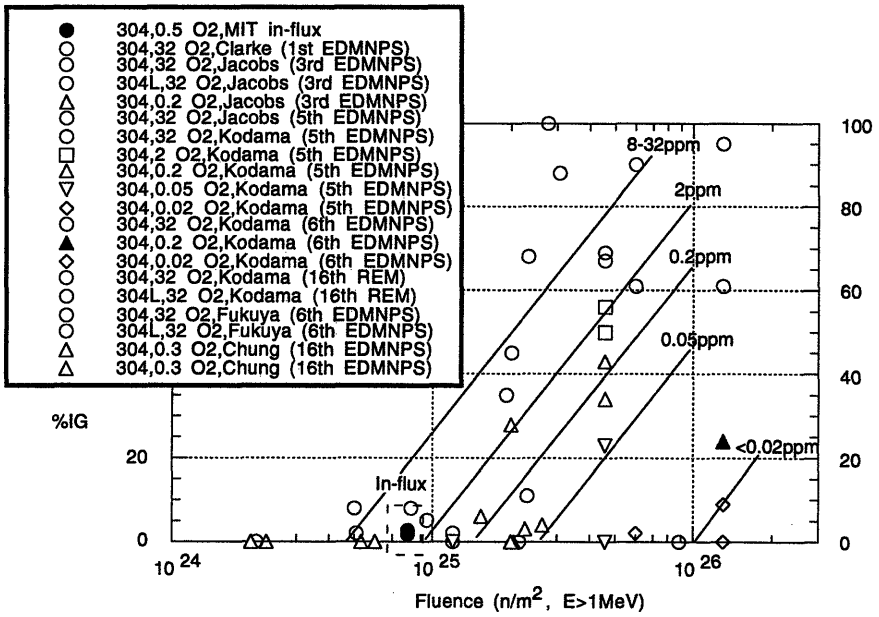

(a)

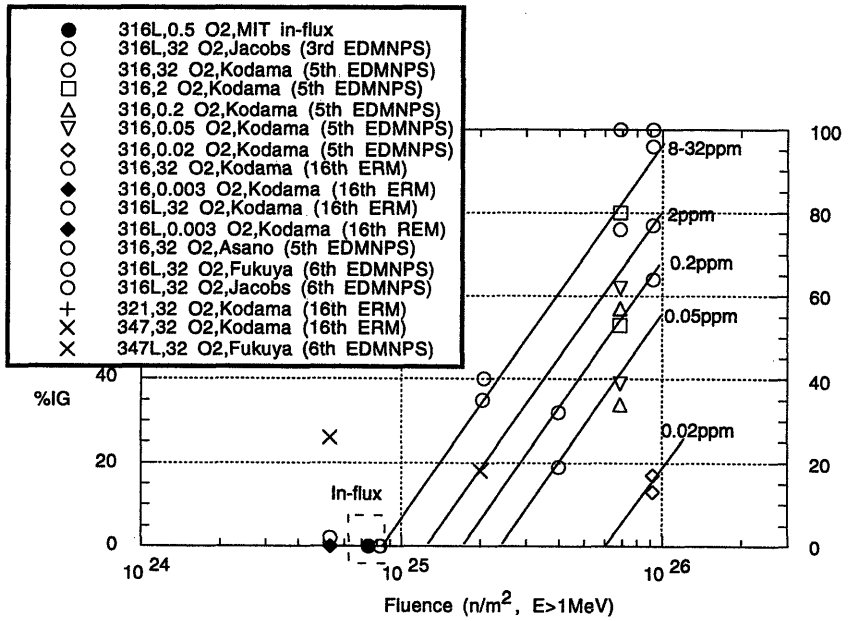

(b)

Figure 7-1. Fluence and dissolved oxygen dependence of IASCC susceptibility in a) types 304, 304L and b) types 316, 316L stainless steel (adopted from Kodama et al.[7]).

0.5×10^{25} n/m^2 as observed by Clarke and Jacobs[2], whereas type 316 does not show susceptibility until fluences exceed ~1×10^{25} n/m^2. It should be noted that Kodama et al., based on their own data[7], concluded that types 304 and 316 stainless steel exhibit similar IASCC characteristics. The acceptance of different susceptibility thresholds for types 304 and 316 in this thesis was a result of interpreting all the data. Furthermore, the in-flux MIT results were consistent with the view that type 316L has a higher threshold fluence than type 304 for IASCC. Data from out-of-flux laboratory tests conducted for a range of oxygen concentrations showed that IASCC susceptibility trends with dissolved oxygen content[7]. A significant observation was that the in-flux results, performed with 0.50 ppm dissolved oxygen, corresponded to the trend of laboratory results obtained with 8-32 ppm dissolved oxygen. This finding was not very startling since the ECPs were similar, although the oxygen content differed by 1.5 orders of magnitude. Indeed, this fact supports the premise that ECP, and not dissolved oxygen, is the defining parameter of environmental aggressiveness for IASCC[11]. An important corollary is that IASCC susceptibility of low fluence materials determined by in-flux SSR tests and zero flux laboratory tests are phenomenologically the same.

The equivalent ECP measured during in-flux and out-of-flux laboratory tests when the predicted oxygen concentration in-flux was only 0.50 ppm compared to 32 ppm out-of-flux may have important consequences for ECP modeling codes. ECP prediction codes assume that the three major radiolysis species (i.e. hydrogen, oxygen and hydrogen peroxide) dominate the electrochemical action and consequently set the corrosion potential (ECP). Under oxidizing conditions, like normal water chemistry in a BWR, the oxygen and hydrogen peroxide concentrations determine the ECP. Since H_2O_2 is predicted to be only 0.50 ppm, the net oxidant concentration for MIT in-flux SSR tests was less than 1 ppm which is ~10-30 times smaller than that used in out-of-flux laboratory SSR tests. This indicates that intermediate species, which have been neglected in current modeling efforts[12,13], play a significant role in the ECP of stainless steel under irradiated water conditions.

The comparison of types 304 and 316L revealed that for different alloys IASCC susceptibilities showed similar qualitative dependence on fluence and oxygen. It was observed that IASCC susceptibility trended with oxygen concentration for both alloys, but the trend lines for type 316L were shifted to higher fluences. It was not too surprising that different alloys exhibited different fluence thresholds to IASCC, since the microstructural and microchemical development under irradiation depends on the elemental composition. Measurements that either directly quantify the micro-scale parameters or relate them to macroscopic properties may exhibit a more material independent correlation. Fluence can be related to IASCC susceptibility. However, susceptibility is material dependent. The varying performance of different alloys and

even different heats of the same alloy with accumulated flux when tested under LWR simulated conditions undermines the utility of fluence as an IASCC service performance indicator.

7.3 MECHANICAL PROPERTIES

The effects of radiation on materials mechanical properties have been studied since the earliest application of fission to the power industry[14]. Hardening and loss of ductility are recognized as important consequences of accumulated radiation damage that seriously affect the service performance of nuclear reactor structural materials. Radiation induced defects act as obstacles to dislocation motion and increase the yield stress. The increased strength is accompanied by a decrease in ductility which is explained by a lower fracture toughness leading to premature plastic instability. The lower ductility is also attributed to localized deformation that occurs as dislocation channeling. When the radiation induced defects are cut by a dislocation, the back stress is lowered significantly allowing an avalanche of dislocations to move along the cleared glide plane or "channel". The impact of these mechanical parameters on irradiation assisted stress corrosion cracking has been investigated using both neutron and proton irradiated stainless steels tested out-of-flux in laboratory[5,7,15-18]. These investigations indicated a dependence of IASCC susceptibility on yield stress, but were inconclusive with regards to ductility and deformation mechanism.

7.3.1 Yield Stress

As discussed above, fluence has traditionally been considered the fundamental parameter to correlate IASCC susceptibility, but recent analyses by Bruemmer and Simonen[15] and Bruemmer et al.[18] reported a better correlation with yield stress than with fluence. The measured percentage intergranular (%IG) for the MIT in-flux SSR tests were plotted along with results from out-of-flux SSR tests[3,5,6,8,10] in Figure 7-2 against the 0.2% offset yield stress. The in-flux results followed the same trend as the laboratory data which indicated a threshold yield stress of ~500 MPa below which IASCC was not observed. For in-flux as well as zero flux conditions, IASCC susceptibility of austenitic stainless steel (types 304(L), 316(L) and 347) correlated well with yield stress.

The validity of correlating IASCC susceptibility with yield stress was supported by results for different stainless steel types. The different stainless steel types which have slightly different yield stresses in the unirradiated condition exhibited quite different hardening and IASCC susceptibility characteristics as a function of fluence (see Figures 7-3 and 7-1, respectively). Thus,

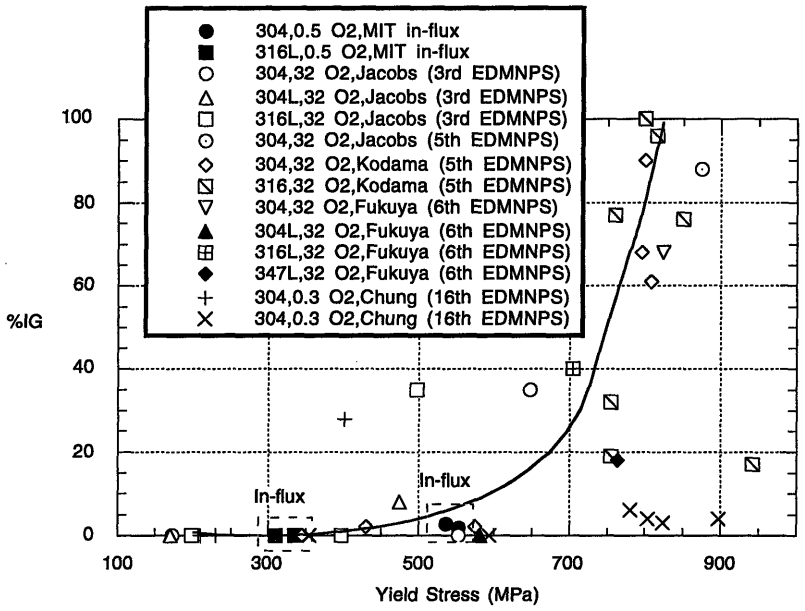

Figure 7-2. IASCC susceptibility dependence on yield stress.

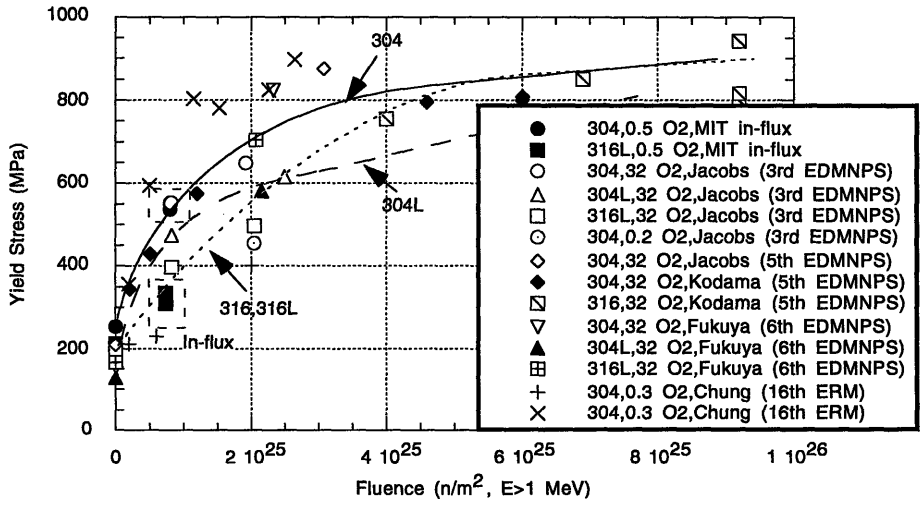

Figure 7-3. Yield stress of types 304(L) and 316(L) stainless steel as a function of fluence.

the yield stress correlation normalized results for different alloys and revealed the yield stress as a fundamental parameter that can be used to interpret current crack growth models.

On a mechanistic level, the observation of a threshold yield stress is appealing since the stress at the crack tip will be equal to the yield stress. This suggests that a critical stress exists for microscopic phenomena that contribute to IASCC. Some candidate phenomena that can be related to a critical stress are decohesion (e.g. intergranular or interatomic) and slip step formation by creep (irradiation or thermal). Further study of these microscopic processes and the yield stress effect on IASCC are recommended for future work.

The increased yield stress observed for in-flux solution annealed material has implications for using the IASCC yield stress correlation. An unirradiated type 304 specimen tested in-flux displayed a yield stress increase of 20% or ~50MPa (cf. section 4.4). There was no increase in %IG for this specimen, but the yield stress of 320 MPa was still well below the critical value of ~500 MPa. However for low fluence materials that have a yield stress slightly below 500 MPa, the increased hardening due to *in situ* radiation damage may make the material susceptible to IASCC. In essence, for in-vessel components subject to a neutron flux, the yield stress (as determined in out-of-flux laboratory tests) threshold for IASCC susceptibility may be more like 400 or 450 MPa.

7.3.2 Ductility

The measure of ductility can be elongation to failure, uniform elongation, or reduction in area. Elongation to failure is the most commonly reported property in the literature so it was used in comparing laboratory data with the in-flux results of this thesis. Figure 7-4 displays the dependence of percentage intergranular fracture on strain to failure for types 304 and 316 stainless steels determined from in-flux SSR tests and reported for post-irradiation tests[3,5-10,19]. There was not a significant difference between the behavior of the two alloys although the type 304 data exhibited a greater amount of scatter than the type 316 data. Most of the low strain results for type 304 were from Chung et al.'s[3] SSR tests which were conducted at lower oxygen levels (i.e. 0.3 ppm compared to 32 ppm) and showed transgranular fracture rather than intergranular fracture. In general, total elongation was ~48% for purely ductile fractures, ~25% when a small percentage of IG fracture was observed and ~5% for purely intergranular fractures. The %IG rose rapidly between 10 and 5% total elongation.

A correlation between low ductility and high IASCC susceptibility was somewhat inevitable, being representative of the embrittling nature of SCC. The ability of the material to deform plastically was reduced and consequently the total elongation, also, as a greater percentage of grains fractured due to the combined effect of stress and environmental attack.

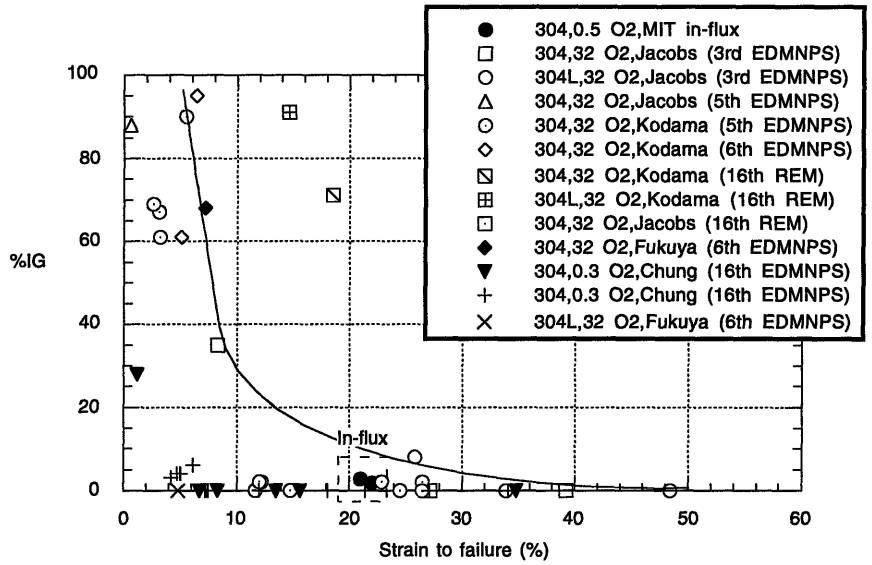

(a)

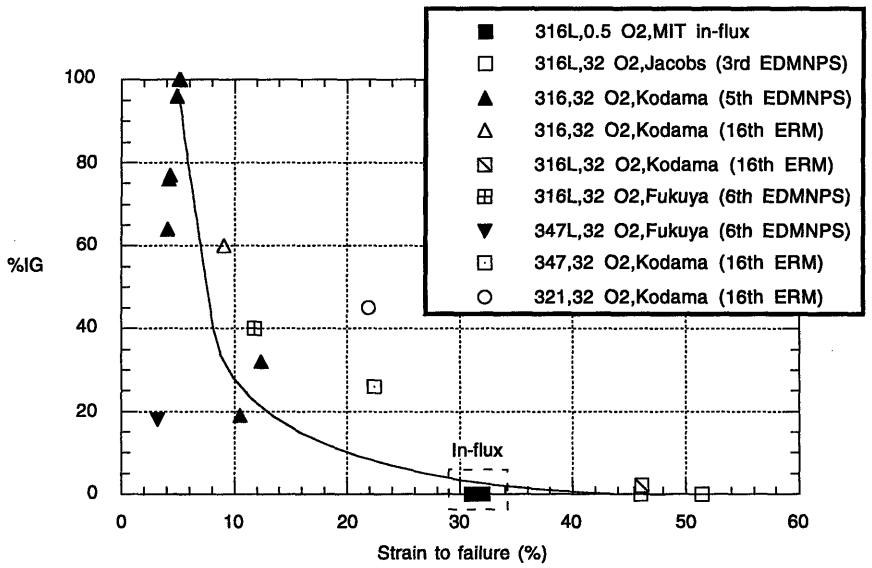

(b)

Figure 7-4. Percentage intergranular fracture versus strain to failure for a) types 304, 304L and b) types 316, 316L, 347, and 321 stainless steels.

Because of the direct dependence of %IG and strain to failure, this correlation did not reveal any new mechanisms. However, this correlation can be compared with data obtained from SSR tests performed at different strain rates. In laboratory SSR tests, Bruemmer et al.[20] showed that for a given failure strain the interfacial chromium concentrations increased significantly when the strain rate was reduced from 1×10^{-6} to 2×10^{-7} s^{-1}. Figure 7-4 can be a reference for SSR tests conducted at strain rates of $2.5\text{-}7 \times 10^{-7}$ s^{-1} and to compare with data from SSR tests conducted at higher or lower strain rates.

7.4 RADIATION INDUCED SEGREGATION PROFILES

The non-equilibrium segregation of major and minor elements is a major constituent of classical irradiation assisted stress corrosion cracking. Traditionally, the decrease in chromium concentration at the grain boundaries has been considered the dominant effect leading to IASCC susceptibility. There are noticeable variations in IASCC susceptibility between alloys and even different heats of the same alloy. Segregation of impurities like silicon and phosphorus is believed to play an important role in these variations.

For the materials investigated as part of the MIT IASCC program, radiation induced segregation profiles were determined by analytical electron microscopy (i.e. STEM-EDX). Details of this work can be found in the theses by Mansoux[21] and Flores[22]. A paper by Mansoux et al.[23] describes the major findings for the pre-irradiated commercial alloys. The measured elemental concentration profiles were comparable to profiles determined by other researchers for similar materials, irradiation conditions and experimental technique (i.e. FEG-STEM EDX). Figure 7-5 displays the chromium, nickel and silicon concentration changes at the grain boundary determined at MIT along with those of Chung et al.[3], Kodama et al.[8], Asano et al.[16], Jacobs[19] and Jacobs et al.[24] as a function of fluence. The MIT results were in general agreement with the other work although it should be noted that the MIT data reported the maximum segregation observed for each alloy from a number of grains profiled.

Figure 7-6 displays the %IG observed from in-flux and out-of-flux SSR tests with the segregation profile results of Cr, Ni, and Si. As with the mechanical property correlations, the in-flux data for RIS seemed to follow the same trend as out-of-flux test data. From this comparison, it appeared that the correlation of RIS grain boundary chemistry and IASCC was quite different for the 304 and 316L alloys. In general, the susceptibility of type 316L was shifted to larger grain boundary chemistry changes. This fact, with the comparable RIS changes observed for the two stainless steel types, gave further support to the impact of yield stress on IASCC susceptibility. It was not definite however because of the corrosion resistant qualities of molybdenum alloyed in

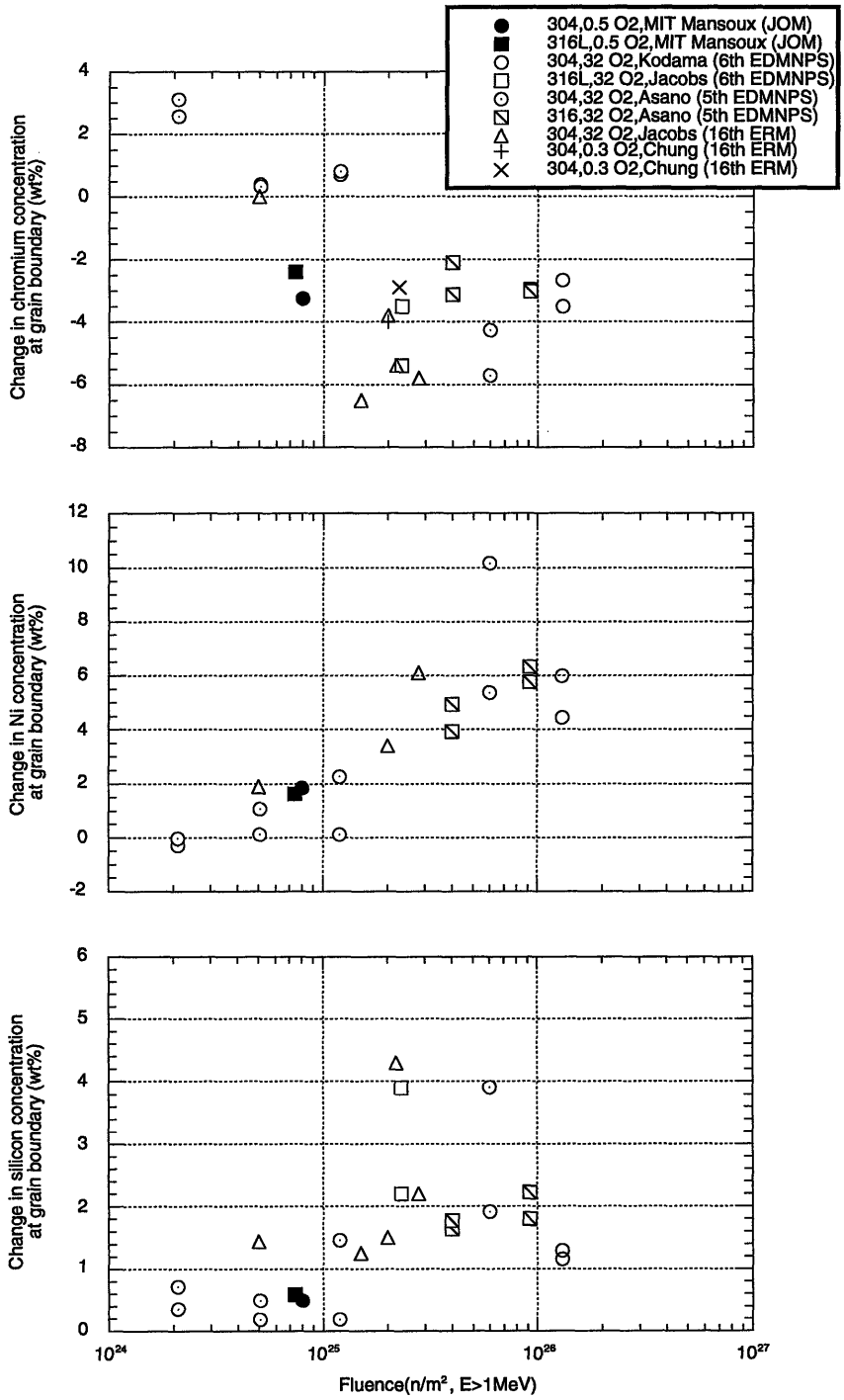

Figure 7-5. Radiation induced segregation grain boundary changes in chromium, nickel and silicon concentrations for types 304 and 316L austenitic stainless steels as a function of fluence.

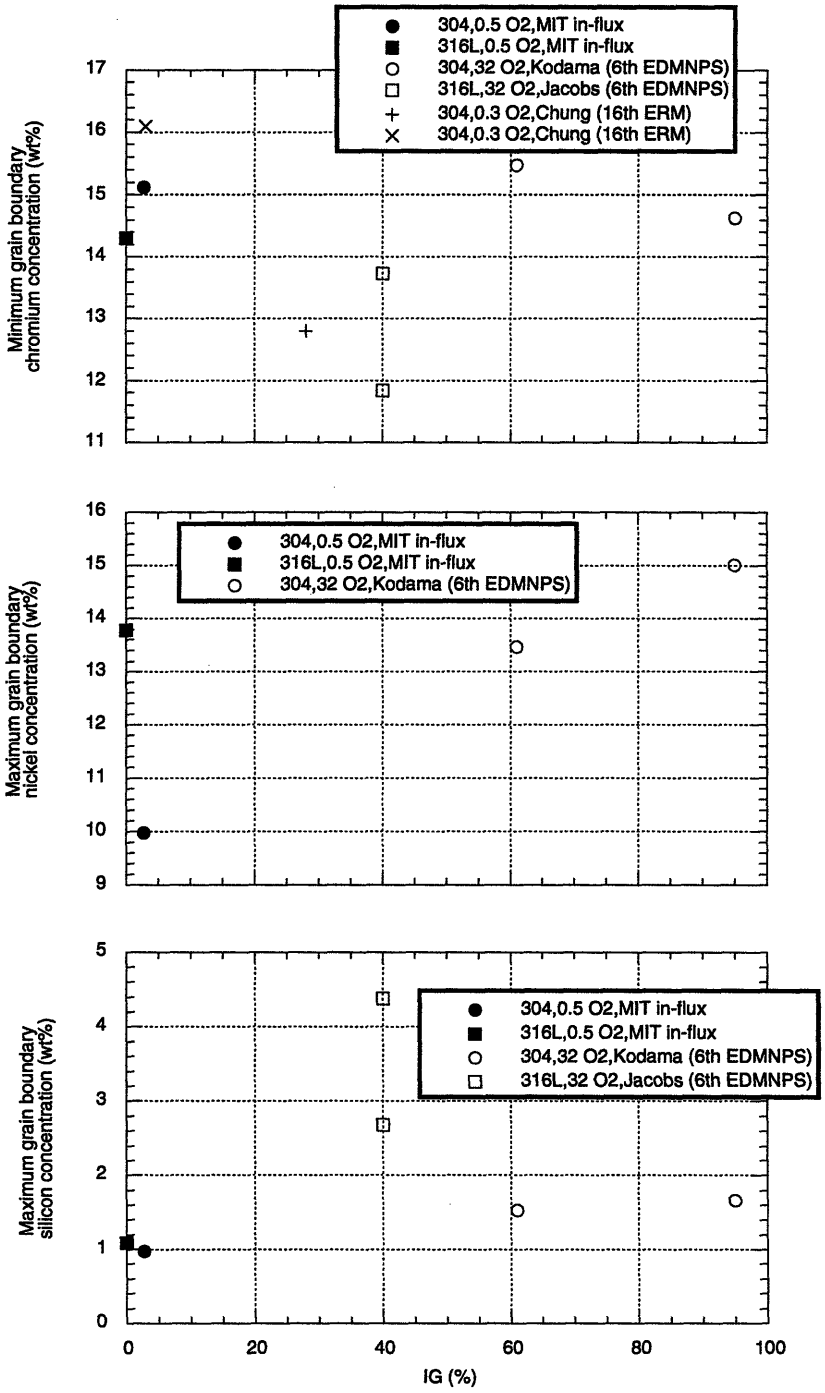

Figure 7-6. IASCC susceptibility of types 304 and 316L austenitic stainless steels dependence on maximum RIS grain boundary changes in chromium, nickel and silicon concentrations.

type 316L. The exact role of Mo was not identified, but its dominat effect was postulated as delaying radiation induced microstructural changes rather than enhancing corrosion resisting characteristics. However distinguishing these two effects in type 316L was difficult because of the similar dependence of Mo RIS and hardening on fluence. For higher fluence irradiation where type 316L showed IASCC susceptibility, the molybdenum concentration was decreased at the boundary as was chromium[24] and the yield stress approached the threshold value of 500 MPa. Whatever the exact role of molybdenum, it was suggested to mark a fundamental difference in the behavior of types 304 and 316 stainless steel.

7.5 ELECTROCHEMICAL AND CORROSION TESTS

Electrochemical or accelerated corrosion tests are frequently used to evaluate stress corrosion cracking resistance. Rather than accelerating the mechanical contribution to SCC as in slow strain rate tests, electrochemical tests increase the corrosive aggressiveness of the environment in contact with the material. For irradiation assisted stress corrosion cracking, this category of tests has provided means of quantifying microstructural and microchemical changes as an alternative to conventional AEM. The two kinds of tests are not completely equivalent since electrochemical tests sample material which contains many crystallites whereas only the grain boundary of one crystallite is sampled during AEM. Since other radiation induced microstructures, e.g. Frank loops, can act as defect sinks and have been shown to be sites for RIS, similar to grain boundaries, a comparison between the correlation of IASCC susceptibility with electrochemical test results and AEM results would reveal the relative influence of grain boundary and and bulk matrix radiation damage. The two electrochemical tests most commonly employed in IASCC studies are electrochemical potentiokinetic reactivation (EPR) and Coriou (HNO_3 Cr^{+6}) tests. These two tests are performed at transition potentials between the active-passive and passive-transpassive regions, respectively, where stainless steel dissolution rates depend on chromium depletion and impurity segregation, respectively. Since changes in the Coriou test solution concentration can affect the potential, a potentiostatic test in the transpassive range was utilized as part of the MIT work to study impurity effects. Results of electrochemical tests are presented below with the %IG measured after in-flux SSR testing. Correlations between the various parameters and comparisons with out-of-flux laboratory SSR test results are also discussed below.

7.5.1 *Electrochemical Potentiokinetic Reactivation (EPR) Tests*

Since high corrosion rates in the EPR test correspond to chromium depletion, this technique was extensively applied during the late 1970s and 1980s for quantifying this characteristic in weld-sensitized stainless steels (typically type 304) and correlating IGSCC susceptibility in BWR recirculation piping. For mildly sensitized materials, the standard EPR technique is not sensitive enough to discriminate chromium depletion however a double loop EPR technique can be applied. This later technique is poor for radiation sensitized materials because of the very narrow depletion profiles, ~10 nm across the grain boundary, compared to weld-sensitized profiles which are ~40 nm across. A modified double loop EPR technique, which was developed by Iwabuchi[25] and was sensitive to the narrow RIS profiles, was employed in the MIT work along with the standard double loop EPR technique. The electrochemical tests were performed by Watanabe and details can be found in an MIT annual report[26].

The results are summarized here. Irradiation increased the amount of dissolution for all the materials studied except the 316L (heat K5) alloy. Surface examination after the tests revealed extensive pitting on the grain face with little or no etching of the grain boundaries. Since radiation induced segregation had been observed at interstitial and vacancy sinks other than the grain boundary, it was concluded that pitting occurred at faulted dislocation loops produced from radiation damage. Because of the observed attack within the grain, it was expected that there should be little correlation between EPR ratio and chromium depletion at the grain boundary[26]. The EPR ratios of the irradiated material were normalized by dividing by the EPR ratios for unirradiated material. Figure 7-7 shows that the normalized EPR ratio did not correlate with the amount of chromium depletion at the grain boundary, as expected. The lack of correlation was also observed for minimum chromium concentration. Although the modified double loop EPR results did not correlate with chromium grain boundary depletion, a correlation between EPR and IASCC susceptibility was considered worthy of investigation. Results from the MIT EPR work and in-flux SSR tests, shown in Figure 7-8, displayed a positive correlation. However, acknowledging that there were just two datum (types 304 and 316L), the observed trend was mostly suggestive at present. Extrapolating the %IG vs. EPR trend from the 316L and 304 data, the predicted IASCC susceptibility of types 304L and 347L was ~5% IG and ~20% IG, respectively.

The postulated trend was evaluated on a preliminary basis by comparing the predicted susceptibility with the %IG observed in out-of-pile SSR tests. Observed %IG in out-of-flux SSR tests was ~1-10% for type 304L pre-irradiated to a fluence 0.5-1 x 10^{25} n/m^2. Results of a higher fluence 347L alloy (2 x 10^{25} n/m^2), from Fukuya et al.[10], exhibited 32% IG. This susceptibility was higher than the predicted value of 20%, but the increased fluence could easily account for the difference. Hence, the predicted susceptibilities of types 304L and 347L irradiated to 0.8 x 10^{25}

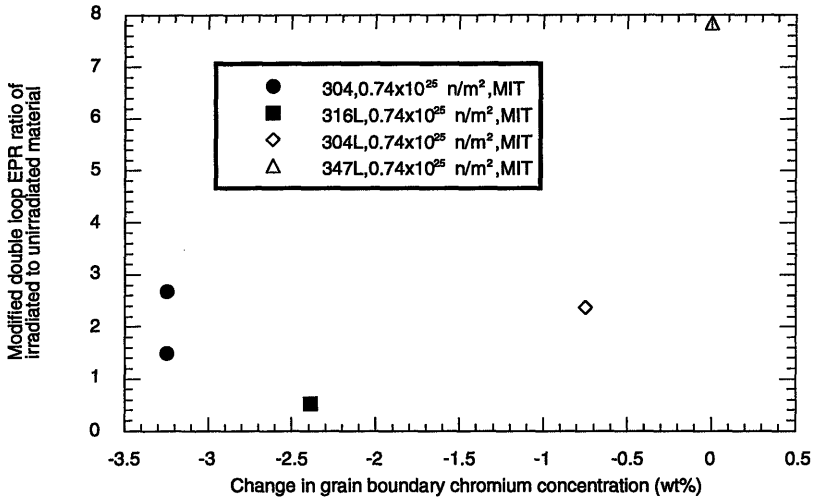

Figure 7-7. EPR results plotted against maximum grain boundary chromium depletion determined by AEM.

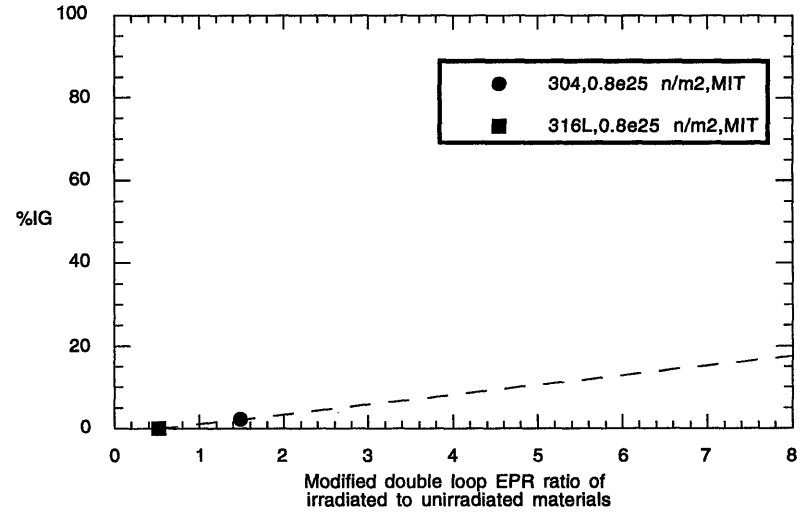

Figure 7-8. EPR results compared with IASCC susceptibility measured by in-flux SSR tests.

n/m^2 based on a linear extrapolation of the 316L and 304 data were consistent with observed values of %IG. Data for materials with a broader range of EPR ratios can help clarify the relationship between EPR and IASCC susceptibility and establish the applicability of double loop EPR as an IASCC service performance indicator.

7.5.2 Transpassive Potentiostatic Dissolution (TPD) and Coriou (HNO_3/Cr^{+6}) Tests

The Coriou test evaluates the corrosion susceptibility at transpassive potentials which corresponds to impurity segregation (e.g. silicon and phosphorus). A constant potential is maintained by a nitric acid-chromate solution but there can be drift due to varying solution consumption and refreshing procedures. Potentiostatic control in the transpassive range was an alternative method that eliminated these uncertainties. This alternative method was developed and employed for the MIT work. For details of the experimental procedures of the transpassive potentiostatic tests see the paper by Watanabe et al.[27] and the MIT IASCC Fifth annual report[26].

Watanabe et al. found that the current density could be correlated with a bulk impurity level given as the sum of weight per cent silicon plus ten times the weight per cent phosphorus (wt%Si + 10•wt%P). Furthermore, they observed that the *change* in current density between irradiated and unirradiated materials could be correlated with this bulk impurity level. Since the transpassive potentiostatic test was developed to match the same electrochemical conditions as the Coriou test (HNO_3/Cr^{+6}), the Coriou results from previous authors[26] should also correlate with this bulk impurity level. Because of the different units involved for the two tests (i.e. areal mass loss for Coriou test and current density for TPD), normalized values were plotted rather than differential quantities. The normalized values were not exactly equivalent to the differential quantity, but the trend with bulk impurity level was still maintained as seen in Figure 7-9. Figure 7-10 displays the results of the TPD test performed at MIT and reported Coriou tests by Jacobs et al.[5] and Kodama et al.[9] plotted against the bulk impurity level. There was quite good agreement at the higher impurity levels with both tests showing a marked increase in dissolution at a bulk impurity level of 0.8%. However, the Coriou test showed high corrosion rates for ultra high purity materials, too. The high dissolution in the Coriou test was attributed to radiation induced defects in the bulk material since no grain boundary attack was observed in these materials[9]. For the high purity materials, the enhanced dissolution also corresponded to higher IASCC susceptibility, so the Coriou test results were not an artifact of the experimental technique. The high dissolution measured for these two materials suggested a region of high susceptibility at low bulk impurity levels (<0.04 wt%). However a plot of %IG (measured in SSR tests for a fluence range of 0.2-2 x 10^{25} n/m^2) against the bulk impurity level did not obviously support this observation, but showed data scatter at all impurity levels (see Figure 7-11). The scatter may be

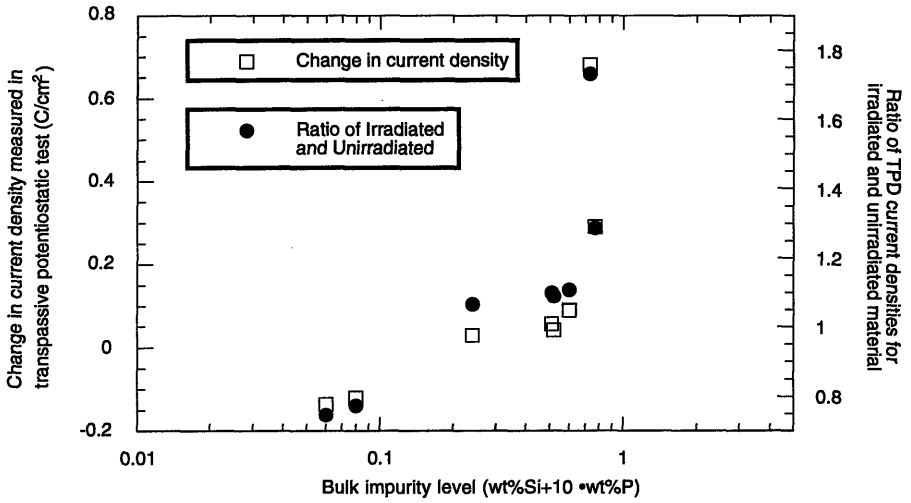

Figure 7-9. Comparison of change in and ratio of Transpassive Potentiostatic current densities for irradiated and unirradiated austenitic stainless steels dependence on bulk impurity level.

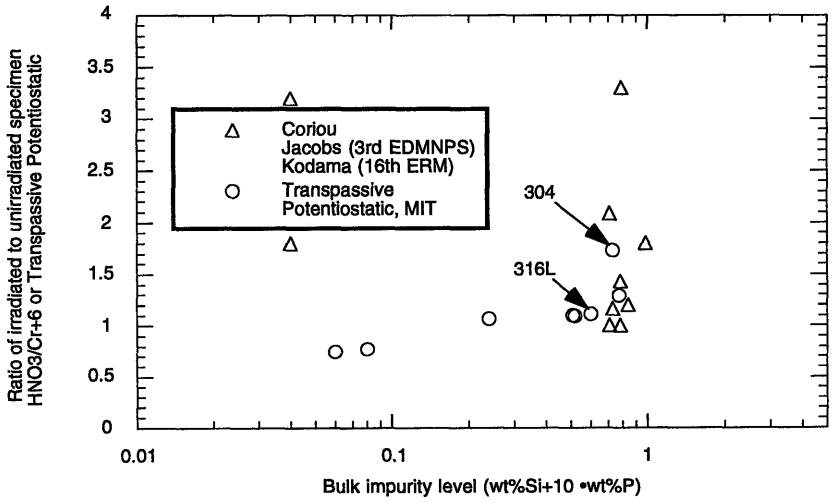

Figure 7-10. Dependence of Coriou and Transpassive Potentiostatic Ratios of irradiated to unirradiated austenitic stainless steels on bulk impurity level.

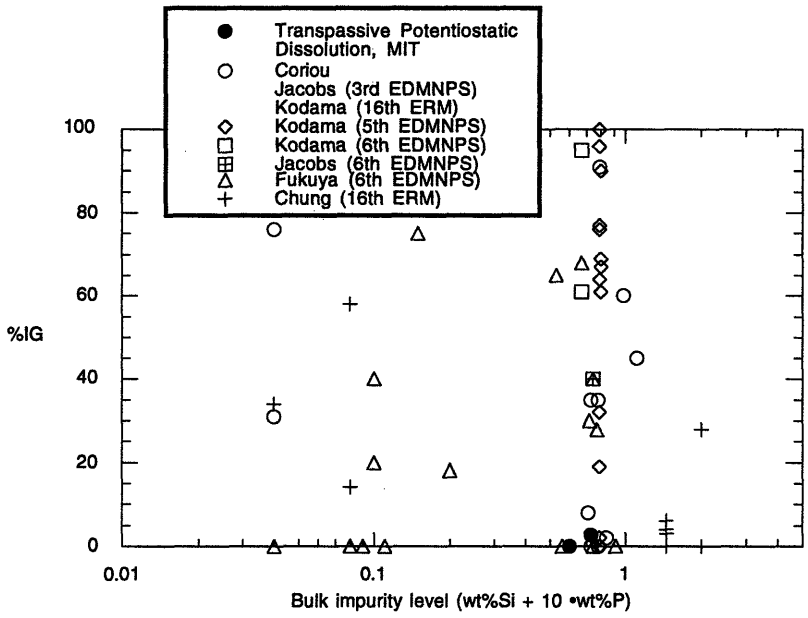

Figure 7-11. Dependence of IASCC susceptibility of irradiated austenitic stainless steels on bulk impurity level (wt%Si + 10 •wt%P).

due to the range of fluence. At higher fluence, the low bulk impurity threshold for IASCC could shift to the right. From this analysis bulk impurity level was not found to be a good indicator of IASCC susceptibility.

In Figure 7-12, the normalized TPD and Coriou test results were plotted against the %IG fracture measured in SSR tests. Bounding curves for the data show that IASCC susceptibility increased with dissolution at transpassive electrochemical potentials. The minimum %IG and the maximum %IG trends showed a linear and power law, exponent ~2, dependence on transpassive dissolution, respectively. The only extraneous data outside the bounded region was the MIT SSR result for type 304. The MIT SSR test was in-flux, but any flux effects involving impurity levels were supposed to enhance, not diminish, susceptibility[24]. Therefore the proposed IASCC mechanism of silicon or phosphorus exacerbating hydrogen embrittlement and cracking was not supported by the MIT in-flux results. However, the time constant for synergistic effects and subsequent diffusion of hydrogen to the crack tip region may be long compared to the SSR test time (nominally 5000 seconds for the pre-irradiated 304 alloy) thus pre-empting this mechanism. The different correlations might point to TPD results having a higher sensitivity to IASCC susceptibility than Coriou tests, although the techniques were supposed to be electrochemically equivalent[26]. Nonetheless, positive correlation of %IG and

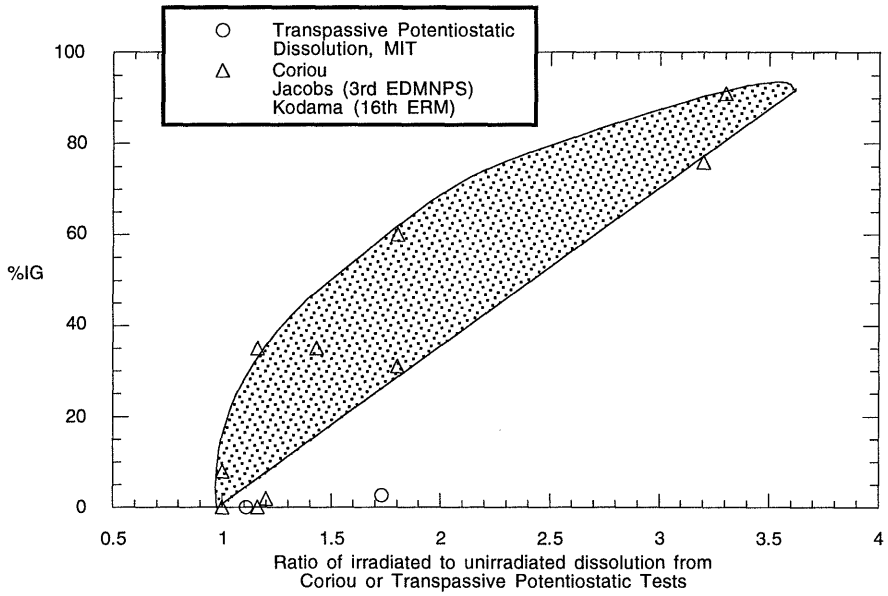

Figure 7-12. Dependence of IASCC susceptibility on Coriou and Transpassive Potentiostatic Ratios of irradiated to unirradiated austenitic stainless steels.

TPD dissolution supported a role for silicon and phosphorus in the IASCC mechanism and suggested that bulk matrix radiation damage, not just grain boundary RIS, contributed to the susceptibility of low fluence stanless steels. Furthermore that normalized TPD and Coriou results can be used as service performance indicators of IASCC susceptibility.

7.6 SUMMARY

Four service performance indicators (fluence, mechanical behavior, grain boundary microchemistry and electrochemical/corrosion affinity) of IASCC susceptibility were evaluated for austenitic stainless steels. Results for type 304 (heat AJ9139) and type 316L (heat K5) measured by in-flux SSR tests and out-of-flux laboratory data for different heats of the same alloys were utilized in evaluating the service performance indicators and for comparing the effects of in-flux radiation on IASCC susceptibility.

Overall, the in-flux %IG fell within the envelope of out-of-flux laboratory results when plotted against each of the four parameters: fluence, yield stress, segregation/depletion of elements at the grain boundary and dissolution current density. Significant trends for each of the parameters are summarized below.

- Different %IG dependence on fluence was observed for types 304 and 316 stainless steel. Susceptibility to IASCC for type 304 showed a threshold fluence of 0.5×10^{25} n/m^2 whereas type 316(L) had a threshold fluence of ~1×10^{25} n/m^2.

- Yield stress was indicated as a fundamental parameter influencing IASCC behavior. A threshold yield stress of 500 MPa (measured at temperature in air) was observed for in-flux and zero flux tests. Because of *in situ* radiation hardening due to the fast neutron flux in-core, it is predicted that the threshold yield stress of in-vessel components will be around 400-450 MPa.

- Modified double loop EPR results for the materials tested at MIT did not correlate with grain boundary chromium depletion. The EPR results trended with %IG measured for in-flux SSR tests, but too few data were available for a certain conclusion.

- Results of irradiated specimens tested by transpassive potentiostatic dissolution method (TPD) and Coriou method were consistent when normalized by unirradiated specimen results. A bulk impurity level (wt%Si + 10•wt%P) correlated with normalized dissolution results but not with IASCC susceptibility. The %IG correlated with the normalized dissolution results falling in a region with an upper bound fit to a power law, exponent ~2, and a lower bound line. Since the TPD specimens showed pitting rather than intergranular attack (IGA), then bulk matrix radiation damage, rather than impurity segration at the grain boundary, was considered a contributing mechanism to irradiation assisted stress corrosion cracking.

7.7 REFERENCES

1. A. Cottrell, Introductory remarks at Conference *Irradiation Embrittlement and Creep in Fuel Cladding and Core Components*, BNES (November 1972) p. 1.

2. W. L. Clarke and A. J. Jacobs, "Effect of Radiation Environment on SCC of Austenitic Materials," *Proc. Int. Symp. on Env. Deg. of Mat. in Nucl. Pow. Systems-Water Reactors*, NACE, Myrtle Beach, SC (1983) p. 451.

3. H. M. Chung, W. E. Ruther, J. E. Sanecki, A. G. Hins and T. F. Kassner, "Stress Corrosion Cracking Susceptibility of Irradiated Type 304 Stainless Steels," *Effects of Radiation on Materials: 16th International Symposium, ASTM STP 1175*, A. S. Kumar, D. S. Gelles, R. K. Nanstad and E. A. Little, Eds., American Society for Testing and Materials, Philadelphia (1993) p. 851.

4. P. L. Andresen and F. P. Ford, "Modeling of Irradiation Effects on Stress Corrosion Crack Growth Rates," *CORROSION /89*, National Association of Corrosion Engineers, New Orleans (April 1989) Paper 497.

5. A. J. Jacobs, G. P. Wozadlo, K. Nakata, T. Yoshida and I. Masaoka, "Radiation Effects on the Stress Corrosion and Other Selected Properties of Type-304 and Type-316 Stainless Steels," *Proc. 3rd Int. Symp. on Env. Deg. of Mat. in Nucl. Pow. Systems-Water Reactors*, TMS, Traverse City, MI (1987) p. 673.

6. A. J. Jacobs, C. M. Shepherd, G. E. C. Bell and G. P. Wozadlo, "High-Temperature Solution Annealing as an IASCC Mitigation Technique," *Proc. 5th Int. Symp. on Env. Deg. of Mat. in Nucl. Pow. Systems-Water Reactors*, ANS, Monterey, CA (1991) p. 917.

7. M. Kodama, S. Nishimura, J. Morisawa, S. Suzuki, S. Shima and M. Yamamoto, "Effects of Fluence and Dissolved Oxygen on IASCC in Austenitic Stainless Steels," *Proc. 5th Int. Symp. on Env. Deg. of Mat. in Nucl. Pow. Systems-Water Reactors*, ANS, Monterey, CA (1991) p. 948.

8. M. Kodama, R. Katsura, J. Morisawa, S. Nishimura, S. Suzuki, K. Asano, K. Fukuya and K. Nakata, "IASCC Susceptibility of Austenitic Stainless Steels Irradiated to High Neutron Fluence," *Proc. 6th Int. Symp. on Env. Deg. of Mat. in Nucl. Pow. Systems-Water Reactors*, TMS, San Diego, CA (1993) p. 583.

9. M. Kodama, K. Fukuya and H. Kayano, "Influence of Impurities and Alloying Elements on IASCC in Neutron Irradiated Austenitic Stainless Steels," *Effects of Radiation on Materials: 16th International Symposium, ASTM STP 1175*, A. S. Kumar, D. S. Gelles, R. K. Nanstad and E. A. Little, Eds., American Society for Testing and Materials, Philadelphia (1993) p. 889.

10. K. Fukuya, S. Shima, K. Nakata, S. Kasahara, A. J. Jacobs. G. P. Wozadlo, S. Suzuki and M. Kitamura, "Mechanical Properties and IASCC Susceptibility in Irradiated Stainless Steels," *Proc. 6th Int. Symp. on Env. Deg. of Mat. in Nucl. Pow. Systems-Water Reactors*, TMS, San Diego, CA (1993) p. 565.

11. P. L. Andresen, F. P. Ford, S. M. Murphy and J. M. Perks, "State of Knowledge of Radiation Effects on Environmental Cracking in Light Water Reactor Core Materials," *Proc. 4th Int. Symp. on Env. Deg. of Mat. in Nucl. Pow. Systems-Water Reactors*, NACE, Jekyll Island, GA (1989) p. 1-83.

12. C. P. Ruiz, C. C. Lin, R. N. Robinson, W. G. Burns, J. Henshaw and R. Pathania, "Model Calculations of Water Radiolysis and Electrochemical Potentials in BWR Primary Coolant II," *Proc. 6th Int. Conf. Water Chemistry Nucl. Reactor Syst., Vol. 2*, BNES, London (1992) p. 141.

13. D. D. MacDonald, "Viability of Hydrogen Water Chemistry for Protecting In-Vessel Components of Boiling Water Reactors," *Corrosion*, 48 (March 1992) p. 194.

14. Proceedings of Symposium on *Radiation Damage in Reactor Materials*, International Atomic Energy Agency (June 1969).

15. S. W. Bruemmer and E. P. Simonen, "Radiation Hardening and Radiation-Induced Chromium Depletion Effects on Intergranular Stress Corrosion Cracking of Stainless Steels," *CORROSION / 93*, National Association of Corrosion Engineers (1993) Paper 616.

16. K. Asano, K. Fukuya, K. Nakata and M. Kodama, "Changes in Grain Boundary composition Induced by Neutron Irradiation on Austenitic Stainless Steels," *Proc. 5th Int. Symp. on Env. Deg. of Mat. in Nucl. Pow. Systems-Water Reactors*, ANS, Monterey, CA (1991) p. 838.

17. J. M. Cookson, D. L. Damcott, G. S .Was and P. L. Andresen, "The Role of Microchemical and Microstructural Effects in the IASCC of High Purity Austenitic Stainless Steels," *Proc. 6th Int. Symp. on Env. Deg. of Mat. in Nucl. Pow. Systems-Water Reactors*, TMS, San Diego, CA (1993) p. 573.

18. S. W. Bruemmer, J. I. Cole, J. L. Brimhall, R. D. Carter and G. S. Was, "Radiation Hardening Effects on Localized Deformation and Stress Corrosion Cracking of Stainless Steels," *Proc. 6th Int. Symp. on Env. Deg. of Mat. in Nucl. Pow. Systems-Water Reactors*, TMS, San Diego, CA (1993) p. 537.

19. A. J. Jacobs, "The Relationship of Grain Boundary Composition in Irradiated Type 304SS to Neutron Fluence and IASCC," *Effects of Radiation on Materials: 16th International Symposium, ASTM STP 1175*, A. S. Kumar, D. S. Gelles, R. K. Nanstad and E. A. Little, Eds., American Society for Testing and Materials, Philadelphia (1993) p. 902.

20. S. W. Bruemmer, B. W. Arey and L. A. Charlot, "Grain Boundary Chromium Concentration Effects on the IGSCC and IASCC of Austenitic Stainless Steels," *Proc. 6th Int. Symp. on Env. Deg. of Mat. in Nucl. Pow. Systems-Water Reactors*, TMS, San Diego, CA (1993) p. 277.

21. H. Mansoux, "Experimental Determination of Radiation Induced Segregation Susceptibility in Austenitic Stainless Steels," SM Thesis, Department of Nuclear Engineering, Massachusetts Institute of Technology, Cambridge, MA (June 1994).

22. C. Flores, "Evaluation of Radiation Induced Segregation in Fe-Ni-Cr Alloys," SM Thesis, Department of Nuclear Engineering, Massachusetts Institute of Technology, Cambridge, MA (June 1994).

23. H. Mansoux, A. Garratt-Reed, R. G. Ballinger, G. Kohse and O. K. Harling, "Experimental Determination of Radiation Induced Segregation Susceptibility in Austenitic Stainless Steels," submitted to *J. Nucl. Mat.*

24. A. J. Jacobs, G. P. Wozadlo, K. Nakata, S. Kasahara, T. Okada, S. Kawano and S. Suzuki, "The Correlation of Grain Boundary Composition in Irradiated Stainless Steel with IASCC Resistance," *Proc. 6th Int. Symp. on Env. Deg. of Mat. in Nucl. Pow. Systems-Water Reactors*, TMS, San Diego, CA (1993) p. 597.

25. Y. Iwabuchi, T. Fujimoto, Y. Watanabe and T Shoji, *Aziryo-to-Kankyo* (in Japanese), 42 (1993) p. 2.

26. Irradiation Assisted Stress Corrosion Cracking and BWR Chemistry Studies, Fifth Annual Progress Report for Period August 1992 - August 1993, Report No. MITNRL-055 (August 1993) p. 2-68.

27. Y. Watanabe, R. G. Ballinger and G. E. Kohse, "Effects of Neutron Irradiation on Transpassive Corrosion Behavior of Austenitic Stainless Steels," submitted to *J. Nucl. Mat.*

CHAPTER 8

CONCLUSIONS AND RECOMMENDATIONS

Man is not born to solve the problems of the universe, but to find out where the problems begin, and then to take his stand within the limits of the intelligible.

Johann Wolfgang von Goethe
(1755- 1802)

8.1 DISCUSSION

This section summarizes the findings of this thesis and presents recommendations for future work and for modifications to the existing facility. The various aspects of irradiation assisted stress corrosion cracking (IASCC) which have been studied in this program have been discussed in each of the respective sections and an attempt to integrate these findings and evaluate their contribution to IASCC will be pursued in greater depth in this section. Figure 8-1 graphically depicts the materials, mechanical and environmental interactions that contribute to IASCC. The neutron radiation causes defects, thermal spikes, which develop into defect clusters and dislocation loops and consequently induce hardening. The integrated flux also causes segregation of the alloying elements resulting in depletion of chromium, iron and molybdenum and enrichment of nickel and phosphorus at the grain boundaries and possibly at other sinks. The radiation flux may enhance film breakup and hence slip dissolution of the material under strain. Certainly the neutron and gamma ray flux cause radiolysis producing chemistry changes in the bulk coolant and at the crack tip. These interactions of radiation on microstructure and microchemistry, water coolant chemistry and mechanical properties have been investigated in this thesis.

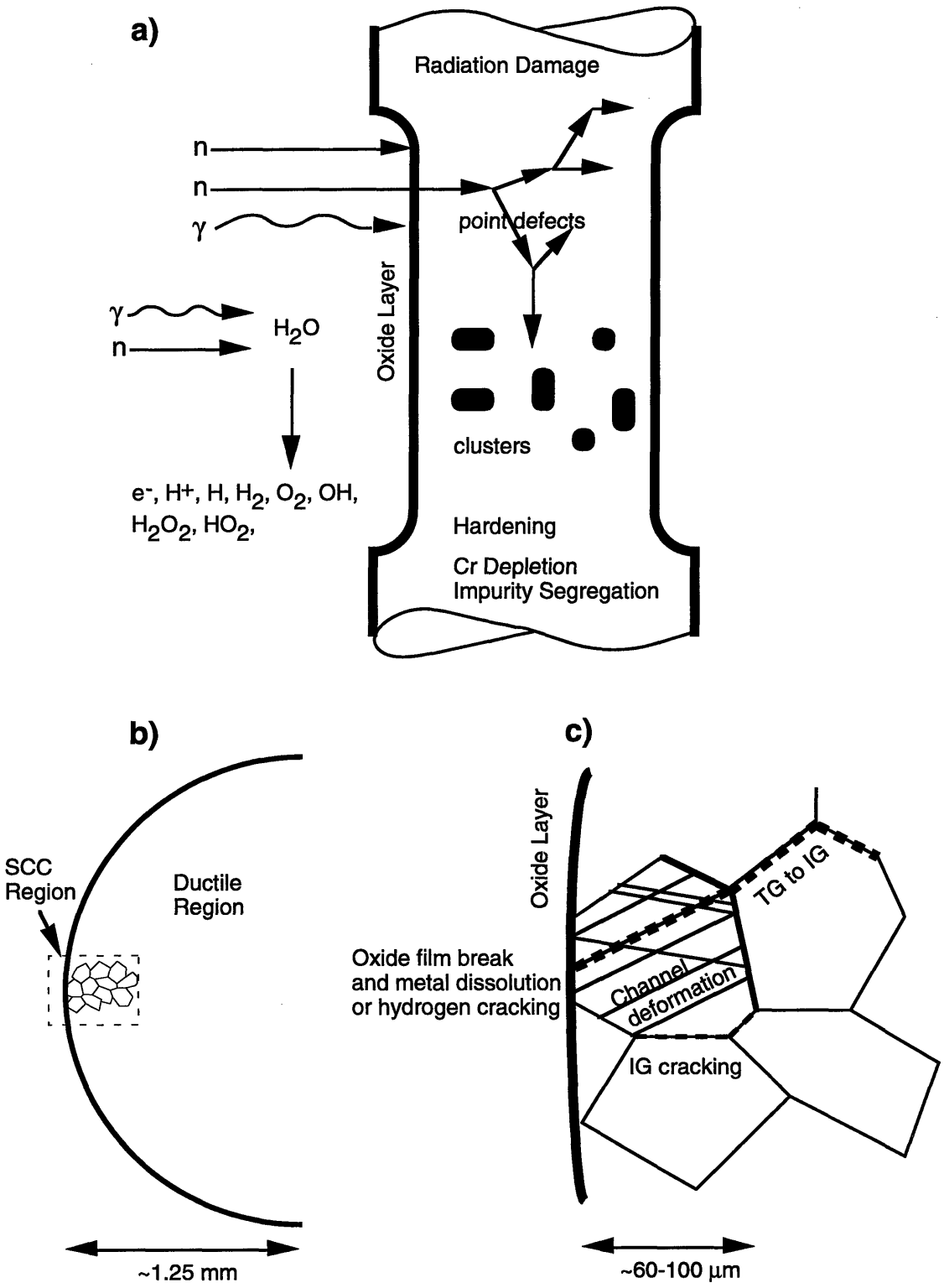

Figure 8-1. IASCC of low fluence stainless steels described by materials, mechanical, environmental and radiation interactions; b) and c) represent plan views of a SSRT specimen.

8.2 MICROSTRUCTURAL AND MICROCHEMICAL PARAMETERS

The contribution of microstructural and microchemical parameters to IASCC was investigated by electrochemical corrosion tests and by analytical electron microscopy. As reported in this thesis, transpassive potentiostatic dissolution behavior, energy dispersive x-ray analysis with a scanning transmission electron microscope and microstructural identification with a transmission electron microscope were used to characterize the microstructure and microchemistry of unirradiated and irradiated austenitic stainless steel alloys tested by in-flux slow strain rate testing. As documented in the MIT IASCC Fifth Annual Report[1], the double loop electrochemical potentiokinetic reactivation (EPR) technique was also employed for this type of characterization.

8.2.1 Electrochemical Corrosion Test Results

The transpassive potentiostatic behavior of the tested irradiated stainless steels indicated the presence of faulted dislocation loops along {111} planes. Furthermore, the observed corrosion behavior suggested a distribution of dislocation loop sizes with greater amounts of RIS preferentially occurring at the larger loops. While a bulk impurity index of the minor elements silicon and phosphorus (wt%Si + wt%P x 10) correlated with intergranular attack and dissolution charge density[2], the bulk impurity index did not correlate with %IGSCC. For the materials tested (300 series austenitic stainless steel), the transpassive corrosion behavior was explained by the expected radiation induced enrichment of silicon and phosphorus at the grain boundaries and at point defect sinks, like faulted dislocation loops, within the matrix. It should be noted that the commercial purity 304 SS had the highest dissolution rates for the TPD technique in both the unirradiated and post-irradiated conditions.

The TPD results were compared with Coriou (HNO_3/Cr^{6+}) results by normalizing the dissolution charge densities of irradiated samples with the dissolution charge densities of unirradiated samples. A plot of %IG against the normalized transpassive charge density indicated a positive correlation with TPD. All data reported in the literature fell within a well-defined region, however the MIT results were below the lower boundary limit (see Figure 8-2). The lower susceptibility of the alloys tested at MIT can be interpreted by two differences in the testing methodologies.

First, the MIT %IG data were obtained from in-flux SSR tests, whereas the literature data were compiled from out-of-flux SSR tests. The different dependence of impurity content on

%IG for in-flux and out-of-flux tests reveals information about an IASCC mechanism. The negative impact of impurities on IASCC resistance has been related to hydrogen-impurity

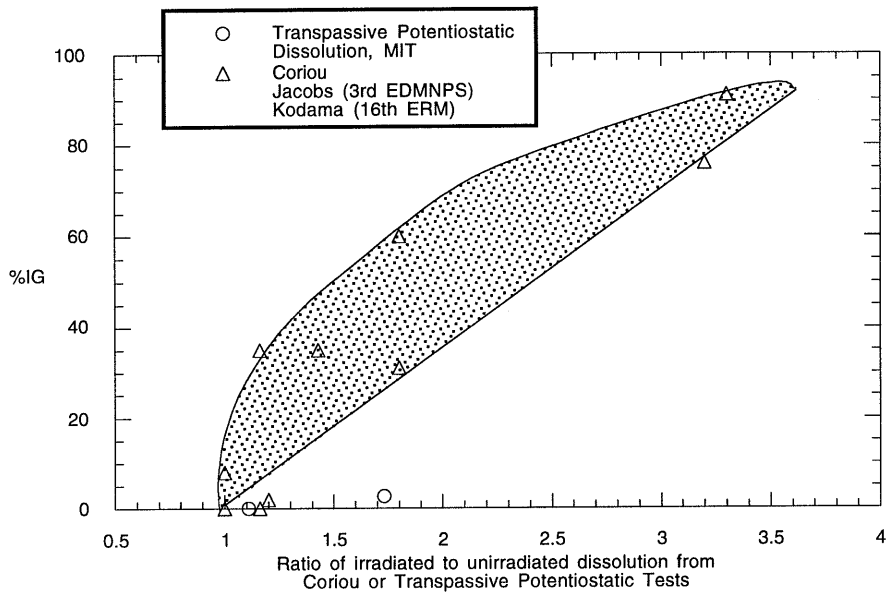

Figure 8-2. Dependence of IASCC susceptibility on Coriou and Transpassive Potentiostatic Ratios of irradiated to unirradiated austenitic stainless steels.

synergisms that induce brittle failure[3]. Post-irradiation chemical analyses of type 304 stainless steel have shown enhanced hydrogen concentrations (by a factor of ~3) and in-flux hydrogen concentrations are expected to be even greater[4]. Based on these observations, in-flux SSRTs should show a stronger correlation between impurity level and IASCC susceptibility than exhibited in out-of-flux SSRTs. Figure 8-2 shows the reverse trend, hence the different behavior observed between the MIT in-flux data and published out-of-flux laboratory data suggests that hydrogen assisted cracking is not the IASCC mechanism.

An alternative explanation is derived from another difference in the MIT and published data test methodologies. The MIT normalized charge densities were obtained from TPD, but the literature charge densities were measured with HNO_3/Cr^{6+} corrosion tests. While the normalized charge densities of the TPD and HNO_3/Cr^{6+} tests showed similar trends with bulk impurity level (see Figure 7-10), the TPD technique may exhibit a greater sensitivity to IASCC susceptibility. A higher sensitivity would shift the lower susceptibility limit down (i.e. decrease the slope) as observed in Figure 8-2. Coriou (HNO_3/Cr^{6+}) tests on irradiated and unirradiated samples of the alloys used in the MIT tests would be the simplest way to distinguish any differences. If there are no differences between the TPD and Coriou normalized dissolution

charge densities results, then flux differences alone remain to explain the lower IASCC susceptibility measured in flux. And the flux differences are inconsistent with current interpretations of a hydrogen embrittlement mechanism and impurity synergisms.

A modified double loop EPR technique was used to indicate radiation-induced chromium depletion on the grain boundaries. According to the SEM analysis after the tests, there was extensive pitting-like dissolution on grain surfaces rather than corrosive attack at the grain boundaries. In addition, EPR ratios did not correlate with grain boundary chromium depletion measured by STEM-EDX. While these observations indicate that EPR ratios of low fluence stainless steels do not represent chromium depletion at the grain boundaries, they demonstrate chromium depletion at intra-grain radiation-produced defects[1]. A more important finding, albeit based on very limited data (two samples: 0.8×10^{25} n/m^2 CP type 304 and 0.74×10^{25} n/m^2 316L), is that EPR ratios correlate with IASCC susceptibility of low fluence stainless steel. The positive correlation between EPR of low fluence materials and %IG observed in this work and the correlation between EPR of high fluence materials and %IG applied in crack growth modeling has the following interpretation. At low fluences, EPR is dominated by bulk radiation damage which is a more reliable measure of microstructure sensitization. At high fluences, EPR is dominated by grain boundary chromium depletion which shows similar trends to thermal sensitized microstructures. Although the data is very scarce, it suggests that EPR can be used as an engineering measure of stainless steel's microstructure sensitization to IASCC.

8.2.2 STEM and TEM Results

Experimentally determined radiation induced segregation (RIS) in the austenitic stainless steels tested by in-flux SSR technique was compared to IASCC susceptibility (%IG). The RIS measurements, performed by STEM/EDX, consisted of five and eight profiles examined on four and seven grain boundaries from CP 304 and 316L alloys, respectively. The amount of segregation observed in samples from the MIT "dry irradiation" experiment fell within the fluence trend observed by other researchers. But it should be noted that the amount of segregation compared represents the maximum observed change in grain boundary composition (i.e. there were a number of grain boundaries that exhibited very little segregation). The variance in grain boundary chemical composition has been observed in other studies on neutron irradiated material, although it is generally not seen in ion irradiated materials. An average value is not considered statistically meaningful because of the small number of grains and profiles sampled. Besides, the difference in RIS between grains may be related to a physical characteristic not determined. Grain boundary geometry or orientation has been suggested to explain the variance between the chemical composition of the grain boundary, but so far no direct evidence has been produced by TEM.

Figure 8-3 depicts the %IG dependence on segregation of Cr, Ni and Si at the grain boundaries of CP type 304 and 316L based on data from the MIT in-flux SSRTs and published data from out-of-flux laboratory tests on similar materials and irradiation conditions. Only modest amounts of segregation were observed in the alloys tested in this thesis. The CP type 304 (heat AJ9139) showed the largest maximum changes and exhibited the greatest IASCC susceptibility in the SSRTs. Yet the magnitude of the changes were just slightly higher than seen in the 316L (heat K5) alloy specimens which exhibited no SCC. Moreover, comparison of the in-flux and out-of-flux data showed no obvious trend of RIS and %IG nor was there a striking difference for the two testing methodologies. Since the observed RIS in these two alloys was not remarkably different, it seems unlikely that their respective RIS behavior is the dominant factor that distinguishes the behavior of their mechanical properties and susceptibility to IASCC as observed in the SSR tests.

8.3 ELECTROCHEMICAL CORROSION POTENTIAL (ECP) MEASUREMENTS

Corrosion potential (ECP) measurements were made for stainless steel in water chemistry conditions simulating single phase BWR coolant. The ECP measurements were correlated with dissolved oxygen and hydrogen concentrations on the letdown line for conditions typical of BWR normal water chemistry (NWC) conditions and hydrogen water chemistry (HWC) conditions. During in-core SSR tests, these species concentrations were used to characterize the bulk water chemistry in-core with an in-core Pt reference sensor used as a secondary measurement. Although the Pt reference ECP sensor is not a reversible electrode under NWC[5], its potential correlated with the ECP of stainless steel and it was therefore used as an engineering tool. As discussed in a previous section, the 304 SS ECP was measured by Pt and Ag/AgCl reference electrodes. The ECP measured by the Ag/AgCl reference sensors is used for NWC conditions, and the ECP measured by the Pt sensors is used for hydrogen addition. In principle both reference sensor types operate under HWC, but in practice the Pt reference sensor is more reliable[5]. This was the experience in the present work (cf. Chapter 5 for details).

Figure 8-4 summarizes the ECP measurements made during the test series at rig position one. For this test series, the lower cluster (1) was at the core midplane and the upper cluster (2) was at 228.6 mm (9 in) above the midplane and cluster 3 was on the letdown line. The dose rates at 4.5 MWt were 2.56×10^5 R/s and 1.47×10^5 R/s for neutron and gamma ray, respectively, at the core midplane and 2.12×10^4 R/s and 2.55×10^4 R/s for neutron and gamma ray, respectively, at the upper core elevation. Figure 8-4a shows the dependence of 304 SS ECP

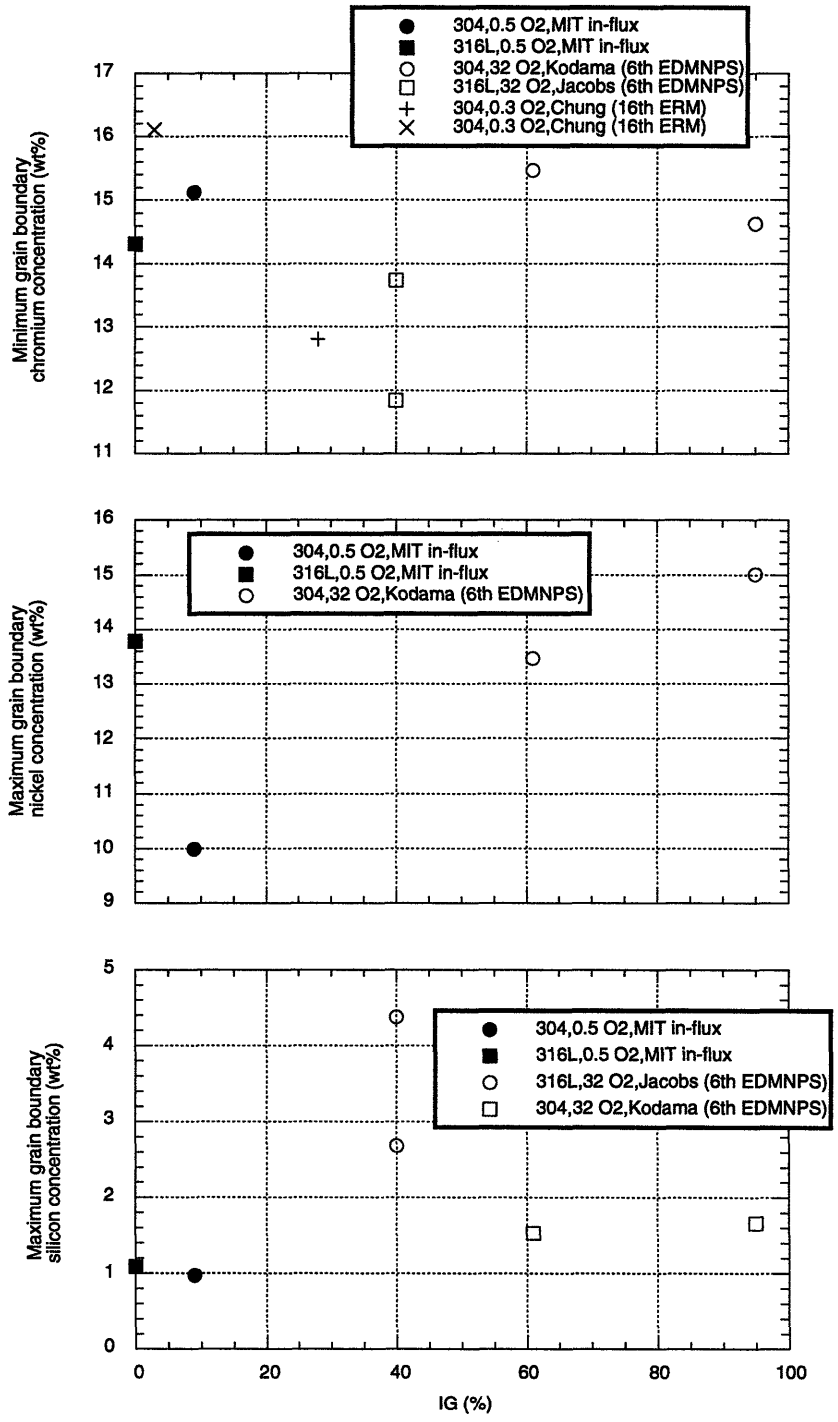

Figure 8-3. IASCC susceptibility of types 304 and 316L austenitic stainless steels dependence on maximum RIS grain boundary changes in chromium, nickel and silicon concentrations.

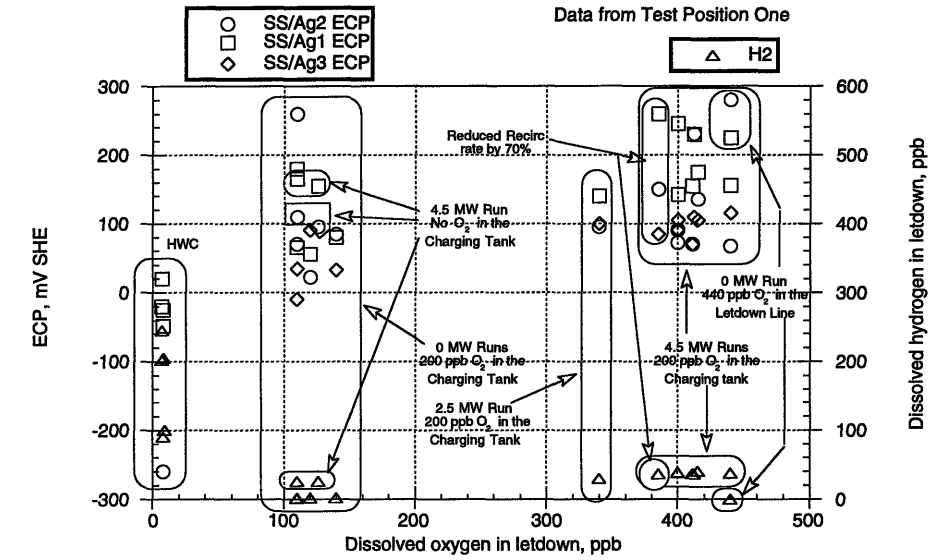

(a)

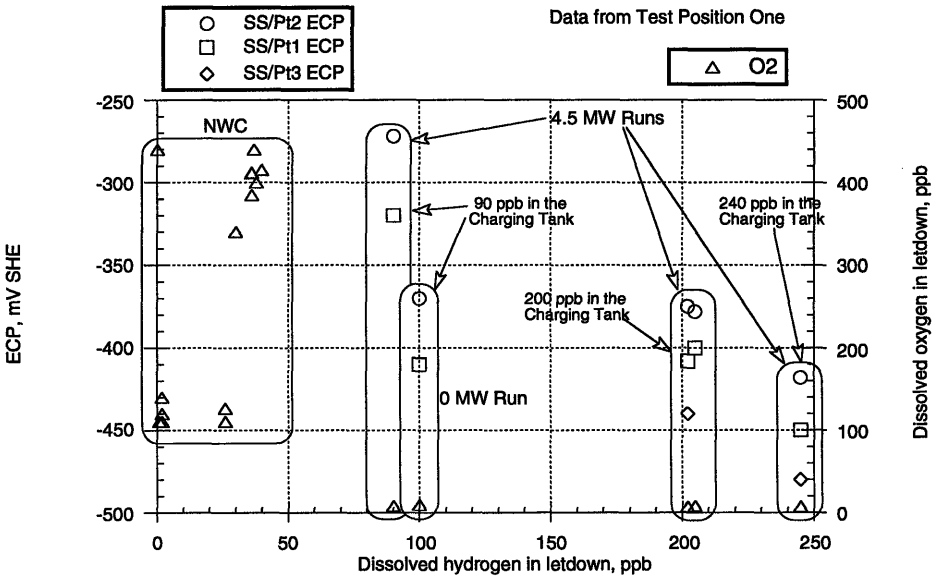

(b)

Figure 8-4. Measurements of 304 SS ECP in MITR-II core under a) NWC and b) HWC.

on recirculation flowrate, reactor power and inlet oxygen concentration under NWC while Figure 8-4b depicts the effect of hydrogen addition concentration and reactor power under HWC.

The most significant results are recapped here. Under NWC, the 304 SS ECP increased by 70-140 mV when the recirculation rate was reduced by 30%. This corresponds to a modest decrease in coolant velocity from 1.3 m/s to 0.91 m/s which is not expected to limit mass transport[6,7] of oxidizing species. The residence time is increased by 50% which would increase radiolysis and net production of oxidant under normal water chemistry. There are no corresponding flowrate effect measurements under HWC to compare. The water radiolysis appears to saturate below a reactor power of 2.5 MWt since the difference between 304 SS ECP at 2.5 MWt and 4.5 MWt is only 20 mV. In fact, the ECP under oxidizing conditions did not vary for the zero flux tests either. However, under HWC the ECP decreased by ~60 mV when ramping the reactor power down from 4.5 MWt to shutdown condition. A final observation from Figure 8-4 is the efficacy of hydrogen addition in suppressing the ECP below the critical potential of -230 mV (SHE) for IGSCC. At 100 ppb hydrogen, the ECP of stainless steel is below -250 mV (SHE) and below -350 mV (SHE) at 200 ppb hydrogen. While hydrogen water chemistry was not utilized during the SSR test phase, the ECP Mapping results demonstrated the feasibility of implementing HWC conditions with this and other in-core materials testing facilities[8,9] designed for use in the MITR-II.

8.4 MECHANICAL PROPERTIES AND FRACTURE MODE

8.4.1 SSRT Results

The in-flux mechanical properties measured for the austenitic stainless steel alloys CP type 304 (heat AJ9139) and 316L (heat K5) pre-irradiated to ~0.8 x 10^{25} n/m^2 are summarized in this section (see Table 8-1). Out-of-pile zero flux data for the same alloys and heats were obtained for comparison with the in-flux SSR results. All MIT tests were performed at BWR simulated conditions: the zero flux tests had a higher oxygen concentration to account for oxidizing species produced by in-core radiolysis. The results were used to identify differences and similarities between instantaneous flux effects and the accumulated radiation damage. As previously discussed (cf. section 4.6), the experimental uncertainty for the zero flux and in-flux properties is estimated to be ~10% because of the different facilities employed. Because of this uncertainty and the few data obtained per specific alloy and material condition (sometimes only one), any mechanical property trends discussed are presently speculative and must be confirmed by

Table 8-1. Summary of SSRT[a] results for MIT IASCC program.

Specimen Description[b]	Spec. No.	Fluence (x10^{25} n/m^2)	S_y (MPa)	S_u (MPa)	n[c] value	t_f (h)	e_f (%)	RA (%)	v_{avg} (10^{-6} mm/s)	TG (%)	IG (%)
Zero-flux CP 304 (AJ9139)	89[d]	0	262	503	0.374	1.78	52	NA	•	yes[d]	0[d]
316L (K5)	17[d]	0	211	440	0.367	1.54	45	72[d]	•	0[d]	0[d]
CP 347 (K12)	32[d]	0	228	440	0.353	0.41	41	70[d]	•	0[d]	0[d]
CP 304 (AJ9139), CW	2005	0	562	865	0.198	3.14	11	30	•	•	0
CP 304 (AJ9139), CW+SEN	2012	0	632	860	0.21	48.6	6	10	3.07	•	12
347L (K12)	2021[e]	0	243	446	0.28	2.2	•	•	•	0	0
In-flux CP 304 (AJ9139)	98	0	316	563	0.328	234	37	73	•	0	0
CP 304 (AJ9139), SEN	2003[f]	0	182	336	0.25	89.2	16	< 5	3.96	0	97
CP 304 (AJ9139)	80[g]	0.80	517	605	0.114	101	•	•	0.113	0.3	0
CP 304 (AJ9139)	81	0.80	570	677	0.114	127	22	59	0.557	1.9	1.8
CP 304 (AJ9139)	82	0.80	536	706	0.119	143	20	48	0.662	2.0	2.7
316L (K5)	10	0.74	294	564	0.298	204	32	84	N/A	0	0
316L (K5)	11	0.74	338	543	0.239	203	31	84	N/A	~0	~0

a SSRTs conducted in 280°C water at strain rate of ~4 x 10^{-7} s^{-1} in-flux and 0.4-60 x 10^{-6} s^{-1} in zero-flux. Feedwater oxygen was 8ppm and 0.5ppm for zero flux and in-flux SSRTs, respectively. In-flux tests were in MITR-II core (~5x10^{13} n/cms).
b All specimens were solution annealed (1050C x 0.5hrs) before any other pretreatment. Abbreviations are sen: furnace sensitized at 650C x 10hrs, cw: 30% cold work.
c n is the strain hardening exponent defined as Stress = m x $(Strain)^n$.
d Data from P. Lidar's DCPD-SSRT autoclave tests[10] The RA, %TG and %IG are from Shoji et al.[11]
e SSRT performed in-core at 0 MWt. Test halted at 36% strain.
f Specimen was bent during SSRT, so mechanical properties are qualitative.
g SSRT halted at 15% strain.

additional SSR tests. With that *proviso* in mind, a more detailed discussion of the in-flux SSR results follows.

The mechanical properties of commercial purity type 304 and 316L alloys measured in zero-flux and in-flux SSRT are summarized in Figure 8-5. Trends observed in the pre-irradiated specimens tested in-flux were similar to results in out-of-flux SSRT. As depicted in a) and b), the yield stress and ultimate stress increased and in c) and d) the strain to failure and strain hardening exponent decreased. In general, changes in mechanical properties of the pre-irradiated CP type 304 were greater than for the pre-irradiated 316L alloy. For the CP 304 alloy, a 20% increase in the yield strength was observed for the unirradiated specimen tested in-flux compared to out-of-flux testing. Assuming the 20% increase in yield is physical, then the damage from an instantaneous radiation flux increases a material's resistance to plastic flow, at least in the initial stages of deformation. This is not too surprising since a prominent feature of accumulated radiation damage in metals is a hardened microstructure manifested as an increase in yield stress[12,13]. A simple extrapolation of post-irradiation material results predicts in-flux hardening via processes that inhibit dislocation motion in irradiated metals out-of-pile.

A simple analysis was used to evaluate the physical interpretation of *in situ* hardening. This simple analysis compared the characteristic time for nucleation and growth of dislocation loops with the interaction time between a glissile dislocation and a radiation produced obstacle. The analysis showed that for slow strain rates the interaction time of a dislocation and an obstacle was much greater than the characteristic time for nucleation of Frank faulted loops. For slow strain rates, a field of dislocation loops would develop to the saturation concentration and a dislocation loop would act as a barrier to dislocation motion. At higher strain rates, the dislocation loops would not have time to develop and the damage would be limited to nascent cascade and the transient point defect population. A transition from slow strain rate to fast strain rate behavior was estimated to occur when the interaction time is equal to the characteristic time for dislocation loop nucleation. Categorizing radiation defects as either long range or short range obstacles based on an Orowan mechanism, the increase in yield stress was calculated as a function of strain rate (see Figure 8-6). The predicted increase in yield stress was less than the measured increase, but was the same order of magnitude. A more detailed calculation of the defect populations for short time scales is recommended for improving the accuracy of the prediction.

According to the analytical model described above, *in situ* hardening is predicted to increase the in-flux yield stress of a pre-irradiated metal by only a small amount. A direct comparison between model predictions and experimental data was not possible because there were no out-of-flux SSRTs on the pre-irradiated CP 304 alloy. And an indirect comparison with out-of-flux autoclave tests on pre-irradiated samples was not conclusive due to the large scatter in

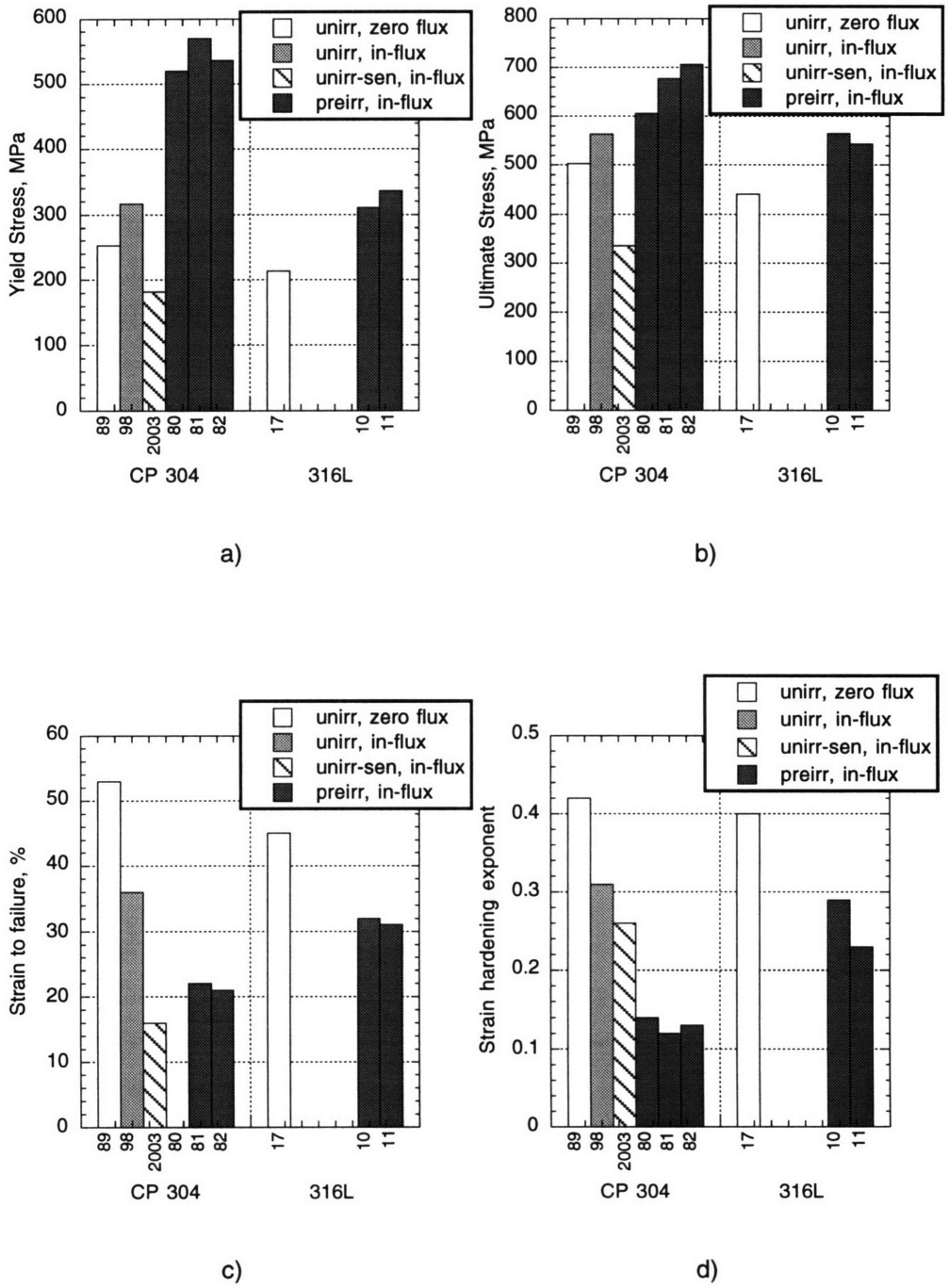

Figure 8-5. Summary of mechanical properties of types 304 SS and 316L SS measured in SSRT:a) yield stress, b) ultimate stress, c) failure strain and d) strain hardening exponent.

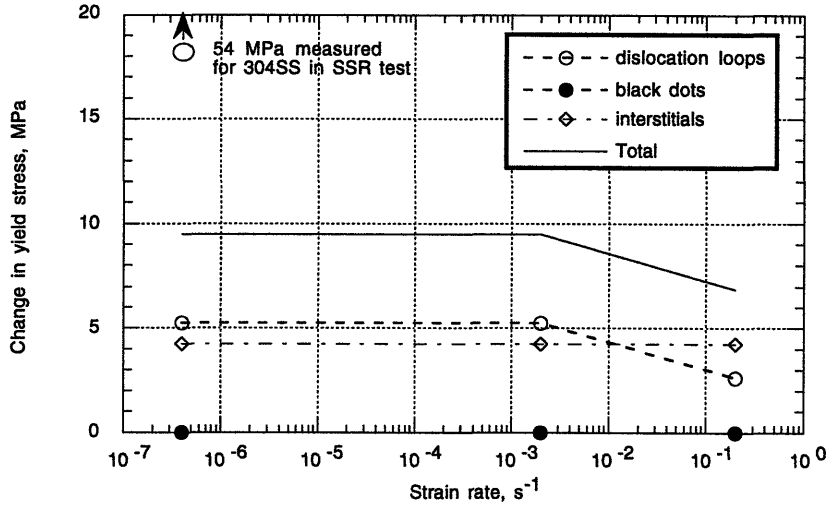

Figure 8-6. Contribution of irradiation induced microstructures to the increased yield stress for in-flux material tests at different strain rates.

data for the different heats (material chemistries) and irradiation conditions. For a fluence of 0.8 x 10^{25} n/m^2, yield stress increases of CP type 304 are reported to be 70-350 MPa or 146-330% of the unirradiated yield stress[14]. Yield stress increases of the CP type 304 (AJ9139) measured in the in-flux SSRTs were 270-320 MPa or 206-225% of the unirradiated yield stress. Since these values fall within the range of out-of-flux tests data, *in situ* radiation damage does not appear to increase the yield stress beyond the hardening from pre-irradiation. But, the incremental difference in yield stress predicted from *in situ* hardening is less than the scatter of out-of-flux data. Therefore the predicted effect may be undetectable by this comparison with the out-of-flux data of other CP type 304 heats. A direct comparison with zero-flux yield stress data of the CP type 304 (AJ9139) pre-irradiated to 0.8 x 10^{25} n/m^2 is necessary to make a conclusive evaluation of the model predictions.

For irradiated austenitic stainless steels, the yield stress increases more than the ultimate stress until they become equal. At high fluences ($\geq$ 1.5 x 10^{25} n/m^2)[15] the effect of radiation reaches a saturation state beyond which the yield and ultimate stresses plateau. The smaller difference in yield and ultimate stress essentially reduces the strain hardenability of the metal after the onset of plastic deformation. For all CP type 304 specimens tested in flux there is a decrease in strain hardening, as depicted by the normalized strain hardening exponent values. The strain hardenability of the pre-irradiated and unirradiated CP type 304 were reduced by 70%

and 30%, respectively, of the unirradiated material tested in zero flux. The loss of strain hardening in the pre-irradiated CP type 304 is similar to that seen in out-of-pile tests and the reduced strain hardening of the unirradiated is consistent with *in situ* embrittlement reflected by changes in other mechanical properties (e.g. yield stress and strain to failure).

In situ embrittlement reflected as a loss of ductility in the unirradiated CP type 304 (#98) tested by in-flux SSRT was proportionally higher than the additional hardening. The decrease in ductility (total elongation) was 30% compared to a 20% increase in hardening (yield stress). While hardening is related to embrittlement, the dislocation channeling deformation mechanism identified in the unirradiated CP 304 alloy would cause a greater decrease in ductility. Still there is a considerably greater loss in ductility for the pre-irradiated CP type 304 specimens (#80, 81, 82) which was around 60%. An almost equal ductility loss was observed for the furnace sensitized specimen (70% loss of ductility).

The 316L alloy normalized mechanical properties indicate that this heat is particularly resistant to radiation damage. The normalized values are quite similar to those observed for the unirradiated CP type 304 sample tested in-core and show much less degradation in performance compared to pre-irradiated CP 304 alloy. The superior mechanical performance of the pre-irradiated type 316L correlated with its relatively higher resistance to IASCC (cf. section 5.3.3). Based on the in-flux SSR tests of samples irradiated to 0.8×10^{25} n/m^2 fluence, type 316L shows much improved IASCC performance based on its mechanical properties compared to commercial purity type 304, which is more commonly found in reactor vessel structural components

The relationships between the mechanical properties and IASCC susceptibility (%IG) were evaluated. Trends for the in-flux SSRT specimens fell within those of out-of-flux SSRT data published in the literature. While a different IASCC susceptibility dependence on fluence was observed for types CP 304 and 316L, the dependence on yield stress was the same. Plotting the MIT in-flux data and out-of-flux laboratory data, the %IG dependence on yield stress for types 304 and 316 stainless steels is shown in Figure 8-7. The different IASCC susceptibilities observed for types 304 and 316L (investigated by in-flux SSRT) also indicate that yield stress is a fundamental parameter influencing IASCC behavior.

8.4.2 SEM Results

The SEM analysis of types 304 and 316L stainless steel tested by in-flux SSR provided information on IASCC susceptibility, fracture morphology and deformation characteristics. IASCC susceptibility was quantified by three parameters: percentage intergranular fracture (%IG), reduction in area (RA) and average crack velocity (v_{avg}). The %IG was used to rank the susceptibility of the samples and to compare the in-flux SSRT results of this work with published out-of-flux SSRT results. V_{avg} and RA, determined by SEM, were also found to be appropriate

IASCC susceptibility indices for the low fluence stainless steels investigated. Trends for the three susceptibility indices were similar as seen from the data in Table 8-1.

All three indices showed that the furnace sensitized CP type 304 had the highest susceptibility and that pre-irradiated CP 304 alloy ranked higher in susceptibility than the pre-irradiated 316L alloy. Considering that %IG was only ~2% for the pre-irradiated CP type 304 specimens, the good agreement between the different indices demonstrated the high sensitivity of each method. While susceptibility to initiate stress corrosion cracks was concluded to be

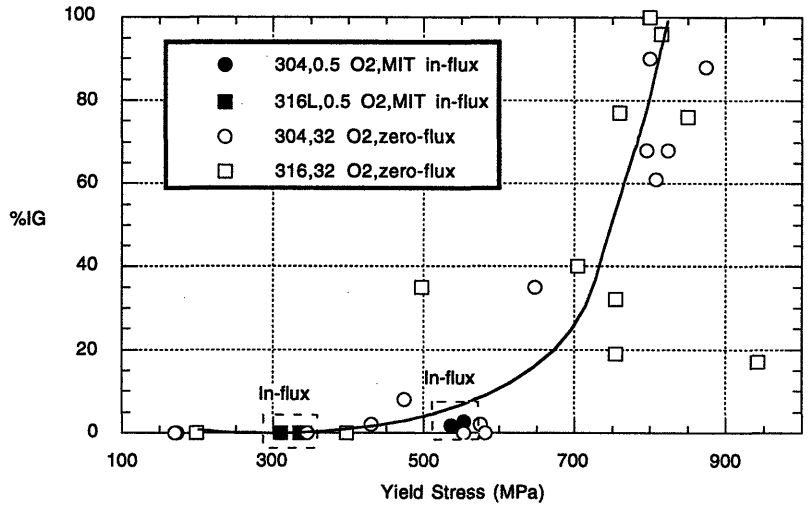

Figure 8-7. IASCC susceptibility dependence on yield stress.

comparable for the furnace sensitized and radiation sensitized CP type 304, susceptibility for continued crack propagation was much smaller in the radiation sensitized specimens. The different susceptibilities were inferred from crack geometry observations on the gage side. Both specimens had many secondary cracks on the gage side, but the furnace sensitized specimen (#2003) had cracks with a high aspect ratio (5:1) while the radiation sensitized specimens (#80, 81 and 82) had many cracks with a low aspect ratio (2:1). The blunted cracks observed on the side and SEM observations of the crack path morphology on the fracture surface can be explained by the dissolution mechanism.

For the furnace sensitized CP type 304 specimen, cracks initiated and propagated intergranularly. This contrasts with the pre-irradiated CP type 304 specimens which showed transgranular cracking at initiation that changed to intergranular paths at ~60-100 μm. Crack growth by a dissolution mechanism involves a balance between the kinetics of film rupture,

dissolution and repassivation. When the crack tip velocity becomes comparable to the crack sides growth rate by dissolution alone, the crack blunts and crack growth ceases. Since transgranular crack velocity is ~5-10 times less than intergranular cracking[16], at the same strain rate, the initial crack tip growth rate of the radiation sensitized CP type 304 would have been much lower than that of the furnace sensitized specimens. While the intergranular crack tip velocity was high enough to maintain sharp cracks, the transgranular crack tip velocity may have been comparable to dissolution on the crack sides resulting in blunted cracks or pits. A transition from transgranular to intergranular fracture within the crack can also be explained by the dissolution mechanism. As the crack grows, the crack tip solution acidifies, even for short cracks, which increases the solubilities of the matrix elements . The low pH of the crack tip solution could favor dissolution at the grain boundaries rather than within the matrix and change the preferred fracture path from transgranular to intergranular. The interpretation of a dissolution mechanism causing crack blunting is straightforward, however the interpretation of the fracture path transition from TG to IG has some inconsistencies. The major inconsistency is the absence of a deformation mechanism since the same chemical acidification process that occurs for the final crack will occur for every crack that initiated. Then every crack should exhibit a fracture morphology transition and there is nothing to distinguish the blunt cracks from the crack that led to failure. Some interesting observations from SEM were made regarding deformation mechanism, but none pertained to the transition question.

The major conclusion on deformation mechanisms was about dislocation channeling. Heavy slip markings were observed on the pre-irradiated CP 304 and 316L alloys and on the unirradiated CP type 304 specimen tested in flux. Comparison of the surface slip markings provided indirect evidence that dislocation channeling was the main deformation mode in the pre-irradiated stainless steel and unirradiated stainless steel under flux. There was no correlation between the intense slip bands and cracking. In fact, SCC areas on the fracture surface were associated with a lower density of slip markings on the side relative to the ductile failure areas. For the specimens that did not exhibit any SCC on the fracture surface (unirradiated CP type 304 and pre-irradiated 316L alloy), slip markings appeared uniformly across the cross section.

8.5 DIFFERENCES IN IASCC PERFORMANCE OF TYPES 304 AND 316L STAINLESS STEEL

The commercial purity type 304 (heat AJ9139) and type 316L (heat K5) which were pre-irradiated to a fluence of ~0.8×10^{25} n/m^2 and tested by in-flux SSR exhibited significantly different susceptibility to IASCC. Although the CP type 304 and type 316L SSRT specimens

utilized for in-flux SSRT were pre-irradiated at different core positions in the Dry Irradiation Rig, the accumulated fluence and irradiation temperature were virtually the same. The CP type 304 specimens accumulated a fluence of 0.8×10^{25} n/m^2 at 287°C and the type 316L specimens accumulated a fluence of 0.74×10^{25} n/m^2 at 287°C. While radiation induced segregation is a nonlinear function of fluence, the estimated material damage did not significantly differ for the small fluence differential of these specimens. More significant than the difference in fluence is the difference in material chemistry of the CP 304 and 316L alloys. The addition of molybdenum and reduction of carbon are recognized as imparting greater resistance to SCC. This may be true for IASCC as well. IASCC studies on ion irradiated high purity 304 stainless steel have indicated a higher nickel content as beneficial for IASCC resistance. The impact different chemical species have on IASCC resistance can be evaluated in terms of each chemical's effect on passive film characteristics (which affect dissolution and hydrogen embrittlement) and radiation damage (which leads to segregation and hardening).

Type 316L has been substituted for type 304 stainless steel for applications that require superior corrosion resistance. The alloying of molybdenum (~2-3%) is generally considered to give the steel a more resilient passive film. In the MIT electrochemical corrosion tests (EPR and TPD), the 316L alloy displayed less dissolution than the CP 304 alloy. This was true for both unirradiated and irradiated samples. Furthermore, the increase in dissolution after irradiation was smaller for the 316L alloy. This observation does not differentiate the compositional element or elements that decreased dissolution rates, yet it suggests that the reasons for 316L alloy's better corrosion resistance after irradiation may be the same as for unirradiated type 316L.

The same alloying elements that increase corrosion resistance have been proposed to increase radiation damage resistance. Theories of radiation induced segregation predict less segregation in the presence of big alloying elements (Mo, Ti and Ni). The predicted effect in suppressing RIS is proportional to the atomic size or more exactly the atomic size mismatch of the big alloying elements with the matrix element. In this regard, the molybdenum increases IASCC resistance indirectly by suppressing RIS and the microstructure sensitization. Since neither alloy exhibited strong RIS and the maximum observed changes were comparable, this predicted effect is not evident. A closer look at the grain boundary profiles suggests that on average, the CP type 304 had greater segregation than the type 316L. Another difference observed during STEM was the grain boundary width. Type 316L grain boundary widths were ~> 2 nm, whereas the grain boundary widths of CP type 304 were ≤ 2 nm. This difference in grain boundary geometry may influence RIS behavior, dissolution characteristics or mechanical strength properties.

The dependence between yield stress and IASCC susceptibility has already been discussed. But this certainly is an obvious difference between types 304 and 316L which correlates with %IG. An understanding of the different radiation hardening behavior will require

a more detailed analysis than presented in Chapter 6. This analysis may include carbide precipitates, dislocation loop formation, or the effect of grain boundary geometry. Based on the results of this thesis, the above reasons are all plausible but there is no definitive explanation of the relatively higher resistance to IASCC of 316L stainless steel compared to CP type 304.

8.6 COMPARISON OF IN-FLUX AND OUT-OF-FLUX SSR TESTS RESULTS

One of the motivating features for this work was to investigate the impact of instantaneous radiation effects on irradiation assisted stress corrosion cracking and to compare in-core data with data obtained in out-of-pile autoclaves using various oxygenated water chemistries to simulate BWR in-core environment. This section summarizes the major findings that distinguish in-flux SSR testing and comments on the relevance of out-of-pile testing for studying IASCC.

Figure 8-8 displays the percentage intergranular (%IG) dependence on fluence for CP type 304 and 316 alloys tested in out-of-pile autoclaves at various dissolved oxygen concentrations as well as the data from in-flux SSR testing. It is seen that the susceptibilities measured by the MIT in-flux SSRTs is within the experimental spread for data obtained in out-of-flux SSRTs at high oxygen levels (i.e. 8-32 ppm dissolved oxygen). Hence, from a phenomenological view point the susceptibility to IASCC of CP 304 and 316L alloys pre-irradiated to fluences ~0.8×10^{25} n/m^2 measured by in-flux SSR tests is comparable to trends observed in out-of-pile SSR tests conducted at high oxygen concentrations. This is an important point since a significant amount of data has been gathered at lower oxygen levels (e.g. 200 ppb) which is representative of recirculation line water chemistry, but not necessarily of the bulk water chemistry condition at in-core and near-core structural components. The phenomenological similarity between in-core SSRTs and out-of-flux SSRTs conducted at high oxygen levels has implications for the relevance of out-of-pile testing.

First, in-core IASCC susceptibility of low fluence stainless steel can be predicted by out-of-core SSRTs provided the dissolved oxygen concentration is at least 8 ppm. Second, the enhanced aggressiveness of out-of-core SSRTs is due solely to the mechanical component of constant straining since the maximum achievable oxygen concentration out-of-core corresponds to the in-core environment. Third, for IASCC studies an out-of-core SSRT environment with 8-32 ppm oxygen appears sufficiently similar to an LWR in-core environment with 0.2-0.5 ppm inlet oxygen. This last observation has implications for characterizing in-flux water chemistry (i.e. corrosion potential).

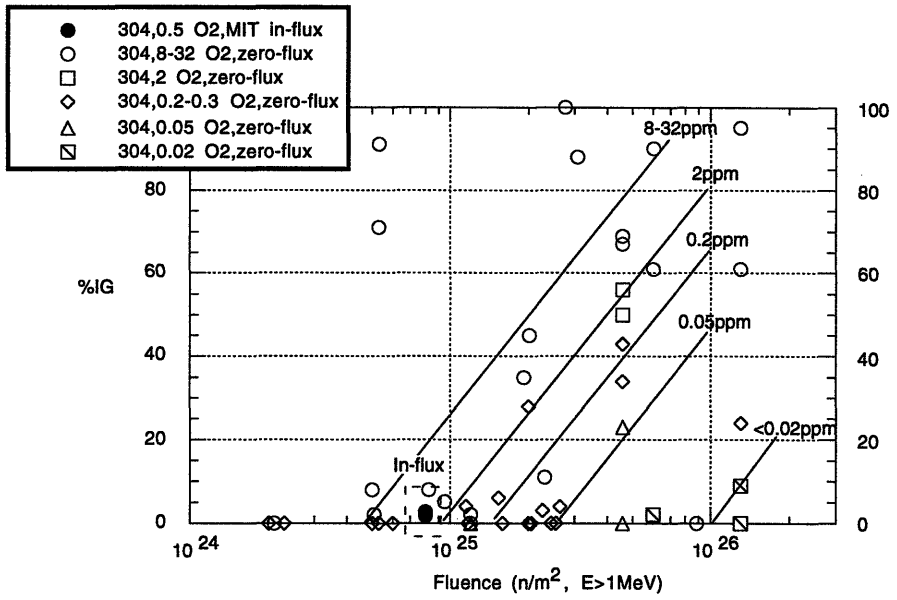

(a)

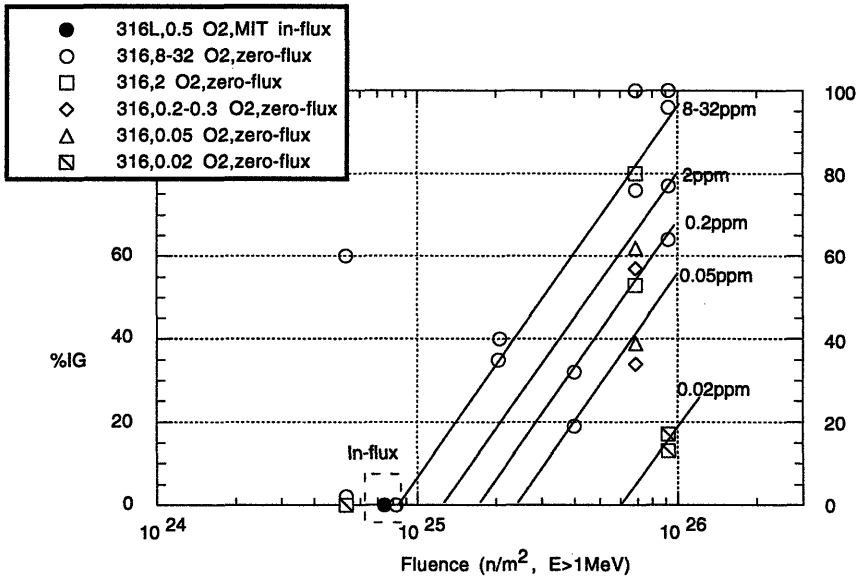

(b)

Figure 8-8. Fluence and dissolved oxygen dependence of IASCC susceptibility in a) types 304, 304L and b) types 316, 316L stainless steel (adapted from Kodama et al.[17]).

The conclusion of equivalent aggressiveness of the two environments based on similar SCC susceptibilities is consistent with the similarity of ECP measurements. While this gives further credence for using ECP as an in-flux environmental monitor, it has conflicting implications for in-flux ECP predictions by computer simulation. Corrosion potential (ECP) modeling relies solely on the concentrations of major oxidant species (oxygen, O_2, and hydrogen peroxide, H_2O_2) as input. In-flux oxidant concentrations change due to radiolysis which will tend to decrease to O_2 and produce H_2O_2. The net oxidant (oxygen + 8/17 hydrogen peroxide) calculated for the in-flux experiments was less than 0.6 ppm, whereas the %IG and ECP data from in-flux tests follows the out-of-pile trends for 8-32 ppm oxygen. While current corrosion potential modeling relies on only the O_2 and H_2O_2 concentrations, these results suggest that the contributions of other transient species or electrochemical reactions to the ECP should be incorporated.

The cracking morphology observed in the SCC susceptible CP 304 alloy tested by in-flux SSR tests was also consistent with fractographic observations made after zero flux SSRTs. The fracture morphology on the pre-irradiated CP type 304 specimens initiated as transgranular (TG) and showed a transition to intergranular (IG) fracture at ~60 μm. In out-of-core SSRTs on thermally treated CP 304 alloy, TG initiation and a transition to IG has been observed in lightly sensitized specimens[16]. Although the 0.8×10^{25} n/m^2 fluence of the specimens tested by in-flux SSRT is above the 0.5×10^{25} n/m^2 "threshold" to IASCC susceptibility, the microchemical and electrochemical tests all indicated a low level of radiation damage in both the CP 304 and 316L alloys. Therefore, the similarity in the fracture morphology of lightly sensitized CP type 304 indicates the SCC mechanism is the same for zero flux and in-flux tests. If more highly irradiated CP type 304 samples showed the same crack morphology in-flux, that would distinguish the in-flux and out-of-flux environments since SCC changes from TG to IG as the fluence increases in out-of-flux laboratory tests.

The deformation mechanism in-flux appears to be the same for stainless steels tested post-irradiation out-of-flux. Slip formations similar to markings identified as dislocation channeling in out-of-pile work[14,18] were observed on the pre-irradiated specimens (CP type 304 and 316L) and on the unirradiated CP 304 alloy. Similar to out-of-pile tests results, no correlation between the intense slip markings (evidence of dislocation channeling) and intergranular cracking was observed in the in-flux tests. In fact, SCC sites were centered in regions of low density of slip deformation.

Provided the trend of higher yield stress observed for the specimens tested in-flux is shown to be physically significant, it may have significant impact on IASCC susceptibility. Although for the in-flux tests a higher flow stress and reduced ductility were observed, these changes in macroscopic properties did not correlate with an increased susceptibility to IASCC.

Therefore, the in-flux hardening effect, although interesting from an academic and perhaps mechanistic view point, did not seem to influence the IASCC susceptibility relative to out-of-flux test results.

In conclusion, the IASCC susceptibility determined for CP type 304 and type 316L at ~0.8 x 10^{25} n/m^2 by in-flux SSR tests is similar to that found in out-of-flux SSR tests conducted at high oxygen concentrations (e.g. 8-32 ppm). Comparison of susceptibility, fracture morphology and deformation mode all showed an equivalence between in-flux and out-of-flux SSRT results for the low dose stainless steel investigated in this thesis. However, these comparisons are definitive. In fact, the *in situ* radiation flux was observed to increase the yield strength and decrease ductility, both of which have the tendency of embrittling a material. The embrittlement of a material could have consequences on IASCC susceptibility not revealed with the current test matrix. To more definitively establish the relationship between in-flux and out-of-flux materials test results, further in-flux testing on materials with a broader range of fluence is recommended.

8.7 FUTURE WORK AND RECOMMENDATIONS

The investigation of irradiation assisted stress corrosion cracking by means of the slow strain rate technique utilized only a small portion of the catalog of pre-irradiated tensile specimens available for testing. A small number of additional tests conducted with different alloys at similar fluences and with the same alloys at different fluences and environmental conditions (i.e. with and without neutron and gamma radiation flux and alternative hydrogen water chemistry) would provide valuable supplemental data for evaluating the independent and synergistic effects of the radiation on IASCC. These additional tests would address the specific issues of irradiation hardening under fast neutron flux, comparative effect of gamma only and gamma plus neutron effect on the specimen under slow strain conditions, and the contribution of minor elements and their role in IASCC mechanisms.

Most of these additional tests can be conducted with the present MITR-II test facility. For tests that will alter the radiation flux on the tensile specimen and the coolant, some straightforward modifications can be made. A simple strategy that will maintain the geometry and testing capability of the current internals facility is to fabricate a second internals facility with the necessary geometry. This can be done at a minimum cost since the material required would be non radioactive and the design work requires only slight modification of current plans (i.e. shortening the pull rod and placing a spacer beneath the lower grip to displace the water volume in-core formerly removed by the pull rod and lower grip assembly). Table 8-2 lists a proposed matrix of tests for future studies of irradiation assisted stress corrosion cracking.

Table 8-2. Proposed tests for future studies of IASCC with the MIT in-core SSR Test Facility.

Specimen	Water Chemistry/Dose Rate	Rig Modification
CP 304, 0 n/m^2	NWC/ neutron + gamma (4.5MW)	none
(2) CP 304, 0.8 x 10^{25} n/m^2	NWC/ zero flux	none with reactor off
(2) CP 304, 0 n/m^2	NWC/ zero flux	none with reactor off
(2) HP 304 (V945), 0.8 x 10^{25} n/m^2	NWC/ neutron + gamma (4.5MW)	none
(2) CP 304, 0.3 x 10^{25} n/m^2	NWC/ neutron + gamma (4.5MW)	none
(2) CP 304, 0.8 x 10^{25} n/m^2	NWC/ gamma (4.5MW)	shorter pull rod
(2) CP 304, 0 n/m^2	NWC/ gamma (4.5MW)	shorter pull rod

8.8 REFERENCES

1. Irradiation Assisted Stress Corrosion Cracking and BWR Chemistry Studies, Fifth Annual Progress Report for Period August 1992 - August 1993, Report No. MITNRL-055 (August 1993) p. 2-68.

2. Y. Watanabe, R. G. Ballinger and G. E. Kohse, "Effects of Neutron Irradiation on Transpassive Corrosion Behavior of Austenitic Stainless Steels," submitted to *J. Nucl. Mat.*

3. A. J. Jacobs, G. P. Wozadlo, K. Nakata, S. Kasahara, T. Okada, S. Kawano and S. Suzuki, "The Correlation of Grain Boundary Composition in Irradiated Stainless Steel with IASCC Resistance," *Proc. 6th Int. Symp. Env. Deg. Mat. Nucl. Power Syst.- Wat. React.*, TMS, San Diego, CA (1993) p. 597.

4. A. J. Jacobs, R. E. Clausing, L. Heatherly and R. M. Kruger, "Irradiation-Assisted Stress Corrosion Cracking and Grain Boundary Segregation in Heat Treated Type 304 SS," *Effects of Radiation on Materials: 14th International Symposium, Vol. I, ASTM STP 1046*, N. H. Packan, R. E. Stoller and A. S. Kumar, Eds., American Society for Testing and Materials, Philadelphia (1989) p. 424.

5. S. Sawochka, "Corrosion Potential (ECP) Measurement Sourcebook," EPRI Report NP-7142, Electric Power Research Institute, Palo Alto, CA (January 1991).

6. C. C. Lin and F. R. Smith, "Electrochemical Potential Measurements Under Simulated BWR Chemistry Conditions," EPRI Report NP-6732, Electric Power Research Institute, Palo Alto, CA (March 1990).

7. D. D. MacDonald, "Viability of Hydrogen Water Chemistry for Protecting In-Vessel Components of Boiling Water Reactors," *Corrosion*, 48 (March 1992) p. 194.

8. J. R. O'Donnell, "Design, Construction, and Commissioning of an In-Core Materials Testing Facility for Slow Strain Rate Testing," PhD Thesis, Department of Nuclear Engineering, Massachusetts Institute of Technology, Cambridge, MA (September 1994).

9. J. A. Vergara Aimone, "The Development of a Facility for the Evaluation of Environmentally Assisted Cracking of In-Core Structural Materials in Light Water Reactors," PhD Thesis, Department of Nuclear Engineering, Massachusetts Institute of Technology, Cambridge, MA (June 1992).

10. P. Lidar, "D. C. Potential Drop System Development," MIT Department of Nuclear Engineering, Cambridge, MA (1991).

11. T. Shoji, K. Yamaki, R. G. Ballinger and I. S. Hwang, "Grain Boundary Segregation and Intergranular Stress Corrosion Cracking Susceptibility of Austenitic Stainless Steels in High Temperature Water," *Proc. 5th Int. Symp. Env. Deg. Mat. Nucl. Power Syst.- Water Reactors,* ANS, Monterey, CA (1991) p. 827.

12. E. E. Bloom, "Irradiation Strengthening and Embrittlement," *Radiation Damage in Metals,* N. L. Peterson and S. D. Harkness, Eds., American Society for Metals, Metals Park, Ohio (1975) p. 295.

13. "The Effects of Radiation on Structural Metals," American Society for Testing and Materials STP 426, Atlantic City, NJ, 1966.

14. S. M. Bruemmer, J. I. Cole, J. L. Brimhall, R. D. Carter and G. S. Was, "Radiation Hardening Effects on Localized Deformation and Stress Corrosion Cracking of Stainless Steels," *Proc. 6th Int. Symp. on Env. Deg. of Mat. in Nucl. Power Systems- Water Reactors,* TMS, San Diego, CA (1993) p. 537.

15. H. M. Chung, W. E. Ruther, J. E. Sanecki, A. G. Hins and T. F. Kassner, "Stress Corrosion Cracking Susceptibility of Irradiated Type 304 Stainless Steels," *Effects of Radiation on Materials: 16th International Symposium, ASTM STP 1175,* A. S. Kumar, D. S. Gelles, R. K. Nanstad and E. A. Little, Eds., American Society for Testing and Materials, Philadelphia (1993) p. 851.

16. F. P. Ford, D. F. Taylor, P. L. Andresen and R. G. Ballinger, "Corrosion-Assisted Cracking of Stainless and Low-Alloy Steels in LWR Environments," EPRI Report NP-5064S, Electric Power Research Institute, Palo Alto, CA (February 1987).

17. M. Kodama, S. Nishimura, J. Morisawa, S. Suzuki, S. Shima and M. Yamamoto, "Effects of Fluence and Dissolved Oxygen on IASCC in Austenitic Stainless Steels," *Proc. 5th Int. Symp. on Env. Deg. Mat. in Nucl. Pow. Systems-Water Reactors,* ANS, Monterey, CA (1991) p. 948.

18. J. M. Cookson, R. D. Carter Jr., D. L. Damcott, M. Atzmon and G. S .Was, "Irradiation Assisted Stress Corrosion Cracking of Controlled Purity 304L Stainless Steels," *J. Nucl. Mat.,* 202 (1993) p. 104.

GLOSSARY

Everything should be made as simple as possible, but no simpler.

Albert Einstein
(1879-1955)

Most non-standard terminology is defined at the location of first use. For reference, less common shorthand designators are listed below.

AEM. Analytical Electron Microscopy.

BCCL. BWR Coolant Chemistry Loop.

BWR. Boiling Water Reactor.

CER. Constant Extension Rate.

CIR. Cooperative IASCC Research.

CP. Commerical Purity.

DCB. Double Cantilever Beam.

DCPD. D. C. voltage Potential Drop. A method for strain measurement which correlates the change in resistance of a tensilely loaded material (due to geometrical and material characteristic changes) with its true elongation.

DI. De-Ionized.

DPA. Displacements Per Atom. Indicative of amount of accumulated radiation damage and used as an equivalent measure of fluence (integrated flux of radiation). In this report 1 dpa ~0.7×10^{21} n/cm^2 (E>1.0 MeV).

EAC. Environmentally Assisted Cracking.

ECP. Electrochemical Potential and/or Corrosion Potential.

EDX. Energy Dispersive X-rays.

EMAC. Electrode MAterial Characterization.

EPR. Electrochemical Potentiokinetic Reactivation.

EPRI. Electric Power Research Institute.

ESEERCO. Empire State Electric Energy Research COrporation.

FEG. Field Emission Gun.

Fluence. Integrated flux of radiation. Indicative of amount of accumulated radiation damage.

GE. General Electric.

HAC. Hydrogen Assisted Cracking.

HE. Hydrogen Embrittlement.

HP. High Purity.

HWC. Hydrogen Water Chemistry.

IASCC. Irradiation Assisted Stress Corrosion Cracking.

IC. Ion Chromatograph analysis.

ICG-IASCC. International Cooperative Group on IASCC.

IG. InterGranular.

IGA. InterGranular Attack.

IGSCC. InterGranular Stress Corrosion Cracking.

LVDT Linear Variable Differential Transformer.

LWR. Light Water Reactor.

MIT NRL. MIT Nuclear Reactor Laboratory.

MITR-II Massachusetts Institute of Technology upgradedresearch Reactor.

NRHX. Non-Regenerative Heat eXchanger.

NRL. Nuclear Reactor Laboratory.

NRT. Norgett-Robinson-Torrens.

NWC. Normal Water Chemistry.

PCCL. PWR Coolant Chemistry Loop.

PKA. Primary Knock-on Atom.

PSB. Persistent Slip Band.

PWR. Pressurized Water Reactor.

RA. Reduction of Area.

RADICAL. RADIation Chemistry Analysis Loop.

RGHX. ReGenerative Heat eXchanger.

RIS. Radiation Induced Segregation.

SCC. Stress Corrosion Cracking.

SEM. Scanning Electron Microscope.

SHE. Standard Hydrogen Electrode.

SSR. Slow Strain Rate.

SSRT. Slow Strain Rate Test.

STEM. Scanning Transmission Electron Microscope.

TEM. Transmission Electron Microscope.

TEPCO. Tokyo Electric Power COmpany.

TG. TransGranular.

TGSCC. TransGranular Stress Corrosion Cracking.

TPD. Transpassive Potentiostatic Dissolution.

UHP. Ultra High Purity.

APPENDIX A

RADICAL INPUT CHEMISTRY SET

Wisdom denotes the pursuing of the best ends by the best means.

Francis Hutcheson
(1694-1746)

A.1 BACKGROUND

Radiolysis water chemistry simulations require a defined chemistry reaction data set and primary radiolysis species production per unit energy values (G values) for neutron and gamma ray radiation. Round robin comparisons of computed chemical concentrations using different radiation water chemistry simulators have shown mutual agreement provided the chemical reactions and G-value data sets are the same[1]. Reaction data sets have increased in complexity including for example, nitrogen reactions for N-16 appraisal and reactions for metal ions like copper and iron that tend to suppress recombination which can affect the amount of hydrogen necessary for HWC implementation. For the ECP modeling discussed in Chapter 3 of this thesis, only the basic "water" reactions are included. Several different sets available in the literature and from personal communication were evaluated in the theses by Chun[2] and Mason[3]. The input chemistry set used in the RADical computer modeling of this thesis was adopted from the reaction rate data (Table A-1) and G-values (Table A-2) agreed to by consensus at the August 1992 MIT Radiolysis Workshop.

Table A-1. Reaction Rate Data Set for the radiation water chemistry simulations using RADical (reaction constants set by consensus at MIT Radiolysis Workshop, August 1992).

Name	Reaction	k_o (s^{-1})	Ea (kJ/mol °K)
F3	$e^- + H_2O \rightarrow H + OH^-$	1.6e1	12.55
F4	$e^- + H^+ \rightarrow H$	3.5e11	0.e0
F5	$e^- + OH \rightarrow OH^-$	2.0e10	12.55
F6	$e^- + H_2O_2 \rightarrow OH + OH^-$	1.3e11	0.e0
F7	$H + H \rightarrow H_2$	8.5e10	0.e0
F8	$e^- + HO_2 \rightarrow HO_2^-$	2.0e10	12.55
F9	$e^- + O_2 \rightarrow O_2^-$	2.6e11	0.e0
*F10	$e^- + e^- \rightarrow OH^- + OH^- + H_2$	5.e9	12.55
F11	$OH + OH \rightarrow H_2O_2$	1.7e10	0.e0
F12	$H + OH^- \rightarrow e^- + H_2O$	2.0e7	18.83
F13	$H + e^- \rightarrow H_2 + OH^-$	2.5e10	12.55
F14	$HO_2^- + e^- \rightarrow OH + OH^- + OH^-$	3.5e9	12.55
F15	$H + OH \rightarrow H_2O$	5.5e10	0.e0
F16	$OH + H_2 \rightarrow H + H_2O$	4.e7	18.02
R16	$H + H_2O \rightarrow OH + H_2$	1.04e-4	85.17
F17	$H + O_2 \rightarrow HO_2$	8.6e10	0.e0
F18	$H + HO_2 \rightarrow H_2O_2$	2.e10	12.55
F19	$H + O_2^- \rightarrow HO_2^-$	2.e10	12.55
*F20	$O_2^- + e^- \rightarrow HO_2^- + OH^-$	1.3e8	18.83
F21	$H + H_2O_2 \rightarrow OH + H_2O$	9.e7	16.61
F22	$H_2O_2 + OH \rightarrow H_2O + HO_2$	3.e7	13.01
F23	$HO_2 + OH \rightarrow O_2 + H_2O$	8.6e10	0.e0
F24	$H_2O_2 + OH^- \rightarrow HO_2^- + H_2O$	1.8e10	12.55
*R24	$HO_2^- \rightarrow H_2O_2 + OH^-$	5.7e5	18.83
F25	$HO_2 + HO_2 \rightarrow O_2 + H_2O_2$	8.5e5	22.82
F26	$HO_2 \rightarrow H^+ + O_2^-$	2.57e4	12.55
R26	$O_2^- + H^+ \rightarrow HO_2$	5.e10	12.55
F27	$HO_2 + O_2^- \rightarrow HO_2^- + O_2$	5.e9	0.e0
F29	$H^+ + OH^- \rightarrow H_2O$	1.44e11	12.55
*R29	$\rightarrow H^+ + OH^-$	0.71	12.55
F30	$OH + O_2^- \rightarrow O_2 + OH^-$	8.6e10	0.e0
TIF	$1/2O_2 + 1/2O_2 \rightarrow O_2$	1.e15	0.e0
TI	$H_2O_2 \rightarrow 1/2O_2$	0.3	0.0
* water implicit reactions			

Table A-2. G-values for the radiation water chemistry simulations using RADical (based on GE High Temperature G-values, 1992)

Species	Neutron (#/100 ev)	Gamma (#/100 ev)
$e(aq)^-$	1.395	3.76
H^+	1.395	3.76
H	0.75	0.70
H_2	1.32	0.80
H_2O_2	1.485	0.28
HO_2	0.06	0.
OH	1.635	5.50
O	0.	0.
H_2O	-4.725	-6.06

A.2 COMMENTS ON DATA INPUT

The data set listing is for the most part self-explanatory, but a few points of clarification are in order. The data set input accepts room temperature reaction rate constants and activation energies used to extrapolate the constants to high temperature. An Arrhenius relationship is used:

$$k = ko \exp\left\{\frac{Ea}{R}\left(\frac{1}{To} - \frac{1}{T}\right)\right\}, \quad \text{(A-1)}$$

where:

T_o is the reference temperature which is taken as room temperature (298°K),

T is the temperature of interest in degrees Kelvin,

k is the reaction rate constant at temperature T and

k_o is the reaction rate constant at the reference temperature, T_o,

The units of reactants and products concentration are moles per liter and the necessary units for reaction rate constants, k_o, based on a first order reaction. The units of k_o, are not given in Table A-2, but can be determined from the generic equation:

$$A + B \rightarrow C + D, \quad \text{(A-2)}$$

$$\frac{d[A]}{dt} = -k[A][B]. \quad \text{(A-3)}$$

where

A and B are reactants,

C and D are products,

[ ] denotes the concentration in moles per liter and

k is the reaction rate constant at the temperature of interest.

One explanatory comment on the hydrogen peroxide, H_2O_2, decomposition reaction employed in RADical. Although RADical is not designed to accept fractional stoichiometry, a realistic H_2O_2 decomposition reaction was used in the reaction data set such that

$$H_2O_2 \rightarrow 1/2\ O_2 + H_2O. \qquad \text{(A-4)}$$

The problem of dealing with a fractional stoichiometric coefficient was solved by assuming 1/2 O_2 as a fictitious species, say X, and adding a reaction between 2 moles of species X that had a very large rate constant. Hence whenever X is generated, O_2 will be produced immediately. Following this scheme the reactions are as follows:

$$H_2O_2 \rightarrow X + H_2O \qquad \text{(A-5)}$$

and

$$X + X \rightarrow O_2,\ ko \approx 1x10^{15}\ s^{-1}. \qquad \text{(A-6)}$$

A.3 REFERENCES

1. L. W. Hu, "Radiolysis Calculations and Hydrogen Peroxide Measurements for the MIT BWR Coolant Chemistry Loop," SM Thesis, Department of Nuclear Engineering, Massachusetts Institute of Technology, Cambridge, MA (June 1993).

2. J. Chun, "Modeling of BWR Chemistry," SM Thesis, Department of Nuclear Engineering, Massachusetts Institute of Technology, Cambridge, MA (September 1990).

3. V. Mason, "Chemical Characterization of Simulated Boiling Water Reactor Coolant," SM Thesis, Department of Nuclear Engineering, Massachusetts Institute of Technology, Cambridge, MA (May 1990).

APPENDIX B

DETERMINATION OF MECHANICAL PROPERTIES

There must be a beginning of any great matter, but the continuing unto the end until it be thoroughly finished yields the true glory.

Sir Francis Drake
(c1540-1596)

B.1 INTRODUCTION

The mechanical properties determined from SSRTs were presented in Chapter 4. In general, standard practices as described in ASTM E-8 were followed and principles of data analysis outlined in an ASM publication on *Tensile Testing*[1] were adhered to. Because some properties were not measured directly and others included special considerations of the in-core facility characteristics, details of the procedures applied in calculating stress, strain and strain rate are presented here.

B.2 ENGINEERING AND TRUE STRESS

The engineering stress was determined from the applied load of the tensile testing machine and the cross sectional area of the SSRT specimen gage section. Because the SSRT was conducted at high pressure (12.1 MPa), it was necessary to calibrate the load machine for this offset at the start of each SSRT. Pressure drift throughout the test was less than 0.07 MPa (10 psi) which corresponded to an uncertainty of 4 MPa (i.e. 0.7-1.0% of yield) in the engineering stress reported. True stress was not determined directly since no *in situ* area measurements were made.

The true stress was calculated assuming constant volume deformation up to the point of necking. The equation is listed below:

$$\sigma = \frac{P}{A_o}(1+e) = s(1+e) \qquad \text{(eq. B-3)}$$

where

σ is the true stress,

P is the load,

A_0 is the initial area,

s is the engineering stress and

e is the engineering strain.

During SSRT, the load was sampled every 22 seconds. For the data reported in Chapter 4, the averages of successive sets of 20 data points were plotted and used for determining the stress.

B.3 ENGINEERING AND TRUE STRAIN AND STRAIN RATE

In calculating the engineering strain of a tensile specimen, the deflection of the loading instrument is a non-negligible component of the total extension. The in-core SSRT Rig was especially flexible due to the very long (4 m) pull rod. Specimen strain was solely determined from the total extension, so the load-deflection (compliance) behavior was quantified prior to commissioning of the SSRT Rig[2]. A linear function of the rig compliance was determined to be adequate for the range of loads applied during SSRT. For the strain calculation, deformation was assumed to be limited to the parallel portion of the gage section which had a length of 12.7mm (0.50±0.01 in.). This neglects any deformation that may have occurred in the radius and shoulder. The latter is justified because the ratio of shoulder to gage section areas exceeded the ratio of ultimate to yield stress of the specimens tested and the former gives only a small uncertainty. The equation used for calculating engineering strain based on the total extension and rig compliance follows:

$$e = \frac{\left[\Delta x - \Delta x_o - (P - P_o)/C\right]}{x} + \frac{P_o}{A_o E}$$

$$e = \frac{\left[\Delta x - \Delta x_o - (P - 156.8)/19706\right]}{0.5} + \frac{156.8}{(\pi 0.05^2)2.486x10^7}, \qquad \text{(eq. B-4)}$$

where

e is the engineering strain,

Δx and Δx_0 are the extension and the pre-load extension,

P and P_0 are the load and pre-load,

C is the rig compliance,

x is the gage length,

A_0 is the initial area and

E is Young's modulus.

The values are for english units which are inches per inch for strain, inches for length, pounds for load, pounds per inch for compliance and pounds per square inch for stress and pressure. Based on the uncertainty of the load and compliance, the experimental uncertainty of the strain measurement is estimated to be less than 3% (i.e. relative error of 8%). Comparison of calculated strain with optical length measurements of specimens 2005, 2012 and 82 after fracture indicated the actual error was smaller.

Since specimen strain was not measured by an *in situ* technique, like reversing DC potential drop (DCPD), true strain was estimated assuming a constant volume during deformation until necking initiated. The expression is listed below,

$$\varepsilon = \ln(1+e), \qquad \text{(eq. B-5)}$$

where

ε is the true strain and

e is the engineering strain.

The same scheme adopted for reporting the stress data was used for the strain data (i.e. averaged over 6.5 minute intervals which consisted of twenty data points taken at 22 second intervals).

The strain rate reported was an estimate of the specimen extension rate based on the increase in engineering strain per unit time interval. The 0.00198 mm/hr (0.001 in/hr) extension rate applied in the in-core SSRT was near the lower resolution limit of the tensile machine's linear variable differential transformer (LVDT). An average strain rate calculated over one hour was considered more representative of the applied strain rate because of this resolution limitation and the effects of noise and small pressure fluctuations in the facility. Therefore the strain rate was determined from the difference in strain measured over a time of one hour.

B.4 REFERENCES

1. *Tensile Testing*, ASM 440, P. Han, Ed., ASM International, Materials Park, OH (1992).

2. J. R. O'Donnell, "Design, Contruction, and Commissioning of an In-Core Materials Testing Facility for Slow Strain Rate Testing," PhD Thesis, Department of Nuclear Engineering, Massachusetts Institute of Technology, Cambridge, Ma (September 1994).